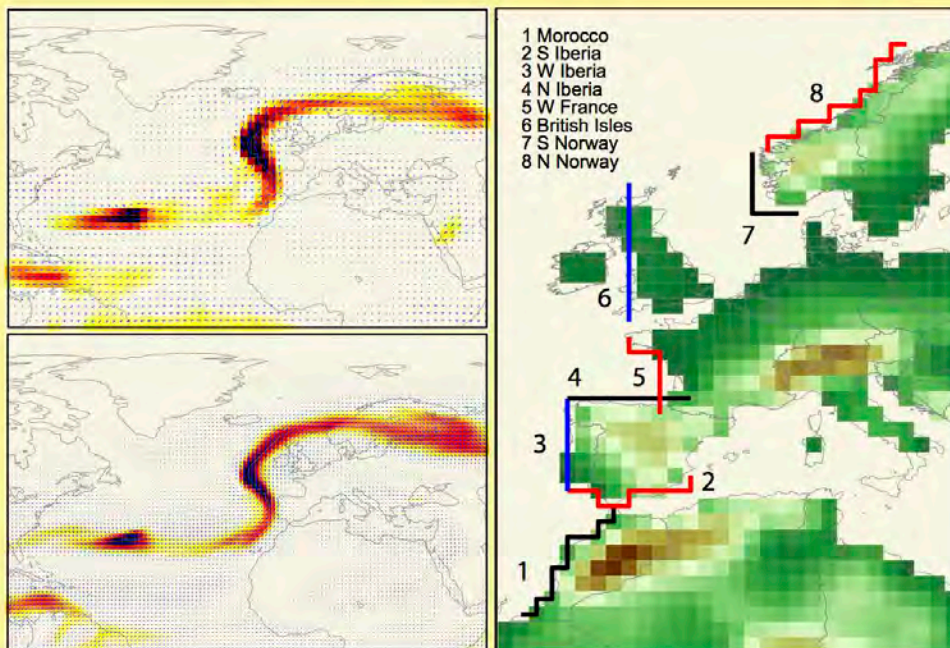


**PhD THESIS**

**OCEANIC AND ATMOSPHERIC PRECURSORS OF  
ATMOSPHERIC RIVER ACTIVITY ALONG THE WEST  
COASTS OF EUROPE AND WESTERN NORTH AMERICA**

**TESIS DOCTORAL**

**RÍOS ATMOSFÉRICOS EN LAS COSTAS OESTE DE  
EUROPA Y AMÉRICA DEL NORTE Y SUS  
PRECURSORES ATMOSFÉRICOS Y OCEÁNICOS**



**AUTHOR:** SWEN BRANDS

**SUPERVISOR:** José Manuel Gutiérrez Llorente

PHD THESIS

Oceanic and Atmospheric Precursors of Atmospheric River  
Activity Along the West Coasts of Europe and Western  
North America

Ríos Atmosféricos en las Costas Oeste de Europa y América  
del Norte y sus Precursores Atmosféricos y Oceánicos

PHD IN SCIENCE, TECHNOLOGY AND COMPUTING

Presented by  
SWEN BRANDS

under the supervision of  
Dr. José Manuel Gutiérrez



University of Cantabria

Santander (Spain), 05 April 2017

---

**Oceanic and atmospheric precursors of atmospheric river activity along the west coasts of Europe and western North America**

Swen Brands  
Physics Institute of Cantabria (IFCA)  
CSIC-University of Cantabria  
Santander, Spain

and

MeteoGalicia - Xunta de Galicia  
Galician Institute for Meteorology and Oceanography  
Santiago de Compostela, Spain

April 2017

---

*Diese Arbeit is meiner Familie und denen gewidment, die einen Platz in meinem Herzen haben. Im Besonderen sind das mein Freund Flo, meine Mutter, mein Vater, Maria, meine Oma, Lucy und mein Sohn Nils.*

---

## Acknowledgements

Several years have now passed since I began to work in the present thesis. During these, I have had the opportunity to collaborate with many devoted researchers from the fields of Meteorology, Informatics, Physics, Mathematics and Environmental Science who all helped me to gain the knowledge I have today. Without the (ongoing) support from these people, it would have been impossible to develop this work.

First, I would like to thank the staff from the Santander Meteorology Group, particularly Dr. Sixto Herrera, for helping me to gain programming skills in the early stage of the PhD programme, and for stretching out a helping hand whenever needed. It has also been a pleasure to share the office with Dr. Joaquín Bedia and Dr. Rodrigo Manzananas during these years when, albeit mostly working on distinct issues, we were all essentially doing the same thing, that is developing our capabilities as young investigators. During this phase, I have also had the opportunity to establish collaborations with Dr. Judah Cohen (MITâs Parsons Lab), whom I would like to thank for supporting my studies. I would also like to thank Dr. Nieves Lorenzo for organizing a research stay at the Environmental Physics Laboratory of the University of Vigo and for letting me collaborate in her studies.

I much appreciate the help of Jorge Eiras and Daniel Garaboa from the Nonlinear Physics Group of the University of Santiago de Compostela for discussing the definition of an atmospheric river and for resolving many issues related to *Unix* systems during a research stay kindly made possible by Dr. Gonzalo Míguez Macho.

The technical staff maintaining the High Performance Cluster of the Santander Meteorology Group, particularly Valvanuz Fernández and Fernando García, Antonio S. Cofiño and Jesús Fernández, played a key role in resolving day-to-day issues related to informatics and also in compiling and running the Community Atmosphere Model for the purposes of the present thesis. Thanks also to Maria Eugenia Magariño for helping to post-process the model data applied here.

With regard to the external data used here, I acknowledge the Joint Institute for the Study of the Atmosphere and Ocean (JISAO), the University Corporation for Atmospheric Research (UCAR) and NOAA's Earth System Research Laboratory (ESRL) for providing their respective climate indices.

The following reanalysis developers are acknowledged (see Table 3.4 for the source URLs of the respective data):

- The National Oceanic and Atmospheric Administration (NOAA) and the Cooperative Institute for Research in Environmental Sciences (CIRES) for providing the Twentieth Century Reanalysis version 2
- The European Centre for Medium-Range Weather Forecasts (ECMWF) for providing the ERA-20C and ERA-Interim reanalyses
- The National Centers for Environmental Prediction (NCEP) and the National Center for Atmospheric Research (NCAR) for providing the NCEP/NCAR reanalysis 1

I also acknowledge the World Climate Research Programme's Working Group on Coupled Modelling, which is responsible for the Fifth Phase of the Coupled Model Intercomparison Project (CMIP5), and I thank the climate modeling groups, particularly 1) the Pierre Simon Laplace Institute (IPSL), 2) the Canadian Centre for Climate Modelling and Analysis (CCCma) and 3) the Bjerknes Centre for Climate Research, for producing and sharing their model output. I am grateful to the United States Department of Energy's Program for Climate Model Diagnosis and Intercomparison, as well as to the Earth System Grid Federation (ESGF), for providing the facilities to retrieve the corresponding data. The output of CCCma's Fourth Generation Atmosphere General Circulation Model was kindly provided by Dr. Viatcheslav Kharin.

I would also like to thank Guillermo Fernández, Pablo Carracedo, Anabela Neto, Pedro Melo Costa and Marcos Tesouro, as well as Juan Taboada and Mariluz Macho, for giving me the opportunity to finish this thesis within the job duties at MeteoGalicía and to Dominic Royé for sharing the perspective of an Earth scientist.

I special thanks goes to Daniel San Martín who mounted the web services for the *Atmospheric River Archive* developed in the framework of the present thesis (see <http://www.meteo.unican.es/atmospheric-rivers>).

Dr. José Manuel Gutiérrez has had the key role in my training. He not only supervised this thesis in an excellent way but also gave me the opportunity to freely develop my own ideas - and to reject them in case they did not make sense.

The present thesis has been funded by the JAE-PREDOC programme of the Spanish National Research Council (CSIC), as well as by the Spanish national research project ESTCENA (code: 200800050084078).

Swen Brands  
Santiago de Compostela, the 1<sup>st</sup> of April 2017

---

## Applied Abbreviations

$\alpha$  = Probability of error within statistical hypothesis testing

**AGCM** = Atmosphere General Circulation Model

**AMIP** = Atmospheric Model Intercomparison Project

**AMO** = Atlantic Multidecadal Oscillation

**AOGCM** = Atmosphere-Ocean General Circulation Model

**AR** = Atmospheric River

$AR_{all}$  = Number of detected ARs

$AR_{noeast}$  = Number of detected ARs with *disabled* eastward tracking

**b** = Group of grid boxes defining a region where ARs are detected in

**CAM3.1** = Community Atmosphere Model version 3.1

**CAM4** = Community Atmosphere Model version 4

**CAM4-Oslo** = “Oslo” version of the Community Atmosphere Model version 4

**CanAM4** = Canadian Fourth Generation Atmospheric Global Climate Model

**CanESM2** = Canadian Earth System Model 2

**CCCma** = Canadian Centre for Climate Modelling and Analysis

**CI** = Confidence Interval

**CIRES** = Cooperative Institute for Research in Environmental Sciences

**CMIP5** = Fifth Phase of the Coupled Model Intercomparison Project

**CPC-NAO** = Climate Prediction Center's North Atlantic Oscillation index

**CPU** = Central Processing Unit

**D** = *Direction* of the vertically integrated water vapour transport

**DJF** = December-to-February

**e** = Grid-box found by the AR detection and tracking algorithm

**EA** = East Atlantic

**eastward tracking** = tracking towards the cardinal directions N, NE, E or SE

**EA/WR** = East Atlantic/Western Russia

**ECMWF** = European Centre for Medium-Range Weather Forecasts

**ENSO** = El Niño-Southern Oscillation

**EOF** = Empirical Orthogonal Function

**ESGF** = Earth System Grid Federation

**ESM** = Earth System Model

**ESRL** = Earth System Research Laboratory

**FMA** = February-to-April

$F_{noeast}$  = Fraction of ARs detected with *disabled* eastward tracking

**Full CI** = CI obtained from modelled values plus the observed value

**Full t-distribution** = T-distr. fitted to modelled values plus the observed value

**g** = Acceleration due to gravity

**Georgia Tech** = Georgia Institute of Technology

**H-NAO** = North Atlantic Oscillation index from James Hurrell

**IPO** = Interdecadal Pacific Oscillation

**IPSL** = Institute Pierre Simon Laplace

**IVT** = *Intensity* of the vertically Integrated water Vapour Transport

$IVT_u$  = Zonal IVT component

$IVT_v$  = Meridional IVT component

**JFM** = January-to-March

**JISAO** = Joint Institute for the Study of the Atmosphere and Ocean

**JJA** = June-to-August

**l** = Length criterion used to define an AR

**LMDZ5A** = Laboratoire de Météorologie Dynamique Zoom 5A

**MAM** = March-to-May

**Modelled CI** = CI obtained from modelled values only

**Modelled t-distribution** = T-distribution fitted to the modelled values only

**MSLP** = Mean Sea Level Pressure

**NAO** = North Atlantic Oscillation

**NCAR** = National Center for Atmospheric Research

**NCEP** = National Centers for Environmental Prediction

**NOAA** = National Oceanic and Atmospheric Administration

**NetCDF** = Network Common Data Form

**Niño 3.4** = Areal average sea surface temperature in the Niño 3.4 region

**NorESM1-M** = Norwegian Climate Center's Earth System Model

**NP** = North Pacific index

**NPGO** = North Pacific Gyre Oscillation

**OND** = October-to-December

**ONDJFM** = October-to-March

**ORCHIDEE** = ORganizing Carbon and Hydrology in Dynamic EcosystEms model

**p** = Pressure

**PC** = Principal Component

**PCA** = Principal Component Analysis

**PDO** = Pacific Decadal Oscillation

**PNA** = Pacific/North American

**POL** = Polar/Eurasia

**PWP** = Pacific Warm Pool

$P_d$  = Percentile threshold used to *detect* an AR

$P_t$  = Percentile threshold used to *track* an AR

**q** = Specific humidity

**r** = Pearson correlation coefficient

**recent past** = 1979-2008, the AMIP period

**rs** = Spearman/rank correlation coefficient

$r_{S_{index}}$  = rs between AR counts and the specified climate *index*, e.g. " $r_{SEA}$ "

**s** = Within an AR, the grid box located upstream of a neighbouring grid-box

**std** = Sample standard deviation

**SCAND** = Scandinavian pattern

**SON** = September-to-November

**SSH** = Sea Surface Height

**SST** = Sea Surface Temperature

**Station-NAO** = Station-based North Atlantic Oscillation index

**T2m** = Two metre air temperature

**TNA** = Tropical North Atlantic

**u** = Zonal wind component

**UCAR** = University Corporation for Atmospheric Research

**URL** = Uniform Resource Locator

**v** = Meridional wind component

**WHWP** = Western Hemisphere Warm Pool

**WP** = West Pacific

**z** = Z-score obtained after standardization

**Z500** = Geopotential at 500 hPa

**Z700** = Geopotential at 700 hPa

---

# Contents

<b>Acknowledgements</b>	<b>i</b>
<b>Applied Abbreviations</b>	<b>iii</b>
<b>1 Resumen en Español (Summary in Spanish Language)</b>	<b>1</b>
1.1 Introducción . . . . .	1
1.2 Contexto y Objetivos de la Tesis . . . . .	5
1.3 Principales Resultados . . . . .	9
1.3.1 Teleconexiones Atmosféricas y ARs Regionales . . . . .	10
1.3.2 Teleconexiones Oceánicas y ARs Regionales . . . . .	13
1.4 Lecciones aprendidas con Modelos Numéricos Idealizados . . . . .	15
1.5 Publicaciones Relacionadas . . . . .	18
<b>2 Introduction</b>	<b>21</b>
2.1 What is an Atmospheric River and How is it Detected and Tracked? .	23
2.2 Why are Atmospheric Rivers Important? . . . . .	23
2.3 What are the Known Drivers and the Implications for Predictability?	27
2.4 What is Internal Atmospheric Variability? . . . . .	29
2.5 How do ENSO Teleconnections Develop in the Context of Internal Atmospheric Variability? . . . . .	30
2.6 What is an Atmosphere General Circulation Model . . . . .	31
2.7 Aims of the Present Thesis . . . . .	35
<b>3 Applied Observational Data and Post-Processing</b>	<b>41</b>
3.1 Climate Indices . . . . .	41
3.2 Reanalysis Data . . . . .	46
3.3 Post-Processing the Reanalysis Data . . . . .	48

<b>4</b>	<b>The Atmospheric River Detection and Tracking Algorithm</b>	<b>51</b>
4.1	Description of the Algorithm . . . . .	52
4.2	Sensitivity Tests Related to the Definition of an AR . . . . .	54
4.3	Construction of an Historical Atmospheric River Archive . . . . .	54
4.4	Performance of the Algorithm . . . . .	55
<b>5</b>	<b>Reanalysis Similarity for Atmospheric Rivers along the Twentieth Century</b>	<b>59</b>
5.1	Differences in the Mean . . . . .	62
5.2	Differences in the Inter-Annual Variability . . . . .	64
5.3	Differences in the Long-Term Trends . . . . .	66
<b>6</b>	<b>Teleconnections in the Observational Record</b>	<b>69</b>
6.1	Atmospheric Teleconnections . . . . .	69
6.1.1	Running Correlation with the NAO and Aleutian Low . . . . .	69
6.1.2	Relationships to Other Atmospheric Circulation Indices . . . . .	73
6.2	Oceanic Teleconnections . . . . .	79
6.2.1	Running Correlation with ENSO and Low Frequency Modulation by the PDO and AMO . . . . .	79
6.2.2	Relationships to Other Oceanic Indices . . . . .	83
<b>7</b>	<b>ENSO Teleconnections in Atmosphere General Circulation Models</b>	<b>87</b>
7.1	Applied Model Experiments . . . . .	88
7.1.1	External Experiments from the Atmospheric Model Intercomparison Project . . . . .	88
7.1.2	Home-Made Experiments with the Community Atmosphere Model . . . . .	90
7.2	Methods . . . . .	91
7.2.1	Internal Atmospheric Variability Estimate . . . . .	92
7.2.2	Model-Performance and Nonstationarity Attribution Tests . . . . .	93
7.3	Results . . . . .	94
7.3.1	Results from the Atmospheric Model Intercomparison Project . . . . .	94
7.3.2	Results from the Community Atmosphere Model . . . . .	103
<b>8</b>	<b>Extension to Other Predictand Variables and Teleconnections</b>	<b>107</b>
8.1	The ERA-20CM Dataset and Applied Methods . . . . .	108
8.2	Results Obtained from ERA-20CM . . . . .	109
8.2.1	ENSO Teleconnections during the 1900-2010 Period . . . . .	109
8.2.2	ENSO Teleconnections during Specific Time Periods . . . . .	114
8.2.3	Teleconnections Triggered by the AMO and PDO . . . . .	120
<b>9</b>	<b>Summary, Discussion and Conclusions</b>	<b>127</b>
9.1	Lessons Learned from Observations . . . . .	127
9.1.1	Atmospheric Teleconnections to Regional AR Counts . . . . .	127

---

9.1.2 Oceanic Teleconnections to Regional AR counts . . . . .	130
9.2 Lessons learned from Idealized Numerical Model Experiments . . . .	133
9.3 Future Work . . . . .	136
<b>References</b>	<b>138</b>

---

# CHAPTER 1

---

## Resumen en Español (Summary in Spanish Language)

### *1.1 Introducción*

El balance energético de la Tierra se caracteriza por un superávit energético en bajas latitudes y un déficit en latitudes elevadas, compensado por los flujos de energía hacia los polos ejercidos por la atmósfera y el océano (Fasullo and Trenberth, 2008). La componente de transporte atmosférico puede descomponerse adicionalmente en los flujos de calor sensible y latente, realizándose este último por medio del transporte de vapor de agua. Tal vez en contraste con lo que cabría esperar, el transporte atmosférico de vapor de agua no se organiza de forma homogénea en el espacio y el tiempo, sino que se logra a través de “ríos atmosféricos”. Estos ríos pueden causar precipitaciones extremas, inundaciones y deslizamientos, especialmente en el caso de que las masas de aire húmedo se vean forzadas a elevarse y precipitar, por ejemplo, por una cordillera (Dettinger et al., 2011). Mientras que los AR se ven típicamente como precursores a gran escala de eventos extremos hidrológicos a escala local, la presente tesis trata de los precursores de los propios ríos atmosféricos, tanto en la atmósfera como en el océano. Esto no se hace para eventos individuales, sino para las ocurrencias atmosféricas agregadas estacionalmente. Esta introducción define brevemente el concepto de río atmosférico y resume el conocimiento actual sobre los precursores y la previsibilidad de estos fenómenos.

Aproximadamente el 90% del transporte de vapor de agua en la atmósfera hacia el polo se logra mediante estructuras estrechas y alargadas de transporte intenso que tienen una vida útil de unos pocos días (Zhu and Newell, 1994, 1998). Debido a su aspecto filamentoso que recuerda el curso de un río a vista de pájaro, estas estructuras se han referido originalmente como “ríos troposféricos”, término que más

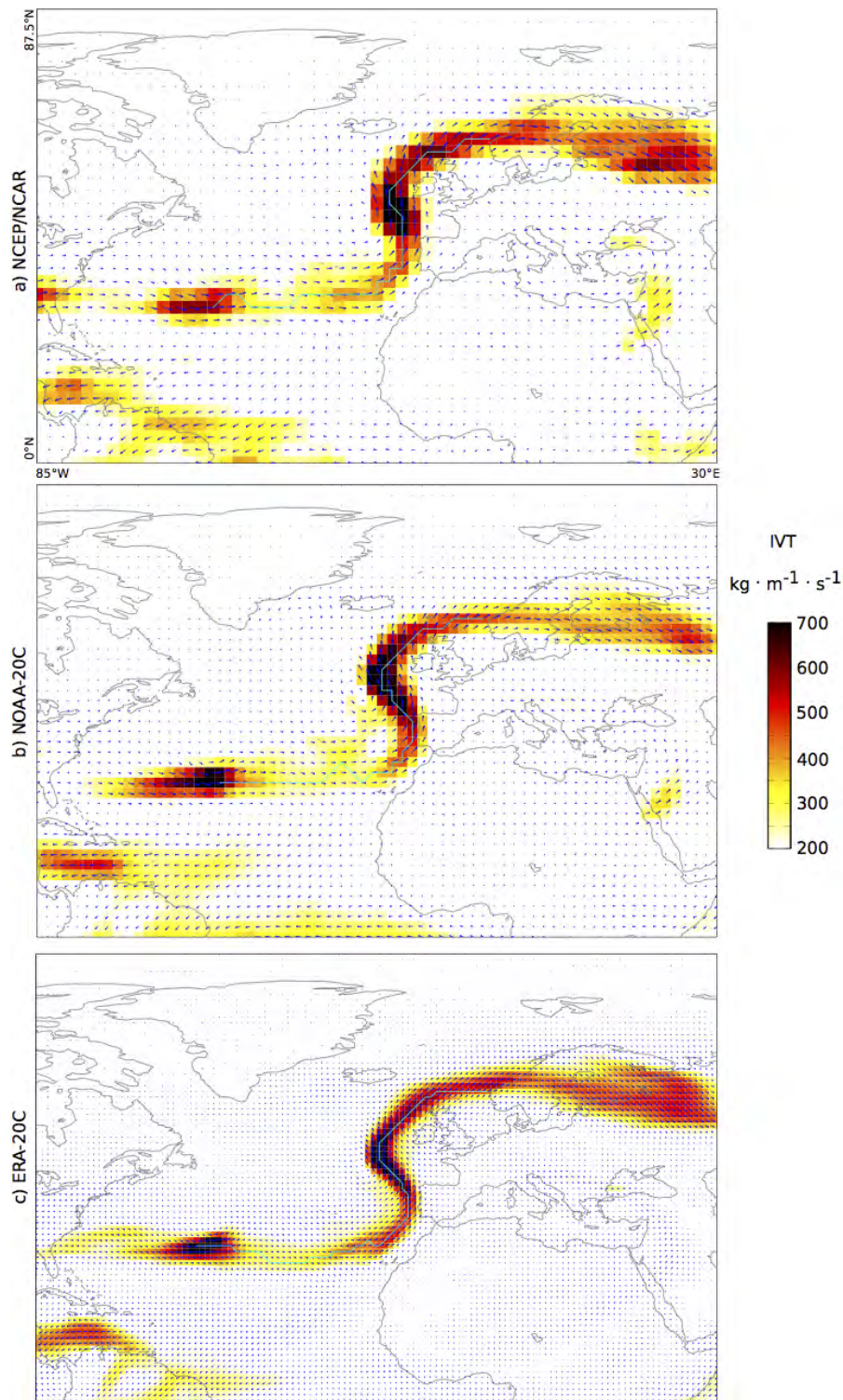


**Figure 1.1:** Ejemplo ilustrativo de un río atmosférico que afectó al sur de Noruega el 11 de enero de 1971 OO UTC para a) Reanálisis NCEP / NCAR 1, b) Reanálisis NOAA-CIRES Twentieth Century v2 y 3) Reanálisis ERA-20C ECMWF. Las sombras de color y las longitudes de los vectores son proporcionales a la intensidad del transporte horizontal de vapor de agua verticalmente integrado (IVT, tal como se define en la sección 3.2). La dirección del flujo se indica por la orientación de los vectores. La línea cian representa el recorrido del AR encontrado por el algoritmo desarrollado en la presente tesis (ver la Sección 4.1). Fuente: ilustración propia.

tarde evolucionó a “ríos atmosféricos” (en lo sucesivo, ARs, por sus siglas en inglés). Un ejemplo ilustrativo se muestra en la Figura 1.1. Dos procesos contribuyen a la formación y mantenimiento del vapor de agua que constituye estas estructuras. La primera es similar al flujo de un río. El agua se evapora en una región remota y luego se transporta miles de kilómetros. Para que este transporte a largo plazo funcione, la evapotranspiración y la condensación deben desempeñar un papel secundario a lo largo de toda la ruta de transporte (Knippertz and Wernli, 2010; Gimeno et al., 2012; Sodemann and Stohl, 2013; Garaboa-Paz et al., 2015). El segundo proceso es el reciclado de humedad a pequeña escala (evapotranspiración, condensación y precipitación). En este caso, el vapor de agua se pierde y se refresca continuamente por delante del frente frío de uno o varios ciclones extratropicales, dando lugar a una estructura que parece un río, pero que no comparte sus propiedades de transporte (Bao et al., 2006). Estudios recientes apuntan al hecho de que, para la mayoría de ARs, el reciclado de humedad es más importante que el transporte a largo alcance (Newman et al., 2012; Dacre et al., 2015).

Los ARs pueden ser identificados y rastreados usando métodos Eulerianos o Lagrangianos (Newell et al., 1992; Bao et al., 2006; Knippertz and Wernli, 2010; Gimeno et al., 2012; Garaboa-Paz et al., 2015). Los algoritmos utilizados en el marco Euleriano, que serán el foco de la presente tesis, son capaces de detectar y rastrear automáticamente las estructuras de AR en un momento dado y usualmente operan en base a la intensidad del transporte de vapor de agua verticalmente integrado (Zhu and Newell, 1998; Lavers et al., 2012; Guan and Waliser, 2015). Los datos correspondientes se toman idealmente de observaciones de radiosondas o de satélite que, sin embargo, tienen una cobertura espacial y temporal limitada (Zhu and Newell, 1998; Ralph et al., 2004; Lavers et al., 2011). Esta es la razón por la que se usan datos de modelos de reanálisis, usualmente denominados “cuasi-observaciones” (por ejemplo Brands et al., 2012b), si se requieren series de tiempo largas y cobertura espacial completa como, por ejemplo, para evaluar los aspectos climatológicos de los ríos atmosféricos (Higgins et al., 2000; Neiman et al., 2008; Knippertz et al., 2013; Dacre et al., 2015).

Mientras que los ARs que desencadenan la precipitación (extrema) han sido estudiados extensamente hasta la fecha, todavía se está intentando construir un marco espaciotemporal completo de las condiciones atmosféricas y oceánicas a gran escala que son precursores de ARs y desencadenan una actividad anómala en los mismos (Gimeno et al., 2014, 2016).

Los precursores atmosféricos de ARs han sido extensamente estudiados para Norteamérica, la “cuna” de la investigación en este campo (Neiman et al., 2002; Ralph et al., 2004). Bao et al. (2006) encontró que un debilitamiento de la cresta subtropical del Pacífico central favorecía el flujo directo de humedad de los trópicos a la Costa Oeste de los Estados Unidos. En un estudio de caso centrado en la temporada de nieve de 2010/11, Guan et al. (2013) concluyó que la excepcional actividad de ARs en la Sierra Nevada de California durante esa temporada en particular estuvo vinculada al hecho de que tanto el patrón PNA como la AO estaban en la fase

negativa. Esta relación de la PNA con los ARs se ha señalado recientemente en [Kim and Alexander \(2015\)](#) y [Guan and Waliser \(2015\)](#). A saber, la fuerza y la posición de la Baja Aleutiana (es decir, uno de los centros de acción del PNA) es clave para la distribución espacial del vapor de agua en esta región. Si este sistema de baja presión es anormalmente profundo (en cuyo caso el PNA es normalmente positivo), el vapor de agua está por encima de lo normal en una región que se extiende desde el noroeste del Pacífico norteamericano hasta Alaska, mientras que cuando se desplaza hacia el sur se observan condiciones húmedas en el suroeste de Estados Unidos y México. Además del efecto de la PNA, las oleadas de frío en Asia Oriental aumentan las probabilidades de llegadas de ARs a lo largo de la costa oeste de Norteamérica durante los días que siguen al pico frío ([Jiang and Deng, 2011](#)).

Se sabe que la circulación atmosférica sobre el Pacífico Norte y América del Norte está asociada con modos de variabilidad de baja frecuencia en 1) las temperaturas superficiales del mar (SSTs) del Océano Pacífico y el 2) Convección tropical ([Straus and Shukla, 2002](#); [Franzke et al., 2011](#)). Todos estos modos tienen periodicidades típicas, que son más o menos regulares, haciéndolas más o menos predecibles. Ordenado de alta a baja periodicidad estos modos son 1) la oscilación de Madden-Julian (MJO, [Madden and Julian, 1971](#)), 2) El Niño-Oscilación del Sur (ENSO, [Trenberth, 1997](#); [McPhaden et al., 2006](#)), y 3) la Oscilación Decadal del Pacífico (PDO), con periodos de pico de aproximadamente 30 a 60 días, siete a ocho años y cinco a siete décadas, respectivamente. De forma similar a la PDO, la Oscilación Multidecadal Atlántica (AMO) es una oscilación multidecadal de las SSTs del Atlántico Norte y está asociada con anomalías climáticas alrededor de esta cuenca oceánica ([Kerr, 2000](#); [Enfield et al., 2001](#)). Para explorar posibles fuentes de predecibilidad a largo plazo, estos modos de variabilidad de baja frecuencia se han asociado con las frecuencias estacionalmente agregados de ARs en Norteamérica. Para la temporada de noviembre a marzo, se han encontrado relaciones significativas con fases específicas del MJO para los recuentos de AR en muchas subregiones de este continente ([Guan et al., 2012, 2013](#); [Guan and Waliser, 2015](#)). Durante los episodios de El Niño, las frecuencias de AR tienden a estar por encima de lo normal en una región que va desde el noroeste de los Estados Unidos hasta Alaska ([Guan et al., 2013](#); [Guan and Waliser, 2015](#)). [Bao et al. \(2006\)](#) concluyó que el transporte directo de la humedad tropical de los trópicos a la costa oeste de los Estados Unidos es muy probable durante los inviernos neutros de ENSO. Sin embargo, señalaron que este tipo de transporte de humedad a largo plazo es bastante inusual en comparación con el transporte debido a la convergencia de la humedad local, hallazgo que ha sido confirmado recientemente por [Dacre et al. \(2015\)](#). Por último, un único estudio está disponible a la fecha sobre potenciales precursores multidecadales de ARs ([Liu et al., 2016](#)), que concluye que la actividad de AR en Invierno (DJF) a lo largo de la costa oeste de Norteamérica están significativamente asociados con la PDO y también con el Giro del Pacífico Norte (NPGO, [Di Lorenzo et al., 2008](#)).

Los precursores atmosféricos y particularmente los oceánicos de la actividad AR en Europa han sido menos estudiados hasta la fecha. [Lavers et al. \(2012\)](#) encontró

que la actividad AR de octubre a marzo sobre las Islas Británicas estaba inversamente relacionada con el patrón escandinavo (Barnston and Livezey, 1987). En un estudio de seguimiento realizado a escala continental, los mapas compuestos de presión al nivel del mar asociados con las llegadas de AR en Europa septentrional y meridional se asemejaron a las fases positiva y negativa de la Oscilación del Atlántico Norte (NAO Hurrell et al., 2003), respectivamente. Ramos et al. (2015) encontró que la actividad AR de ONDJFM sobre la Península Ibérica estaba positivamente relacionada con el patrón del Atlántico Este en primer lugar. A diferencia de Lavers and Villarini (2013), el enlace "AR-NAO" resultó ser no significativo en Ramos et al. (2015), lo que quizás sea algo no intuitivo, ya que la NAO es conocida por describir una gran fracción de la variabilidad del invierno en esta región (Hurrell, 1995; Trigo et al., 2004). Las razones para este desacuerdo pueden encontrarse en las diferencias en los conjuntos de datos considerados, los períodos de tiempo y las definiciones de la temporada.

Recientemente, Guan and Waliser (2015) han analizado si las frecuencias estacionales de AR en Europa están asociadas estadísticamente con variaciones en los modos predecibles de variabilidad de baja frecuencia (que, a excepción del MJO y NPGO, se describen comúnmente por las variaciones de SST). Este estudio concluye que la actividad de AR en Europa se asocia significativamente con las fases 3 y 4 del MJO, mientras que el papel de ENSO es no significativo excepto en el sur y el oeste de la Península Ibérica.

## 1.2 Contexto y Objetivos de la Tesis

Muchos estudios sobre teleconexiones presumiblemente provocadas por las variaciones de SST y teleconexiones que involucran ríos atmosféricos, se basan en el registro observacional. Sin embargo, la respuesta atmosférica al forzamiento externo (por ejemplo, las variaciones de la SST) es modificada por la variabilidad atmosférica interna y, por tanto, no es determinista. La atmósfera acoplada a los agentes de forzamiento externos puede describirse mejor en términos de un sistema probabilístico (Lorenz, 1963; Palmer et al., 2005). Como se señaló en la sección 2.4, en un sistema de este tipo, dos estados inicialmente muy diferenciados divergen en gran medida si se permite que el sistema avance en el tiempo. En el caso de las teleconexiones de ENSO, esto significa que *no* se puede esperar que incluso dos eventos distintos de El Niño con el mismo patrón de anomalías de SST tengan el mismo impacto en el clima a miles de kilómetros, ya que el estado de la atmósfera diferiría de un evento a otro. Desde este punto de vista, el registro observacional es sólo el reflejo de una única respuesta atmosférica al forzamiento externo.

De hecho, se ha mostrado que las teleconexiones inducidas por las variaciones de la SST varían en intensidad (y también en significación) de un periodo de tiempo a otro. En lugar de atribuir estas "no estacionariedades" a la naturaleza probabilística del sistema climático, a menudo se las atribuye a algún tipo de agente de forzamiento externo, que varía en escalas de tiempo mayores que la teleconexión en estudio.

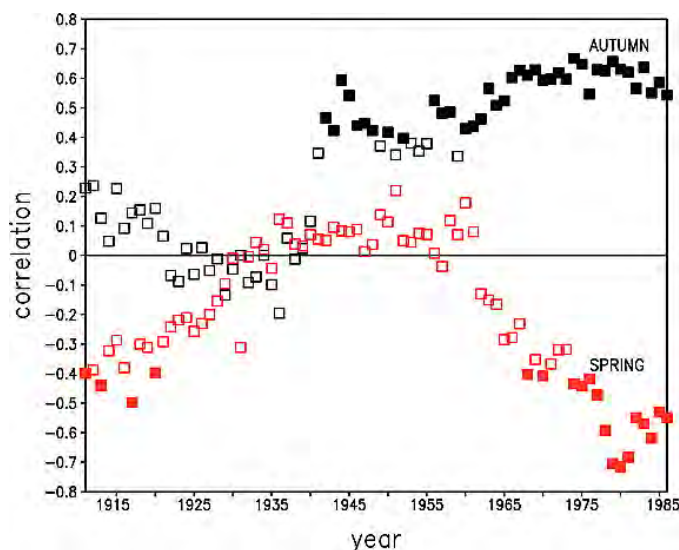


**Figure 1.2:** Coeficiente de correlación de Pearson entre la precipitación del Mediterráneo occidental ( $30^{\circ}\text{N} - 45^{\circ}\text{N}, 10^{\circ}\text{W} - 20^{\circ}\text{E}$ ) y el índice Niño 3.4 para SON (negro) y MAM (rojo). Cada valor se refiere a la correlación para la ventana de 20 años centrada en el símbolo. Los símbolos rellenos son para valores que son significativos en el nivel 95 %, símbolos vacíos son para valores no significativos. La Figura es una reimpresión de la Figura 6 en [Mariotti et al. \(2002\)](#). Los datos subyacentes para esta figura son de [Rayner et al. \(1996\)](#) y [New et al. \(2000\)](#).

Quizás el ejemplo más destacado de esta “modulación” presumible es el vínculo observado entre el ENSO y el clima norteamericano, que es particularmente fuerte durante la fase positiva de la PDO y más débil durante la fase negativa ([Gershunov and Barnett, 1998](#); [Diaz et al., 2001](#)).

Del mismo modo, se han encontrado profundas no-estacionariedades para la conexión del ENSO con la precipitación en el sur de Europa en el registro observacional del siglo XX ([Mariotti et al., 2002](#)). La correlación entre ambos es significativa durante la segunda mitad de siglo en Otoño (SON), mientras que es significativa al inicio y al final en Primavera (MAM) (véase la Figura 1.2). Al igual que las causas propuestas para América del Norte, las variaciones de la fuerza en el enlace del ENSO al clima en Europa se han atribuido a la modulación por la PDO y AMO ([Lopez-Parages and Rodriguez-Fonseca, 2012](#); [Rodriguez-Fonseca et al., 2016](#)), así como a las variaciones en la intensidad de los eventos ENSO ([Mariotti et al., 2002](#)). En esta tesis, estos resultados serán re-evaluados críticamente teniendo en cuenta los efectos de la variabilidad climática interna (ver la Sección 8.2.2).

Como alternativa al forzamiento externo, teniendo en cuenta que el sistema climático es probabilístico, hay por lo menos tres explicaciones distintas e igualmente plausibles para explicar las no-estacionariedades halladas en observaciones ([Sterl et al., 2007](#)). En primer lugar, el fortalecimiento (o el debilitamiento) de una teleconexión durante un período de tiempo específico puede surgir simplemente del azar, en cuyo caso las variaciones de la SST de baja frecuencia no ejercerían un efecto modulador sobre la teleconexión estudiada. En segundo lugar, las variaciones de SST de baja

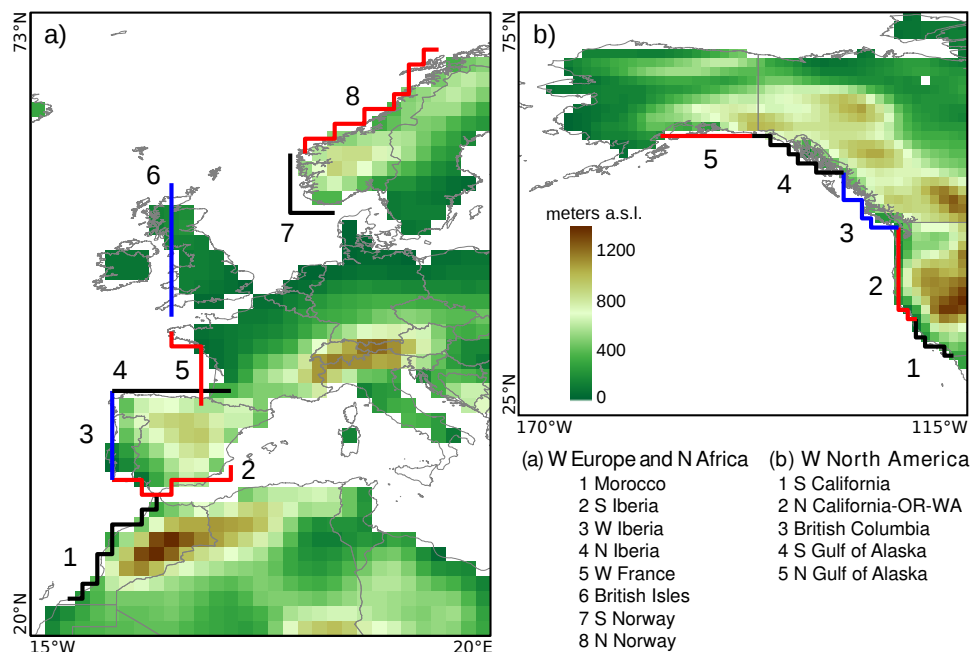


**Figure 1.3:** Regiones objetivo utilizadas para la detección y el seguimiento de AR para el caso del reanálisis del ECMWF ERA-20C. También se muestra la orografía correspondiente. Las “barreras” de detección utilizadas para los reanálisis restantes y los experimentos de modelos numéricos idealizados se encuentran en las proximidades directas de las mostradas aquí. Fuente: ilustración propia

frecuencia pueden tener un efecto modulador, pero la teleconexión podría surgir sólo porque la realización única de la variabilidad atmosférica interna fue favorable durante ese período de tiempo específico. En tercer lugar, las variaciones de SST que son la causa aparente de la teleconexión podrían covariar con algún otro forzamiento desconocido que fuese la verdadera causa de la teleconexión.

En este punto entra en juego la presente tesis. En ella se evalúan los ríos atmosféricos (AR) en 13 regiones a lo largo de las costas occidentales de Europa y Norteamérica (véase la figura 1.3). Esto se hace desde un punto de vista climatológico, con un enfoque en la temporada de ONDJFM durante la cual este fenómeno es más relevante en las dos regiones antes mencionadas (por ejemplo [Lavers and Villarini, 2013, 2015](#)). Se propone un nuevo algoritmo de detección y seguimiento de AR y se aplica a datos instantáneos seis horarios de cuatro reanálisis atmosféricos distintos, dos de los cuales se remontan al año 1900 (véase la sección 3.2 y Capítulo 4). De esta manera, se construirá un archivo AR histórico exhaustivo para las regiones anteriores (ver Sección 4.3). Este archivo consta de más de cientocincuentamil mapas que documentan todos los ARs detectados en las 13 regiones objetivo consideradas durante el período 1900-2014. Más allá del alcance de la presente tesis, el archivo AR puede aplicarse fácilmente para comprobar si los sucesos hidrológicos extremos individuales registrados en el pasado coinciden con la presencia de un río atmosférico (por ejemplo [Pereira et al., 2016](#)).

Es un hecho bien conocido que los datos de reanálisis, particularmente en los trópicos y para variables relacionadas con la humedad atmosférica, pueden sufrir de considerables incertidumbres incluso en el pasado reciente (Brands et al., 2012b,a, 2013; Manzanas et al., 2015). Estas incertidumbres aumentan a medida que se va hacia atrás en el tiempo, lo que se debe a una disminución en la densidad de las observaciones disponibles (Compo et al., 2011; Poli et al., 2016). Puesto que todo el siglo XX será tomado en cuenta en esta tesis, la incertidumbre de reanálisis es relevante para la misma y, por tanto, será evaluada en el Capítulo 5.

Posteriormente, se evalúan las teleconexiones entre los índices de circulación atmosférica y las frecuencias estacionales de AR en las 13 regiones objetivo consideradas (véase el Capítulo 6). Para los índices que describen la NAO en Europa y la intensidad de la Baja Aleutiana en el oeste de América del Norte, esto se hará a través de un análisis de correlación móvil cubriendo el período 1900-2010. Para el período 1950-presente, durante el cual las incertidumbres observacionales son generalmente de importancia secundaria en estas regiones, se tendrán en cuenta otros índices de circulación atmosférica que describen los patrones Atlántico Este o Pacífico-Norteamericano. En este caso se repiten exactamente los mismos análisis, pero para el uso de las variables del predictor de SST. Es decir, el índice de Niño 3.4 se utiliza para los análisis de correlación móvil y luego se complementa con otros índices SST relevantes (véase la sección 3.1 para una visión general de todos los índices aplicados). Aunque las teleconexiones impulsadas por ENSO son particularmente importantes para América del Norte, también son relevantes para Europa, como se señaló anteriormente. La parte observacional de la presente tesis se cierra con un análisis sobre el posible papel de la PDO y la AMO en la modulación de la fuerza de la conexión ENSO-AR a lo largo del siglo XX.

En el Capítulo 7, la tesis se centra en las respuestas alternativas y físicamente plausibles de la atmósfera al forzamiento externo observado. Para ello se utilizan experimentos idealizados con modelos numéricos atmosféricos (Gates, 1992). En particular, el capítulo se centra en las teleconexiones relacionadas con ENSO tratando de responder a las siguientes preguntas:

- A ¿Las teleconexiones observadas durante el período 1979-2008 son robustas a los efectos de la variabilidad atmosférica interna?. Aquí, se tiene explícitamente en cuenta que las teleconexiones podrían haber sido diferentes si se hubiera permitido que la atmósfera volviera a funcionar con el forzamiento externo observado.
- B ¿Podrían explicarse las variaciones no estacionarias observadas en la fuerza de las teleconexiones a lo largo del siglo XX por la variabilidad atmosférica interna del período 1979-2008?. Si no pueden, entonces los cambios en el forzamiento externo deben haber desempeñado un papel.
- C ¿Se mantienen las teleconexiones ENSO observadas si el forzado externo prescrito se limita a las variaciones de SST en el Pacífico tropical, eliminando así

el impacto de ENSO en la atmósfera?.

Para las dos primeras preguntas se utilizará un conjunto de simulaciones atmosféricas que comprende 13 experimentos del Proyecto de Intercomparación de Modelos Atmosféricos (AMIP, [Gates, 1992](#)), realizado dentro del marco del CMIP5 ([Taylor et al., 2012](#)). Estos experimentos se llevaron a cabo con condiciones de SST y de cubierta de hielo marino prescritas alrededor del globo entero (véase la sección 7.1.1).

Para responder a la tercera pregunta, se llevaron a cabo experimentos adicionales con el Modelo Atmosférico Comunitario, versión 3.1 (CAM3.1, [Collins et al., 2006](#)), en el Cluster de Alto Rendimiento (HPCC) del Grupo de Meteorología de Santander. Al contrario de los experimentos de AMIP, en estos experimentos se permitió que las SST prescritas variaran en la región Niño 3.4, mientras que los valores de SST y cubierta de hielo marino en otras regiones se establecieron constantes a sus valores medios climatológicos mensuales (ver Sección 7.1.2).

El Capítulo 8 demuestra lo que se puede aprender de los métodos propuestos en la presente tesis si los análisis desarrollados para conteos de ARs se extienden a las variables clásicas *predictand* usadas comúnmente en los estudios de teleconexión y predecibilidad (p.e. [Ropelewski and Halpert, 1987](#)), es decir, el geopotencial a 500 hPa, la presión media del nivel del mar, la temperatura y la precipitación. No sólo se analiza si las teleconexiones de estas variables clásicas con ENSO son robustas a la variabilidad climática interna (véase la Sección 8.2.1), sino también si las no estacionariedades en el enlace ENSO con el sur de Europa documentadas en [Mariotti et al. \(2002\)](#) se mantienen teniendo en cuenta la variabilidad atmosférica interna ([Brands, 2017](#)) (Sección 8.2.2). En el último paso de trabajo (véase la Sección 8.2.3), los análisis se extienden a otras teleconexiones, a saber, la PDO y la AMO. Estas extensiones se llevan a cabo a escala global, utilizando el nuevo conjunto de diez miembros de experimentos tipo AMIP ejecutados dentro del proyecto ERA-20CM ([Hersbach et al., 2015](#)). Al contrario de los experimentos AMIP de CMIP5, los experimentos ERA-20CM se llevaron a cabo durante un período mucho más largo (1900-2010). Por lo tanto, pueden utilizarse para evaluar las teleconexiones ejercidas por la PDO y la AMO, así como las no estacionariedades en las teleconexiones ENSO analizados anteriormente.

### 1.3 Principales Resultados

El capítulo final de esta tesis proporciona la síntesis de los resultados y una comparación con los resultados de estudios previos. Esto se hace por separado para los resultados obtenidos con observaciones (Sección 9.1) y con experimentos de modelos numéricos idealizados (Sección 9.2). Esta última sección subraya el error que se podría cometer cuando se evalúa un sistema probabilístico, las teleconexiones analizadas en esta tesis, con métodos deterministas.

### 1.3.1 *Teleconexiones Atmosféricas y ARs Regionales*

En el Capítulo 4 de la presente tesis, se desarrolló un nuevo algoritmo para la detección y rastreo de ríos atmosféricos que opera sobre la intensidad y dirección del transporte horizontal de vapor de agua verticalmente integrado, tomado de los datos de reanálisis. Este algoritmo se aplicó a cuatro conjuntos de datos de reanálisis distintos para detectar la presencia y características de los ARs en 13 regiones objetivo a lo largo de las costas occidentales de Europa (incluyendo África del Norte) y América del Norte en escala seis horaria.

Sobre esta base, se generaron más de cientocinquantamil mapas que documentan cada evento AR individual en las regiones anteriores, cubriendo el período de tiempo 1900-2014. Con estos mapas, se construyó el archivo AR más extenso disponible públicamente hasta la fecha (véase <http://www.meteo.unican.es/atmosphericrivers>). Además de su propósito para los objetivos de esta tesis, este archivo puede servir para otros estudios, como realizar comparaciones con variables hidrológicas a escala local (por ejemplo, precipitaciones extremas, inundaciones y deslizamientos), etc.

Esta tesis se enfocó a las ocurrencias estacionales de ARs y se analizó si se pueden encontrar relaciones empíricas-estadísticas con los índices climáticos atmosféricos y oceánicos relevantes para el clima en Europa y Norteamérica. Este enfoque es útil 1) porque se sabe que las ocurrencias estacionales de AR están estrechamente relacionadas con la precipitación (e.g. Neiman et al., 2008; Lavers and Villarini, 2015) y 2) debido a que las variaciones de SST en los trópicos son predecibles con meses de antelación (e.g. Barnston et al., 2012). Por consiguiente, cualquier relación remota entre los AR y las SST tropicales podría ser potencialmente explotada con el propósito de pronósticos de abastecimiento de agua a largo plazo (Gamiz-Fortis et al., 2008), siempre que esta teleconexión sea robusta a los efectos de la variabilidad climática interna.

Dado que los datos de reanálisis son inciertos, particularmente a comienzos del siglo XX, particularmente con respecto a las variables relacionadas con la humedad atmosférica, se ha realizado un estudio previo sobre cómo afecta esta incertidumbre a las frecuencias estacionales de ARs, antes de analizar las teleconexiones. Para ello, en el Capítulo 5, se compararon mutuamente las frecuencias de AR de los reanálisis NOAA-CIRES Twentieth Century y ECMWF ERA-20C, usando una ventana móvil de un año en cada paso. Además, se calcularon las tendencias decadales para el período 1950-2010. Esto se hizo por separado para las estaciones de octubre a diciembre (OND) y de enero a marzo (JFM). Se obtuvieron los siguientes resultados principales:

1. Las diferencias en la media de los dos reanálisis (es decir, los sesgos) son especialmente pronunciadas en (pero no se limitan a) principios del siglo XX. Los sesgos durante este período temprano son más severos en el oeste de América del Norte que en Europa (ver la sección 5.1 para más detalles).

2. A lo largo de la costa oeste de Europa, los dos reanálisis producen una variabilidad interanual similar, incluso a comienzos del siglo XX, con coeficientes de correlación ( $rs$ )  $\geq +0.6$ . Esto contrasta fuertemente con el casi cero  $rs$  encontrado a lo largo de la costa oeste de Norteamérica durante el mismo período. En esta región,  $rs$  aumenta constantemente hasta aproximadamente 1945-75 y después permanece constante en un nivel  $\geq +0.8$  (ver la sección 5.2 para más detalles).
3. Ambos reanálisis indican una tendencia lineal positiva para las frecuencias OND en Europa. También coinciden en un dipolo meridional en el signo de la tendencia durante la temporada JFM, con valores positivos en el norte y valores negativos en el sur de Europa. En el oeste de América del Norte, las tendencias son consistentemente positivas desde Columbia Británica hasta el norte del Golfo de Alaska. Sin embargo, aunque los dos reanálisis generalmente coinciden en el signo de las tendencias, no están de acuerdo en si las tendencias son significativas o no, ni en Europa ni en el oeste de Norteamérica (ver la sección 5.3 para más detalles).

Estos resultados deben tenerse en cuenta al evaluar el sesgo a largo plazo de, por ejemplo, los ESMs del CMIP5 (Taylor et al., 2012), particularmente a principios del siglo XX.

La búsqueda de los *precursores* de la actividad estacional de ARs se realizó en el Capítulo 6, que se subdivide en el análisis de los precursores atmosféricos y oceánicos. En lo que respecta a los precursores de la atmósfera, la primera etapa de trabajo consistió en rastrear la relación de las frecuencias de AR con el NAO o la Baja Aleutiana (para el caso de Europa y Norteamérica respectivamente) utilizando el mismo análisis de correlación móvil aplicado anteriormente para la comparación de reanálisis. Si no se indica de otra manera, los siguientes resultados se mantienen válidos independientemente del reanálisis aplicado y los umbrales (percentiles) utilizados para definir un AR. Para la comparación con otros estudios (por ejemplo Lavers et al., 2012; Ramos et al., 2015), se considera adicionalmente la temporada de octubre a marzo (ONDJFM). Se obtuvieron los siguientes resultados principales (ver la sección 6.1.1 para más detalles):

4. Los enlaces AR-NAO encontrados en Europa representan un dipolo de correlación con valores positivos en el norte y negativos en el sur que recuerda al dipolo encontrado para la precipitación en muchos estudios anteriores (por ejemplo Hurrell, 1995).
5. Durante el transcurso del siglo XX, el dipolo de correlación en OND se mueve gradualmente hacia el norte hasta aprox. 1925-1955. Desde aprox. 1955-1985 hasta 1980-2010, se mueve de nuevo al sur.
6. Debido a las grandes incertidumbres de reanálisis a comienzos del siglo, los patrones de teleconexión para el oeste de América del Norte difieren en gran

medida entre los dos reanálisis a largo plazo hasta aproximadamente 1940-1970. A partir de 1940-1970 en adelante, estas incertidumbres son generalmente pequeñas y los resultados son probables de reflejar procesos verdaderos.

7. El grado de estacionariedad de la relación con la Baja Aleutiana depende en gran medida de la temporada considerada. En la Columbia Británica y el sur del Golfo de Alaska un vínculo significativamente negativo se encuentra durante la temporada JFM de 1955-85 en adelante. Durante la temporada OND, este vínculo desaparece gradualmente en el mismo período. En el norte del Golfo de Alaska, el enlace OND está constantemente en el límite de importancia durante toda la segunda mitad del siglo. El enlace JFM respectivo se debilita constantemente, llegando a ser insignificante a partir de 1970-2000 en adelante.

En la sección 6.1.2, la búsqueda de precursores atmosféricos de AR se extendió a patrones de circulación distintos del NAO y de la Baja Aleutiana. Esto se hizo para el período 1950-2010, durante el cual las diferencias de reanálisis se encontraron en general pequeñas en el Capítulo 5. Se obtuvieron los siguientes resultados principales:

8. Si los resultados se consideran en su conjunto, el patrón NAO es el conductor atmosférico más importante de la actividad AR en Europa occidental, en comparación con otros índices de circulación.
9. Durante la temporada OND, se encontraron vínculos significativamente positivos con el patrón del Atlántico Este a lo largo de la costa atlántica de Iberia y Francia. Durante esta temporada, éstos son más fuertes en magnitud que los enlaces negativos con el NAO, que es consecuente con los resultados de [Ramos et al. \(2015\)](#).
10. Durante OND y JFM, se encontraron enlaces significativamente negativos al índice escandinavo sobre las Islas Británicas, lo cual es consistente con los resultados de [Lavers et al. \(2012\)](#).
11. También se demostró que estos enlaces negativos se mantienen sobre Noruega y que son generalmente más fuertes durante JFM que durante OND.
12. Si se consideran ARs persistentes en lugar de instantáneos, los enlaces NAO son no significativos sobre las islas británicas y el oeste de Iberia. Esto puede explicar en parte por qué los respectivos enlaces encontrados en [Lavers et al. \(2012\)](#) y [Ramos et al. \(2015\)](#), obtenidos considerando sólo eventos persistentes, son débiles o incluso insignificantes.
13. Durante la temporada JFM, se encontraron enlaces significativamente positivos con la PNA en Columbia Británica y en todo el Golfo de Alaska, lo cual está de acuerdo con los resultados de [Guan and Waliser \(2015\)](#). Durante la temporada OND, estos enlaces son generalmente más débiles e insignificantes en la Columbia Británica.

14. Durante la temporada JFM, se encontraron vínculos significativamente negativos con el patrón del Pacífico Occidental a lo largo de la costa oeste de los Estados Unidos.

### 1.3.2 Teleconexiones Oceánicas y ARs Regionales

En la sección 6.2, los métodos aplicados para evaluar las teleconexiones desencadenadas por la atmósfera (véase la sección 6.2), se replicaron exactamente para las teleconexiones provocadas por la SST. Para este propósito, en la sección 6.2.1, se realizó el análisis de correlación móvil para el enlace entre el índice Niño 3.4 y las frecuencias regionales de AR en el oeste de Europa y América del Norte. Se obtuvieron los siguientes resultados principales:

15. En *ninguno* de las 13 regiones objetivo consideradas, este enlace es significativo durante todo el período del estudio. Por el contrario, se caracteriza por fuertes no estacionariedades y sólo se obtienen resultados significativos durante ciertos subperíodos y temporadas, especificados a continuación.
16. Desde aproximadamente 1955-1975, el enlace es significativamente positivo a lo largo del Golfo de Vizcaya (es decir, en el norte de Iberia y el oeste de Francia) durante la temporada OND. Antes de ese período, es decir entre aprox. 1945-75 y 1950-80, el enlace se desplaza hacia el sur, siendo significativo en Marruecos, el sur y el oeste de Iberia (en esta última región hasta 1974-2004).
17. En Europa, el vínculo es más fuerte durante el comienzo del siglo XX y la temporada JFM. Para este período, se obtienen  $rs$  positivos y significantes desde Marruecos hasta el oeste de Francia, parcialmente superiores a +0.8. Éste vínculo experimenta una drástica caída en la magnitud en los períodos de tiempo centrados en la década de 1930.
18. En Escandinavia, el enlace JFM es significativamente negativo durante el período 1915-45 a 1925-55.
19. Sobre las Islas Británicas, el enlace es no significativo durante todo el período de estudio.
20. En el oeste de América del Norte, el vínculo es significativamente positivo desde el norte de California a la Columbia Británica, pero sólo después del Gran Cambio Climático del Pacífico en 1976/77 (Mantua et al., 1997) y durante la temporada JFM. Estos resultados están de acuerdo con Guan and Waliser (2015).
21. En el sur del Golfo de Alaska, el enlace OND es significativamente positivo entre 1931-61 y 1943-73, es decir, antes del Gran Cambio Climático del Pacífico.

22. Aunque algunas variaciones en la intensidad del enlace están correlacionadas con el promedio temporal de los índices AMO y/o PDO en algunas regiones, esta correlación no es significativa si se tiene en cuenta la correlación serial. Esto significa que la evidencia estadística para una modulación a través de la AMO o PDO es débil.

El vínculo estacional de las frecuencias de AR con variables predictoras oceánicas distintas de las variaciones de SST en la región Niño 3.4 fue evaluado en la Sección 6.2.2 para el período fijo 1950-2010. Se hicieron las siguientes conclusiones principales:

23. Los vínculos con la Piscina Caliente del Pacífico (Pacific Warm Pool) y las SSTs en la región Niño 3.4 son muy similares, indicando que los dos índices correspondientes pueden usarse indistintamente para evaluar las teleconexiones ENSO en el contexto de la presente tesis.
24. Durante la temporada OND, se encontraron vínculos significativamente positivos con el patrón del Atlántico Norte Tropical (TNA) en Marruecos y el sur de Iberia. Durante la temporada JFM, estos enlaces son significativos sólo en Marruecos.
25. Durante la temporada OND, las relaciones con la Piscina Caliente del Hemisferio Occidental (Western Hemisphere Warm Pool) son similares a las encontradas para el TNA. Durante la temporada JFM, estas relaciones son insignificantes.
26. Para las relaciones con el AMO, se detectó un dipolo de correlación con  $rs$  positivo en el norte y  $rs$  negativo en el sur de Europa durante la temporada OND. Sin embargo, sólo las relaciones negativas que se encuentran en Marruecos son significativas.
27. Con excepción de algunos umbrales de percentiles individuales, se encontró una relación significativamente positiva con la PDO en el norte de Iberia y el oeste de Francia durante la temporada de ONDJFM.
28. Las frecuencias de AR en el oeste de América del Norte están más estrechamente vinculados a la PDO que a cualquiera de los dos índices ENSO. Durante la temporada OND, un vínculo significativamente positivo se encuentra en el norte del Golfo de Alaska. Durante la estación JFM, este eslabón se desplaza hacia el sur, dando significado en el sur del Golfo de Alaska y Columbia Británica. Los resultados de ONDJFM son significativos en el sur y el norte del Golfo de Alaska.
29. Los enlaces a la Oscilación Interdecadal del Pacífico (IPO) son similares a los obtenidos para la PDO, pero sistemáticamente más débiles.
30. Las relaciones con el NPGO son generalmente no significativas, excepto en el norte de California-Oregon-Washington, donde este enlace es significativamente negativo durante la temporada JFM para aproximadamente la mitad de

las combinaciones de umbral de percentil aplicadas, independientemente del reanálisis considerado.

En general, los resultados observacionales para Europa indican que las frecuencias de AR en OND alrededor del Golfo de Vizcaya están vinculados al ENSO a finales del siglo XX y en el pasado reciente y que un enlace ENSO más general que involucra a toda la costa occidental europea, fue activo en JFM durante la primera mitad del siglo. Este enlace tiene un carácter dipolar que recuerda al vínculo antes mencionado con la NAO, pero con los signos invertidos, es decir, El Niño está asociado con una actividad AR superior a la normal en el sur de Europa y una actividad inferior a la normal en el norte de Europa. Es la manifestación AR de la señal de El Niño de invierno (Broennimann, 2007), que fue descrita por primera vez en Walker (1923, 1924) y Walker and Bliss (1932). Se encontraron enlaces ENSO-AR significativos en regiones más europeas que occidentales de América del Norte. Esto es quizás sorprendente, dada la distancia geográfica más corta a la región fuente de la teleconexión, pero puede explicarse por la pobre concordancia de los reanálisis en el oeste de América del Norte a principios del siglo y también por el impacto de la variabilidad atmosférica interna en dicha teleconexión.

## 1.4 Lecciones aprendidas con Modelos Numéricos Idealizados

Aparte del enfoque observacional resumido anteriormente, en el Capítulo 7 se aplicó un segundo enfoque basado en los resultados de experimentos idealizados de modelación numérica para arrojar alguna luz sobre la pregunta de cómo interpretar los resultados observacionales teniendo en cuenta los efectos de la variabilidad interna de la atmósfera. Desde este punto de vista, una teleconexión obtenida a partir de una observación es el resultado de una única realización de la atmósfera que responde al forzamiento externo observado. Sin embargo, debido a la naturaleza probabilística del sistema climático (Lorenz, 1963), esta respuesta podría haber sido diferente en una realización diferente de la atmósfera, sujeta al mismo forzamiento. En las secciones 2.4, 2.5 y 2.7 se proporcionó una descripción detallada de este concepto teórico y sus implicaciones para el estudio de las teleconexiones. En la presente tesis, se ha podido trabajar con múltiples realizaciones de la atmósfera utilizando experimentos idealizados con modelos de circulación general de la atmósfera (AGCM), utilizados como sustitutos de la atmósfera real (von Storch et al., 2004). En aras de la concisión, sólo las teleconexiones con ENSO fueron consideradas en el mundo del modelo. Para este propósito se utilizaron tres familias distintas de experimentos AGCM y cada familia se asocia a pruebas estadísticas específicas que hubieran sido imposibles de realizar sobre la base del registro de observación (determinista). Los experimentos y el test asociado, descritos en detalle en la sección 7.1.1, 7.1.2 y 7.2, comprendían:

A Los experimentos AMIP llevados a cabo en el marco de CMIP5 (Gates, 1992; Taylor et al., 2012), que cubren el período 1979-2008. Se aplicaron un total de

13 experimentos de 3 AGCM diferentes. Estos experimentos se llevaron a cabo con las variaciones observadas de la SST y la cubierta de hielo marino alrededor del globo entero y se utilizan para preguntar 1) si las teleconexiones ENSO-AR observadas son robustas a la perturbación debida a la variabilidad atmosférica interna y 2) si la no estacionariedad en la fuerza de las teleconexiones, vista en el registro observacional del siglo XX, puede atribuirse a este tipo de variabilidad.

B Experimentos propios con el Modelo Atmosférico Comunitario 3.1 (CAM3.1 [Collins et al., 2006](#)). Se realizaron un total de 10 experimentos con 32 años cada uno. Cada año del modelo corresponde a un forzamiento distinto ejercido por la SST en la región de la Piscina Caliente del Pacífico [Hoerling et al. \(2001\)](#). En cada año, el patrón de anomalía de SST aumenta gradualmente de condiciones de frío realistas a condiciones cálidas realistas, reflejando eventos de la Niña, eventos neutrales y eventos de El Niño. Los diez ciclos de modelos distintos se realizaron en el Cluster de Alto Rendimiento del Grupo de Meteorología de Santander y difieren entre sí sólo por las condiciones iniciales desde las que se iniciaron. A diferencia de los experimentos de AMIP, el forzamiento de SST utilizado para estos experimentos fue confinado al Pacífico tropical solamente. Esta familia de experimentos se utilizó para analizar si las teleconexiones ENSO a las frecuencias de AR en OND en Europa se mantienen si se emplea una estrategia de forzamiento regional en lugar de la global utilizada para ejecutar los experimentos AMIP. La confirmación fortalecería la hipótesis de que las variaciones de SST en el Pacífico tropical son de hecho causales para el desarrollo de la teleconexión.

C Los diez experimentos AGCM del ECMWF denominados ERA-20CM que cubren el período extendido 1900-2010 ([Hersbach et al., 2015](#)). El forzamiento de estos experimentos es similar al de los experimentos AMIP, pero más realista, ya que comprende los efectos de otros agentes externos. Esta familia de experimentos se utilizó para extender los conceptos metodológicos presentados aquí a 1) otras variables más comúnmente usadas que los recuentos estacionales de AR, como la presión al nivel del mar, la temperatura y la precipitación y 2) otras teleconexiones diferentes al ENSO, a saber, la PDO y la AMO. De este modo, se revisaron críticamente los conocidos mapas de teleconexiones de ENSO (eg [Ropelewski and Halpert, 1987](#)) y algunas no estacionariedades observadas en estudios previos basados en observaciones (e.g. [Mariotti et al., 2002](#)), teniendo en cuenta el efecto de la variabilidad interna.

Con esta configuración experimental, se obtuvieron los siguientes resultados principales:

31. Las teleconexiones ENSO a las frecuencias regionales de AR no son en modo alguno robustos a la perturbación causada por la variabilidad atmosférica interna. Esto indica que los pocos resultados significativos observados en las

- observaciones, por ejemplo, para las frecuencias de ARs en OND en el sur de Europa, han surgido debido a que la realización única de la variabilidad atmosférica interna fue favorable durante el período de tiempo considerado (1979-2008). Esto implica que la sincronización de condiciones favorables futuras es esencialmente impredecible (véase la sección 7.3.1).
32. Para los experimentos AMIP y CAM3.1, la respuesta del recuento AR promedio del *conjunto* a ENSO es a menudo similar a la respuesta observada, mientras que la respuesta del recuento de los experimentos *individuales* no lo es (véase la sección 7.3.1 y 7.3.2). Una explicación para esto no se pudo encontrar en el marco de la presente tesis.
  33. De forma similar a lo obtenido con las observaciones, la respuesta AR en OND obtenida con el conjunto de experimentos CAM3.1 es significativamente positiva desde Marruecos hasta el oeste de Francia (véase la sección 7.3.2). Esto apunta al hecho de que estos recuentos están *causalmente* vinculados con variaciones de la SST en el Pacífico tropical y corrobora los resultados similares encontrados para la precipitación en estudios anteriores (Shaman and Tziperman, 2011; Shaman, 2014b,a).
  34. La asociación positiva particularmente fuerte entre el ENSO y las frecuencias de AR en el sur de Europa, observados a principios del siglo XX en JFM, muy probablemente *no* puede atribuirse únicamente a las variaciones debidas a la variabilidad atmosférica interna en el pasado reciente ( $\alpha = 0.05$  en la mayoría de los casos). Por tanto, los cambios en el forzamiento externo probablemente contribuyeron al desarrollo de las relaciones fuertes a principios del siglo XX (véase la sección 7.3.1).
  35. Las relaciones entre ENSO y los recuentos occidentales de América del Norte observados antes del Gran Cambio Climático del Pacífico (Mantua et al., 1997) sí pueden explicarse únicamente por variaciones posteriores al cambio debido a la variabilidad interna del clima ( $\alpha = 0.05$  en cualquier caso). Esto indica que el forzamiento externo, como por ejemplo, el ejercido por el PDO, probablemente no es necesario para explicar las no estacionariedades que se encuentran en las observaciones (por ejemplo Gershunov and Barnett, 1998). Consulte la sección 7.3.1 para obtener más detalles.
  36. Una extensión de los conceptos metodológicos a los diez experimentos de ERA-20CM revela que las teleconexiones ENSO en los trópicos son robustas, mientras que en las zonas extratropicales generalmente no lo son, excepto en las áreas afectadas por los patrones Pacífico-Norteamérica y Pacífico-Sudamérica (véase la sección 8.2.1).
  37. Los resultados generalmente no mejoran en las zonas extratropicales cuando la prueba de la robustez se aplica a sub-períodos específicos del siglo XX, durante

los cuales se encontraron correlaciones significativas en estudios previos basados en observaciones (véase la sección 8.2.2).

38. Las teleconexiones de ENSO a Norteamérica durante la temporada de FMA, documentadas en observaciones por [Diaz et al. \(2001\)](#), constituyen una excepción de este hallazgo general. A saber, en el sur de los Estados Unidos y México, así como al sur de las islas Aleutianas, la prueba de robustez propuesta aquí es pasada después del Gran Cambio Climático del Pacífico pero no lo es antes del cambio (véase la sección 8.2.2).
39. El resultado más sorprendente de la presente tesis es que la no estacionariedad de la teleconexión ENSO con la precipitación del Mediterráneo occidental establecida con datos observacionales ([Mariotti et al., 2002](#)) no se cumple cuando se tiene en cuenta la variabilidad atmosférica interna. Independientemente de la temporada considerada, se considera que esta teleconexión en particular *no* es robusta en ningún período de 20 años del siglo XX (ver la sección 8.2.2).
40. Dado que el intervalo de confianza que describe las variaciones en la intensidad de la teleconexión antes mencionada es aproximadamente constante a lo largo de todo el siglo XX, no existe ninguna indicación para una modulación de baja frecuencia a través de cualquier agente forzante externo sugerida, por ejemplo, en [Lopez-Parages and Rodriguez-Fonseca \(2012\)](#).
41. En los extratropicos, las teleconexiones ejercidas por la PDO y la AMO son generalmente robustas sólo en la vecindad directa de las regiones de origen, es decir, en y alrededor de las cuencas del Pacífico Norte y del Atlántico Norte y más aún para temperaturas que para precipitación y variables que describen la circulación atmosférica. Esto apunta al hecho de que sólo es robusta la respuesta en la absorción de calor (o enfriamiento) de las masas de aire que superponen las SST anómalas, mientras que la respuesta de circulación no lo es. Se encontraron excepciones al sur de las islas Aleutianas y en el Pacífico central subtropical, donde la circulación atmosférica responde de forma robusta a las variaciones de la PDO. Además de la respuesta general de la circulación en los trópicos, éstos pueden, sin embargo, surgir simplemente de la co-variabilidad con ENSO. Se necesitan trabajos futuros para evaluar estos problemas (véase la sección 8.2.3).

## 1.5 Publicaciones Relacionadas

Parte de los resultados centrales de esta tesis doctoral han dado lugar a publicaciones en revistas científicas de reconocido prestigio en el campo de las ciencias atmosféricas. En particular:

- Brands, S., J. M. Gutiérrez, and D. San-Martín, 2016: Twentieth-century atmospheric river activity along the west coasts of Europe and North America:

algorithm formulation, reanalysis uncertainty and links to atmospheric circulation patterns. *Clim. Dyn.*, 48 (9), 2771â2795, doi:10.1007/s00382-016-3095-6.

- Brands, S., 2017: Which ENSO teleconnections are robust to internal atmospheric variability? *Geophys. Res. Lett.*, 44 (3), 1483â1493, doi:10.1002/2016GL071529.

habiendo también participado en un estudio sobre el impacto de ARs en la precipitación local que no forma parte de la tesis:

- Eiras-Barca, J., S. Brands, and G. Miguez-Macho, 2016: Seasonal variations in North Atlantic atmospheric river activity and associations with anomalous precipitation over the Iberian Atlantic Margin. *J. Geophys. Res.-Atmos.*, 121 (2), 931-948, doi:10.1002/2015JD023379.

Otros siete artículos escritos por el doctorando han sido publicados en temas relacionados con la tesis, como la incertidumbre del reanálisis:

- Brands, S., J. M. Gutiérrez, A. S. Cofiño, and S. Herrera, 2012: Comments on “Global and Regional Comparison of Daily 2-m and 1000-hPa Maximum and Minimum Temperatures in Three Global Reanalyses”. *J. Clim.*, 25 (22), 8004-8006, doi:10.1175/JCLI-D-12-00122.1.
- Brands, S., J. M. Gutierrez, S. Herrera, and A. S. Cofino, 2012: On the use of reanalysis data for downscaling. *J. Clim.*, 25 (7), 2517-2526, doi:10.1175/JCLI-D-11-00251.1.
- Brands, S., S. Herrera, J. Fernández, and J. M. Gutiérrez, 2013: How well do CMIP5 Earth System Models simulate present climate conditions in Europe and Africa? *Clim. Dyn.*, 41 (3-4), 803-817, doi:10.1007/s00382-013-1742-8.

o distintos estudios de teleconexiones:

- Brands, S., R. Manzananas, J. M. Gutiérrez, and J. Cohen, 2012: Seasonal predictability of wintertime precipitation in Europe using the snow advance index. *J. Clim.*, 25 (12), 4023-4028, doi:10.1175/JCLI-D-12-00083.1.
- Brands, S., 2013: Skillful seasonal predictions of boreal winter accumulated heating degree-days and relevance for the weather derivative market. *J. Appl. Meteorol. Climatol.*, 52 (6), 1297-1302, doi:10.1175/JAMC-D-12-0303.1.
- Brands, S., 2014: Predicting average wintertime wind and wave conditions in the North Atlantic sector from Eurasian snow cover in October. *Environ. Res. Lett.*, 9 (4), doi:10.1088/1748-9326/9/4/045006.
- Brands, S., S. Herrera, and J. M. Gutiérrez, 2014: Is Eurasian snow cover in October a reliable statistical predictor for the wintertime climate on the Iberian Peninsula? *Int. J. Climatol.*, 34 (5), 1615-1627, doi:10.1002/joc.3788.



---

## CHAPTER 2

---

### Introduction

Earth’s energy budget is characterized by an energy surplus at low latitudes and a deficit at high latitudes, this imbalance being compensated for by poleward energy fluxes exerted by the atmosphere and ocean (Fasullo and Trenberth, 2008). The atmospheric transport component can be further decomposed into the fluxes of sensible and latent heat, the latter being accomplished by means of water vapour transport. Perhaps in contrast to what one might expect, atmospheric water vapour transport is not organized homogeneously in space and time but is achieved via filamentary “channels” of intense flux having a lifetime of a few days at the utmost (Zhu and Newell, 1994). Reminiscent of river meanders seen from bird’s eye perspective (see Figure 2.1), these “atmospheric rivers” potentially cause extreme precipitation, flooding and landslide events, especially in case the moist air masses are forced to rise and precipitate on the wind-side of a mountain range (e.g. Neiman et al., 2002; Dettinger et al., 2011). While typically seen as large-scale precursors of local-scale hydrological extreme events, the present thesis deals with the precursors of the atmospheric rivers themselves. This is not done for individual events but for seasonally aggregated atmospheric river occurrences. Precursor are searched for in atmosphere and ocean and links are established on the basis of observations and idealized numerical model experiments.

This introduction first defines the term “atmospheric river”, then describes the implications for hydrology and the Earth sciences with more detail and summarizes what is currently known about the precursors and predictability of these phenomena. Then, the aims of the present thesis are presented and the structure is outlined.

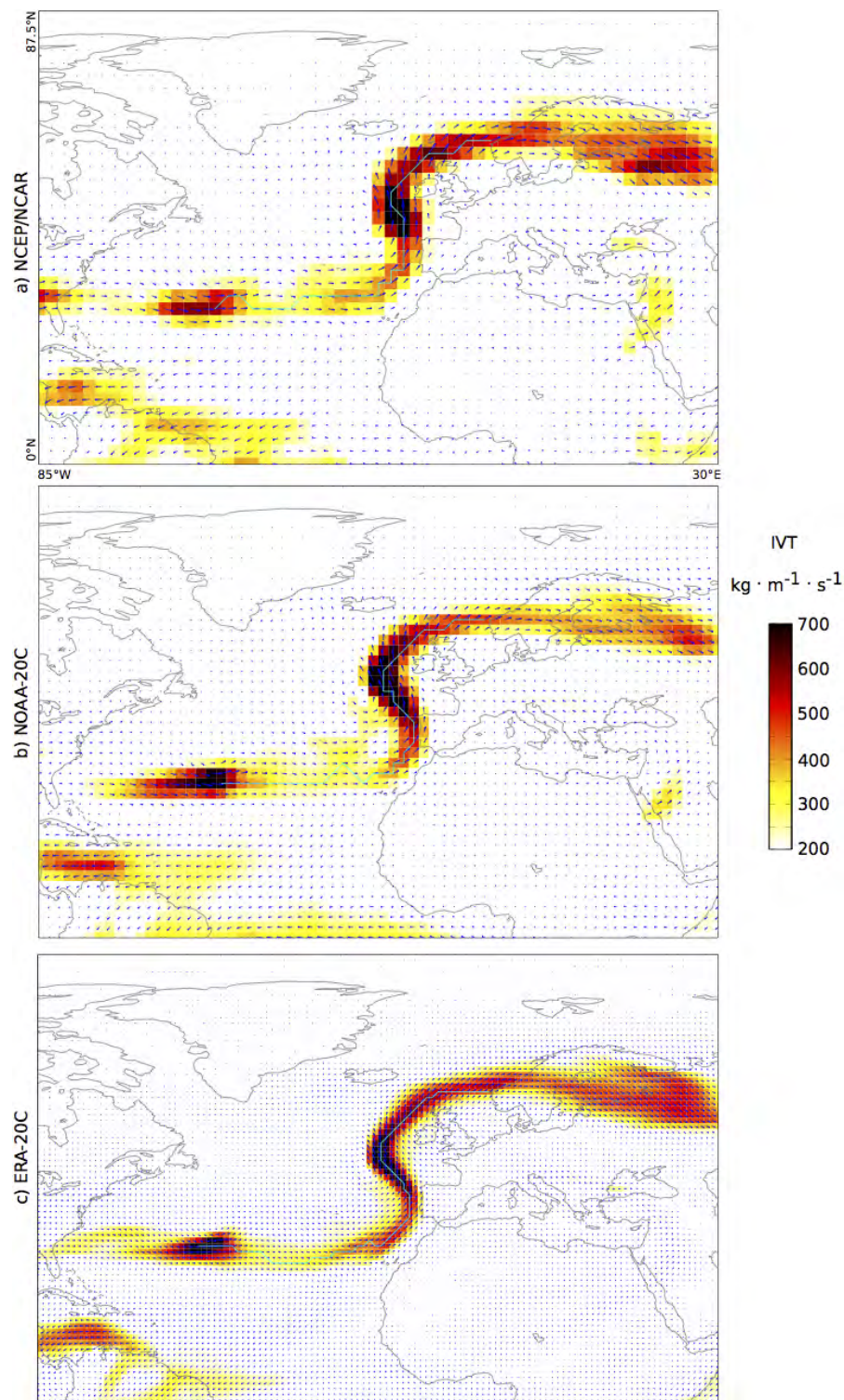


**Figure 2.1:** Illustrative example for an AR affecting southern Norway on 11 January 1971 00 UTC for a) NCEP/NCAR reanalysis 1, b) NOAA-CIRES Twentieth-Century Reanalysis v2, and c) ECMWF ERA-20C reanalysis. Colour shadings and vector lengths are proportional to the intensity of the vertically integrated water vapour transport (IVT, as defined in Section 3.2). The direction of the flow is indicated by the orientation of the vectors. The cyan line represents the AR track found by the algorithm developed in the present thesis (see Section 4.1). Source: own illustration

## 2.1 *What is an Atmospheric River and How is it Detected and Tracked?*

Approximately 90% of the poleward water vapour transport in the atmosphere is accomplished by narrow and elongated structures of intense transport having a lifetime of a few days at the utmost (Zhu and Newell, 1994, 1998). Due to their filamentary appearance reminiscent of a river’s course seen from bird’s-eye perspective, these structures have been originally referred to as “tropospheric rivers” (Newell et al., 1992), a term which later on developed to “atmospheric rivers” (hereafter referred to as “ARs”). Two processes contribute to the formation and maintenance of the water vapour constituting these structures. The first one is similar to the flow of a river. Water evaporates in a remote source region and is then transported over thousands of kilometres. For this long-range transport to work, evapotranspiration and condensation must play a minor role along the entire transport route (Knippertz and Wernli, 2010; Gimeno et al., 2012; Sodemann and Stohl, 2013; Garaboa-Paz et al., 2015). The second process is small-scale moisture recycling (evapotranspiration, condensation and precipitation). In this case, water vapour is continuously lost and refreshed ahead of the cold front(s) of one or several extratropical cyclones, leading to a structure looking like a river but not sharing its transport properties (Bao et al., 2006). Recent studies point to the fact that, for most ARs, moisture recycling is more important than long-range transport (Newman et al., 2012; Dacre et al., 2015).

ARs can be identified and tracked using either Eulerian or Lagrangian methods (Newell et al., 1992; Bao et al., 2006; Knippertz and Wernli, 2010; Gimeno et al., 2012; Garaboa-Paz et al., 2015). The algorithms used within the Eulerian framework, which will be the focus of the present thesis, are capable to automatically detect and track AR structures at a given point in time and usually operate on the *intensity of the vertically integrated water vapour transport* (IVT, Zhu and Newell, 1998; Lavers et al., 2012; Guan and Waliser, 2015). The corresponding data are ideally taken from dropsonde or satellite observations which, however, have a limited spatial and temporal coverage (Zhu and Newell, 1998; Ralph et al., 2004; Lavers et al., 2011). This is why model data from reanalyses, usually referred to as “quasi-observations” (e.g. Brands et al., 2012b), are used if long time series and complete spatial coverage is required, e. g. for assessing the *climatological* aspects of atmospheric rivers (Higgins et al., 2000; Neiman et al., 2008; Knippertz et al., 2013; Payne and Magnusdottir, 2014).

## 2.2 *Why are Atmospheric Rivers Important?*

ARs are considered important mainly because they contribute to the seasonal precipitation totals of a given region and because they are precursors of extreme precipitation events (e.g. Neiman et al., 2002; Lavers et al., 2011). Dynamically, ARs are related to precipitation through the so-called “seeder-feeder” effect (Browning,

1974; Neiman et al., 2002). Namely, upper-level precipitation caused by ascending air masses associated with fronts (the seeder) falls through, and is thus reinforced by, lower tropospheric precipitation caused by moisture advection which, in turn, is driven by an AR. It is the coincidence of both precipitation types that leads to large precipitation intensities. Thus, on the one hand, ARs are beneficial for a region's water supply but, on the other, are potentially harmful since they can trigger river flooding and landslide events, hereafter jointly referred to as "hydrological extreme events" (Lavers et al., 2011), especially in case they coincide with previously accumulated thick snow packs and/or water-saturated soils (Leung and Qian, 2009; Ralph et al., 2013). These relationships are particularly strong for regions where the seeder-feeder effect can be efficient, i.e. along mountain ranges that are orientated perpendicular to the main direction of the moisture flow (e.g. Neiman et al., 2002, 2004; Guan et al., 2012; Kim et al., 2013; Ramos et al., 2015).

In the observational record, up to the 90% of the extreme precipitation events occurring along the west coasts of Europe and North America were preceded by an AR (e.g. Lavers and Villarini, 2013), which is exemplified in Figure 2.2 for the case of the western Iberian Peninsula (Eiras-Barca et al., 2016). However, percentages considerably decrease if the fraction of ARs coinciding with extreme precipitation is considered instead, i.e. if AR occurrence is interpreted as an early warning system of extreme precipitation. This ratio, which would be referred to as "hit rate" in the field of forecast verification (Murphy and Winkler, 1987), is usually not larger than 50% and during the summer half-year, when convective precipitation becomes more important than during the winter half-year, can even decrease to 10% (Eiras-Barca et al., 2016) (see Figure 2.3). Unfortunately, little is known about the respective "false alarm rates", i.e. the percentage of ARs not leading to extreme precipitation, which is an important research gap since both the hit and false alarm rates must be considered when evaluating the skill of an early warning system (Murphy and Winkler, 1987).

Since the number of ARs affecting a region in a given time period (the seasonal to decadal timescale will be relevant here) is closely linked to the precipitation accumulated in that period, in the polar regions, these "AR counts" largely control the accumulation of snow over the Greenland and Antarctic ice sheets. Consequently, as long as precipitation is solid, ARs are positive contributors to the mass balance of the latter, meaning that they negatively contribute to the global sea level (Gorodetskaya et al., 2014).

On the climatological timescale, an increase in the frequency of ARs (Lavers et al., 2013; Ramos et al., 2016), and/or in the average moisture transport achieved per event (Payne and Magnúsdóttir, 2015; Rivera and Dominguez, 2016; Shields and Kiehl, 2016), would point to an enhanced global water cycle caused by multidecadal natural variability and/or anthropogenic climate change (Stocker et al., 2013).

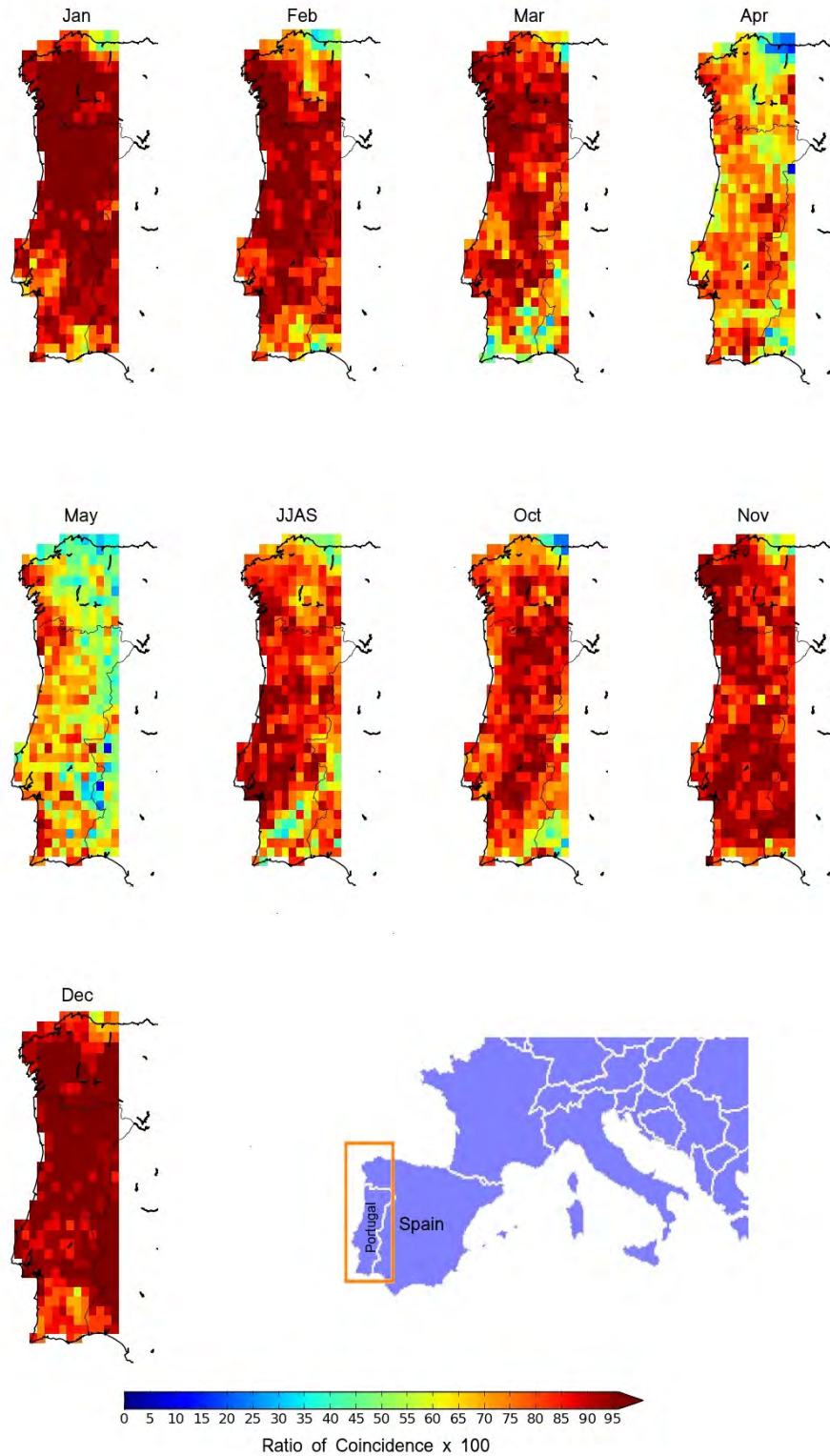


**Figure 2.2:** Relevance of atmospheric rivers for regional extreme precipitation events for the example of the western Iberian Peninsula. Shown is the percentage of extreme precipitation events associated with an AR. Results are for the 1979-2008 period and were obtained from an independent AR detection and tracking algorithm and the Iberia02 dataset. See [Eiras-Barca et al. \(2016\)](#) for more details.

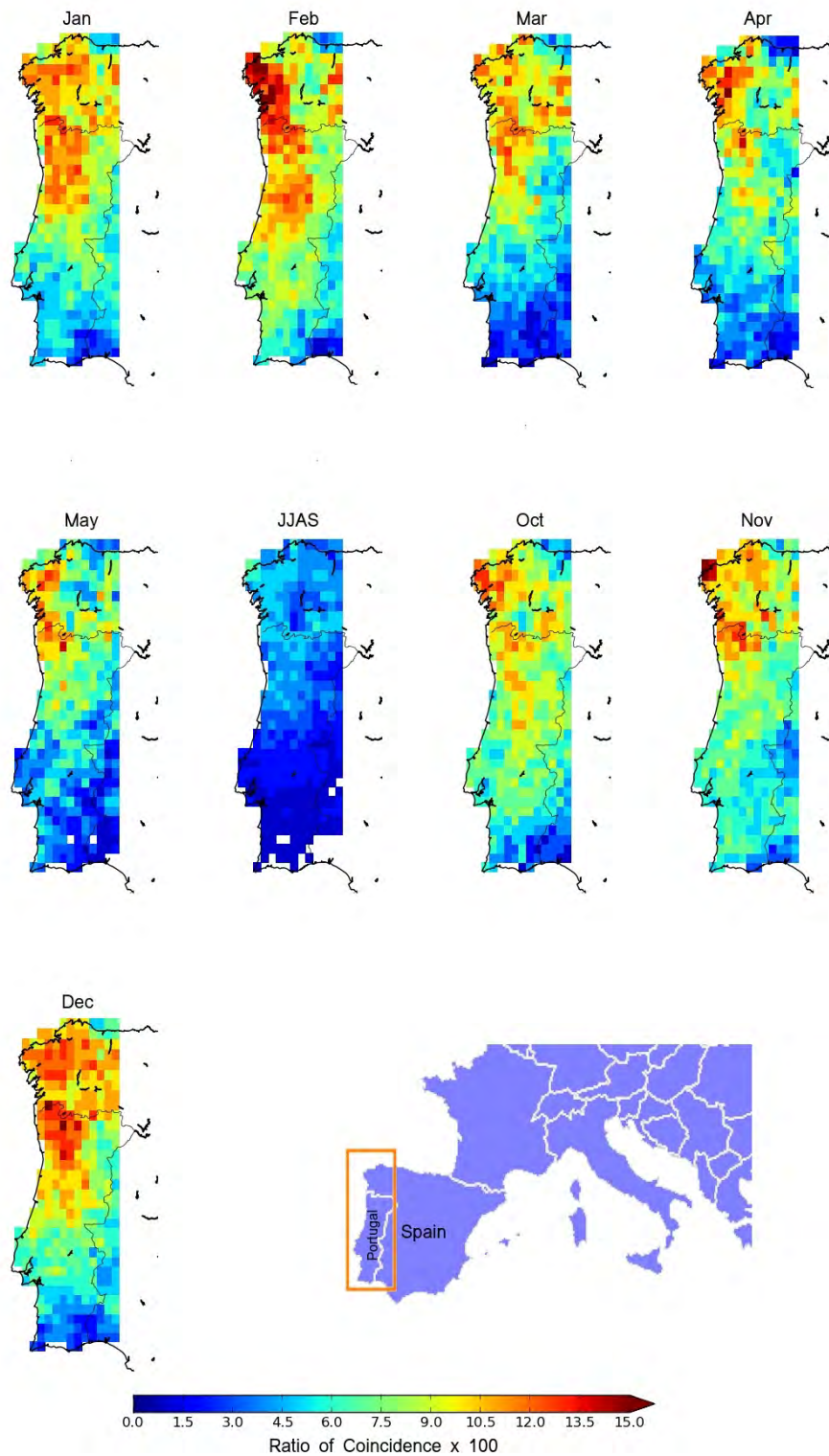


**Figure 2.3:** As Figure 2.2, but for the percentage of ARs leading to local-scale extreme precipitation. This rate is equivalent to the “hit rate” commonly used in forecast verification (see text for more details). Source: (Eiras-Barca et al., 2016)

## 2.3 What are the Known Drivers and the Implications for Predictability?

Whereas ARs triggering (extreme) precipitation have been studied extensively to date, a spatially (and also temporally) complete picture on the large-scale atmospheric and oceanic conditions triggering above or below normal AR activity is yet “under construction” (Gimeno et al., 2014, 2016).

The atmospheric precursors driving seasonally aggregated AR counts or, alternatively, IVT (see Section 3.2 for a definition) have been extensively studied for North America, the “cradle” of atmospheric river research (Neiman et al., 2002; Ralph et al., 2004). Bao et al. (2006) found a weakening of the central Pacific subtropical ridge to favour the direct moisture flux from the tropics to the West Coast of the United States (U.S.). In a case study focussing on the 2010/11 snow season, Guan et al. (2013) concluded that the exceptional AR activity over California’s Sierra Nevada during that particular season was linked to the fact that both the Pacific-North American pattern and the Arctic Oscillation<sup>1</sup> (PNA and AO) were in the negative phase. The particular role of the PNA in “driving” the seasonal-mean IVT and associated AR counts has been recently pointed out in Kim and Alexander (2015) and Guan and Waliser (2015). Namely, the strength and position of the Aleutian Low (i.e. one of the PNA’s centres of action) is key for the spatial distribution of the IVT in this region. If this low pressure system is anomalously deep (in which case the PNA is normally positive), the IVT is above normal in a region extending from the U.S. Pacific Northwest to Alaska whereas, when it is displaced to the South, moist conditions are exhibited by the southwestern U.S. and Mexico. Besides the effect of the PNA, East-Asian cold surges increase the odds for AR landfalls along the west coast of North America during the days following the peak of the cold surge (Jiang and Deng, 2011).

The atmospheric circulation over the North Pacific and North America is known to be associated with low-frequency modes of variability in 1) the sea surface temperatures (SSTs) of the Pacific Ocean (e.g. Mantua et al., 1997; Trenberth et al., 1998) and 2) tropical convection (Straus and Shukla, 2002; Franzke et al., 2011). All of these modes have typical periodicities, which are more or less regular, making them more or less predictable. Ordered from high to low periodicity these modes are 1) the Madden-Julian Oscillation (MJO, Madden and Julian, 1971), 2) the El Niño-Southern Oscillation (ENSO, Trenberth, 1997; McPhaden et al., 2006) and 3) the Pacific Decadal Oscillation (PDO, Zhang et al., 1997; Mantua et al., 1997), having peak periodicities of approximately 30 to 60 *days*, seven to eight *years* and five to seven *decades* respectively. Similar to the PDO, the Atlantic Multidecadal Oscillation (AMO) is a multidecadal oscillation of the North Atlantic SSTs and is associated with climate anomalies in and around this ocean basin respectively (Kerr, 2000; Enfield et al., 2001). To explore possible sources of long-range predictability, these

---

<sup>1</sup>see Barnston and Livezey (1987) for a definition of these atmospheric circulation indices

modes of low-frequency variability (hereafter referred to as the “predictable modes”) have been associated with the seasonally aggregated AR counts and IVT in North America. For the November-through-March season, significant relationships with specific phases of the MJO have been found for the AR counts in many subregions of this continent (Guan et al., 2012, 2013; Guan and Waliser, 2015). During El Niño events, AR counts tend to be above-normal in a region ranging from the U.S. Pacific Northwest to Alaska (Guan et al., 2013; Guan and Waliser, 2015). Bao et al. (2006) concluded that the direct transport of tropical moisture from the tropics to the the U.S. west coast is most likely during neutral ENSO winters. However, they pointed out that such a long-range moisture transport is rather unusual compared to transport due to local moisture convergence, a finding which has been recently confirmed by Dacre et al. (2015). Finally, only one single study on the role of potential multidecadal drivers of AR frequencies is available to date (Liu et al., 2016). Using the Zhu and Newell (1998) AR detection algorithm, Liu et al. (2016) conclude that the December-January-February (DJF) AR counts along the west coast of North America are significantly associated with the PDO, and also with the North Pacific Gyre Oscillation (NPGO, Di Lorenzo et al., 2008), which are index time series based on Principal Component Analysis describing distinct multi-decadal oscillations of the SSTs in the North Pacific Ocean. In Section 3.1 these indices are described in detail. Liu et al. (2016) found the PDO to be positively related to AR frequencies around the Gulf of Alaska and the NPGO to be inversely related to AR frequencies around Baja California.

The atmospheric and particularly the oceanic precursors of the AR activity in Europe have been less extensively studied to date. Lavers et al. (2012) found the October-through-March AR activity over the British Isles to be inversely related to the Scandinavian Pattern (Barnston and Livezey, 1987). In a follow-up study conducted on continental scale (Lavers and Villarini, 2013), the sea level pressure composite maps associated with AR arrivals in northern and southern Europe were found to resemble the positive and negative phases of the North Atlantic Oscillation (NAO Hurrell et al., 2003) respectively. Ramos et al. (2015) found the ONDJFM AR-activity over the Iberian Peninsula to be positively related to the East Atlantic pattern in first place. Unlike in Lavers and Villarini (2013), the “AR-NAO” link was found to be insignificant in Ramos et al. (2015) which is perhaps somewhat counter-intuitive since the NAO is known to describe a large fraction of variability of the wintertime precipitation totals in this region (Hurrell, 1995; Trigo et al., 2004). Reasons for this disagreement might be found in differences in the considered datasets, time periods and season definitions.

Whether the seasonal AR frequencies in *Europe* are statistically associated with the above mentioned *predictable modes* of low frequency variability (which, except for the MJO and NPGO, are commonly described by SST variations) has been assessed only in the recent landmark paper by Guan and Waliser (2015). Focussing on the November-through-March season, this study concludes that AR activity in Europe is significantly associated with phase 3 and 4 of the MJO, whereas the role of ENSO is

insignificant except over the southern and western Iberian Peninsula.

Since ENSO teleconnections will play the most important role in the context of the present thesis (see Section 6.2, and Chapters 7 and 8), their development and distortion due to internal atmospheric variability will be described in detail in Section 2.5 of this introduction.

## 2.4 What is Internal Atmospheric Variability?

The climate system comprises the subsystems atmosphere, ocean, cryosphere and biosphere. The mutual interaction between these subsystems, as well as the interaction between the phenomena of an individual subsystem—the focus of the present thesis is on the atmosphere—, is highly nonlinear (Palmer, 1999). As a result, the behaviour of the subsystems, and of the climate system as a whole, can be described by “chaotic” dynamics (Lorenz, 1963) that manifest in the irregular, quasi-periodic variability of their phenomena (e.g. the NAO in the atmosphere or ENSO in ocean and atmosphere). This behaviour is very sensitive to small perturbations, and this is why two initially only very slightly differing atmospheric states, during a time period of about two weeks<sup>2</sup>, evolve to distinct states (Lorenz, 1963)<sup>3</sup>. This implies that different realizations of the atmosphere may exhibit different climatological features.

Variability developing due to interaction within the system, i.e. without the influence of any factor born outside the system, is commonly referred to as “internal” climate variability (Stocker et al., 2013), and is typically analyzed by considering different realizations (model runs) of the system. In turn, variability caused by external factors such as, e.g., solar radiation is denominated “external climate variability”. Since external [climate] variability is imposed from outside the system whereas internal variability is not, the terms “forced” and “unforced” variability are often used instead (e.g. Hardiman et al., 2007). The drivers of external variability are usually referred to as “external forcing agents” (Stocker et al., 2013).

*If the climate system is seen as whole*, i.e. if the aforementioned subsystems are seen in conjunction, which is commonly emphasized by the term “extended climate system”, then the most prominent external forcing agents are the sun, the orbital parameters of the Earth, volcanic activities and the human race (Stocker et al., 2013). Among the countless interferences with nature, the human actions that most efficiently impact on climate are greenhouse gas and aerosol emissions, land-use changes, as well as the generation of tropospheric and the depletion of stratospheric ozone. Whereas external variability can thus arise from natural and anthropogenic forcing agents, internal variability is, in principle, a natural process which, however, might be modified by anthropogenic climate change (Palmer, 1999).

Alternatively, *if the focus is put on one of the subsystems* of the extended climate

---

<sup>2</sup>i.e. the maximum lead-time weather predictions have skill for

<sup>3</sup>see Garaboa-Paz et al. (2015) for an application of the Lorenz theory to atmospheric rivers

system—here: the atmosphere—, then the biosphere, cryosphere and—here of particular interest—the ocean can be seen as additional *external* forcing agents whereas the variability arising from nonlinear interactions *within* the atmosphere can be denominated *internal atmospheric variability*. With this in mind, in the following Section, the ENSO phenomenon, the associated teleconnections and the internal atmospheric variability sources favouring their propagation will be introduced.

## 2.5 *How do ENSO Teleconnections Develop in the Context of Internal Atmospheric Variability?*

ENSO is triggered by anomalously cold or warm SSTs in the central and eastern equatorial Pacific (e.g. Trenberth, 1997; McPhaden et al., 2006). It has long been recognized that it not only influences the climate in the Pacific Ocean basin itself but also in much more remote regions such as North America, northeast Brazil or sub-Saharan Africa (Halpert and Ropelewski, 1992; Ropelewski and Halpert, 1996; Trenberth et al., 1998; Diaz et al., 2001). Such a remote association between climate anomalies is commonly referred to as a “teleconnection” (Bjerknes, 1969). ENSO-induced teleconnections in and around the tropical Pacific can be conceptually explained with the Walker circulation (Bjerknes, 1969). In its normal state, this circulation is maintained by the temperature and pressure gradient between the warm western tropical Pacific and Maritime Continent on the one hand, and the colder eastern tropical Pacific off the coast of South America on the other. This configuration leads to a thermal circulation system with easterly winds near the surface contrasted by westerlies in the upper troposphere, accompanied by convection in the western Pacific and large-scale subsidence in the eastern tropical Pacific. During La Niña events, the Walker circulation is reinforced whereas under El Niño conditions it weakens and occasionally even reverses. For the case of El Niño, this, in turn, favours above-normal precipitation along the west coast of South America and dry conditions over the Maritime Continent. Anomalies in the strength of the Walker Circulation are known to affect other thermal circulation systems covering the remainder of the tropics, thereby favouring climate anomalies in the entire tropical belt (e.g. Wallace et al., 1998; Kumar et al., 1999; Chiang et al., 2002). Other mechanisms relevant for the propagation of the teleconnection throughout the tropics include 1) a mechanism arising from the temperature increase in the entire tropical troposphere (i.e. also beyond the boundaries of the Pacific Ocean basin) due to the fact that pressure gradients cannot persist there (Yulaeva and Wallace, 1994; Chiang and Sobel, 2002) and 2) modulations of extratropical modes of circulation variability (such as the Pacific-North American pattern) that, in turn, feed back onto SSTs in other ocean basins such as, e.g., the northern tropical Atlantic (Nobre and Shukla, 1996).

ENSO-induced teleconnections to the extratropics are, for the case of El Niño events, initially triggered by enhanced tropical convection in the region with positive

SST anomalies (Trenberth et al., 1998). The associated latent heat release and upper tropospheric divergence warms up the tropical troposphere (i.e. the ascending branch of a regional Hadley circulation). This, in turn, enhances upper-tropospheric convergence and large-scale subsidence within the subtropical anticyclones (i.e. the descending branch of the Hadley cell), thereby establishing a link between the anomalous Walker and Hadley cells (Wang and Enfield, 2003). Within the subtropical anticyclones, anomalous upper-tropospheric convergence is the most important source of Rossby wave forcing and these waves can eventually propagate to the mid and high latitudes where they form the typical ridges and troughs in the geopotential height field which govern the local weather on time scales up to several weeks. To a good approximation, dynamics are inverse during La Niña events (Trenberth et al., 1998).

However, since the internal atmospheric variability is much more pronounced in the extratropics than in the tropics (e.g. Kumar and Hoerling, 1995), the development of the extratropical teleconnection pathway critically depends on the “background” state of the atmosphere during the timing of the event. For instance, conditions are favourable when the wave train triggered by ENSO propagates through the exit region of an extratropical jet (Branstator, 1985), in which case it may eventually modify the low and high pressure systems over the North Atlantic-European sector which, if averaged in time, have preferred geographical locations (i.e. Iceland and the Azores). If these events occur with above-normal frequency, measurable deviations from the seasonal mean climate conditions are the consequence (Trenberth et al., 1998; Shaman and Tziperman, 2011). Other agents favouring the extratropical pathway are many-fold and comprise momentum fluxes by high-frequency eddies (Kok and Opsteegh, 1985), two-way coupling between the troposphere and stratosphere, as well as sudden stratospheric warmings (Ineson and Scaife, 2009; Butler et al., 2014). For a detailed explanation of these mechanism, as well as of potential nonlinear relationships (Toniazzo and Scaife, 2006), the interested reader is referred to the reference list.

## 2.6 What is an Atmosphere General Circulation Model

From planetary-scale Rossby Waves to local-scale precipitation, Atmosphere General Circulation Models (AGCMs) are mathematical expressions of all relevant atmospheric processes that compensate Earth’s energy imbalance between the equator and the poles in order to assure that the energy leaving at the top of the atmosphere equals the entering solar energy plus the energy originating from Earth’s interior, so that the system is in equilibrium (Gutiérrez et al., 2004). The main phenomenon simulated by these models is the *general circulation of the atmosphere*, i.e. the flow of air masses in the free troposphere, where friction from the ground is negligible, resulting from the energy surplus in the tropics and the energy deficit at high latitudes. The associated meridional temperature gradient leads to a meridional pressure gradient which, in combination with the Coriolis force, would result in a

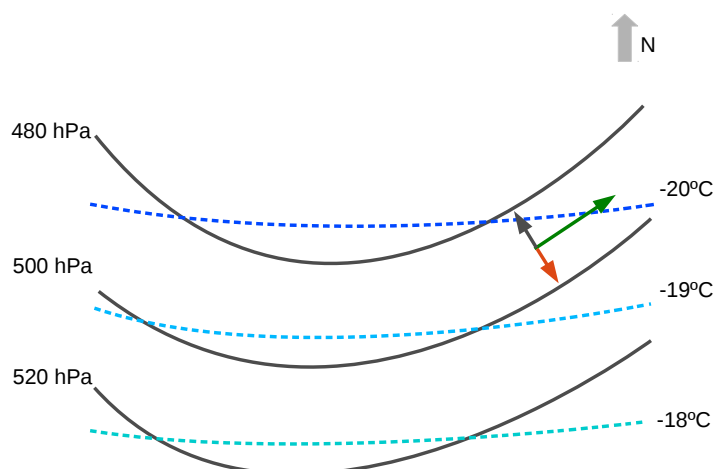


**Figure 2.4:** Schematic representation of a baroclinic situation in the middle troposphere of the Northern Hemisphere extratropics. The block arrow at the top right indicates the direction of the North Pole. The isobars (solid lines) cross the isotherms (dashed lines) so that relatively warm air masses are transported polewards by the geostrophic wind (the green arrow). Note that the Coriolis force (red arrow) and the force exerted by the pressure gradient (dark grey arrow) are in equilibrium. Source: own representation.

purely zonal (eastward) flow in the mid latitudes, blowing parallel to both isotherms and isobars. In this hypothetical configuration, the meridional temperature gradient would ever increase. In reality, if the meridional temperature gradient surpasses a certain threshold, the zonal flow begins to form meanders resulting in a crossing between the isolines of temperature and pressure. The resulting “geostrophic wind”<sup>4</sup> triggers a “baroclinic flow” of thermal energy to the Pole (see Figure 2.4). The meanders causing the barotropic flow are commonly referred to as “Rossby Waves”. Their amplitude can be reinforced by large-scale temperature gradients, e.g. between sea and land masses, or between cool and warm ocean areas, and also by mountain barriers perpendicular to the flow<sup>5</sup>. These waves form the typical ridges and troughs, e.g. visible in the geopotential height field, that govern the weather in a given region up to several weeks. The troughs, in turn, are associated with low pressure systems carrying fronts that themselves account for a large fraction of the poleward transport of sensible and latent heat, the latter being caused by the large-scale ascent of moist air masses leading to condensation (Barry and Carleton, 2001), the moisture being supplied, e.g., by an AR (see Section 2.1).

Governed by the conservation of energy, mass and momentum, the variables through which the general circulation manifests are simulated with equations that are integrated in time on a discrete three dimensional coordinate system that is commonly referred to as the model’s “grid” (see Figure 2.5). The spatial resolution of the grid is associated with the temporal distance between two integration steps, the spatiotemporal resolution being the main factor of the computational requirements

<sup>4</sup>i.e. the wind blowing parallel to the isobars, friction from the ground is zero

<sup>5</sup>such as the Rocky Mountains in the Northern Hemisphere

needed to “run” the model, i.e. to integrate it in time (Gutiérrez et al., 2004). Since these requirements are huge, AGCMs are normally run on High Performance Computing Clusters, i.e. hardware architectures comprising hundreds of Central Processor Units (CPUs) with distributed memory. The current generation of AGCMs, applied in the framework of the present thesis, typically have a horizontal resolution of approx. one to three degrees in latitude and one to four degrees in longitude (see Sections 7.1.1 and 8.1). In the vertical, they typically comprise several tens of model levels, having a model top somewhere in between the middle stratosphere and lower mesosphere (Charlton-Perez et al., 2013).

In order to preserve the energy equilibrium, atmospheric phenomena operating below the resolution of the AGCM, like e.g. cumulus convection and convective precipitation, cannot be omitted and are included by means of statistical relationships which, in turn, are empirically estimated from field campaigns. These statistical relationships are described by the so-called “parametrization schemes” (Stensrud, 2007) and are of particular importance e.g. for the modelled precipitation and radiation, which can considerably vary from one scheme to another.

In the context of the present thesis, AGCMs are a formidable tool to assess the *internal variability* of a *model* atmosphere that is externally forced by observed variations in SSTs and sea-ice cover (Gates, 1992; Taylor et al., 2012) and, for the case of the most recent generation of AGCM experiments (see Chapter 8), also greenhouse gas and aerosol emissions, ozone and volcanic activity (Hersbach et al., 2015). It should be pointed out that AGCMs, in contrast to Atmosphere Ocean General Circulation Models (AOGCMs) or the recently developed Earth System Models (ESMs) are not coupled to an ocean model or even to a sea-ice or biochemical model. Rather, they are driven by a “data ocean”, i.e. by the *observed* SST and sea-ice cover values which are *prescribed* instead of being internally simulated. Thus, AGCMs are less complex than the fully coupled Earth System Models used to derive transient climate predictions for the 21st century, the latter being intended to simulate the *extended* climate system with all of its subcomponents and feedbacks in the future, when no observations are available (Taylor et al., 2012). However, this complexity is not convenient for the purpose of the present study since the best approximation for real SST variations are the *observations* rather than the output of a numerical ocean model.

In the present thesis, external AGCM output as well as home-made AGCM simulations will be used in addition to the data from atmospheric reanalyses (see Sections 3.2, 7.1.1, 7.1.2 and 8.1). In this context, it is interesting to note that atmospheric reanalyses are nothing more than AGCM<sup>6</sup> experiments driven by the aforementioned external forcing agents and *synoptic observations*, the latter usually comprising any reliable observation available during the reanalysis period. When synoptic observations are sparse or even missing, which particularly is the case in the early twentieth century, reanalysis data should be expected to be similar to a “freely

---

<sup>6</sup>AOGCMs are also used for this purpose

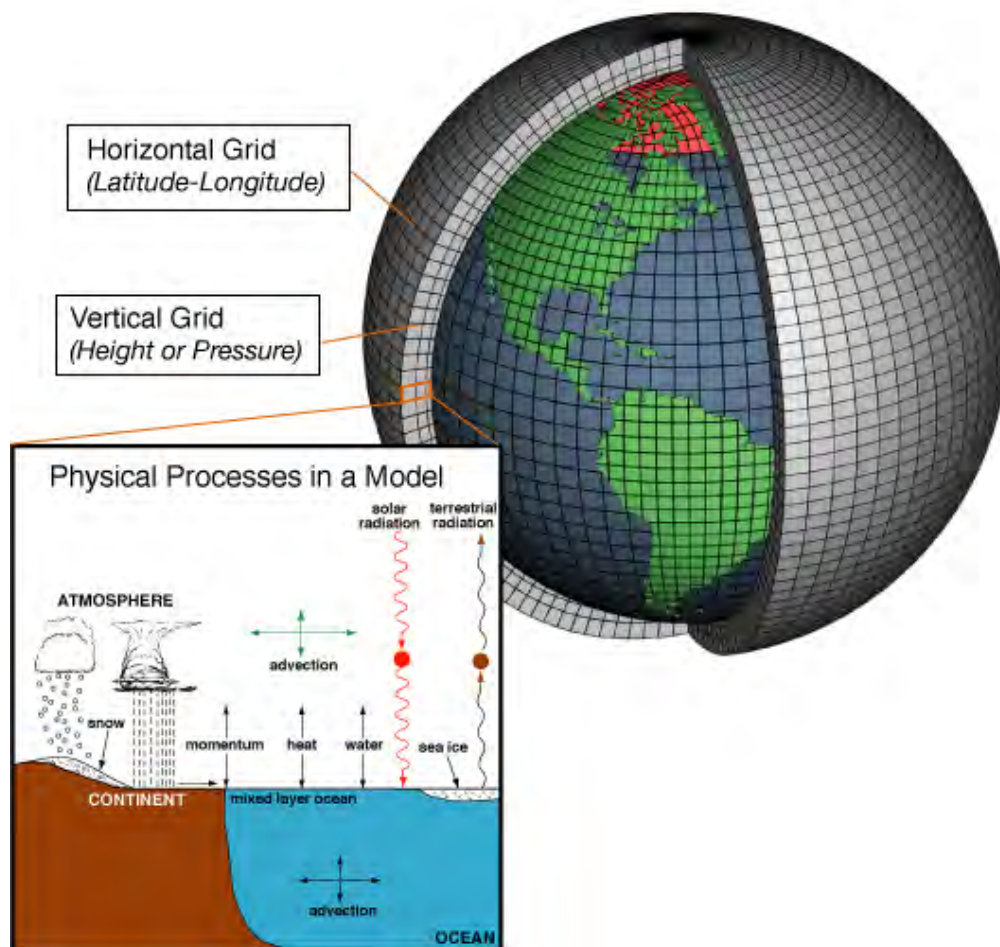


**Figure 2.5:** Schematic representation of an Atmosphere General Circulation Model. Shown is the model's grid and an overview of the subgrid processes not resolved by the model that must be parametrized. Source: [http://celebrating200years.noaa.gov/breakthroughs/climate\\_model/AtmosphericModelSchematic.png](http://celebrating200years.noaa.gov/breakthroughs/climate_model/AtmosphericModelSchematic.png)

run” AGCM bound to the external forcing agents only, in which case the model generates its own internal variability (Sterl, 2004).

## 2.7 Aims of the Present Thesis

Many studies on teleconnections presumably triggered by SST variations, and essentially all teleconnection studies involving atmospheric rivers, are based on the observational record. However, as has been pointed out in Sections 2.4 and 2.5, the atmospheric response to external forcing as e.g. exerted by SST variations is modified by internal atmospheric variability and is therefore not deterministic. The atmosphere coupled to the external forcing agents can be better described in terms of a *probabilistic system*, defined as a system whose present state is an insufficient estimator of its future state (Lorenz, 1963; Palmer et al., 2005). As pointed out in Section 2.4, in such a system, two initially only very slightly differing states largely diverge if the system is allowed to run forward in time. For the example of ENSO teleconnections, this means that even in the hypothetical case of two distinct El Niño events having the same equatorial Pacific SST anomaly patterns, the two events cannot be expected to have the same impact on the climate thousands of kilometres away since the state of the overlaying atmosphere *differs* from one event to another (van Den Dool, 1994). In this view, the observational record is just the reflection of a *single* and *unique* atmospheric response to the external forcing. This response might have been *different* if the atmosphere would have been allowed to run once again with exactly the same external forcing and with slightly different atmospheric states at the start of the realization, the latter commonly referred to as the “initial conditions” (Stainforth et al., 2007).

In fact, the observed teleconnections induced by SST variations have been reported to vary in strength (and also significance) from one time period to another. Instead of attributing these “nonstationarities” to the probabilistic nature of the climate system, they are often attributed to some kind of external forcing agent varying on larger timescales than the teleconnection under study. Perhaps the most prominent example for such a presumable “modulation” is the observed ENSO link to the North American climate, which is particularly strong during the positive phase of the PDO and weaker during the negative phase (Gershunov and Barnett, 1998; Diaz et al., 2001).

Likewise, profound nonstationarities have been found for *ENSO links to precipitation in southern Europe* in the observational record of the twentieth century (Mariotti et al., 2002). The links for the September-to-November (SON) season were found to be significant during the second half of the century, whereas the March-to-May (MAM) links were found to be significant at the start and the end of the century only (see Figure 2.6). Similar to the proposed causes for North America, strength variations in the ENSO link to the climate in Europe have been attributed to modulation by the PDO and AMO (Lopez-Parages and Rodriguez-Fonseca, 2012; Rodriguez-Fonseca et al., 2016), as well to variations in the intensity of the ENSO

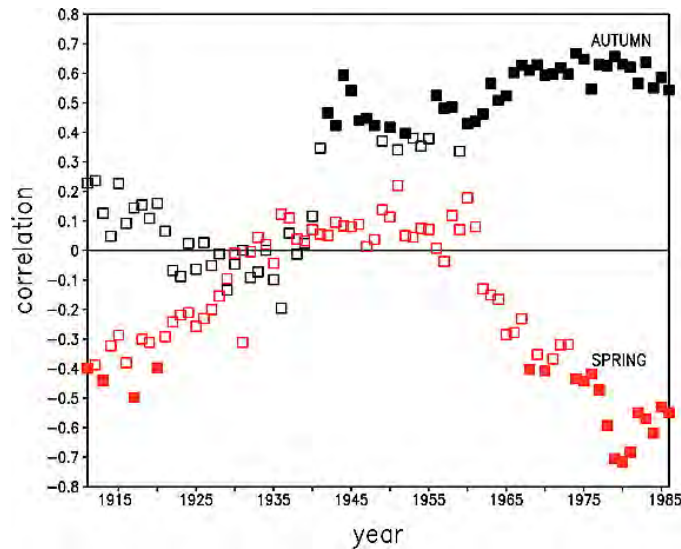


**Figure 2.6:** Pearson correlation coefficient between western Mediterranean precipitation ( $30^{\circ}\text{N} - 45^{\circ}\text{N}, 10^{\circ}\text{W} - 20^{\circ}\text{E}$ ) and the Niño 3.4 index for SON (black) and MAM (red). Each value refers to the correlation for the 20-year window centered at the symbol. Full symbols are for values which are significant at the 95% level, empty symbols are for insignificant values. The Figure is a reprint of Figure 6 in Mariotti et al. (2002). The data underlying for this figure is from Rayner et al. (1996) and New et al. (2000).

events themselves (Mariotti et al., 2002).

However, taking into account that the climate system is probabilistic, there are at least three alternative explanations that are equally plausible (Sterl et al., 2007). First, the strengthening (or weakening) of a teleconnection found in observations during a specific time period might have simply arisen from chance, in which case low-frequency SST variations would not exert a modulating effect on the teleconnection under study. Second, low-frequency SST variations indeed had a modulating effect but were conducive to the development of the teleconnection only because the unique realization of internal atmospheric variability was favourable during that specific time period. Third, the SST variations seemingly causing the teleconnection just covary with another (probably unknown) forcing agent that is the true cause. If either of the three alternative explanations was true, the timing of future favourable conditions would be essentially unpredictable.

At this point, *the present thesis comes into play*. Here, the atmospheric river phenomenon will be assessed in 13 regions along the west coasts of Europe and North America (see Figure 2.7). This will be done from a climatological point of view, with a focus on the ONDJFM season during which this phenomenon is most relevant in the two aforementioned regions (e.g. Lavers and Villarini, 2013, 2015). A new AR detection and tracking algorithm will be proposed and applied to six-hourly instantaneous data from four distinct atmospheric reanalyses, two of which date back to the year 1900 (see Section 3.2 and Chapter 4). In this way, an exhaustive historical AR archive will be built for the above regions (see Section 4.3). This

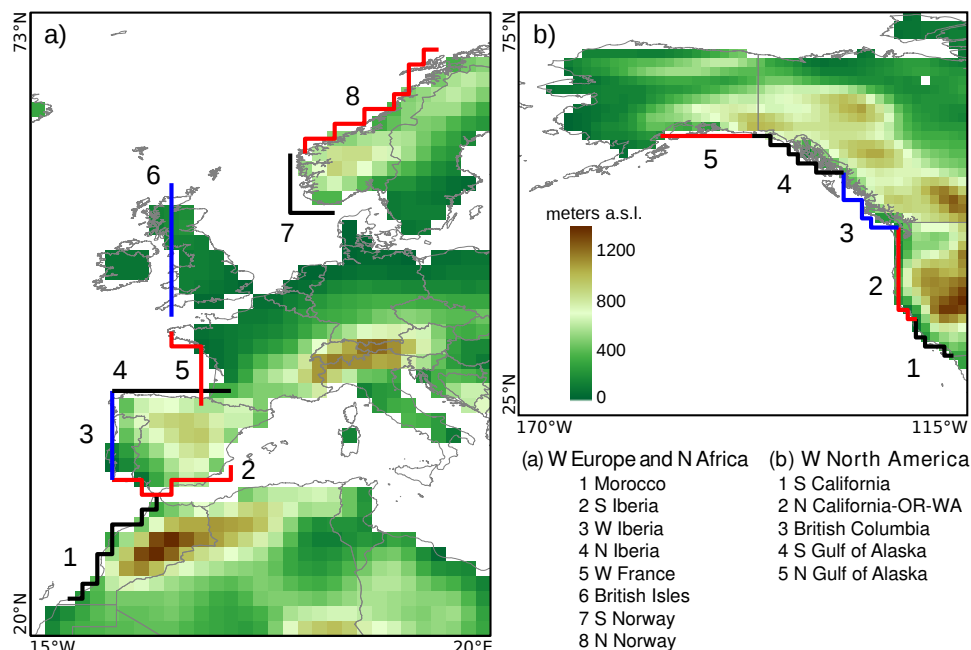


**Figure 2.7:** Target regions used for AR detection and tracking for the case of ECMWF ERA-20C reanalysis. Also shown is the corresponding orography. The detection “barriers” used for the remaining reanalyses and idealized numerical model experiments are in the direct vicinity of those shown here. Source: own illustration

archive consists of more than 150 thousand maps documenting all ARs occurring in the 13 considered target regions over the time period 1900-2014. It will be used to test the capability of the AR detection and tracking algorithm to correctly track filamentary AR structures by eye for thousands of individual cases. Beyond the scope of the present thesis, the AR archive can be easily applied to check whether individual hydrological extreme events registered in the past coincided with the presence of an atmospheric river (e.g. [Pereira et al., 2016](#)).

It is a well known fact that reanalysis data, particularly in the tropics and for variables related to atmospheric moisture, can suffer from considerable uncertainties (as measured by, e.g., the differences between two distinct reanalyses) even in the recent past ([Brands et al., 2012b,a, 2013](#); [Manzanas et al., 2015](#)). These uncertainties augment as one goes backwards in time, which is due to a decrease in the density of the available observations ([Compo et al., 2011](#); [Poli et al., 2016](#)). Since the entire twentieth century will be taken into account, reanalysis uncertainty is relevant for the present thesis and thus will be assessed in Chapter 5. This is done before the seasonal AR counts derived from reanalysis data are related to potential predictor variables from other sources, such as e.g. SST indices (see Chapter 6).

Thereafter, teleconnections between atmospheric circulation indices and the seasonal AR counts in the 13 target regions considered here (see Figure 2.7) will be assessed in Section 6.1. For the indices describing the NAO in Europe and the strength of the Aleutian Low in western North American, this will be done by means

of a running correlation analysis covering the time period 1900-2010. For the period 1950-present, during which observational uncertainties are generally of secondary importance in these regions, other atmospheric circulation indices describing the East Atlantic or Pacific-North American patterns will be additionally taken into account. Then, in Section 6.2, the analyses are exactly repeated, but for the use of SST predictor variables. Namely, the Niño 3.4 index is used for the running correlation analyses and is then complemented by other relevant SST indices (see Section 3.1 for an overview of all applied indices). Although teleconnections driven by ENSO are particularly important for North America (e.g. Trenberth et al., 1998), they are also relevant for Europe, as outlined above. The observational part of the present thesis closes with an analysis on the possible role of the PDO and AMO in modulating the strength of the ENSO-AR links along the course of the twentieth century.

In Chapter 7, the thesis then turns to the alternative, physically plausible responses of the atmosphere to the observed external forcing, as provided by idealized numerical model experiments run with AGCMs (Gates, 1992). This chapter focusses on the teleconnections triggered by ENSO. First, a series of statistical tests are defined in Section 7.2 which are then applied to answer the following questions:

- A Are the observed teleconnections during the 1979-2008 period robust to the effects of internal atmospheric variability? Here, it is explicitly taken into account that the teleconnections might have been different if the atmosphere would have been allowed to re-run with the observed external forcing.
- B Can the nonstationarities in the teleconnections' strength seen in observations along the course of the twentieth century be explained by the internal atmospheric variability of the 1979-2008 period alone? If they can not, then changes in the external forcing must have played a role.
- C Do the ENSO teleconnections seen in observations hold if the prescribed external forcing is limited to SST variations in the tropical Pacific, thereby "filtering out" the impact of ENSO on the atmosphere?.

For the first and second steps, an "ensemble of opportunity" (Tebaldi and Knutti, 2007) comprising 13 experiments from the Atmospheric Model Intercomparison Project (AMIP, Gates, 1992), run within the CMIP5 framework (Taylor et al., 2012), is used. These experiments were run with prescribed SST and sea-ice cover variations around the entire globe (see Section 7.1.1).

For the third step, additional experiments with the Community Atmosphere Model version 3.1 (Collins et al., 2006) (CAM3.1) were conducted on the High Performance Computing Cluster (HPCC) of the Santander Meteorology Group. As opposite to the AMIP experiments, in these experiments, the prescribed SSTs were allowed to vary in the Niño 3.4 region only while the SSTs and sea-ice cover values in other regions were set constant to their monthly climatological mean values (see

Section 7.1.2). For the sake of simplicity, the CAM3.1 experiments will hereafter also be referred to as the “home-made” experiments.

Chapter 8 demonstrates what can be further learned from the methods proposed in the present thesis if the analyses are extended from seasonal AR counts to classical *predictand* variables commonly used in teleconnection and predictability studies (e.g. Ropelewski and Halpert, 1987), namely the geopotential at 500hPa, mean sea level pressure, temperature and precipitation. It is not only asked whether ENSO teleconnections to these classical variables are robust to internal climate variability (see Section 8.2.1), but also whether the nonstationarities in the ENSO link to southern Europe documented in Mariotti et al. (2002) hold if internal atmospheric variability is taken into account (see Section 8.2.2). In the last working step (see Section 8.2.3), the robustness test is extended to other *predictor* variables, namely to the PDO and AMO. These extensions are conducted on the on the global scale, using the newly available ten member ensemble of “AMIP-like” experiments run within the ERA-20CM project (Hersbach et al., 2015). As opposite to the AMIP experiments from CMIP5, the ERA-20CM experiments cover a much longer period (1900-2010). They can therefore be used to assess teleconnections exerted by the PDO and AMO, as well as the nonstationarities in the ENSO links discussed above.

Finally, it is noted that the main results of the present thesis have been published in Brands et al. (2017) and Brands (2017). Another seven articles are related to the subjects of the thesis, such as reanalysis uncertainty (Brands et al., 2012b,a, 2013) and teleconnections (Brands et al., 2012c; Brands, 2013; Brands et al., 2014; Brands, 2014). Apart, there has been already a collaboration in topics for further research, such as the impact of ARs on local precipitation Eiras-Barca et al. (2016).



---

## CHAPTER 3

---

### Applied Observational Data and Post-Processing

This section describes the observational data used in the present thesis, as well as their post-processing. Two types of observational data are applied: climate indices and reanalysis data, the latter commonly referred to as “quasi-observations” (e.g. [Brands et al., 2012b](#)). Apart from observations, data from a wide range of idealized numerical model experiments are used in the present thesis. These are described in Sections [7.1.1](#) and [8.1](#).

#### 3.1 *Climate Indices*

In this thesis, a large number of climate indices representing low-frequency variations in atmospheric circulation and sea surface temperatures<sup>1</sup> are used that have been associated with the climate in Europe and North America in countless previous teleconnection studies (e.g. [Leathers et al., 1991](#); [Hurrell, 1995](#); [Rodo et al., 1997](#); [Trigo et al., 2004](#)). Here, these indices are used as predictor variables of the seasonal AR counts obtained from *observations*, in which case the whole range of indices is considered (see Chapter [6](#)), and *numerical model experiments* (see Chapter [7](#)), in which case the focus is set on the Niño 3.4 index. In Chapter [8](#), the model analyses are extended to other SST predictors and “classical” predictand variables such as temperature and precipitation.

Perhaps the most commonly used atmospheric circulation indices are those distributed by the Climate Prediction Center (CPC). These are obtained from rotated principal component analysis (PCA, [Hannachi et al., 2007](#)), applied to the 500 hPa geopotential height (Z500) fields of the NCEP/NCAR reanalysis 1 ([Kalnay](#)

---

<sup>1</sup>except for the WHWP and NPGO indices

et al., 1996)<sup>2</sup> poleward of 20°N (Wallace and Gutzler, 1981; Barnston and Livezey, 1987). Here, only the Northern Hemisphere indices associated with the climate in Europe and North America are relevant, which are the NAO and PNA in first place. The NAO *pattern* is the leading Empirical Orthogonal Function (EOF) obtained from rotated PCA in this case and the NAO *index* is the corresponding principal component (PC) containing the weights of the EOF at each time step (months in this thesis). The NAO pattern describes the well-known dipole of opposite sign between Iceland and the Azores. If the NAO index is positive (positive phase of the NAO), then the pressure gradient over the mid-latitude northeastern Atlantic is above normal, leading to an enhanced zonal flow from the west in this sector. The PNA pattern comprises a quadrupole in and around North America. Its most pronounced centre of action is the Aleutian Low in the north Pacific, mirrored by a weaker center of action of the same sign in the western North Atlantic. The two remaining centres of action are of opposite sign. They are located near the western boarder of the United States (U.S.) and Canada and in the central subtropical Pacific to the south of the Aleutian Low. The positive phase of the PNA is associated with southerly (meridional) flow in western North America and the negative phase, vice versa, with a westerly (zonal) flow in this area (Barnston and Livezey, 1987; Leathers et al., 1991). Secondary atmospheric circulation patterns (associated with PCs explaining a smaller fraction of variance) are also considered here because, on the regional scale, they can be more important than the NAO or PNA.

The East Atlantic (EA) pattern is a NAO-like zonal dipole pattern displaced to the south, and appears as the second EOF of Northern Hemisphere Z500 fields. The positive phase of the EA is associated with an enhanced zonal flow from the west in southwestern Europe (France and the Iberian Peninsula), where this pattern is at least as important for the regional climate as the NAO (Rodríguez-Puebla et al., 2001; Lorenzo et al., 2008; Casanueva et al., 2014). The SCAND pattern consists of a strong centre of action over Scandinavia and two weaker centres of opposite sign, one located over southwestern Europe and the other over central Asia. The positive phase of the SCAND is associated with below-normal geopotential heights over the Scandinavian Peninsula (Barnston and Livezey, 1987). Contrary to the NAO and EA, the East Atlantic/Western Russia (EA/WR) pattern is a *meridional* dipole with one centre over western Europe and the other over the Caspian Sea. Over western Europe it is of similar importance than the NAO and EA (Rodríguez-Puebla et al., 2001). The Polar/Eurasia (POL) pattern, originally referred to as the “Eurasia pattern type 1” in Barnston and Livezey (1987) comprises four centres, two of which lie in the European-Atlantic sector<sup>3</sup>. The first is a pronounced centre located to the northeast of Scandinavia and the second is a weaker centre of opposite sign located over the Mediterranean Sea. During the positive phase, this pattern is associated with below-normal geopotential heights in the polar region and an enhanced circumpolar flow (Barnston and Livezey, 1987). The West Pacific (WP) pattern, originally referred to

<sup>2</sup>this and other reanalysis datasets are described in detail in Section 3.2

<sup>3</sup>the other two are located over central Asia and Japan

as the “West Pacific Oscillation” (Barnston and Livezey, 1987) is a tripole pattern comprising two centres of action of the same sign located over the U.S. West Coast and the Kamchatka Peninsula, and a belt of opposite sign covering a large area of the subtropical North Pacific. Relevant for the present thesis, the positive phase of this pattern is associated with an enhanced zonal flow from the west over the northwestern U.S. and southwestern Canada.

Due to the sparse radiosonde network prior to the *International Geophysical Year 1958* (Winckler, 1960), some of the aforementioned circulation indices (e.g. the PNA) are prone to relatively large observational uncertainties during the first half of the twentieth century (Broennimann et al., 2009). This might be one reason why index values prior to 1950 are not distributed by the CPC. Here, this issue is circumvented by using other, more reliable indices describing the same, or at least related, atmospheric circulation patterns. Namely, the NAO-index based on the pressure differences between Lisbon, Portugal<sup>4</sup> and Stykkisholmur/Reykjavik, Iceland, hereafter referred to as “station-NAO” (Hurrell et al., 2003), is used for this purpose in the North Atlantic sector. Since the Aleutian Low is one centre of action of the PNA, the North Pacific (NP) Index (Trenberth and Hurrell, 1994)<sup>5</sup> is used for the North Pacific sector. The NP is the areal average MSLP in the Aleutian Low region. For comparison with the NAO provided by the CPC (hereafter: “CPC-NAO”), the NAO index obtained from applying ordinary PCA to the MSLP fields of the North Atlantic-European sector (H-NAO, Hurrell et al., 2003) is used in addition. Both the NP and H-NAO are based on the Trenberth and Paolino (1980) dataset. An overview of all considered atmospheric circulation indices, including the geographical areas and datasets used by the external data providers, is given in Table 3.1. The corresponding source URLs are listed in Table 3.4.

In what concerns the *oceanic* predictor variables, the Niño 3.4 index describing areal average SSTs in the eastern equatorial Pacific is used here as the first ENSO descriptor (Trenberth, 1997). It was retrieved from NOAA’s Earth System Research Laboratory (ESRL). The associated teleconnections are described in detail in Section 2.5. The AMO describes multidecadal variations the *detrended* areal average SSTs of the North Atlantic Ocean, from the equator to 60°N (Kerr, 2000; Enfield et al., 2001; Trenberth and Shea, 2006). Several indices are available for this phenomenon which mainly differ from each other due distinct detrending methods. For the index available from NOAA’s ESRL the linear trend calculated from the entire time series is removed (Enfield et al., 2001). Since this version is commonly applied in teleconnection studies (e.g Lopez-Parages and Rodriguez-Fonseca, 2012), it is used here for the mainstay of analyses and will be hereafter referred to as the “AMO index” if not stated otherwise in the text. However, Trenberth and Shea (2006) argue that some time series aspects of the so defined AMO index are statistical artefacts arising from the (wrong) assumption of a linear trend. They therefore propose to subtract the global average SST from the grid-box values on a month-to-month basis, as done

<sup>4</sup>or Ponta Delgada, Azores

<sup>5</sup>considered reliable from 1920 onwards

**Table 3.1:** External *atmospheric circulation* indices applied here. The abbreviations can refer to the phenomenon or the index describing it. The domains refer to the geographical regions considered for principal component analysis or areal averaging.

Acronym	Full Name	Domain	Provider	Reference	Underlying Data
NP	North Pacific / Aleutian Low	30°N-65°N, 160°E-140°W	UCAR	Trenberth and Hurrell (1994)	MSLP from Trenberth and Paolino (1980)
H-NAO	NAO based on ordinary PCA	20°N-80°N, 90°W-40°E	UCAR	Hurrell et al. (2003)	"
Station-NAO	NAO based on MSLP differences	station data, see text	"	"	MSLP from Quayle (1989)
CPC-NAO	NAO based on rotated PCA	15°N-90°N, 180°W-180°E	CPC	Barnston and Livezey (1987)	Z500 from Kalnay et al. (1996)
EA	East Atlantic pattern	"	"	"	"
SCAND	Scandinavian pattern	"	"	"	"
EA/WR	East Atlantic/Western Russia pattern	"	"	"	"
PNA	Pacific-North American pattern	"	"	"	"
WP	West Pacific pattern	"	"	"	"
POL	Polar/Eurasia pattern	"	"	"	"

**Table 3.2:** External *sea surface temperature* indices applied here. The abbreviations can refer to the phenomenon or the index describing it.

Acronym	Full Name	Domain	Provider	Reference	Underlying Data
Niño 3.4	Areal mean SST in the Niño 3.4 region	5°S-5°N, 170°W-120°W	ESRL	Trenberth (1997)	SST from Rayner et al. (2003)
IPO	Interdecadal Pacific Oscillation	3 domains, see reference	"	Henley et al. (2015)	"
AMO	Atlantic Multidecadal Oscillation	Atlantic Ocean 0°N-60°N	"	Enfield et al. (2001)	"
TNA	Tropical North Atlantic	5.5°N-23.5°N, 15°W-57.5°W	"	Enfield et al. (1999)	SST from Rayner et al. (2003)*
PDO	Pacific Decadal Oscillation	Pacific Ocean > 20°N	JISAO	Zhang et al. (1997)	"
WHWP	Western Hemisphere Warm Pool	SSTs > 28.5°C, see text	"	Wang and Enfield (2001)	"
NPGO	North Pacific Gyre Oscillation	25°N-62°N, 180°W-110°W	Georgia Tech	Di Lorenzo et al. (2008)	SSH from Niiler et al. (2003)

\*extended with Reynolds et al. (2002)

**Table 3.3:** Considered reanalysis datasets, six-hourly instantaneous values are applied in any case. Listed are the acronyms used throughout the study, the full names, horizontal resolutions (lat. × lon.), reference publications and the number of runs conducted for each reanalysis. The ensemble-mean data from NOAA-20C are used here.

Acronym	Full Name	Resolution	Reference	Nr. runs
NGEP/NCAR	NGEP/NCAR Reanalysis 1	2.5° × 2.5°	Kalnay et al. (1996)	1 run
NOAA-20C	NOAA CIRES 20th-Century Reanalysis v2	2° × 2°	Compo et al. (2011)	56-member ensemble
ERA-20C	ECMWF ERA-20C Reanalysis	1.125° × 1.125°	Poli et al. (2016)	1 run
ERA-Interim	ECMWF ERA-Interim Reanalysis	0.75° × 0.75°	Dee et al. (2011)	1 run

for the calculation of the PDO (Zhang et al., 1997). In the the last results Section of the present thesis, which of exploratory nature, this improved AMO index will be used (see Section 8.2.3).

Similar to the AMO, the PDO is a multidecadal SST oscillation of the North Pacific SSTs whose pattern is reminiscent of a “horseshoe” extending from Gulf of Alaska in the north to the coast of California in the south, thereby embracing a centre of opposite sign in the North Pacific (Mantua et al., 1997). This index is defined as the PC of the leading EOF of the North Pacific SSTs, the latter being detrended as described above (Zhang et al., 1997). It is provided by the Joint Institute for the Study of the Atmosphere and Ocean (JISAO). For the sake of comparison with the PDO, the Pacific Interdecadal Oscillation (IPO) is also considered here. Similar to the PDO, the index describing the IPO describes multidecadal oscillation in the Pacific. Unlike the PDO, it is not confined to the north Pacific, but is defined as a linear combination of the SSTs in three Pacific subregions: the subtropical North Pacific, the central to eastern equatorial Pacific and the Southern Hemisphere ocean area around New Zealand (Henley et al., 2015). Note that the phenomenon is referred to as the IPO, while the corresponding index has been named “Pacific Tripole Index” (TPI). This index is provided by NOAA’s ESRL. Since SST variations in the Caribbean Sea and Gulf of Mexico originate in the eastern tropical Pacific off the coast of central America, this ocean area is commonly referred to as the “Western Pacific Warm Pool” (Wang and Enfield, 2001). Unlike the aforementioned SST indices, the WHWP index is defined as the ocean *area* where the SSTs exceed a threshold temperature of 28.5°C. This index is positively correlated with the frequency of Atlantic hurricanes which, transformed to extratropical cyclones, can affect the climate in Europe, and is thus applied in the present thesis. The areal average SSTs in the Tropical North Atlantic (TNA) (Enfield et al., 1999) are used in addition for exploratory purposes. Both the WHWP and TNA indices were retrieved from NOAA’s ESRL. The *Pacific Gyre Oscillation* pattern is defined as the second EOF of the *sea surface height* (SSH) fields in the northeastern Pacific and is therefore not defined on SSTs. It has been associated mainly with biogeochemical phenomena in the ocean rather than atmospheric variables (Di Lorenzo et al., 2008). The associated PC index is was provided by the Georgia Institute of Technology and is here applied in an exploratory context. An overview of the external oceanic indices considered here, including the geographical regions and underlying datasets used by the data providers, is given in Table 3.2. The corresponding source URLs are listed in Table 3.4. Note that *non-smoothed* index values were retrieved from the data providers in any case.

In addition to these external indices, the Pacific Warmpool (PWP) index was obtained from own calculations on the basis of the HadISST1 dataset (Rayner et al., 2003). Following Hoerling et al. (2001), this index is defined as the first PC of the monthly SST anomalies in the tropical Pacific (30°S to 30°N and 120°E to 60°W). SST anomalies were calculated with respect to the 1971-2000 climatological mean and the 1949-2000 anomalies were then used to calculate the first EOF. Thereafter,

**Table 3.4:** Source information about the applied *external* climate indices, reanalyses and AGCM data, see Tables 3.1, 3.2, 3.3 and 7.1 for the full names and more details. The ERA-20CM dataset is described in Section 8.1.

Data Acronym	Source
H-NAO	<a href="https://climatedataguide.ucar.edu/sites/default/files/nao_pc_monthly.txt">https://climatedataguide.ucar.edu/sites/default/files/nao_pc_monthly.txt</a>
Station-NAO	<a href="https://climatedataguide.ucar.edu/sites/default/files/nao_station_monthly.txt">https://climatedataguide.ucar.edu/sites/default/files/nao_station_monthly.txt</a>
CPC-NAO	<a href="http://www.cpc.ncep.noaa.gov/products/precip/CWlink/pna/norm.nao.monthly.b5001.current.ascii.table">http://www.cpc.ncep.noaa.gov/products/precip/CWlink/pna/norm.nao.monthly.b5001.current.ascii.table</a>
EA	<a href="http://www.cpc.ncep.noaa.gov/data/teledoc/ea.shtml">http://www.cpc.ncep.noaa.gov/data/teledoc/ea.shtml</a>
SCAND	<a href="http://www.cpc.ncep.noaa.gov/data/teledoc/scand.shtml">http://www.cpc.ncep.noaa.gov/data/teledoc/scand.shtml</a>
EA/WR	<a href="http://www.cpc.ncep.noaa.gov/data/teledoc/eawruss.shtml">http://www.cpc.ncep.noaa.gov/data/teledoc/eawruss.shtml</a>
PNA	<a href="http://www.cpc.ncep.noaa.gov/products/precip/CWlink/pna/norm.pna.monthly.b5001.current.ascii.table">http://www.cpc.ncep.noaa.gov/products/precip/CWlink/pna/norm.pna.monthly.b5001.current.ascii.table</a>
WP	<a href="http://www.cpc.ncep.noaa.gov/data/teledoc/wp.shtml">http://www.cpc.ncep.noaa.gov/data/teledoc/wp.shtml</a>
NP	<a href="https://climatedataguide.ucar.edu/sites/default/files/npindex_monthly.txt">https://climatedataguide.ucar.edu/sites/default/files/npindex_monthly.txt</a>
Niño 3.4	<a href="http://www.esrl.noaa.gov/psd/gcos_wgsp/Timeseries/Nino34">http://www.esrl.noaa.gov/psd/gcos_wgsp/Timeseries/Nino34</a>
AMO	<a href="http://www.esrl.noaa.gov/psd/data/timeseries/AMO">http://www.esrl.noaa.gov/psd/data/timeseries/AMO</a>
TNA	<a href="http://www.esrl.noaa.gov/psd/data/correlation/tna.data">http://www.esrl.noaa.gov/psd/data/correlation/tna.data</a>
WHWP	<a href="http://www.esrl.noaa.gov/psd/data/correlation/whwp.data">http://www.esrl.noaa.gov/psd/data/correlation/whwp.data</a>
IPO	<a href="http://www.esrl.noaa.gov/psd/data/timeseries/IPOTPI">http://www.esrl.noaa.gov/psd/data/timeseries/IPOTPI</a>
NPGO	<a href="http://www.o3d.org/nngo/nngo.php">http://www.o3d.org/nngo/nngo.php</a>
PDO	<a href="http://jisao.washington.edu/pdo/PDO.latest">http://jisao.washington.edu/pdo/PDO.latest</a>
NOAA-20C	<a href="ftp://ftp.cdc.noaa.gov/Datasets/20thC_ReanV2">ftp://ftp.cdc.noaa.gov/Datasets/20thC_ReanV2</a>
ERA-20C	<a href="http://apps.ecmwf.int/datasets/data/era20c-daily/levtype=sfc/type=an">http://apps.ecmwf.int/datasets/data/era20c-daily/levtype=sfc/type=an</a>
ERA-Interim	<a href="http://apps.ecmwf.int/datasets/data/interim-full-daily/levtype=sfc">http://apps.ecmwf.int/datasets/data/interim-full-daily/levtype=sfc</a>
NCEP-NCAR	<a href="ftp://ftp.cdc.noaa.gov/Datasets/ncep.reanalysis">ftp://ftp.cdc.noaa.gov/Datasets/ncep.reanalysis</a>
AMIP runs	Data portals of the ESGF, e.g. <a href="https://esgf-node.llnl.gov/projects/esgf-llnl">https://esgf-node.llnl.gov/projects/esgf-llnl</a>
ERA-20CM	<a href="http://apps.ecmwf.int/datasets/data/era20cm-edmo/levtype=sfc">http://apps.ecmwf.int/datasets/data/era20cm-edmo/levtype=sfc</a>

the entire anomaly time series was projected onto the first EOF to obtain the PWP index (represented by the first PC). Note that the spatial pattern described by the first EOF was applied to define the SST variations used to force the numerical model experiments conducted with the Community Atmosphere Model 3.1 (see Section 7.1.2).

For correlation with the numerical model output from the ECMWF ERA-20CM model ensemble, the Niño 3.4, AMO and PDO indices were calculated upon the HadISST2 dataset (Titchner and Rayner, 2014; Kennedy et al., 2015) used to force these model integrations (see Chapter 8 for further details).

## 3.2 Reanalysis Data

In modern atmospheric science, “reanalysis” (e.g. Kalnay et al., 1996; Uppala et al., 2005) is by far the most commonly used method to gain a spatially and temporally complete picture of the atmosphere and ocean. The basic idea underlying an atmospheric reanalysis (oceanic reanalyses are not relevant for the present thesis) is to feed historical data from a wide range of observational platforms (meteorological stations, buoys, radiosondes, aircraft, ships and satellites) into a constant data assimilation and numerical weather prediction (NWP) system (Bengtsson and Shukla, 1988). This system then calculates an internally coherent, spatially and qualitatively (i.e. in terms of variables) complete picture of the atmosphere. This is done on six-hourly to hourly timescale, covering a period of a few years to one and a half

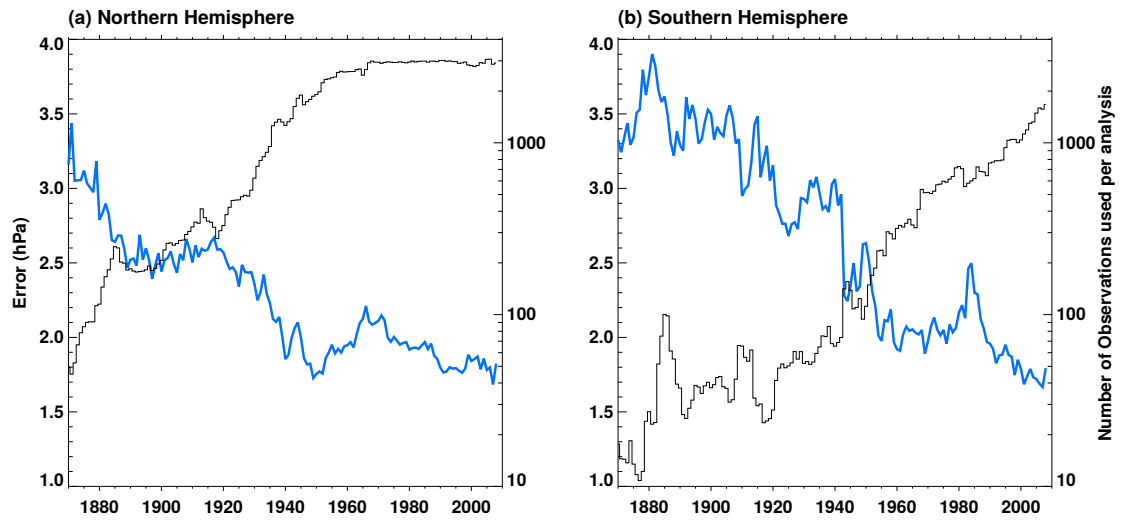


**Figure 3.1:** Time series of the six-hourly first-guess root-mean-square (r.m.s.) difference between pressure estimates from the Twentieth Century Reanalysis v2 and pressure observations (blue) calculated over individual years from 1870 to 2008 for the extratropical (a) Northern Hemisphere ( $20^{\circ}$  N -  $90^{\circ}$  N) and (b) Southern Hemisphere ( $20^{\circ}$  S -  $90^{\circ}$  S). The square root is calculated on the annual mean square values. The thin black curve shows the average number of pressure observations for each analysis in the indicated year (note the logarithmic scale). This is a simplified version of Figure 3 in [Compo et al. \(2011\)](#), with kind permission of Dr. Gilbert Compo (personal communication). The pressure observations assimilated in the reanalysis are from the International Surface Pressure Databank ([Cram et al., 2015](#)), and so are the independent data used for verification.

centuries. These datasets, in principle, are ideal for undertaking climatological studies. However, the realism of the simulated atmospheric states critically depends on the density of the assimilated observations. In case observations are available, the system is constrained to them and the re-analysed atmospheric states are realistic. In case observations are absent or sparse, the system generates its own, “unbound” variability which is unrealistic and largely varies between different reanalysis systems ([Sterl, 2004](#)).

Before the introduction of satellite data in 1979, the observational network was particularly sparse in the tropics and southern Hemisphere. Going further backwards in time, observations fade out (see [Figure 3.1](#)) and, at the start of the 20th century, are essentially only available for Europe, North America and Australia ([Compo et al., 2011](#); [Stickler et al., 2014](#)).

Another problem are small-scale atmospheric dynamics which are not resolved by coarse-resolution global numerical weather prediction models ([Grotch and MacCracken, 1991](#); [Maraun et al., 2010](#)). These are particularly relevant in those regions where regional topographic features notably modify the impact of the large-scale flow and in regions where this flow is generally weak or missing. Thus, reanalyses generally perform poorer for mountain terrain, the polar regions and the inner tropics than for other regions (see [Figure 3.2](#)). In the framework of the present thesis, a detailed assessment of reanalysis uncertainty was conducted and the interested reader

is referred to Brands et al. (2012b), Brands et al. (2012a), Brands et al. (2013) and Manzananas et al. (2015) at this point.

Finally, the accuracy of reanalysis data suffers from measurement uncertainties which are particularly large for atmospheric moisture (e.g. Wang et al., 2002). Actually, in the aforementioned study series on reanalysis uncertainty, particularly the estimates for six-hourly specific humidity in the lower troposphere were found to largely vary from one reanalysis system to another (see Figure 3.2). This issue is of practical importance for the present thesis since specific humidity is needed to calculate the IVT, which then serves to detect and track AR structures (see further below in this Section).

From the point of view of temporal homogeneity, the strategy of using all available observations for re-analysing is not optimal. Namely, during the course of the twentieth century, the observational network is marked by abrupt improvements, the extension of the radiosonde network (1958) and introduction of satellite data (1979) being the most relevant examples (Kalnay et al., 1996). Thus, considering all available observations in the reanalysis is on the one hand beneficial since it reduces the bias of the reanalysis data (w.r.t independent observations), but on the other hand leads to artificial shifts in the re-analysed time series that are commonly referred to as “inhomogeneities” or “observational shocks” (Sturaro, 2003; Sterl, 2004). These inhomogeneities can e.g. lead to the detection of false long-term trends if the reanalysis is seen on its own (Thorne and Vose, 2010).

In the present thesis, six-hourly instantaneous data from the four reanalyses specified in Table 3.3 are used, which, if taken together, cover the period 1900-2014.

### 3.3 Post-Processing the Reanalysis Data

The AR detection and tracking algorithm described in Section 4.1 operates on the *intensity* ( $IVT$ , in  $kg\ m^{-1}\ s^{-1}$ ) and *direction* ( $D$  in degrees) of the vertically integrated water vapour transport, calculated as follows:

$$IVT = \sqrt{IVT_u^2 + IVT_v^2} \quad (3.1)$$

$$D = \text{atan2} \left( \frac{IVT_u}{IVT}, \frac{IVT_v}{IVT} \right) \frac{180}{\pi} + 180 \quad (3.2)$$

where  $IVT_u$  and  $IVT_v$  are the vertical integrals of the zonal and meridional water vapour transport components respectively. The *atan2* function returns the four-quadrant inverse tangent ranging in between  $-\pi$  and  $\pi$  which is then transformed to degree values ranging in between  $0^\circ$  and  $360^\circ$ .

$IVT_u$  and  $IVT_v$  were calculated from 2-dimensional pressure-level data between 1000 and 300 hPa (Lavers et al., 2012).

$$IVT_u = \frac{1}{g} \int_{1000}^{300} qu\ dp \quad (3.3)$$

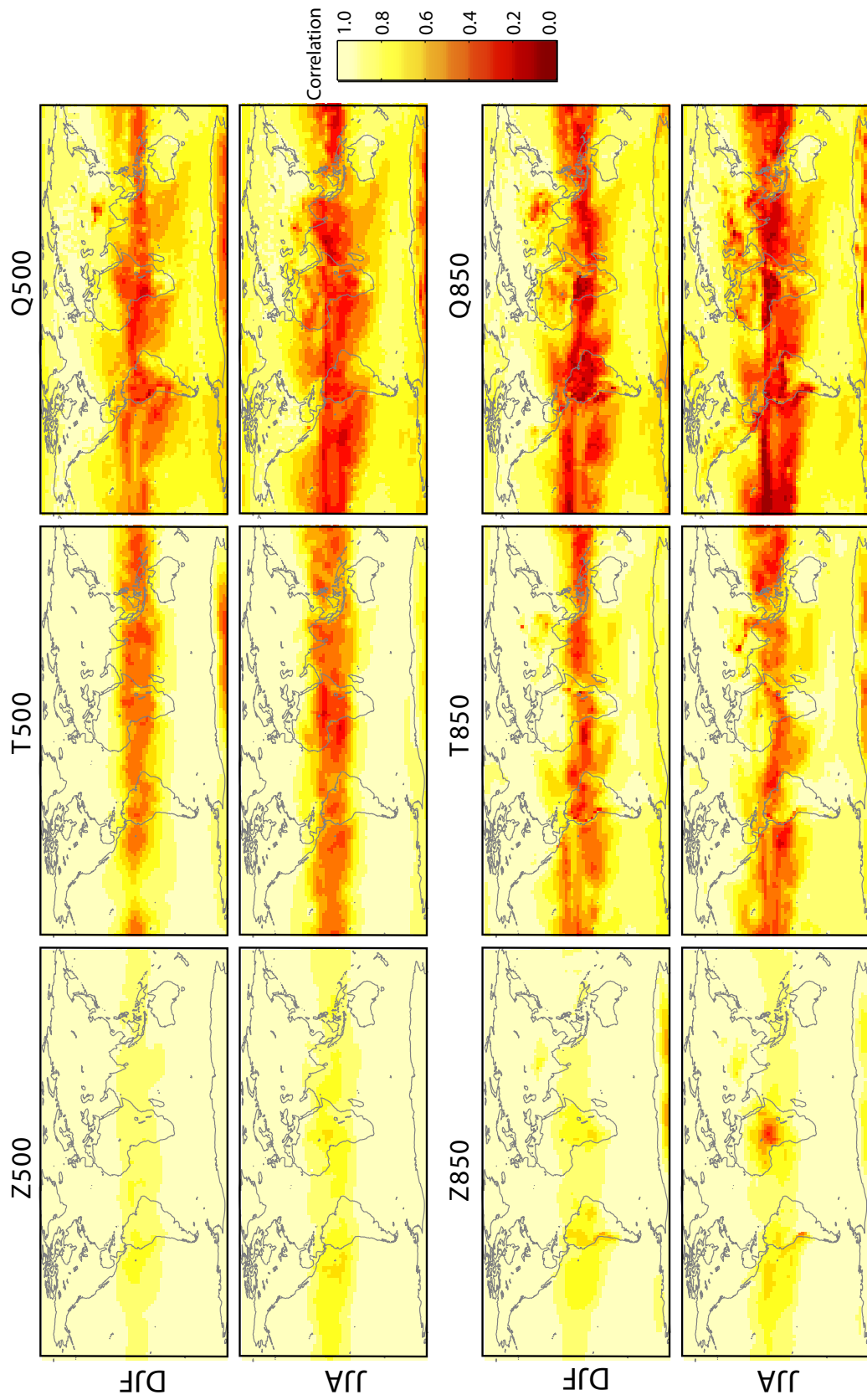


**Figure 3.2:** Degree of similarity in the day-to-day sequence of the 00 UTC time series from ERA-40 vs. NCEP/NCAR for the geopotential ( $Z$ ), temperature ( $T$ ) and specific humidity ( $Q$ ) at (top) 500 and (bottom) 850 hPa, as revealed by the Pearson correlation coefficient. Colour darkening from yellow to black indicates increasing dissimilarity. Source: own illustration

and

$$IVT_v = \frac{1}{g} \int_{1000}^{300} qv \, dp \quad (3.4)$$

where  $q$ ,  $u$  and  $v$  refer to specific humidity (in  $kg \, kg^{-1}$ ), zonal and meridional wind (in  $m \, s^{-1}$ ) at pressure level  $p$ ,  $g$  to acceleration due to gravity and  $dp$  to the difference between adjacent pressure levels (in Pa).

For NCEP/NCAR and NOAA-20C, 7 and 15 vertical pressure levels between 1000 and 300 hPa were available from the data providers respectively. Vertical integration is achieved by multiplying  $qu$  and  $qv$  at the pressure level  $p$  by a multiplier describing its contribution (as represented by the number of pressure levels in  $Pa$ ) to the entire column extending from 1000 to 300  $hPa$  (see Table 3.5), followed by summing up the resulting products. Since ECMWF's public server already provides  $IVT_u$  and  $IVT_v$  as vertical integrals between the pressure level at model surface and the top of the atmosphere (ECMWF, personal communication), it was not necessary to apply Equations 3.3 and 3.4 for ERA-20C and ERA-Interim. Note that  $q$ ,  $u$  and  $v$  from NOAA-20C are ensemble-mean data.

Apart from the reanalysis data presented in this section, AGCM data from the AMIP experiments developed within the framework of CMIP5 will be applied in the present thesis. These model data are described in detail in Section 7.1.1 and at this point it is worth anticipating that their post-processing is identical to that of the NOAA-20C data described above.

**Table 3.5:** List of multipliers used for multiplication with  $qu$  and  $qv$  at a given pressure level  $p$ . Horizontal bars indicate that the data at the corresponding pressure level were not available from the data provider. See text for more details.

$p$	NCEP/NCAR	NOAA – 20C
300	5000	2500
350	-	5000
400	10000	5000
450	-	5000
500	10000	5000
550	-	5000
600	10000	5000
650	-	5000
700	12500	5000
750	-	5000
800	-	5000
850	11250	5000
900	-	5000
925	7500	-
950	-	5000
1000	3750	2500

---

## CHAPTER 4

---

# The Atmospheric River Detection and Tracking Algorithm

In this section, an algorithm used to detect and track AR structures in reanalysis and general circulation model data is presented. This algorithm has been developed in the framework of the present thesis and represents one out of several possible ways to define these structures. Similar algorithms operating on the regional scale have been developed by other research teams (e.g. [Lavers et al., 2012](#); [Lavers and Villarini, 2013](#); [Garaboa-Paz et al., 2015](#)) and, recently, the first algorithm operating on the global scale has been published ([Guan and Waliser, 2015](#)). At this point it is noteworthy that the author of the present thesis contributed to a research article introducing one of these alternative algorithms (see [Eiras-Barca et al., 2016](#)).

This chapter is outlined as follows. The algorithm used here is formally described in Section 4.1. A set of sensitivity tests, related to the parameters this algorithm works with, is presented in Section 4.2. Then, an historical web archive based on the results is introduced in Section 4.3. This archive is an exhaustive *electronic appendix* to the present thesis. The chapter ends with a description of the algorithm’s specific advantages and with a comparison of the results to those obtained in [Dettinger et al. \(2011\)](#) with an independent algorithm (see Section 4.4).

Since atmospheric rivers are more conducive to precipitation in the winter half-year ([Champion et al., 2015](#); [Eiras-Barca et al., 2016](#)), at least in the extra-tropics, the algorithm developed here has been run for the ONDJFM season. The large number of distinct detection algorithms developed during the last decade reflects the fact that a commonly accepted definition of the term “atmospheric river” is yet under development ([Dacre et al., 2015](#)), particularly in what concerns atmospheric rivers during the warm season (see e.g. [Eiras-Barca et al., 2016](#)). This “definition uncertainty” is accounted for in the present thesis by 1) the above mentioned

sensitivity tests and 2) by showing the algorithm’s output at the above mentioned archive for thousands of individual AR events, thereby providing a public platform to discuss its weaknesses and strong points.

## 4.1 Description of the Algorithm

In the present thesis, ARs are detected separately in 8 regions ranging from Morocco to northern Norway and 5 regions ranging from southern California to the northern Gulf of Alaska respectively (see Fig. 2.7). Each detection region is defined as a “barrier” of grid-boxes approximately following the coastline. Due to distinct native horizontal resolutions, the exact coordinates of these barriers slightly differ from one dataset to another (the barriers shown in Fig. 2.7 refer to the ERA-20C dataset). Using the native resolution is preferable to interpolating to a common coarse grid, which would lead to a degradation of the higher-resolution datasets.

For a given detection region formed by a barrier of  $b$  grid-boxes (displayed in Figure 2.7), the following detection and tracking algorithm was applied every six hours (a schematic overview of the algorithm is provided in Figure 4.1).

1. The grid-box of maximum IVT along  $b$  is retained. This grid-box is hereafter referred to as the “targeted grid-box”  $e$ .
2. If the IVT value at  $e$  exceeds the predefined percentile threshold  $P_d$  (the detection percentile) the AR-tracking algorithm is activated, otherwise it proceeds to the next point in time.
3. Then, the direction ( $D$ ) of the vertically integrated water vapour flow at  $e$  is calculated (see Equation 3.2) and discretized into the 8 cardinal directions: N, NE, E, SE, S, SW, W, NW. In the following example, we assume that  $D$  is from the W.
4. Out of the 8 possible neighbouring grid-boxes surrounding  $e$ , the algorithm considers the upstream grid-box  $s$  as well as the two grid-boxes neighbouring  $s$  (i.e., following the example, the 3 grid-boxes to the West, North-West and South-West of  $e$ ). Among these 3 candidate grid-boxes the grid-box of maximum IVT is detected.
5. If this maximum IVT value exceeds the predefined percentile threshold  $P_t$  (the tracking percentile which not necessarily equals  $P_d$ , see also Table 4.1), the grid-box is retained as the new targeted grid box  $e$ . In this case, the algorithm proceeds to 3). Otherwise, it is stopped at this point in time and proceeds to the next point in time.
6. The algorithm continues until 5) is not met any more or until the detected structure exceeds a length of  $l$  grid-boxes or in case a grid-box is detected

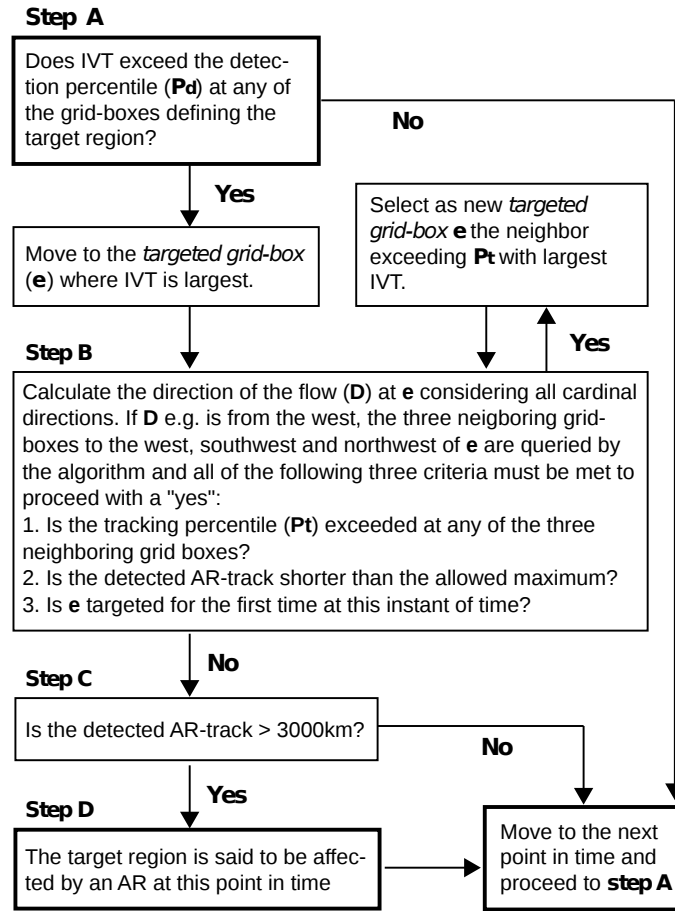


**Figure 4.1:** Schematic overview of the AR detection and tracking algorithm developed in the present thesis. Source: own illustration

twice, which can occur if the algorithm completely orbits a low pressure system. Note that  $l$  depends on the horizontal resolution of the dataset and equals 32, 40, 70 and 107 grid-boxes for NCEP/NCAR, NOAA-20C, ERA-20C and ERA-Interim respectively. For the ideal case of a purely meridional AR with no zonal displacement, this roughly corresponds to a longitude of 9000 km.

7. If the longitude of the detected structure exceeds a threshold of 3000 km (spherical distance is considered), the detection region  $b$  is said to be affected by an AR at this point in time. If it is shorter than 3000 km, the structure is not considered an AR.

## 4.2 Sensitivity Tests Related to the Definition of an AR

Considering the reference period 1979-2009<sup>1</sup>,  $P_d$  and  $P_t$  were calculated separately for each grid box and month. Based on a comparison with the ARs detected in Neiman et al. (2008) and Dettinger et al. (2011), Lavers et al. (2012) suggested the use of the 85<sup>th</sup> percentile for  $P_d$  which, however, was replaced by other plausible values in some studies [e.g. Warner et al. (2015)]. Thus, a secondary goal of the present thesis is to explore how sensitive the results are to variations in  $P_d$ , and also  $P_t$ . To this aim, the AR detection and tracking algorithm is applied 6 times using 6 distinct combinations of the two parameters (see Table 4.1). The corresponding six values will hereafter be referred to as the “percentile sample”. Its range describes the method-related sensitivity of the results. Additional sensitivity tests were conducted 1) taking into account persistent and independent AR events only and/or 2) intentionally turning-off our algorithm’s capability to track towards the N, NE, E and SE and/or 3) considering a length criterion of  $> 2000$  instead of  $> 3000$  km. An event is considered “persistent” if a given target region is continuously affected by an AR for at least 18 hours and if it is separated from other events by more than 24 hours (Lavers et al., 2012).

**Table 4.1:** The 6 percentile combinations used for AR detection and tracking.  $P_d$  is the percentile threshold used for detection at the region of AR-arrival and  $P_t$  is the percentile threshold used along the track of the AR.

Number	$P_d$	$P_t$
1	85	75
2	85	80
3	85	85
4	90	75
5	90	80
6	90	85

## 4.3 Construction of an Historical Atmospheric River Archive

Hosted at <http://www.meteo.unican.es/atmospheric-rivers>, the *Atmospheric River Archive* is a visual register of all atmospheric rivers detected in the six-hourly time series of the three reanalyses NOAA-20, ERA-20C and ERA-Interim during the ONDJFM season. In what concerns the two long-term reanalyses, the period 1900-2010 is covered by the archive and all instants in time are displayed for which an AR is detected in either NOAA-20C or ERA-20C, or in both of them. Thus, the differences between the two datasets can be easily assessed for each AR event.

<sup>1</sup>common to all applied reanalysis datasets

For the period 1979-2014, the archive also shows the ARs detected in ERA-Interim. Visualization is based on the algorithm working with percentile combination 4, except in Morocco and southern Iberia, where combination 6 is used instead to avoid that the absolute IVT values to be surpassed is not too low. All in all, more than 150 *thousand* individual maps were stored and can be requested and downloaded at any time. In addition, the respective six-hourly AR occurrence/absence times series can be retrieved in netCDF format.

## 4.4 Performance of the Algorithm

Figure 2.1 provides an illustrative example of the algorithm’s capability to detect and track AR structures. The figure shows an AR affecting southern Norway on 11 January 1971 00 UTC, as retrieved from NCEP/NCAR, NOAA-20C and ERA-20C (panels a, b and c respectively). Colour shadings and vector lengths are proportional to the intensity of the vertically integrated water vapour transport. The direction of the flow is indicated by the orientation of the vectors and the cyan line represents the AR-track found by the algorithm. The initial landfall of this AR was detected earlier and this particular point in time is chosen to show the algorithm’s capability to track towards the N, NE, E and SE (SE in this case, as described below) at any point along the AR track. This “eastward tracking” capability was not accounted for in the initial formulation of the Lavers et al. (2012) algorithm, able to track towards the S, SW, W, NW only. Albeit this was corrected in the later versions of this algorithm (Lavers and Villarini, 2013, 2015), these do not do account for  $\approx 180^\circ$  curves as those shown in Figure 2.1. Starting from a given detection barrier (e. g.  $10^\circ\text{W}$  for the case of western Europe), the Lavers and Villarini (2013) algorithm moves towards the West and tracks the maximum IVT threshold at each longitude. For the structure being an AR in Lavers and Villarini (2013), the tracked IVT values must exceed the assumed percentile threshold along a longitudinal distance of  $20^\circ$ . What is key for the understanding of our method is that the Lavers and Villarini (2013) algorithm only detects *one* grid-box per longitude. To perform a  $180^\circ$  turn, however, a second IVT value exceeding the threshold must be located at the *same* longitude further to the South (see Figure 2.1c) and this is not accounted for by Lavers and Villarini (2013), to the author’s knowledge. Telling the algorithm to move to the east, starting from the detection barrier, does not solve this problem either. Here, it will be shown that even though this limitation is of minor importance in Europe, it is detrimental to AR-detection in some regions along the west coast of North America (see below).

In spite of distinct native horizontal resolutions and applied data assimilation strategies, the three reanalyses produce virtually identical results for the AR event shown in Figure 2.1. Since the direction of the flow is scanned prior to searching the grid-box of maximum IVT, the algorithm correctly moves upstream after detecting the AR in southern Norway. The “curves” of the flow are captured well and so is the SE flow between the British Isles and the Iberian Peninsula. Finally, the algorithm stops in the central subtropical Atlantic because the allowed maximum of

tracked grid-boxes ( $l$ ) is exceeded. As an extension to this illustrative example, the performance of the algorithm can be verified for thousands of individual AR events by consulting the *Atmospheric River Archive* (see Section 4.3).

To draw some more general conclusions on the relevance of the “eastward tracking” capability, Figure 4.2 displays the fraction of ARs that are detected if this capability is intentionally turned off ( $F_{noeast}$ ):

$$F_{noeast} = \frac{AR_{noeast}}{AR_{all}} \times 100 \quad (4.1)$$

where  $AR_{noeast}$  is the seasonal AR-count retrieved from an algorithm not capable to track towards the N, NE, E and SE, and  $AR_{all}$  is the respective count obtained from the fully capable algorithm as described above.

Figure 4.2 illustrates that eastward tracking is more relevant during OND than during JFM and more so in North America than in Europe. In the Gulf of Alaska, up to 70% of the ARs are “lost” if eastward tracking is not considered, which is due to the fact that ARs approaching this region from southerly directions frequently have a slight eastward component near landfall and turn to westerly directions when further tracked upstream. For an illustrative example of this phenomenon, the interested reader is referred to the AR-detections in December 2014 (see reanalysis: “ERA-Interim”, continent: “western North America” and region: “northern Gulf of Alaska” at <http://www.meteo.unican.es/atmospheric-rivers>).

Finally, 90% of the AR-events documented in Dettinger et al. (2011) (see their table 1) coincide with the ERA-Interim based AR-detections provided by the *Atmospheric River Archive* if the target day documented in Dettinger et al. (2011) is “relaxed” by  $\pm 18$  hours. The “missing” 10% can largely be explained by the comparatively long AR-length criterion applied here ( $> 3000$  km). If the algorithm proposed here is re-run with a shorter length criterion ( $> 2000$  km), the coincidence rate rises to 97%. Interestingly, even though a longer length criterion is assumed, the AR archive developed here contains more events than the Dettinger et al. (2011) archive.

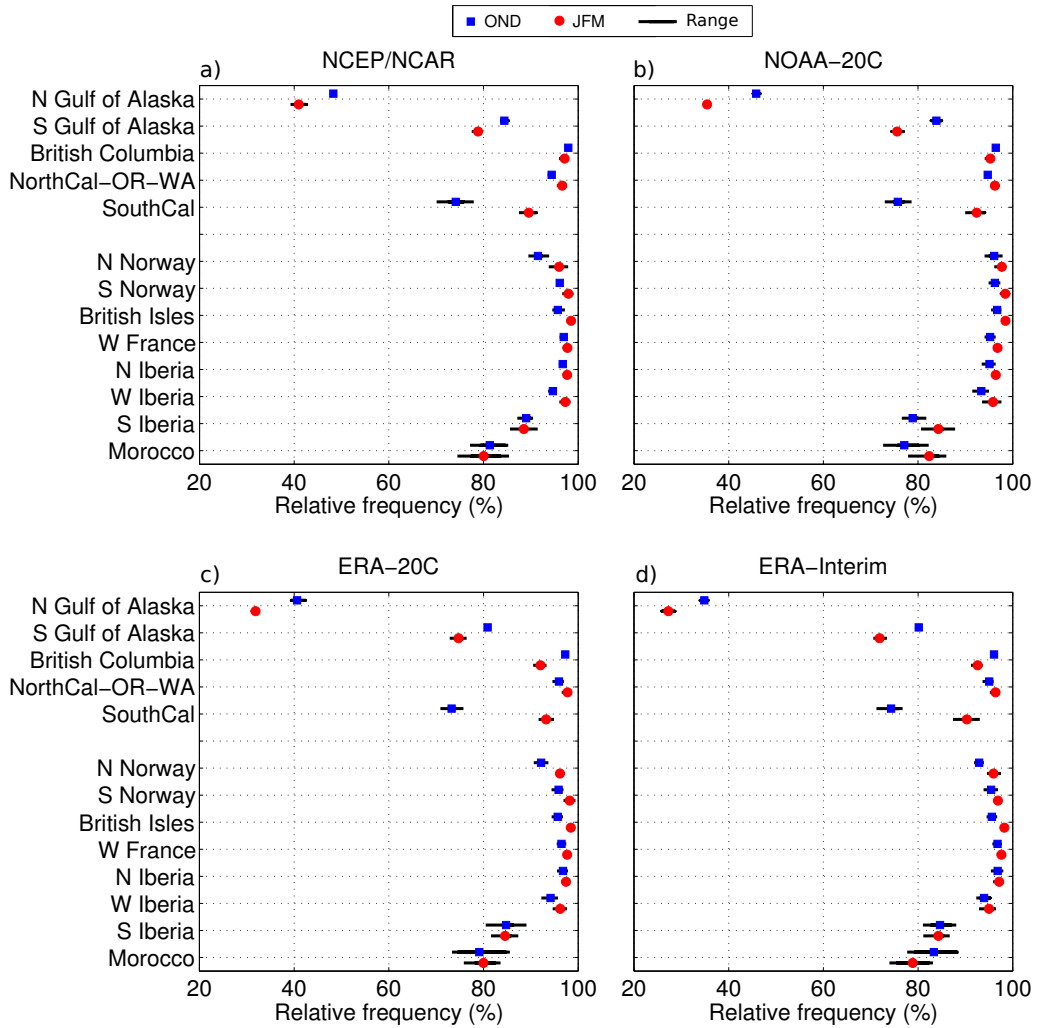


**Figure 4.2:** Fraction of ARs that are detected if the capability to track towards the north, north-east, east or south-east is intentionally disabled (see Equation 4.1) for a) NCEP/NCAR, b) NOAA-20C, c) ERA-20C and d) ERA-Interim. Results are for the October-to-December (OND) and January-to-March (JFM) seasons, considering the time period 1979-2010. Squares / circles and errorbars refer to the mean and range of the 6 results obtained from the 6 considered percentile-threshold combinations listed in Table 4.1, i. e. refer to the method-related uncertainty of the results. Source: own illustration



---

## CHAPTER 5

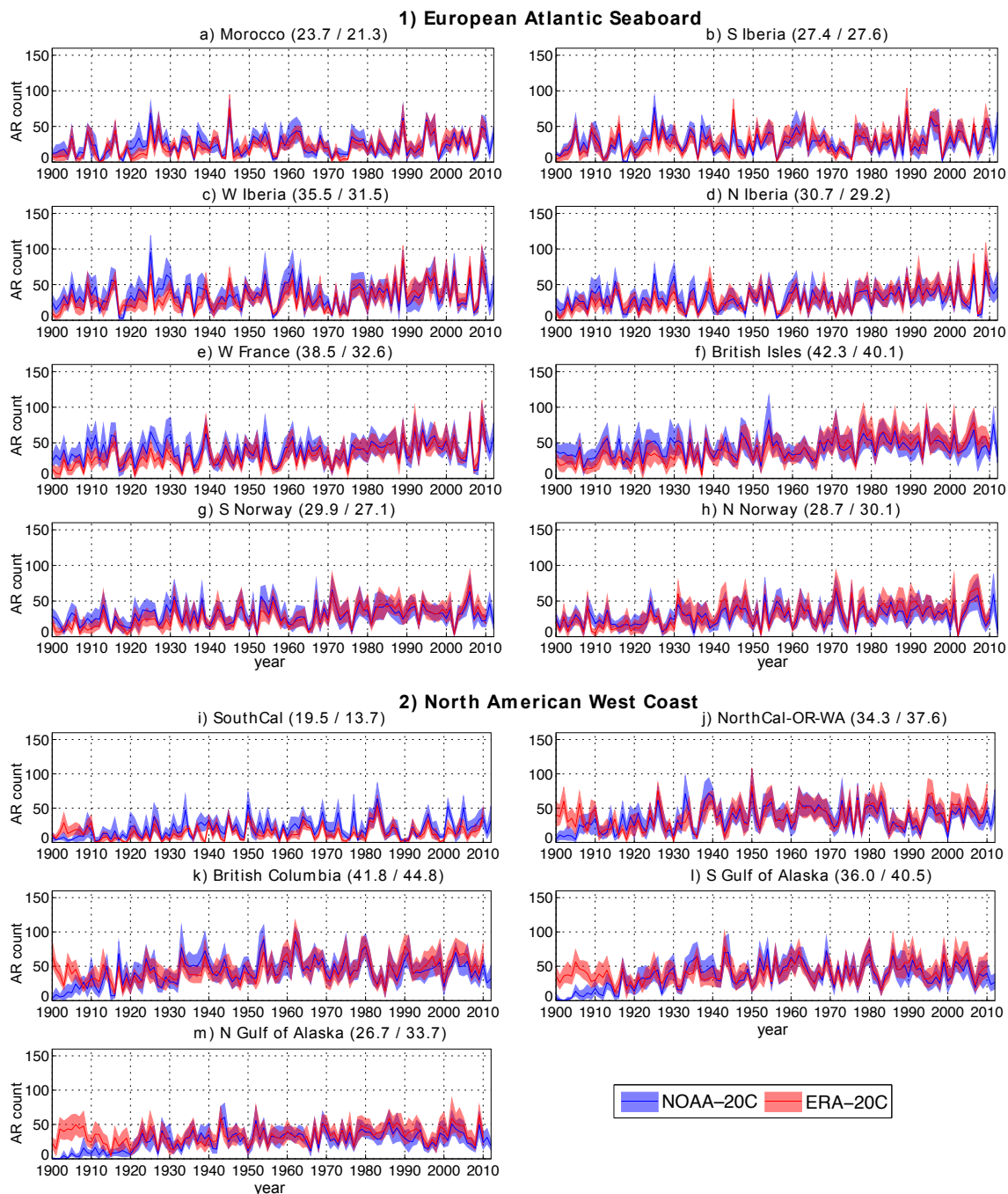
---

# Reanalysis Similarity for Atmospheric Rivers along the Twentieth Century

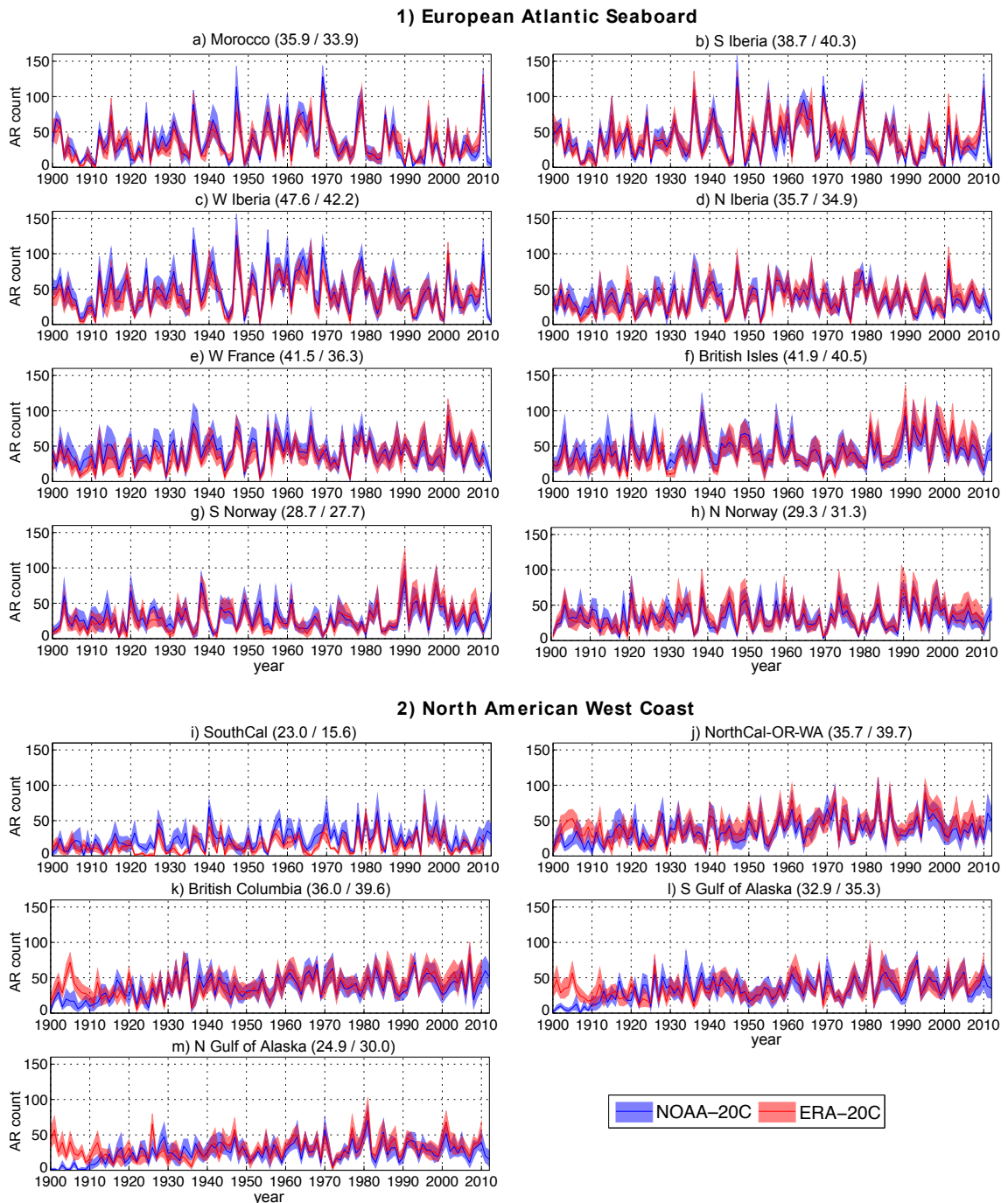
After applying the AR detection and tracking algorithm to the six-hourly time series of the four reanalyses listed in Table 3.3, the obtained occurrences were accumulated for the OND and JFM seasons. If not otherwise stated in the text, these “AR counts” are based on instantaneous ARs. The persistence criterion defined in [Lavers et al. \(2012\)](#), as well as an additional season definition comprising the entire winter half-year (ONDJFM) will be used in Section 6.1.2 for comparison with previous studies. Since reanalysis uncertainty is most relevant at the start of the century ([Compo et al., 2011](#); [Poli et al., 2016](#)), this chapter focusses on a comparison of the two long-term reanalyses.

Figure 5.1 displays the year-to-year AR count sequence obtained from NOAA-20C (blue) and ERA-20C (red) respectively; results are for the OND season in this case. As above, the lines and shadings refer to the mean and range of the 6 seasonal AR count values per season obtained from the 6 considered percentile combinations listed in Table 4.1. AR counts from ERA-20C cover the period 1900 to 2010, and those from NOAA-20C extend to 2012. Panels a to h refer to the results for Europe, panels i to m to the results for western North America. Figure 5.2 shows the respective results for the JFM season. For each of the two datasets (first number = NOAA-20C, second number = ERA-20C), the mean value for the 1900-2010 period is displayed in the header of each panel.

These simple time series plots already reveal some basic features. First, the method-related sensitivity of the results is small in comparison to the mean value (compare shadings with lines in Figures 5.1 to 5.2), which is generally also the case for the forthcoming results. Also, at the start of the century, large differences between



**Figure 5.1:** Year-to-year sequence of seasonal AR occurrence counts during the OND season for NOAA-20C (blue) and ERA-20C (red). The lines and shadings refer to the mean and range of the percentile sample (see Table 4.1), i.e. refer to the method-related uncertainty of the results. Displayed are 1900-2012 time series for NOAA-20C and 1900-2010 time series for ERA-20C. Source: own illustration



**Figure 5.2:** As Figure 5.1, but for the JFM season. Source: own illustration

the climatological mean AR counts are evident along the North American West coast (see panels j to m in Figures 5.1 and 5.2).

The objective of the present chapter is to quantify these “reanalysis-induced” differences in the seasonal AR counts in detail. These differences will be measured in terms of 1. differences in the mean (*bias*), 2. differences in the inter-annual variability, revealed by the rank correlation coefficient (*rs*), and 3. differences in the long term tendencies, revealed by conducting separate trend analyses for each reanalysis. To identify possible variations along the course of the study period (1900-2010), the *bias* and *rs* are calculated for a 31-year sliding window moving forward from the start of this period (1900-1930) till its end (1980-2010) by one year in each step. In contrast, the long term trends are calculated *once* (i.e. not in “running” mode) for the periods 1900-2010 and 1950-2010.

Recall that albeit it is impossible to estimate which reanalysis is the “correct” one from these analyses, it is, as argued in Section 3.2, the difference that tells us whether the two of them are realistic or not. If the two reanalyses agree on a given time series aspect, then they are constrained to the assimilated observations representing the real world. On the contrary, if a large disagreement is found, then the constraint to reality is weak or even missing, meaning that the time series aspect cannot be realistically estimated neither by one reanalysis nor by the other (see also Sterl, 2004; Brands et al., 2012b, 2013).

All analyses of the present thesis were conducted on both the raw and linearly detrended time series<sup>1</sup>. Since the obtained differences are generally negligible, the text and figures will hereafter refer to the results obtained from the *raw* time series if not otherwise stated.

## 5.1 Differences in the Mean

Results for the 31-year “running” *bias* in the AR counts are shown in Figure 5.3.

$$bias = \frac{\bar{y} - \bar{x}}{\bar{x}} \times 100 \quad (5.1)$$

where  $\bar{x}$  and  $\bar{y}$  are the climatological mean values of the seasonal AR counts from NOAA-20C and ERA-20C respectively. Here, NOAA-20C is assumed to be the reference reanalysis  $x$ .

On the x-axis of each panel, the centre year of a specific subperiod is displayed (e. g. “1920” refers to the time period 1905-1935). We will hereafter refer to this centre year instead of mentioning the entire subperiod. On the y-axis, the *bias* is displayed as the percentage deviation from the mean of the reference reanalysis for that subperiod, which is NOAA-20C. Again, the lines and shadings refer to the mean and range of the 6 *bias* values obtained from the percentile sample. To measure the stationarity of the *bias*, the standard deviation (std) of the 81 percentile-sample

<sup>1</sup>for the “running” analyses, the trend was removed separately in each 31-year subperiod

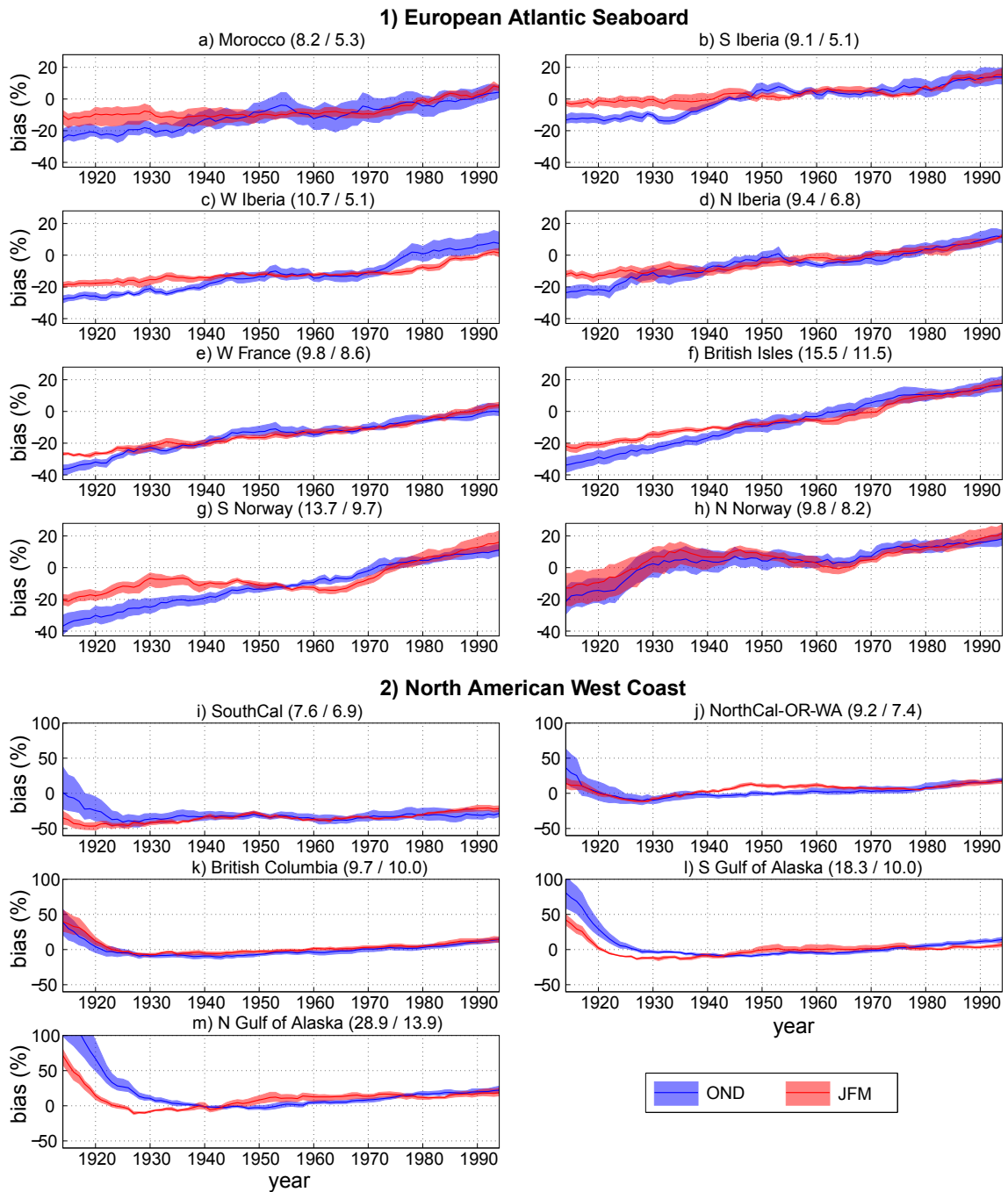


**Figure 5.3:** Bias in the climatological mean AR occurrence counts (in %, see Equation 5.1) along the course of the 20th century, using a 31-year sliding window starting in 1900-1931 and ending in 1900-2010, looping forward by one year in each step. Along the x-axis of each panel, the centre years of the subperiods are displayed. Lines and shadings refer to the mean and range of the percentile sample (see Table 4.1), i. e. refer to the method-related uncertainty of the results; blue = OND season, red = JFM season. To measure the stationarity of the the bias, the standard deviation (std) of the 81 mean bias values (as depicted by the lines) is displayed in the header of each panel. The first number refers to std for OND, the second to std for JFM. Note the distinct scale of the y-axes for Europe/North Africa and western North America. Source: own illustration

mean values for a given season and target region is displayed in the header of each panel (first number = OND std, second number = JFM std).

A visual inspection of the year-to-year time series relevant for Europe (see panels a to h in Figures 5.1 and 5.2) reveals that up to at least the 1970s (1930s in northern Norway and 1940s in northern Iberia) NOAA-20C produces systematically more ARs than ERA-20C whereas the opposite is the case from approximately the 1980s onward. This translates into a change in the sign of the bias from negative values down to approximately  $-40\%$  at the start of the twentieth century to positive values up to approximately  $+25\%$  in the recent past (see panels a to h in Figure 5.3). As indicated by the standard deviation in the header of each panel, the nonstationarity of the bias is more pronounced in OND than in JFM, with the largest values obtained for the British Isles.

Contrary to what was found for Europe, ERA-20C produces up to twice as many ARs as NOAA-20C in western North America (exception: southern California, see panels i to m in 5.3). Such a large *bias*<sup>2</sup> might be explained by the fact that the 56-member ensemble of NOAA-20C, during the “data-sparse” start of the twentieth century, suffers such a large spread that the percentile thresholds listed in Table 4.1 are exceeded by the ensemble-mean values far less often than during the later (“data-rich”) period, leading to a reduction in AR detections for this reanalysis [see also Champion et al. (2015)]. ERA-20C is a deterministic reanalysis and is therefore not affected by this issue. Nevertheless, due to the general lack of data, it cannot be expected to provide realistic AR counts at the start of the century either. By approximately 1920s (with the exception of the northern Gulf of Alaska), the *bias* for western North America decreases to a magnitude comparable to the that found for Europe. As for Europe, temporal variations in the bias are more pronounced during the OND than during the JFM season, particularly over the southern and northern Gulf of Alaska.

## 5.2 Differences in the Inter-Annual Variability

Figure 5.4 displays the results of the running rank correlation analyses. On the y-axis, the rank correlation coefficient ( $rs$ ), as well as the critical values for a two-tailed t-test applied at a test-level of 5% are shown (see dashed lines). Regarding the European regions (see panels a to h),  $rs$  is systematically lower and its range (reflecting the method related uncertainty) systematically larger during the OND than during the JFM season. Values generally decrease as one moves backward in time. With  $rs$  exceeding  $+0.6$  in nearly any case, the AR counts’ inter-annual variability is roughly similar in both datasets even at the very beginning of the 20th century. From 1955 onwards,  $rs$  is greater than, or close to,  $+0.8$ , indicating a close similarity during the last 7 decades of comparison. However, OND values in Norway

---

<sup>2</sup>note that the scale of the y-axes is distinct for the panels referring to the western North American regions

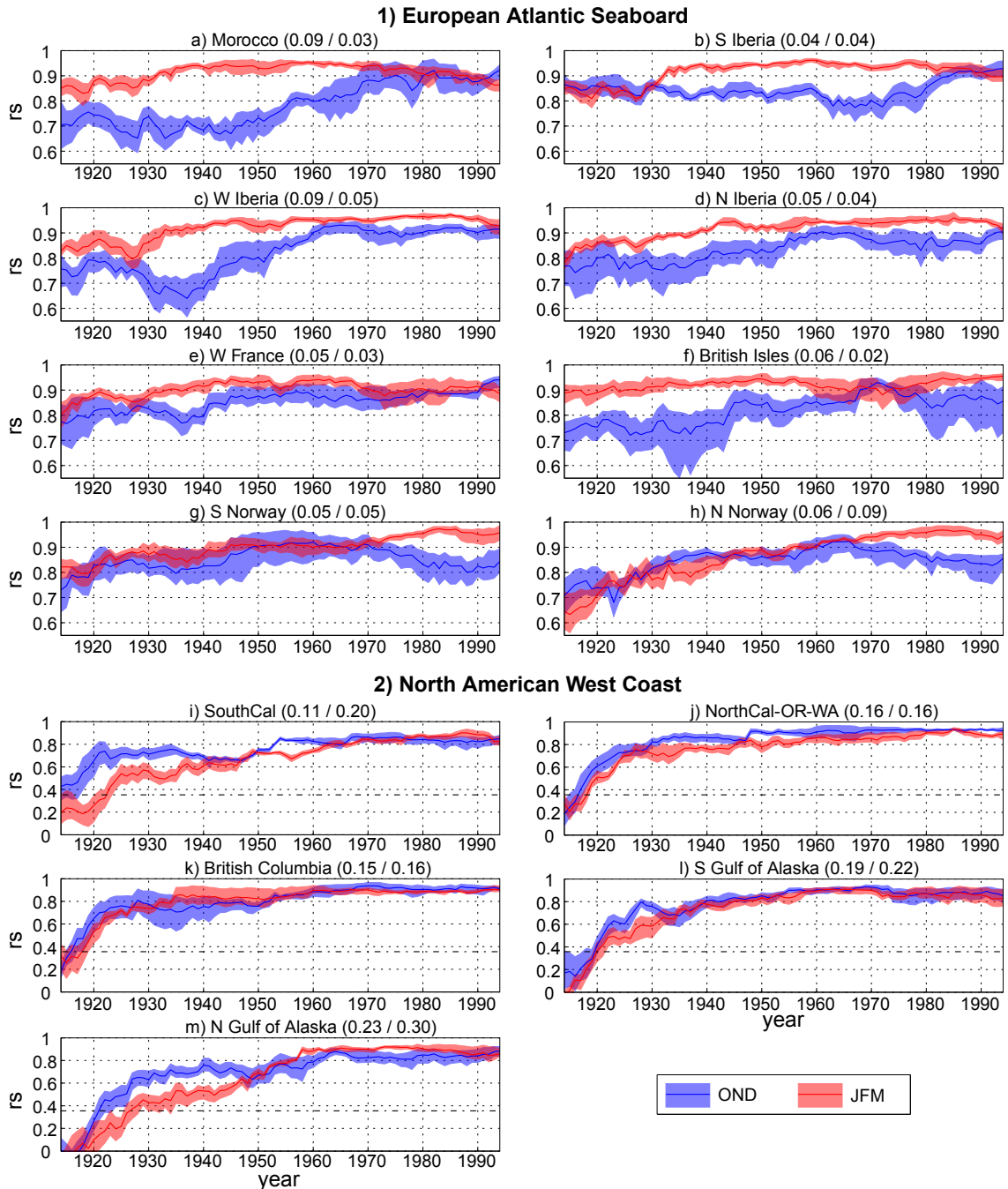


**Figure 5.4:** As Figure 5.3 but for the rank correlation coefficient ( $r_s$ ) between the seasonal AR occurrence counts from NOAA-20C and ERA-20C. Dashed horizontal lines mark the critical values below / above which  $r_s$  is significant at a test-level of 5%. Note the distinct scale of the y-axes for Europe/North Africa and western North America. Source: own illustration

—for unknown reasons— are smaller during the recent past than during the mid twentieth century (see panels g and h in Figure 5.4).

In contrast to the result for Europe,  $rs$  values along the west coast of North America (see panels i to m) are insignificant or even negative at the start of the century<sup>3</sup>. Another distinction is that the  $rs$  values in OND are much closer to those obtained for JFM and actually are larger during the first decades of the 20th century. Following the running  $rs$  forward in time, a value of approximately +0.5 is at the latest reached around 1935 and a value of approximately +0,8 is so around 1965.

### 5.3 Differences in the Long-Term Trends

The magnitude and significance of the linear decadal trends in the seasonal AR counts of the period 1950-2010 is displayed in Figure 5.5. Four panel packages are shown for two distinct datasets (NOAA-20C and ERA-20C) and seasons of the year (OND and JFM). Each panel package comprises the results for the 13 target regions shown in Figure 2.7 and 6 percentile combination listed in Table 4.1, displayed along the y and x-axes respectively. The trends were obtained from ordinary least squares regression and their significance is estimated with a two-tailed Mann-Kendall test conducted at a test-level of 5% (Mann, H. B., 1945; Bedia et al., 2012). The serial correlation in the year-to-year times series is assumed to be zero at this point<sup>4</sup>. The period 1950-2010 was chosen because of the large bias and low correlation values found for the AR counts in western North America at the start of the twentieth century (see Sections 5.1 and 5.2). Particularly the low AR counts found for NOAA-20C are very likely to be wrong, meaning that the full time series (1900-2010) are not homogeneous. This, in turn, would lead to artificial positive trends if the full period was considered.

With regard to the European AR counts in OND, the two long-term reanalyses agree on positive trends and on the approximate geographical location of the maximum trend magnitude, lying in between western Iberia and the British Isles. However, only the ERA-20C dataset indicates that these trends are significant ( $\alpha = 0.05$ ) in most regions. The opposite is found for the OND counts in western North America, where the two datasets generally agree on a lack of significance, but disagree on the sign of the trends.

During the JFM season, the two reanalyses are generally in closer agreement than during OND. For the JFM counts in Europe, both datasets agree on a dipole in the sign of the trend. A reduction of -1.5 to -5.5 AR counts per decade is found in the southernmost European regions which is contrasted by an increase in between +0.5 and 4.5 over the British Isles and southern Norway. However, the two reanalyses do generally not agree on the significance of these trends. For the JFM counts in

<sup>3</sup>again, the scale of the y-axes is distinct for the western North American regions

<sup>4</sup>which, for the case of the Iberian Peninsula, was proven by Brands et al. (2014) by means of Monte-Carlo testing

western North America, the agreement is similarly large. In both datasets, positive trends are found for the AR counts from British Columbia to the northern Gulf of Alaska. Among all considered regions and seasons, the agreement is closest for the AR counts in the southern Gulf of Alaska, which are significantly positive in any case.

In comparison to the reanalysis uncertainties, result differences are small when the percentile thresholds used to define an AR are modified.

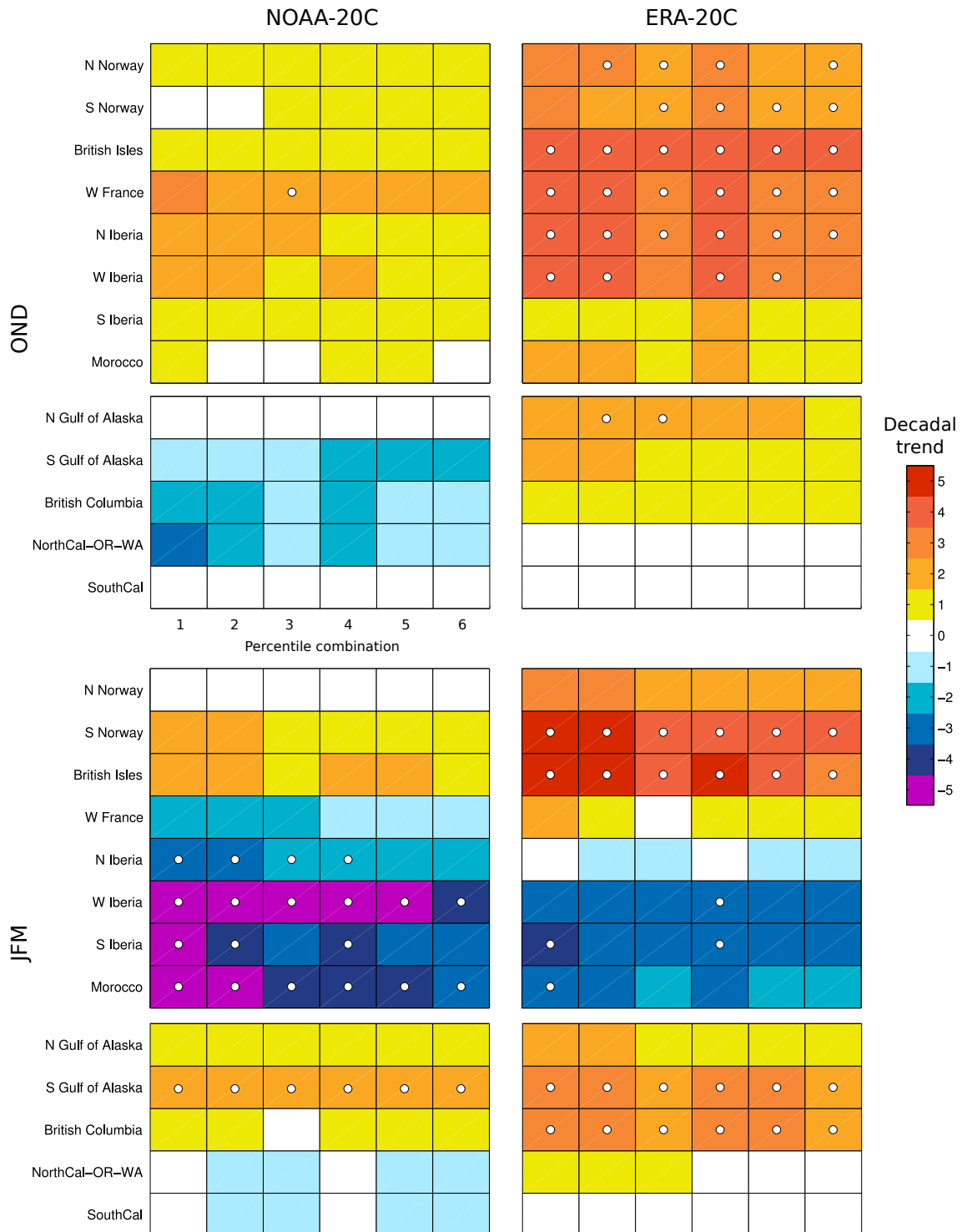


**Figure 5.5:** Magnitude and significance of the linear decadal trend in the seasonal AR counts of the period 1950-2010. Results are for NOAA-20C and ERA-20C (left and right column respectively) and for the OND and JFM seasons (upper and lower panel packages respectively). The rows in each panel package refer to the results for the 13 target regions, the columns to the results for the 6 percentile combinations listed in Table 4.1. Significant trends, obtained from a two-tailed Mann-Kendall test ( $\alpha = 0.05$ ), are indicated by white dots. Source: own illustration

---

## CHAPTER 6

---

### Teleconnections in the Observational Record

After assessing the reanalysis-induced uncertainties in the seasonal AR counts themselves, in this chapter, these counts are statistically associated with *atmospheric* and *oceanic* predictor variables known or assumed to exert teleconnections on the climate in Europe and western North America (see Section 3.1 for an overview of the applied indices). In what concerns the atmospheric predictors, the stationarity of the links to the NAO and Aleutian Low will be assessed by means of running correlation analysis and the links to other relevant atmospheric circulation patterns, such as the EA and PNA, by fixing the correlation analysis on one period (1950-2010). Analogous analyses for the oceanic indices consider the Niño 3.4 index in “running mode” and other relevant indices such as WHWP, PDO and AMO in “fixed mode”. Within the running analyses, possible modulating effects of the PDO and/or AMO on the strength of the ENSO links are assessed as well.

This Chapter is subdivided into two sections, one for *atmospheric* and the other for *oceanic* predictors (see Section 6.1 and 6.2 respectively). As pointed out in Chapter 5, the displayed results are based on the raw time series. The corresponding results for the linearly detrended series are in close agreement and are therefore not shown.

#### 6.1 *Atmospheric Teleconnections*

##### 6.1.1 *Running Correlation with the NAO and Aleutian Low*

In this section, the seasonal AR counts in Europe are statistically associated with the seasonal mean values of the NAO (the station-based index is used here), and the western North American counts are linked to the strength of the Aleutian Low

as measured by the North Pacific index. Temporal variations in the strength of these relationships, hereafter also simply referred to as “NAO link” or “NP link”, are assessed with the same running correlation analysis that was previously applied for comparing the two long-term reanalyses among each other, i.e. with a 31-year sliding window moving forward through 1900-2010 by one year in each step.

The results for the OND and JFM seasons are displayed in Figures 6.1 and 6.2 respectively. Blue lines and shadings are for AR counts from NOAA-20C and red ones are for AR counts from ERA-20C. Also shown are the critical values for a significant  $rs$  at a test-level of 5% (see dashed lines). In the header of each panel, the standard deviation ( $std$ ) of the 81 averaged  $rs$  values<sup>1</sup> is shown to measure the stationarity of the teleconnections. The first number refers to the  $std$  from NOAA-20C and the second to the  $std$  from ERA-20C respectively.

Similar to the well-known correlation dipole for seasonal precipitation totals (Hurrell, 1995), AR counts in southern Europe are inversely related to the NAO whereas in northern Europe a positive relationship is found, which is in agreement with the Lavers and Villarini (2013) results (see panels a to h in Figures 6.1 and 6.2). These relationships are generally weaker and less stationary (i.e. variable in time) during OND than during JFM. In the two southernmost and the two northernmost regions,  $rs$  in JFM is significant for any of the 81 considered subperiods indicating a temporally robust link to the NAO during this season. In northern Iberia and western France, however,  $rs$  is only significant from 1940 until the end of the 1970s. Similarly, over the British Isles,  $rs$  is insignificant from approximately 1915 to 1921 and —for NOAA-20C— also from 1960 to 1970, indicating that the NAO-link in the three central western European regions is subject to non-negligible variations along the course of the century. During the OND season,  $rs$  is generally insignificant except for Morocco and southern Iberia from approximately 1915 to 1930 and from 1975 onwards, and for southern Norway from approximately 1940 to 1970. Albeit somewhat larger during OND than during JFM, dataset-induced differences are generally small for Europe. Remarkably, the geographical location of the correlation dipole describing the NAO-links in OND gradually changes during the course of the twentieth century. From the start of the century until approx. 1925-55, the dipole moves to the north, whereas from approx. 1955-85 to 1980-2010 it moves back to the south (compare panels a and g in Figure 6.1).

As expected from the results of the reanalysis comparison (see Section 5.2), reanalysis-induced differences in the link between the western North American AR counts and the Aleutian Low can be larger than 0.5 correlation points at the start of the century (see panels i to m in Figures 6.1 and 6.2). In the two southernmost regions,  $rs$  is insignificant or prone to large reanalysis differences along the entire study period, except during the JFM season where significantly negative  $rs$  are obtained from 1945 to 1960 (in North California-Oregon-Washington only) and from 1990 onwards (in both regions). In the 3 remaining regions,  $rs$  for JFM is significantly

<sup>1</sup>for each of the 81 subperiods, the six  $rs$  values obtained from the six percentile threshold combinations listed in Table 4.1 are averaged

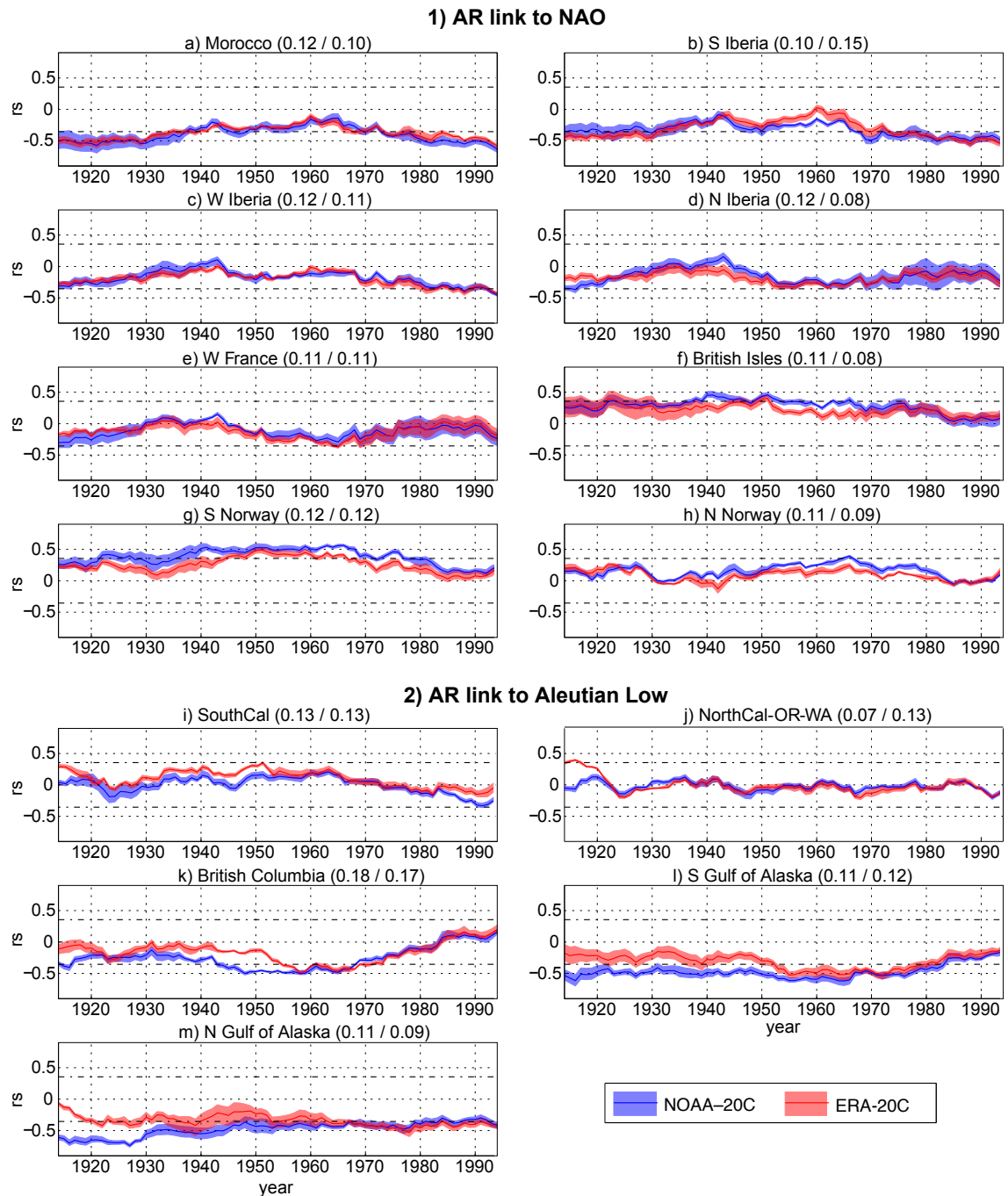


**Figure 6.1:** Running rank correlation ( $rs$ ) analysis between the AR occurrence counts in NOAA-20C (blue) or ERA-20C (red) and the station-based NAO or North Pacific index, using a 31-year sliding window starting in 1900-1931 and ending in 1900-2010, looping forward by one year in each step. Along the x-axis of each panel, the centre years of the subperiods are displayed. Dashed horizontal lines mark the critical values below / above which  $rs$  is significant at a test-level of 5%. In the header of each panel, the  $std$  of the 81 average  $rs$  values is shown to measure the stationarity of the teleconnections (see text for details). The first number refers to the  $std$  from NOAA-20C and the second to the  $std$  from ERA-20C respectively. Results are for the OND season. Source: own illustration

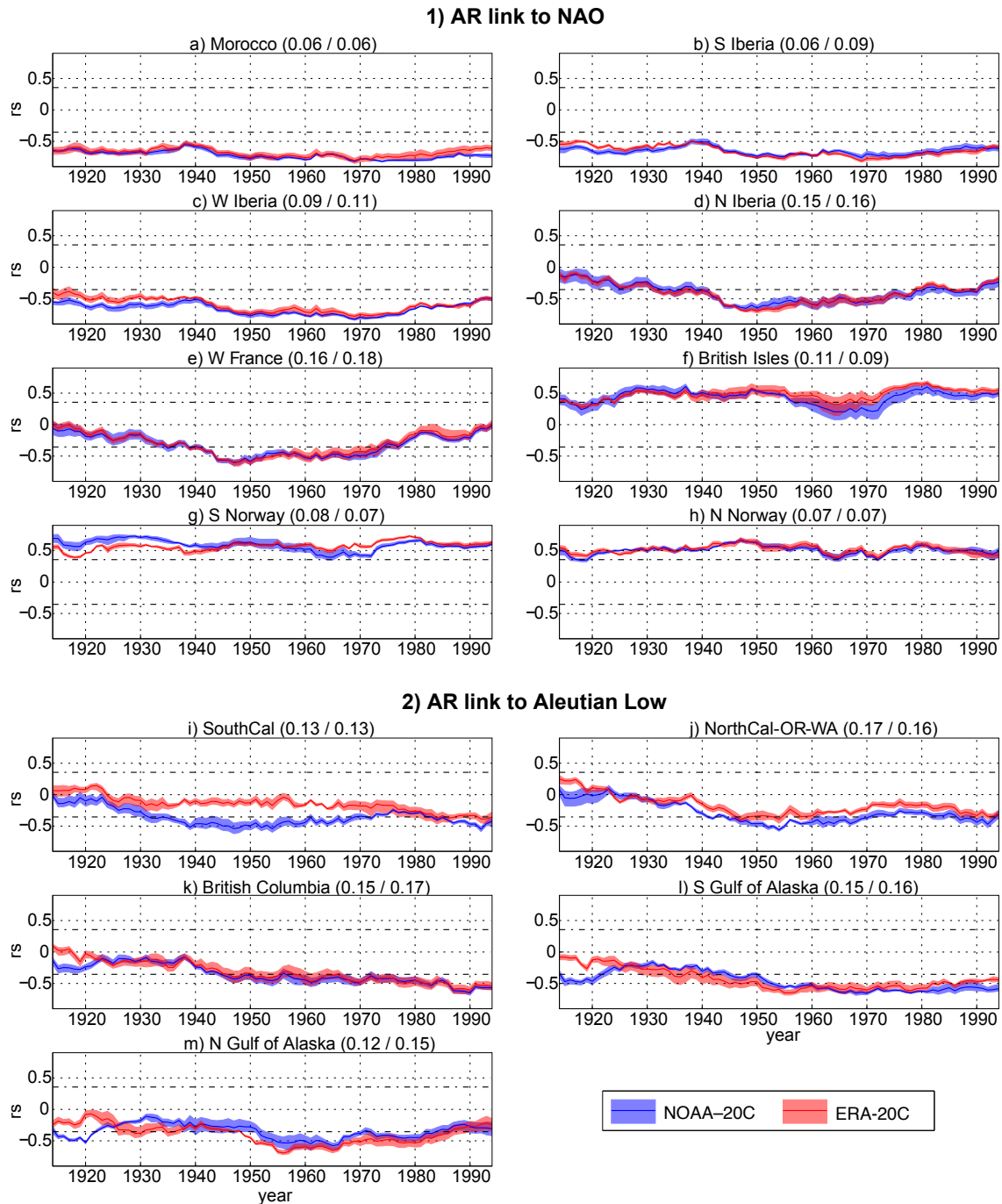


**Figure 6.2:** As Figure 6.1, but for the JFM season. Source: own illustration

negative from approximately 1950 onwards, except for the northern Gulf of Alaska where insignificant values are obtained in the very recent past (from 1990 onwards). During OND, reanalysis differences in the results are relatively large until at least 1955. Thereafter, these differences diminish, revealing significantly negative  $rs$  in British Columbia and the southern Gulf of Alaska, which, however, vanish when approaching the present, eventually becoming insignificant from 1970 / 1980 onwards. This weakening is most pronounced in British Columbia. In the northern Gulf of Alaska,  $rs$  in OND is significantly negative from approximately 1955 onwards.

### 6.1.2 Relationships to Other Atmospheric Circulation Indices

Figure 6.3 shows the  $rs$  between the seasonal AR counts in the eight considered European target regions and the seasonal-mean large-scale circulation indices relevant there. Unlike the running analyses conducted above, in this section,  $rs$  is calculated once for the period 1950-2010<sup>2</sup>, or 1979-2013 in case ARs from ERA-Interim are considered. As above, the bars and errorbars in a given panel refer to the mean and range of the six results obtained from the six distinct percentile-threshold combinations (see Table 4.1). The critical values obtained from a two-tailed t-test conducted at a test-level of 5% are indicated by dashed lines. Along the rows, results for the ARs retrieved from NCEP/NCAR, NOAA-20C, ERA-20C and ERA-Interim are displayed from the top to the bottom. The OND, JFM and ONDJFM results are provided in columns 1-3. For the sake of simplicity,  $rs_{index}$  will hereafter refer to the  $rs$  between the AR counts in a given region and the indicated climate *index*.

The three reanalyses covering the 1950-2010 period produce very similar results (see rows 1-3 in Figure 6.3). During both OND and JFM (see columns 1+2), the NAO links are strongly negative in the southern European regions, weaker in the central regions and strongly positive in the northern regions, thereby depicting the well-known correlation dipole found for precipitation in earlier studies (Hurrell, 1995; Qian et al., 2000). Since  $rs_{H-NAO}$  over the period 1950-2010 is significant for almost any region irrespective of the considered season and dataset and since the magnitude of  $rs$  is close to 0.8 in some cases, the NAO, and particularly the NAO based on SLP<sup>3</sup>, is the most important circulation pattern for the AR counts in Europe if the results are seen as a whole. Exceptions from this general finding are mainly found during the OND season, when the AR counts over western Iberia, northern Iberia and western France are more strongly linked to the EA than to the NAO ( $rs_{EA}$  lies in between +0.5 and +0.7) and those over the British Isles are more strongly linked to the SCAND. The NAO and SCAND links are more pronounced during the JFM than during the OND season whereas the opposite is found for the links to the EA. During JFM, a north-south correlation dipole similar to the NAO, but of opposite

<sup>2</sup>note that the indices provided by the Climate Prediction Center are available from 1950 onwards only

<sup>3</sup>Recall that the  $H-NAO$  is based on SLP where as the  $CPC-NAO$  is based on the geopotential at 500 hPa (see Table 3.1)

sign, is found for the SCAND links, yielding significance in the two southernmost and three northernmost regions, where  $r_{SCAND}$  can reach values down to approx.  $-0.7$ . During OND, the SCAND link is significant in the three northernmost regions only. The EA/WR link is significant in the latter three regions during OND and in northern Norway during JFM. The POL link is generally insignificant except during JFM in northern Iberia and western France. When the entire winter half-year is considered (ONDJFM, see column 3 in Figure 6.3), the strength of the teleconnections generally lies in between the values obtained for OND and JFM.

Additional sensitivity tests were conducted for the ONDJFM season and the respective results are displayed in Figure 6.4. The first column refers to solely considering persistent ARs, the second to “turning off” the algorithm’s capability to track towards the N, NE, E and SE, and the third to using a length criterion of  $> 2000$  instead of  $3000$  km (over the sphere). Following Lavers et al. (2012) a “persistent AR” is here defined as the continuous presence of an AR during at least 18 hours and two persistent events are assumed to be independent if they are separated by more than one day (24 hours).

From these additional experiments, it becomes obvious that the inclusion of the persistence criterion weakens the link between the ONDJFM AR counts and the NAO indices particularly over the British Isles (compare first column in Figure 6.4 with last column in Figure 6.3). This effect is most appreciable in case the experimental setup considered in Lavers et al. (2012)<sup>4</sup> is used in combination with a length criterion of  $> 3000$  km, in which case  $r_{SCPC-NAO}$  is consistently insignificant (see setup 1 in Table 6.1). For the experimental setup used in Ramos et al. (2015)<sup>5</sup>, the detrimental effect of the persistence criterion leads to insignificant  $r_{SCPC-NAO}$  for at least two out of six percentile combinations (see setup 2 in Table 6.1). Finally, neither disabling the algorithm’s capability to track towards the N, NE, E and SE nor applying the alternative length criterion does notably alter the results in this region of the world (compare columns 2 and 3 in Figure 6.4 with the last column in Figure 6.3).

The respective results for the west coast of North America and the circulation indices relevant there are shown in Figure 6.5 and Figure 6.6 respectively. Instantaneous AR counts along the Gulf of Alaska are positively correlated with the PNA and negatively correlated with the NP (see Figure 6.5). Yet significant in both seasons, these links are more pronounced during JFM than during OND (compare first and second column). During JFM, the AR counts in SouthCal, NorthCal-OR-WA and British Columbia are also significantly associated with the NP index, with the exception of the AR counts in SouthCal and NorthCal-OR-WA obtained from ERA-20C, in which case the results are on the limit to significance (see panel h). It is during the JFM season only when ARs over the two aforementioned regions are significantly related to the WP. Teleconnections involving the AR counts in the Gulf of Alaska are systematically weaker during 1979-2013 than during 1950-2010 (compare last

<sup>4</sup>i.e. considering persistent ARs during ONDJFM 1979/80-2009/10 derived from ERA-Interim

<sup>5</sup>i.e. considering persistent ARs during ONDJFM 1950/51-2011/12 derived from NCEP/NCAR

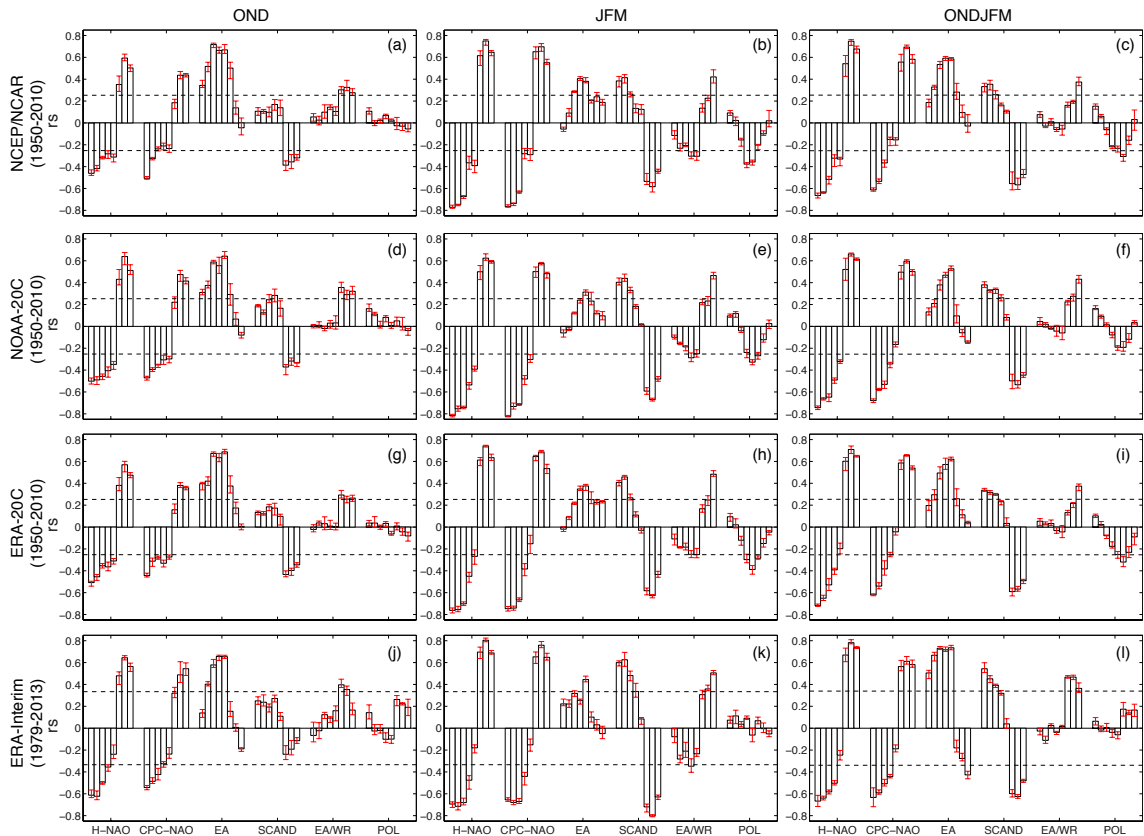


**Figure 6.3:** Rank correlation coefficient ( $r_s$ ) between seasonal AR occurrence counts and seasonal-mean atmospheric circulation indices for the eight considered target regions in Europe/North Africa ordered from the South to the North, i.e. the first bar or each group of bars refers to Morocco and the last to northern Norway respectively. Results are for NCEP/NCAR, NOAA-20C, ERA-20C and ERA-Interim (each row corresponds to a specific dataset) and for OND, JFM and ONDJFM (each column corresponds to a specific season). Bars and errorbars refer to the mean and range of the six results obtained from the six considered percentile-threshold combinations, i.e. refer to the method-related uncertainty of the results. Dashed horizontal lines mark the critical values below / above which  $r$  is significant at a test-level of 5%. Results are for 1950-2010 except for ERA-Interim in which case they are for 1979-2013. Source: own illustration

**Table 6.1:** Rank correlation coefficient (rounded to the next integer  $\times 100$ ) measuring the link between the AR counts in western Iberia (setup 1) or the British Isles (setup 2) and Climate Prediction Center's NAO index during the ONDJFM-season, with and without considering the [Lavers et al. \(2012\)](#) persistence criterion (see text for details). Results are for the experimental setups most closely reflecting [Lavers et al. \(2012\)](#) (setup 1) and [Ramos et al. \(2015\)](#) (setup 2); see text for more details. Significant results ( $\alpha = 0.05$ , two-tailed t-test) are printed in bold. a) results for an AR length criterion of  $> 3000$  km, b) results for  $> 2000$  km.

a) 3000 km	Setup 1	Setup 2
Without persistence criterion	<b>48, 49, 46, 45, 45, 40</b>	<b>-37, -38, -37, -39, -40, -41</b>
With persistence criterion	17, 15, 14, 24, 19, 26	<b>-26, -35, -21, -32, -23, -34</b>
b) 2000 km		
Without persistence criterion	<b>52, 54, 55, 53, 53, 51</b>	<b>-33, -33, -32, 33, -35, -36</b>
With persistence criterion	<b>44, 40, 37, 34, 42, 48</b>	<b>-18, -31, -20, -31, -25, -32</b>

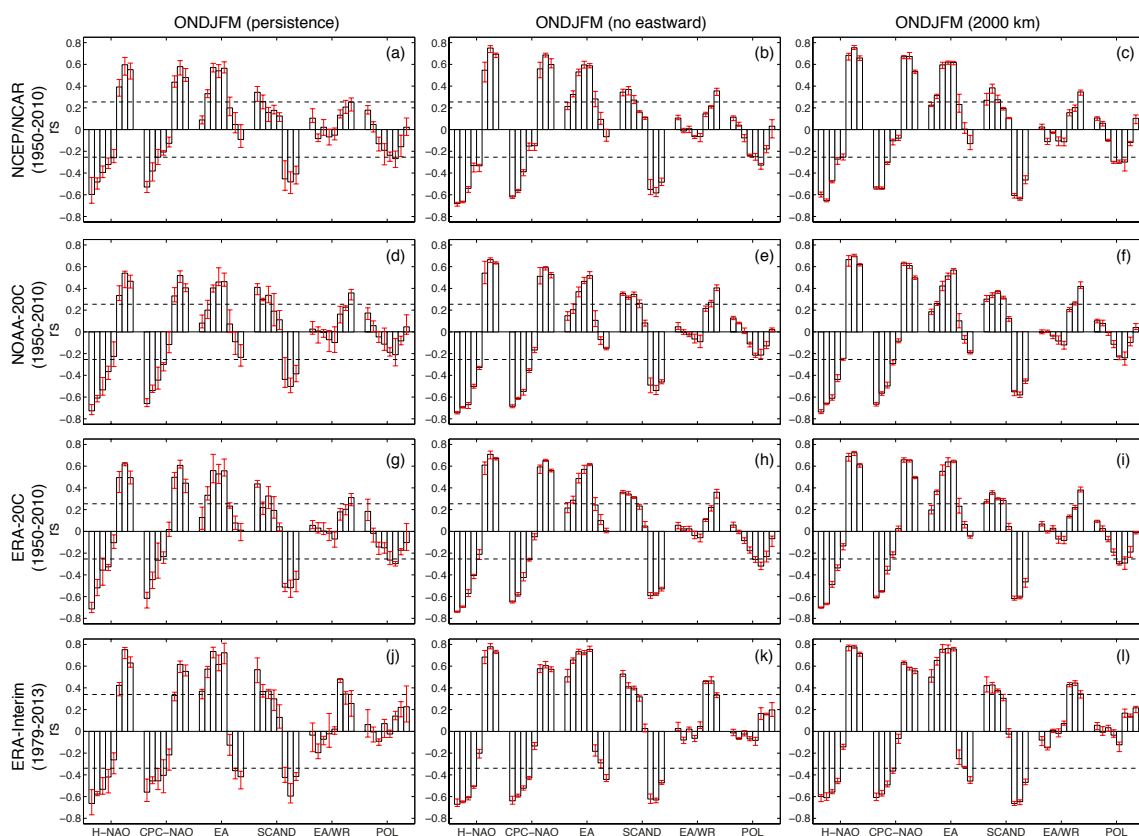


**Figure 6.4:** As Figure 6.3, but for AR counts obtained (first column) from persistent events only, (second column) *without* eastward tracking capability, (third column) with a length criterion of  $> 2000$  km. Source: own illustration

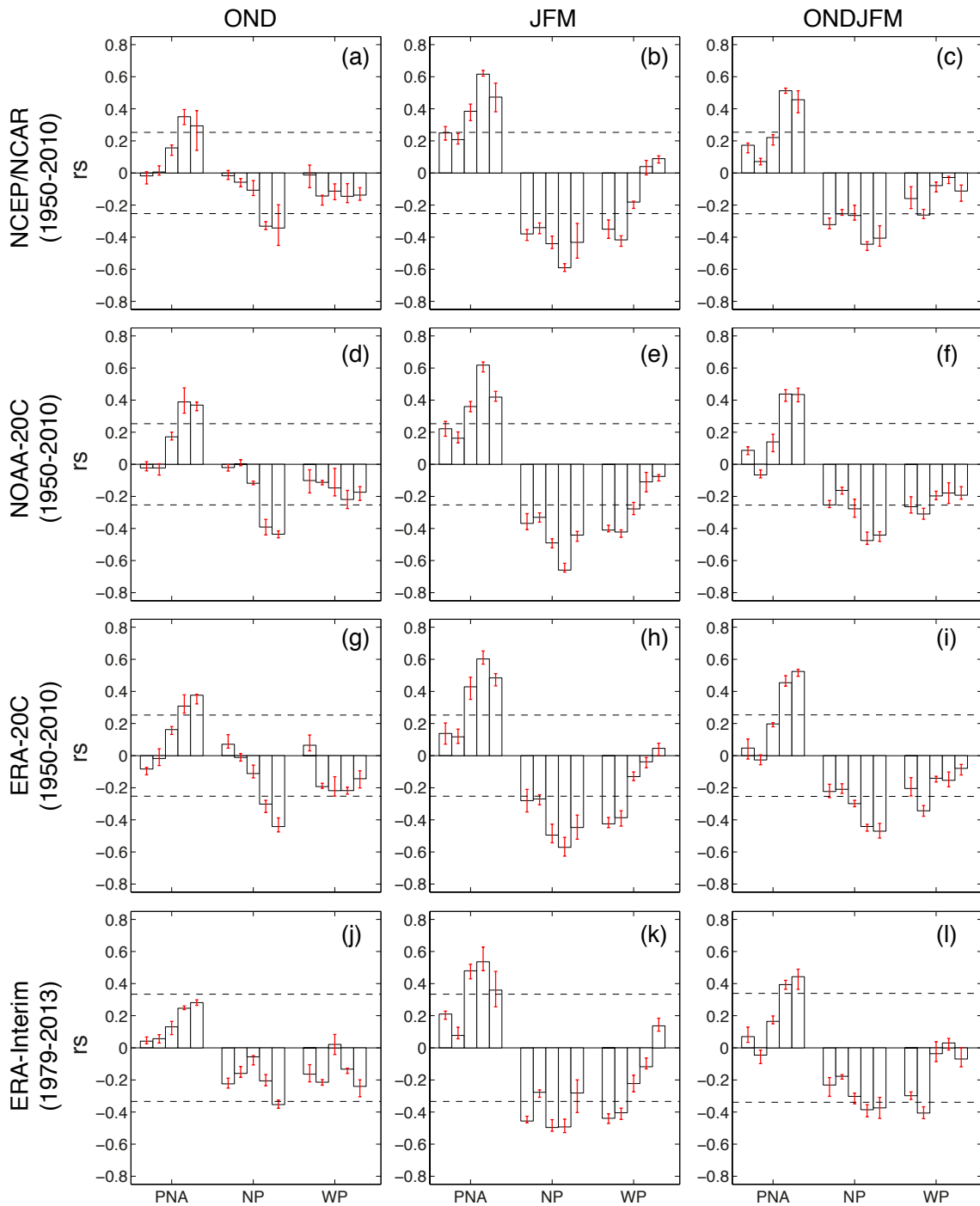


**Figure 6.5:** As Figure 6.3, but for the  $r_s$  between the seasonal AR occurrence counts in the five western North American target regions and the atmospheric circulation indices relevant there: PNA = Pacific-North American, NP = North Pacific, WP = West Pacific. The first bar or each group of bars refers to southern California, the last one to the northern Gulf of Alaska. Source: own illustration

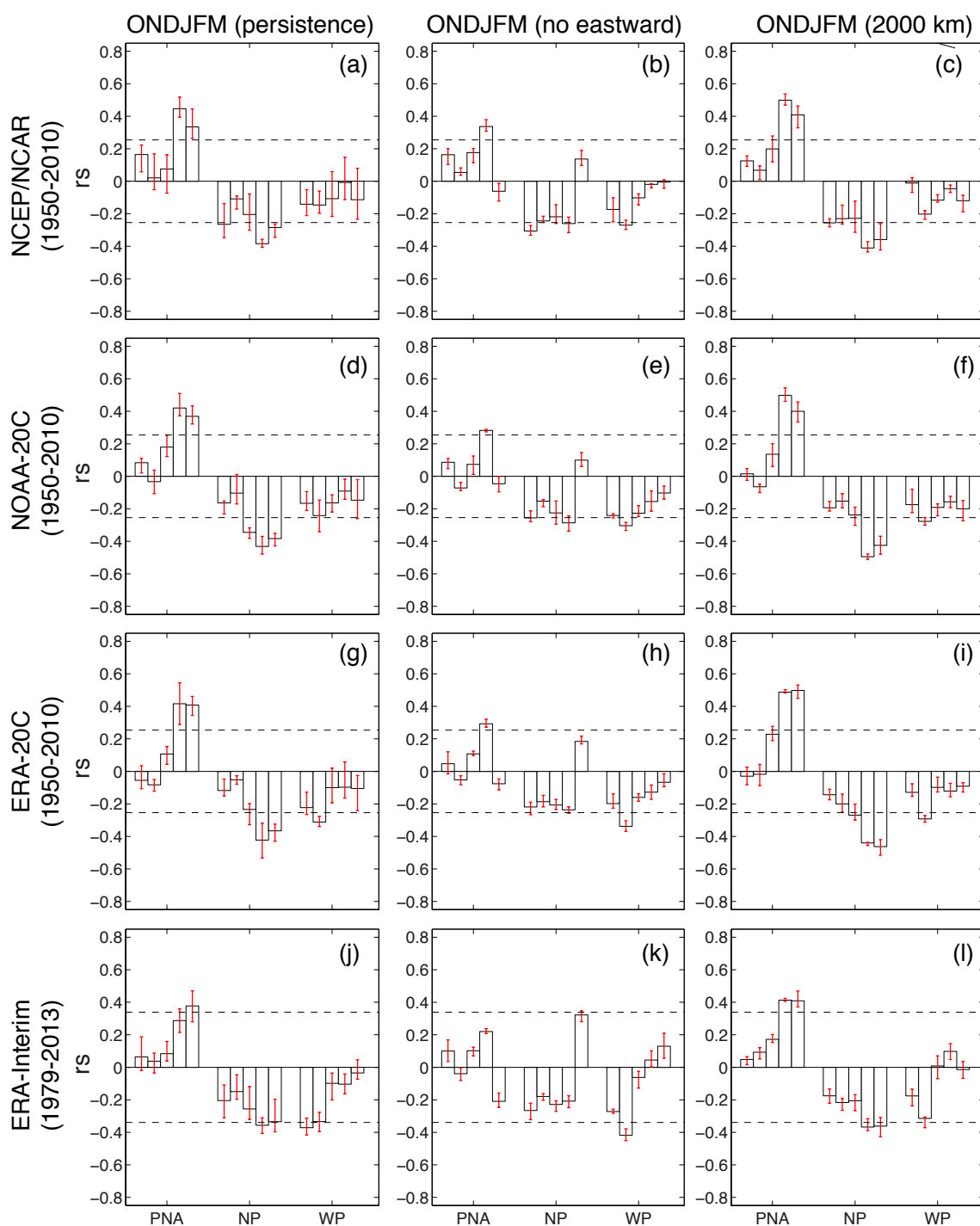


**Figure 6.6:** As Figure 6.3, but for the  $r_s$  between the seasonal AR occurrence counts in the five western North American target regions and the atmospheric circulation indices relevant there: PNA = Pacific-North American, NP = North Pacific / strength of the Aleutian Low, WP = West Pacific. The first bar or each group of bars refers to southern California, the last one to the northern Gulf of Alaska. In contrast to Figure 6.5, results are for AR counts obtained (first column) from persistent events only, (second column) *without* eastward tracking capability, (third column) with a length criterion of  $> 2000$  km. Source: own illustration

row to rows 1-3 in Figure 6.5 and also see Figure 6.1l and 6.2m).

Unlike in Europe, the persistence criterion's effect on  $rs$  is not systematic along the west coast of North America, i.e. can lead to a slight increase or decrease in  $rs$  (compare first column in Figure 6.6 with last column in Figure 6.5). If the algorithm's capability to track towards the N, NE, E and SE is disabled, teleconnections with the PNA and NP mostly become insignificant in the northern and southern Gulf of Alaska (compare second column in Figure 6.6 with last column in Figure 6.5). Thus, the inclusion of this capability is key to properly capture the inter-annual variability of the AR counts in these regions. As was the case for Europe, applying the alternative length criterion does not notably alter the results (compare last column in Figure 6.6 with last column in Figure 6.5).

## 6.2 Oceanic Teleconnections

Some of the aforementioned large-scale atmospheric circulation patterns, particularly the EA in the European and PNA in the North American sector, are known to be associated with SST variations in the tropics, most prominently in the Niño regions (e.g. Horel and Wallace, 1981; Casanueva et al., 2014; Iglesias et al., 2014). Since SST variations in these regions can be generally predicted with sufficient accuracy several months in advance (Barnston et al., 2012), any statistical relationship to the regional AR counts assessed here would offer a “window of opportunity” for long-range predictions (Frias et al., 2010), if it can be shown that the relationship is robust to the effects of internal climate variability. In this section, the windows of opportunity *seen in observations* will be assessed. In Chapter 7 it will then be asked if these are robust to internal climate variability.

### 6.2.1 Running Correlation with ENSO and Low Frequency Modulation by the PDO and AMO

Figures 6.7 and 6.8 show the results of the running correlation analysis for the relationship between the Niño 3.4 index and the AR counts, using the same temporal setup as for Figures 6.1 and 6.2 above. To estimate whether the ENSO-AR link is modulated by the PDO, the 31-year running mean of the PDO index is superimposed on the running correlation results (see red lines in Figures 6.7 and 6.8) and the latter two time series are then correlated for each of six percentile-threshold combinations listed in Table 4.1, using the Pearson correlation coefficient ( $r$ ). The six corresponding results are then averaged and this average, hereafter referred to as the “mean strength of the modulation” ( $r_{mod}$ ), is printed in the header of each panel for the ARs derived from NOAA-20C (first number) and ERA-20C (second number). Since reanalysis differences are larger for western North America than for Europe,  $r_{mod}$  is calculated from the 1915-45 period onwards in the former region and from 1900-30 onwards in the latter one. By definition, the two time series containing the running correlation

coefficients and running mean PDO index values are heavily autocorrelated in time. To put it in another way, the number of independent observations, the so called effective samples size ( $n^*$ , see Equation 6.1), is much smaller than the nominal sample size ( $n$ ) (Bretherton et al., 1999; Brands et al., 2014):

$$n^* = n \frac{1 - l1 \times l2}{1 + l1 \times l2} \quad (6.1)$$

where  $l1$  and  $l2$  are the lag-1 autocorrelation coefficients of the first and second time series, respectively.

This is of practical importance because the standard t-test on the significance of a correlation assumes independent observations (Bretherton et al., 1999). Hence,  $n^*$  instead of  $n$  is applied here to estimate whether the modulating effect of the PDO on the ENSO-AR links is significant or not. To address a possible low-frequency modulation by the AMO, these analyses have been repeated with the AMO index.

Results for the OND season indicate that, in the European regions, a significantly positive link to ENSO is found for the AR counts around the Bay of Biscay, i.e. in the northern Iberian Peninsula and western France, from approximately 1955-1975 until the present (note that the centre of the the 31-year running periods is indicated along the x-axes of the figure). Prior to that period, namely in between approx. 1945-75 and 1950-80, these links seem to be displaced to the south, yielding significant results for the ARs in Morocco, southern and western Iberia. In the latter region, the link remains significant until 1974-2004.

The corresponding results for the JFM season are remarkable. For the AR counts from Morocco to western France, i.e. in five target regions, both long-term reanalyses agree on a significantly positive link to ENSO during the early twentieth century, which, with values of up to  $r = +0.8$ , is stronger than any of the the aforementioned OND links. This early link suffers a sudden drop during the time periods centred on the late 1930s but, in the three southern regions, is still significant thereafter until 1953-83. Whereas the ENSO-AR link is entirely insignificant over the British Isles, significant negative links are found in the two Scandinavian regions during the time period 1915-45 to 1925-55, and in northern Norway also earlier.

Surprisingly, results are less conclusive for the AR counts along the west coast of North America, which is partly due to the fact that the agreement of the two long-term reanalyses is poorer in this region than in Europe. As can be seen from Figure panels i-l in Figures 6.7 and 6.8, a consistently significant link to ENSO<sup>6</sup> is only obtained at the end of the century, and only in British Columbia and North California-Oregon-Washington (NorthCal-OR-WA) during the JFM season. This link is positive in any case. An exception from this general finding is found for the AR counts in the southern Gulf of Alaska during JFM, when the link to ENSO is significant (in case of ERA-20C) or on the limit to significance (in case of NOAA-20C) in between 1931-61 and 1943-73, i.e. prior to the Great Pacific Climate Shift (Deser et al., 2004).

<sup>6</sup>i.e. found in both reanalyses and for all percentile threshold combinations

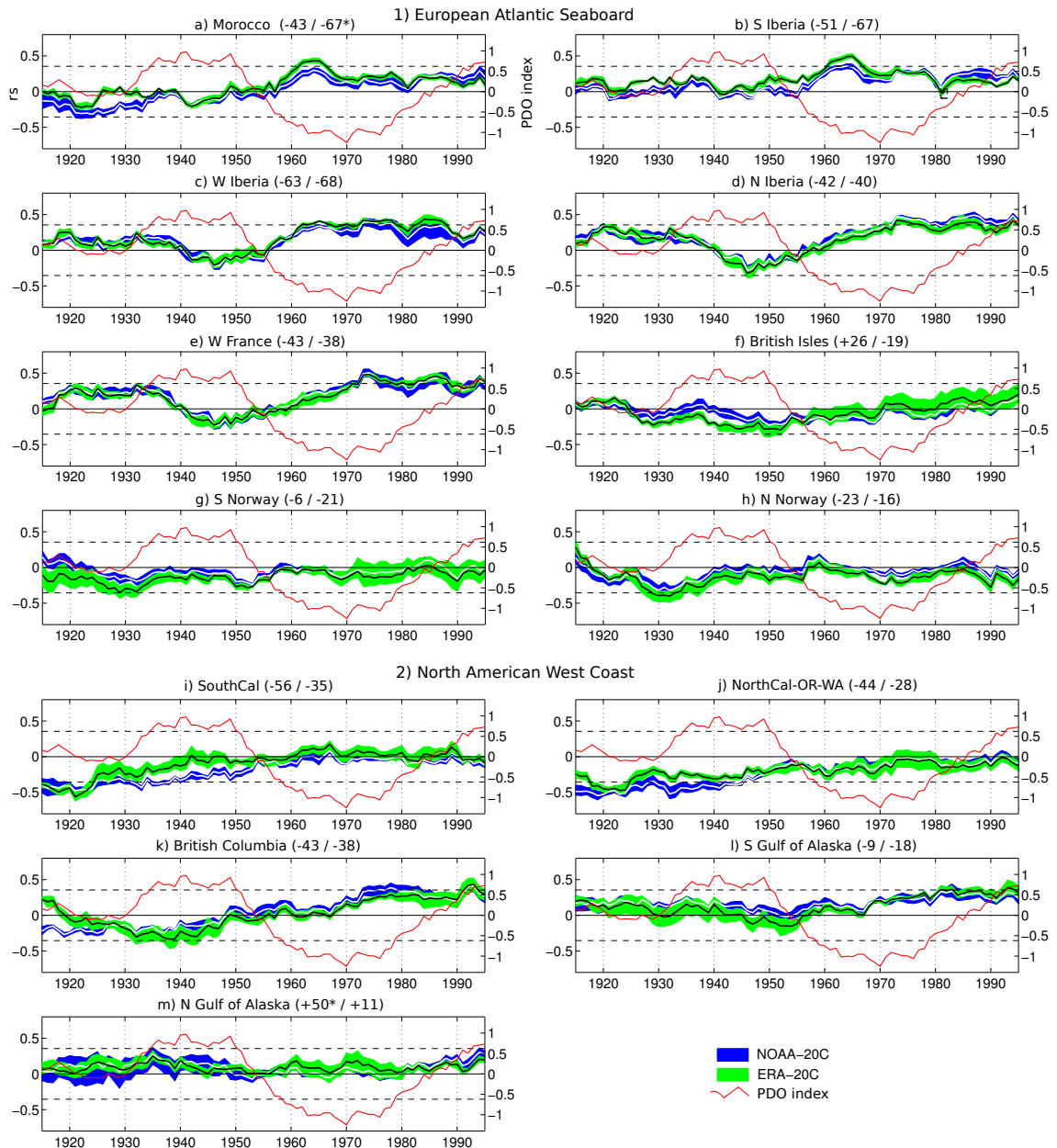


**Figure 6.7:** Running rank correlation ( $r_s$ ) analysis between the AR occurrence counts in NOAA-20C (blue) or ERA-20C (green) and the Niño 3.4 index, using a 31-year sliding window starting in 1900-1931 and ending in 1900-2010, looping forward by one year in each step. Along the x-axis of each panel, the centre years of the subperiods are displayed. Dashed horizontal lines mark the critical values below / above which  $r_s$  is significant at a test-level of 5% (the standard t-test is used). In the header of each panel, the *average out of six* Pearson correlation coefficients ( $\times 100$ ) between the time-mean PDO index and the running  $r_s$  values from NOAA-20C (first number) and ERA-20C (second number) is shown. If a least one out of the six correlation coefficients is significant at a test-level of 10% (correcting for serial correlation), the number is marked with an asterisk. See text for more details. Results are for the OND season. Source: own illustration

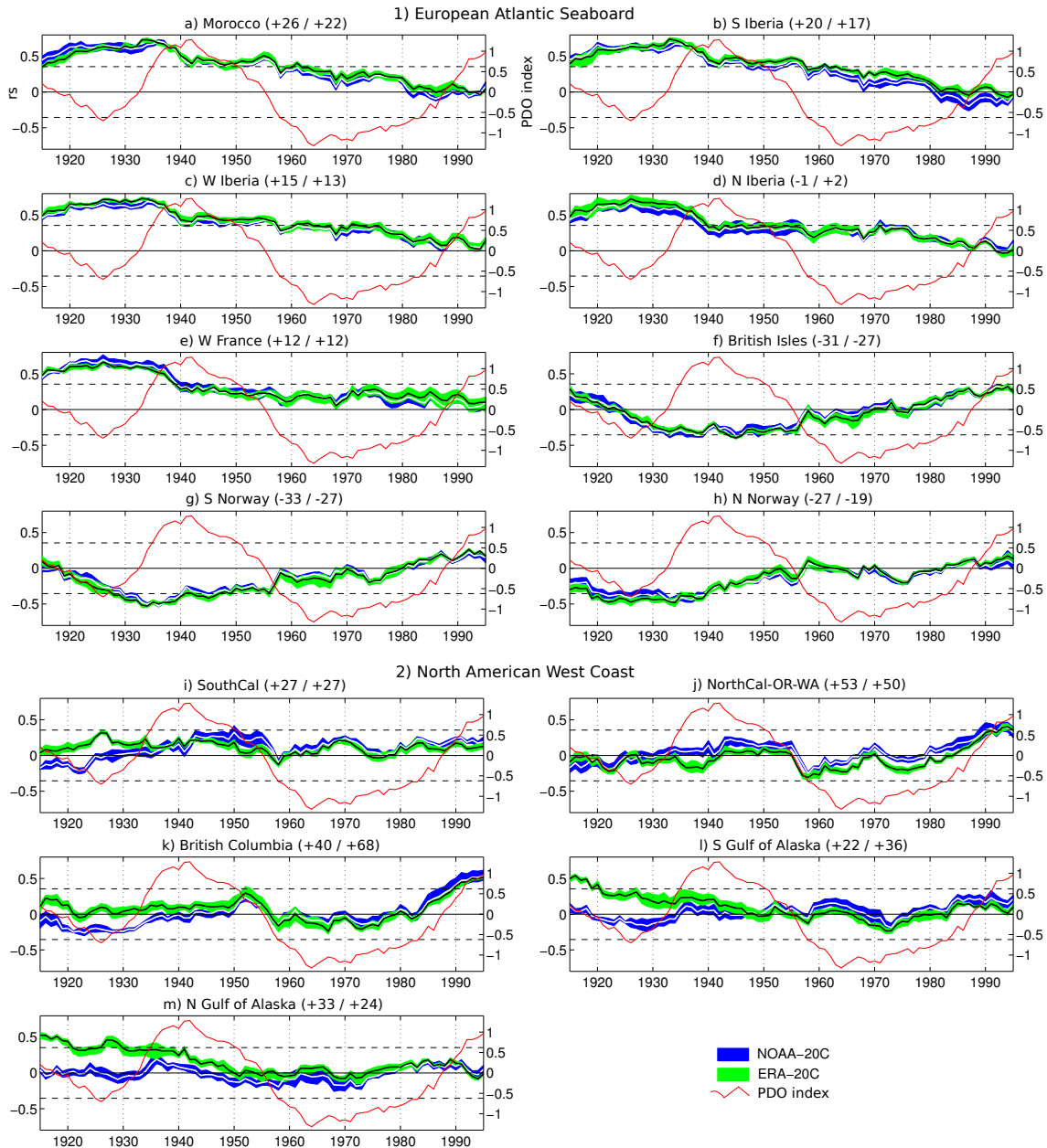


Figure 6.8: As Figure 6.7, but for the JFM season. Source: own illustration

Due to their (previously discussed) close agreement, the two long-term reanalyses generally agree on the results for Europe even at the start of the twentieth century, particularly during the JFM season.

As documented by  $r_{mod}$  values of down to -0.68, the PDO *seemingly* exerts a modulating effect on the western North American AR counts during both seasons, and on the European counts during the OND season. However, since  $n^* = 6$  on average, the magnitude of the critical value to be surpassed to yield a significant correlation is 0.729 on average even if a test-level of 10% is assumed. In Figures 6.7 and 6.8,  $r_{mod}$  is marked with an asterisk if significant results are obtained for at least *one* out of the six percentile threshold combinations listed in Table 4.1. As can be seen from these figures, if serial correlation is taken into account, the low-frequency modulation by the PDO is *insignificant* in almost any case. Exceptions are found for the AR counts in the northern Gulf of Alaska and Morocco during the OND season. However, even in these latter cases, significance is yielded only for *one* of the two long-term reanalyses and/or some specific percentile threshold combinations. In summary, there is no consistent evidence for a statistical relationship between changes in the strength of the ENSO-AR link and variations in the PDO.

Qualitatively similar results are obtained when these analyses are repeated for the AMO instead of the PDO. In this case, some significant relationships are found for the AR counts over the British Isles, the southern and northern Gulf of Alaska during the OND season, and in southern California and the northern Gulf of Alaska during the JFM season. As for the case of the PDO, however, significant results are not consistently found in both reanalyses and/or are limited to specific percentile threshold combinations.

### 6.2.2 Relationships to Other Oceanic Indices

Analogous to Figures 6.3 and 6.5, Figures 6.9 and 6.10 show the  $rs$  between the European and western North American AR counts and the distinct oceanic indices described in Section 3.1. The interpretation of the results focusses on the AR counts from NCEP/NCAR, NOAA-20C and ERA-20C, considering the period 1950-2010 (see rows 1-3 in Figures 6.9 and 6.10). For the sake of completeness, results for the counts from ERA-Interim (1979-2013) are shown in addition (see last row).

In both continents, the *Niño 3.4 links* (described in detail in Section 6.2.1) closely resemble those found for the *PWP*, indicating that these two indices can be used virtually interchangeable in the context of the present thesis.

Regarding the AR counts in Europe (see Figure 6.9), the *TNA links* are significantly positive in Morocco and southern Iberia during the OND season. During JFM and ONDJFM, however, these links are weaker and significant only in Morocco. The *WHWP links* closely resemble those of the TNA during the OND season. During JFM and ONDJFM, this similarity vanishes and the WHWP links become insignificant in virtually any case.

The *AMO links* describe a clear correlation dipole with positive  $rs$  in the north

and negative  $rs$  in the south. However, this dipole is bound to the OND season only, and only the link in Morocco is consistently significant irrespective of the applied reanalysis and percentile combinations. Regarding the *PDO links*, such consistent results are only found in northern Iberia and western France during the ONDJFM season, in which case these links are significantly positive. The AMO and PDO links are both generally stronger during OND than during JFM.

The AR counts along the *west coast of North America* are generally more closely related to the PDO than to any of the two ENSO indices (see Figure 6.9). During ONDFJM season, the *PDO link* in the southern and northern Gulf of Alaska is significantly positive irrespective of the applied reanalysis<sup>7</sup> and percentile threshold combination. During JFM, significant links are additionally obtained in British Columbia whereas the link in the northern Gulf of Alaska drops to partly insignificant values. During the OND season, the stronger links move to the north, i.e. consistently significant positive  $rs$  are obtained only in the northern Gulf of Alaska whereas the links in the southern Gulf of Alaska drop to insignificance for some reanalyses and percentile threshold combinations.

The *IPO links* are similar to those found for the PDO in what concerns the spatial patterns. The magnitude of these links, however, is systematically weaker. The *NPGO links* are generally insignificant, except in NorthCal-OR-WA during JFM, when significantly negative relationships are found for some percentile combinations irrespective of the considered reanalysis.

---

<sup>7</sup>recall that ERA-Interim is not considered due to its limited temporal coverage

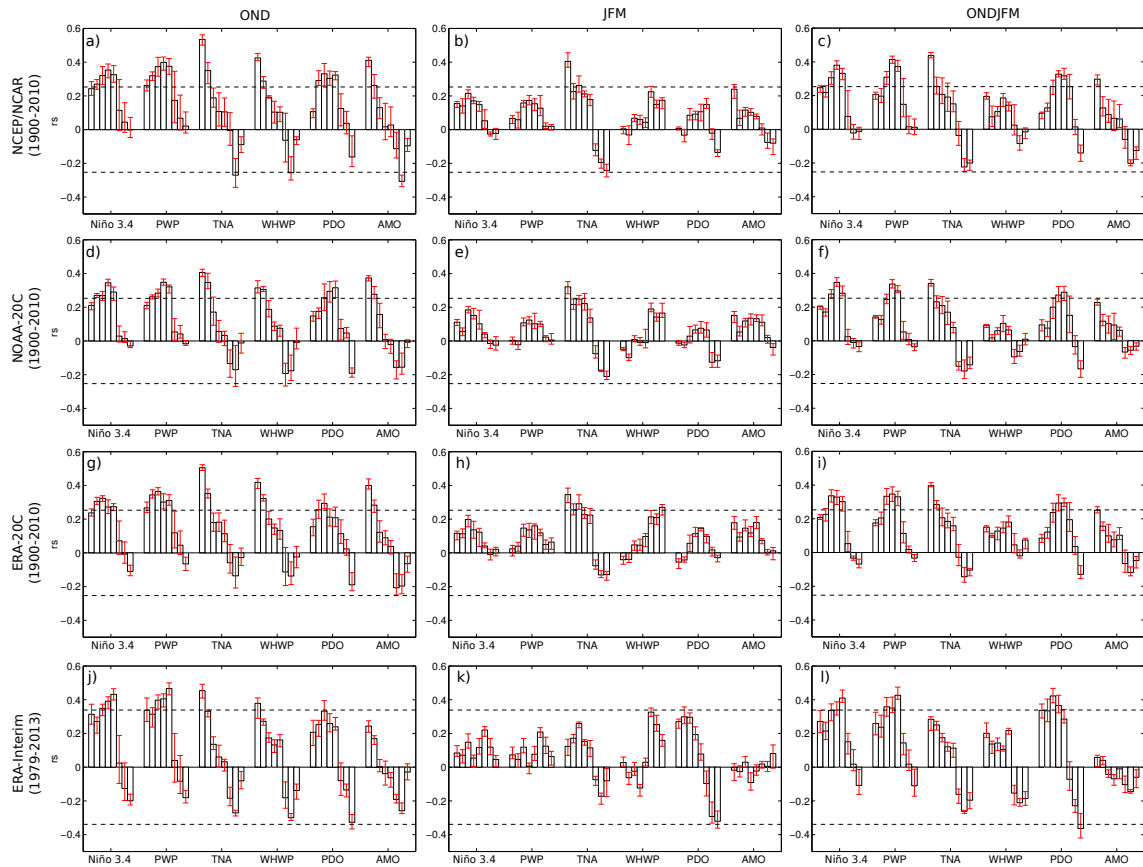


**Figure 6.9:** Rank correlation coefficient ( $r_s$ ) between seasonal AR occurrence counts and different seasonal-mean oceanic indices for the eight considered target regions in Europe/North Africa ordered from the South to the North, i.e. the first bar or each group of bars refers to Morocco and the last to northern Norway, respectively. Results are for NCEP/NCAR, NOAA-20C, ERA-20C and ERA-Interim (each row corresponds to a dataset) and for OND, JFM and ONDJFM (each column corresponds to a season-definition). Bars and errorbars refer to the mean and range of the 6 results obtained from the 6 considered percentile-threshold combinations, i.e. refer to the method-related uncertainty of the results. Dashed horizontal lines mark the critical values below / above which  $r$  is significant at a test-level of 5%. Results are for 1950-2010 except for ERA-Interim in which case they are for 1979-2013. Source: own illustration

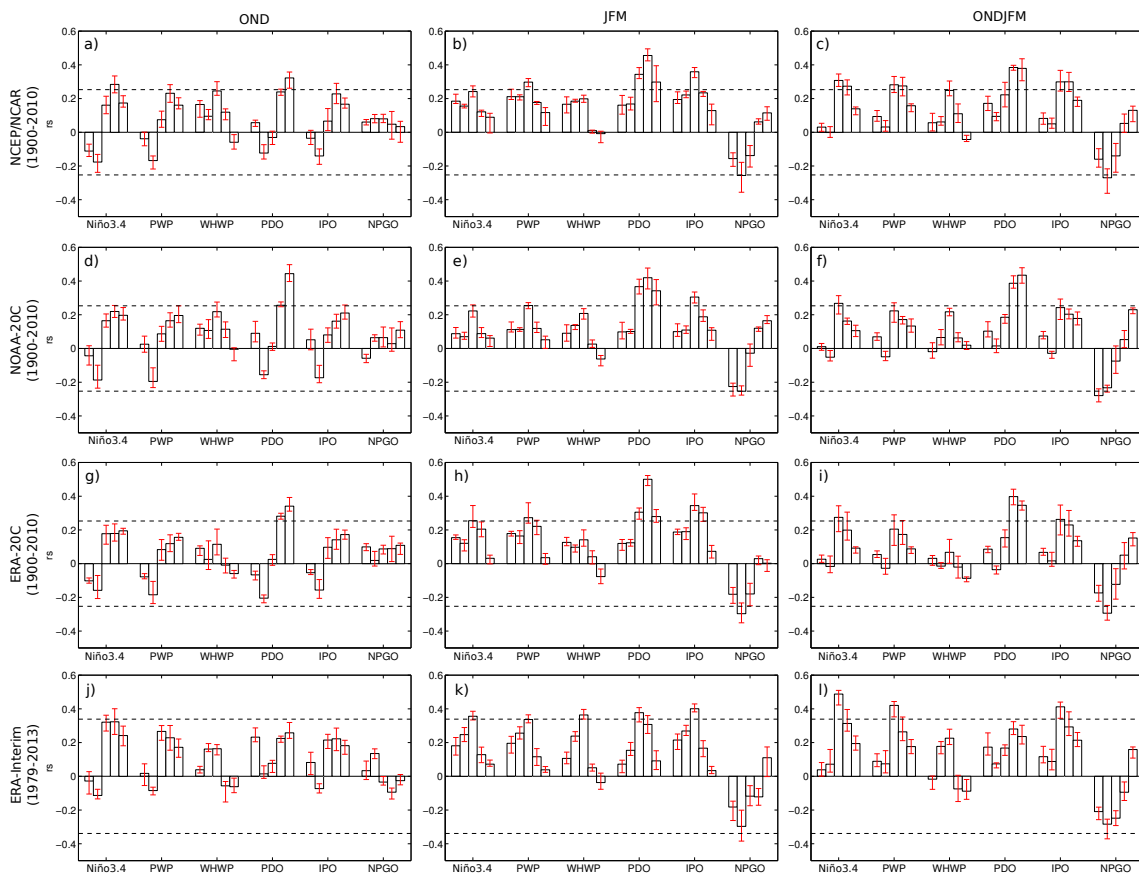


**Figure 6.10:** As Figure 6.9, but for the AR counts along the west coast of North America. Source: own illustration

---

## CHAPTER 7

---

# ENSO Teleconnections in Atmosphere General Circulation Models

In Chapter 6, teleconnections *presumably* exerted by sea surface temperature variations were detected in the observational record and it was pointed out that particularly the teleconnections triggered by ENSO are of interest for long range forecasts. As described in Section 2.5, however, precisely these teleconnections can be modified by internal atmospheric variability and are therefore not deterministic. This chapter focusses on *ENSO teleconnections* to the AR counts in Europe and western North America. After describing the theoretical concepts and a set of statistical tests in Section 7.2, the following three questions will be answered with the help of idealized numerical modelling experiments:

- A Are the teleconnections robust to internal atmospheric variability?
- B Are time variations in the strength of the teleconnections externally forced?
- C Do the teleconnections hold if the prescribed external forcing is limited to SST variations in the Niño 3.4 region only?

To this aim, two distinct model experiment families are used:

1. 13 runs from the Atmospheric Model Intercomparison Project (AMIP, [Gates, 1992](#)) of the Fifth Phase of the Coupled Model Intercomparison Project (CMIP5, [Taylor et al., 2012](#)). These runs are from three distinct Atmosphere General Circulation Models (AGCMs).
2. 10 runs of the Community Atmosphere Model 3.1 (CAM3.1, [Collins et al., 2006](#)), conducted specifically for the purpose of the present thesis.

Question A and B will be answered with the AMIP experiments (see Section 7.1.1) and question C with the CAM3.1 experiments (see Section 7.1.2).

## 7.1 Applied Model Experiments

### 7.1.1 External Experiments from the Atmospheric Model Intercomparison Project

In the present thesis, a total of 13 AMIP experiments from CMIP5 are used (Gates, 1992; Taylor et al., 2012). The 13 experiments are from three distinct AGCMs describing the atmospheric branch of their respective fully-coupled “Earth System Models” (Taylor et al., 2012). The main specifications of these 3 AGCMs are listed in Table 7.1. All experiments were run with the observed monthly SST and sea-ice cover values all around the globe and cover the period 1979-2008<sup>1</sup>, which permits to correlate the *observed* Niño 3.4 index (see Table 3.2) with the *modelled* AR-counts from these experiments. With the exception of one AGCM, the corresponding data were retrieved from the data portals of the Earth System Grid Federation (ESGF, see e.g. <https://pcmdi.llnl.gov/search/cmip5/>), which are the primary providers of CMIP5 data.

The main constraint for choosing the AGCMs for this “ensemble of opportunity” (Tebaldi and Knutti, 2007) was the availability of six-hourly instantaneous data for specific humidity, as well as the zonal and meridional wind components on all vertical model levels from the ESGF portals. From the original sigma/hybrid levels, these three variables were interpolated to the 15 pressure levels of NOAA-20C (see Table 3.5) using the Climate Data Operators (Schulzweida, 2017) and were then further postprocessed as described in Section 3.2.

The six-member ensemble available for Institut Pierre Simon Laplace’s AGCM “Laboratoire de Météorologie Dynamique Zoom 5A” (LMDZA, Hourdin et al., 2013) was found to be the largest AMIP ensemble available from the ESGF data portals meeting the aforementioned data resolution criteria. LMDZ5A is coupled to the ORCHIDEE land surface model and both models are components of the IPSL-CM5A-LR Earth System Model (Dufresne et al., 2013). For the AMIP experiments mentioned above, LMDZ5A was run at a horizontal resolution of 3.75° in longitude and 1.875° in latitude. With 39 vertical levels, among which 15 are above 20 km, and a model top at 0.04 hPa<sup>2</sup>, it is considered a “high-top” model (Dufresne et al., 2013; Charlton-Perez et al., 2013).

The Canadian Fourth Generation Atmospheric Global Climate Model (CanAM4, von Salzen et al., 2013) is an independent AGCM developed by the Canadian Centre for Climate Modelling and Analysis (CCCma) and belongs to the CanESM2 Earth System Model. For the AMIP experiments in CMIP5, CanAM4 was run at a

<sup>1</sup>Some experiments were run from 1979 to 2009 and one from 1950 to 2009.

<sup>2</sup>i.e. reaching well into the mesosphere

**Table 7.1:** Considered AGCM ensembles from the AMIP experiments conducted within CMIP5, and the Earth System Models (ESMs) they belong to. Note that in the forthcoming, the more commonly used ESM acronym will be used to refer to these models.

ESM	AGCM	Resolution (lat × lon)	Nr. of vertical levels	Reference	Nr. of runs
IPSL-CM5A-LR	LMDZ5A	$3.75^\circ \times 1.875^\circ$	39	<a href="#">Hourdin et al. (2013)</a>	6
CanESM2	CanAM4	$2.8^\circ \times 2.8^\circ$	35	<a href="#">von Salzen et al. (2013)</a>	4
NorESM1-M	CAM4-Oslo	$2.5^\circ \times 1.875^\circ$	26	<a href="#">Bentsen et al. (2013)</a>	3

horizontal resolution of  $2.8^\circ$  in longitude and  $2.8^\circ$  in latitude. With 35 vertical levels and a model top at 0.5 hPa (i.e. near the stratopause), CanAM4 is a “mid-top” model ([Charlton-Perez et al., 2013](#)). For this AGCM, only one out of four AMIP runs was available from the ESGF data portals and this is why the four runs were directly retrieved from CCCma, with kind permission of Dr. Viatcheslav Kharin (personal communication).

The “Oslo” version of the Community Atmosphere Model version 4 (CAM4-Oslo, [Kirkevåg et al., 2013](#)) is the atmospheric component of the Norwegian Earth System Model NorESM1-M ([Bentsen et al., 2013](#)). It comprises parametrization schemes for the interaction between atmospheric chemistry, aerosols, clouds and radiation that have been developed in Norway and differ from the schemes used in the original version of the model (CAM4, [Neale et al., 2013](#)). With respect to the remaining parameters describing the model physics, CAM-Oslo uses the standard CAM4 configuration. For the AMIP experiments conducted within the framework of CMIP5, CAM-Oslo was run at a horizontal resolution of  $2.5^\circ$  in longitude and  $1.875^\circ$  in latitude, and with 26 levels in the vertical. With a model top is at 2.917 hPa, it is considered a “low-top” model ([Charlton-Perez et al., 2013](#)). For CAM4-Oslo, three AMIP experiments were available from the ESGF portals.

In the context of the present thesis, not only the horizontal, but also the vertical resolution of the AGCMs matters to correctly reproduce the tropospheric and stratospheric pathways of ENSO teleconnections ([Butler et al., 2014](#)). High-top models such as IPSL-CM5A-LR, more so than low-top models such as CAM-Oslo, more accurately reproduce the two-way coupling between the troposphere and stratosphere, and also the number of sudden stratospheric warmings ([Charlton-Perez et al., 2013](#)). Both factors are known to favour the stratospheric pathway of ENSO teleconnections to the extratropics ([Butler et al., 2014](#)).

In the forthcoming, the AGCMs will be referred to by using the more commonly used acronyms of their respective *ESMs* (see Table 7.1). Subsequent analyses involving these AMIP experiments will be conducted for the 1979-2008 period, common to all experiments.

### 7.1.2 Home-Made Experiments with the Community Atmosphere Model

In the framework of the present thesis, the Community Atmosphere Model version 3.1 (CAM3.1, Collins et al., 2006), coupled to the Community Land Model version 2.1 (Bonan et al., 2002), was run in standalone mode with prescribed SSTs and sea-ice cover from the HadISST dataset (Rayner et al., 2003). The source code was downloaded from <http://www.cesm.ucar.edu/models/atm-cam/download/> and the model was compiled on the high performance cluster of the Santander Meteorology Group ([www.meteo.unican.es](http://www.meteo.unican.es)), using Eulerian dynamics, a horizontal resolution of  $\approx 1.41^\circ \times 1.41^\circ$  (T85 in spectral terms), a time step of 600 seconds and 26 levels in the vertical. This configuration is equal or superior to the CAM4-Oslo configuration used for the AMIP experiments described above (see Section 7.1.1). CAM3.1 was run in parallel-mode using distributed memory.

The prescribed SSTs are allowed to vary in the tropical Pacific only. The monthly climatological mean value is set for the SSTs in all other regions, as well as for sea-ice cover, greenhouse gases and all other external forcing agents considered by the model (Hoerling et al., 2001). This experimental setup ensures that the modelled ENSO teleconnections cannot be perturbed neither by SST forcing from regions outside the tropical Pacific nor by other external forcing agents. In comparison with the AMIP forcing, this setup on the one hand allows to filter out the role of tropical Pacific SSTs, but on the other hand is less realistic because the external forcing in the real world is of global nature and cannot be confined to certain regions and forcing agents.

Similar to Hoerling et al. (2001), the spatial pattern of SST variations in the tropical Pacific is described by the EOF corresponding to the Pacific Warm Pool described in Section 3.1. Since the magnitude of the EOF loadings (i.e. the individual elements of the eigenvector) decreases gradually towards the subtropics, this SST-forcing pattern has no abrupt and unrealistic gradients (see Figure 7.1). For each SST-forcing scenario, the EOF loadings are multiplied by a constant so that the maximum of the resulting products (located near the equator) yields the following SST anomalies with respect to the 1951-2000 monthly mean value:

$$F = \{-2.6, -2.4, \dots, +3.6^\circ\text{C}\} \quad (7.1)$$

, where  $F$  is a vector ranging between  $-2.6$  to  $+3.6^\circ\text{C}$  with an interval of  $0.2^\circ\text{C}$  (see Figure 7.1).

Added to the monthly climatological mean pattern, these anomaly patterns are surrogates for an SST-forcing that gradually changes from realistic La Niña to El Niño conditions. For each of these 32 SST forcing scenarios, the model was run ten times from September 01 to December 31, using ten distinct initial conditions corresponding to the data provided with the standard CAM3.1 package *plus* nine additional initial conditions for August 15, September 01 and September 15 of the years 1953, 1954 and 1955, respectively. The additional initial conditions were obtained from running the model once for each of the three aforementioned years

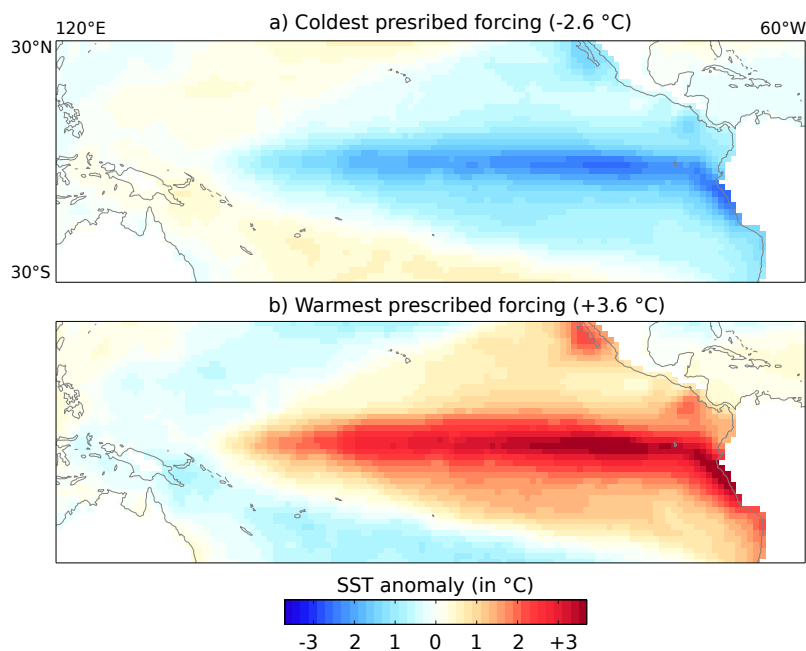


**Figure 7.1:** Pattern and magnitude of the prescribed SST variations used to force the AGCM experiments conducted with CAM3.1. Source: own illustration

from January 01 to September 15. For the statistical analyses conducted here, the 15 to 46 days prior to October 1st are not considered since the model needs to adjust to equilibrium during the first two weeks of the integration in what is commonly referred to as the “spin-up”.

All in all, CAM3.1 was executed for 320 OND seasons (32 forcing scenarios  $\times$  10 initial conditions). The 32 simulated OND seasons pertaining to a given initial condition are hereafter to as “model run” or simply “run”. The aforementioned SST forcing strategy will hereafter also simply be referred to as the “filtered” forcing, as opposed to the “global” forcing of the AMIP experiments.

## 7.2 Methods

Under the assumption that AGCM experiments provide realistic estimates of the the atmosphere’s response to the observed external forcing in a given period, each experiment can be seen as a surrogate of how the atmosphere might have developed if it would have been allowed to “re-run” many times (up to 13 times in the present thesis) with that forcing (von Storch et al., 2004). This approach explicitly takes into account that the above response is probabilistic, as is the climate system in general (Lorenz, 1963).

In this framework, a specific teleconnection —as e.g. described by the rank correlation coefficient between the *observed* Niño 3.4 index and the *modelled* AR-counts in a specific region— can be calculated  $m$  times, where  $m$  is the available

number of AGCM runs. Thereby, a “pseudo-empirical” (von Storch et al., 2004)<sup>3</sup> sample of  $m$  correlation coefficients is obtained whose dispersion is an estimator for variations in the strength (and sometimes also the sign) of the teleconnection caused by internal atmospheric variability. Note that the *observed* AR-count response will be optionally added to the  $m$  modelled responses as defined above if the reanalysis data used to derive these counts can be assumed to be reliable (see Chapter 5). Otherwise, it is preferable to work with AGCM output only (see Chapter 8).

### 7.2.1 Internal Atmospheric Variability Estimate

Assuming that the pseudo-empirical sample of  $m$  correlation coefficients follows a cumulative Student t-distribution with  $m - 1$  degrees of freedom, the two z-scores corresponding to a probability of 2.5 and 97.5%<sup>4</sup> are transformed to correlation units using the mean ( $\mu$ ) and standard deviation ( $\sigma$ ) of the above sample,

$$r_{lower} = -z \times \sigma + \mu \quad (7.2)$$

$$r_{upper} = +z \times \sigma + \mu \quad (7.3)$$

and represent the lower and upper bounds ( $r_{lower}$  and  $r_{upper}$ ) of the 95% confidence interval for variations in the teleconnection caused by internal atmospheric variability. If both bounds are either smaller than the critical value for a significantly negative correlation (indicating an inverse ENSO-predictand relationship) or larger than the critical value for a significantly positive one (indicating a positive relationship), then the corresponding teleconnection is said to be “robust” (in the sense of “robustly significant”), meaning that its sensitivity to internal atmospheric variability is negligible. Otherwise, the teleconnection is said to be “not robust” to this kind of variability. The critical values are obtained from a two-tailed t-test, optionally corrected for the effect of serial correlation (see Equation 6.1 in Section 6.2.1). This correction will be applied when the serial correlation in the year-to-year time series applied here is a clear practical rather than theoretical problem (Brands et al., 2014; Guemas et al., 2014), i.e. only in case predictands in the tropics are considered (see Chapter 8).

As the forcing exerted by SST variations associated with ENSO propagates through the atmosphere, it is not only perturbed by internal/unforced atmospheric variability alone but also by atmospheric variability originating from other external forcing agents. By design of the setup followed in the AMIP experiments, these are SSTs in other regions (i.e. not associated with ENSO) and sea-ice cover (Gates, 1992). For the case of ERA-20CM (see Chapter 8), additional time-varying forcing agents comprising greenhouse gases, ozone, aerosols and solar activity were included

<sup>3</sup>“pseudo” because surrogates for the real world are taken from numerical model experiments

<sup>4</sup>e.g.  $z = \pm 2.262$  for  $m - 1 = 9$  in case of the ten-member ensemble of run with CAM3.1, see Section 7.1.2

(Hersbach et al., 2015). Since these setups do not allow to completely filter out the effect of SST variations in the Niño 3.4 region, additional experiments were conducted with CAM3.1 (Collins et al., 2006). In this case, the prescribed SSTs are allowed to vary in the tropical Pacific only and all other external forcing agents are set constant (see Section 7.1.2). This is done to assess whether ENSO-related SST variations are indeed causal to the development of a given teleconnection. However, since external forcing agents unrelated to ENSO cannot be “turned off” in the real world, the more complete the list of external forcing agents considered in the experiment, the higher the realism of the internal atmospheric variability estimates obtained here and, thus, the greater the statistical power (Wilks, 2006) of the robustness test described above. From this point of view, the results drawn from the AMIP and ERA-20CM experiments should be expected to be in closer agreement with the real world than those obtained from the CAM3.1 experiments.

For the sake of simplicity, both, unforced atmospheric variability and atmospheric variability originating from external forcing agents others than SST variations related to ENSO will be hereafter jointly referred to as “internal atmospheric variability”.

### 7.2.2 Model-Performance and Nonstationarity Attribution Tests

If the confidence interval for variations in the correlation coefficient is obtained from the model runs only, i.e. if the observed value is left out when fitting the t-distribution, the following “model-performance test” (Giorgi and Francisco, 2000; Brands et al., 2011) can be formulated. If the cumulative probability of the observed correlation within this t-distribution is smaller than 2.5% or larger than 97.5%, i.e. lies beyond the limit of the 95% confidence interval, then the teleconnection’s strength seen in observations significantly differs from the modelled one, meaning that the perfect model assumption does likely not hold. On the other hand, the perfect model assumption likely holds if the observed correlation lies within the aforementioned probability limits. Note that for this test to work, both the modelled and observed correlations must be calculated for the *same* period (here: 1979-2008, the “recent past”).

Apart from asking whether the AGCM experiments are reliable or not, once they pass the performance test, they can be used to test whether the particularly strong teleconnections found in observations during specific periods of the *mid* and *early* twentieth-century (see Section 6.2) can be explained by the internal atmospheric variability of the period for which the model output is available (here: 1979-2008). To this aim, a second cumulative t-distribution is fitted to the  $m$  modelled correlations *plus* the observed value for 1979-2008, i.e. to a total of  $m + 1$  values describing variations in the AR-response that are attributed to the internal atmospheric variability of the recent past. Analogous to the above described model performance test, the strength of a teleconnection in a given early period significantly differs from the strength in the recent past if the observed correlation in the early period lies outside the 95% confidence interval obtained from the second fit. In this

case, the teleconnection’s strength in the early period cannot be explained by the internal variability of the recent past, and this points to the fact that changes in the external forcing are needed to explain the strength differences<sup>5</sup> found in observations. This test will hereafter be referred to as the “nonstationarity attribution test”.

### 7.3 Results

#### 7.3.1 Results from the Atmospheric Model Intercomparison Project

Figure 7.2 shows the statistical relationships between the *observed* Niño 3.4 index and the European AR-counts from both observations and AMIP experiments for JFM season in this case. Each panel refers to one percentile threshold combination as defined in Table 4.1 and the target regions numbered along the x-axes are ordered from the south to the north (see Figure 2.7). As above, the strength and sign of the relationship is represented by  $rs$ . Relationships for the observed AR-counts during the recent past (obtained from ERA-20C in this case) are depicted by green dots and are compared to the relationships for the modelled AR-counts drawn from the 13 AMIP experiments run over the same period. Each of the three considered AGCMs is represented by a specific colour. Yellow is assigned to IPSL-CM5A-LR, red to CanESM2, and white to NorESM1-M. Circles refer to the individual members of a given model and squares to the results for the year-to-year AR response averaged over all members of that model. The year-to-year AR response averaged over all the 13 model runs (hereafter: the “multi-model-mean”) is represented by magenta squares. At this point it is important to recall that the predictor variable is the *observed* Niño 3.4 index in any case, i.e. SST variations are *not* internally modelled, as would be the case for the fully coupled Earth System Models used in CMIP5 (see e.g. Brands et al., 2013), but prescribed using observed values.

The 95% confidence interval (CI) for variations in  $rs$  due to internal atmospheric variability in the recent past, *as simulated by the models only* (hereafter: “*modelled* CI”), is represented by dark grey bars and was obtained from fitting the t-distribution to the 13 modelled  $rs$  (hereafter: “*modelled* t-distribution”). If the observed teleconnection during the same period (1979-2008, depicted by a green dot) lies outside the modelled CI, then it significantly differs from the modelled teleconnections meaning that the perfect model assumption does likely not hold. On the other hand, if the green dot lies within these limits, this assumption likely holds. The upper row of numbers at the bottom of each panel refers to the cumulative probability of the observed  $rs$  within the modelled t-distribution. If this value is smaller than 2.5% or larger than 97.5%, then the perfect model assumption is rejected at a test-level of 5% and the number is printed in red.

The modelled CI considerably vary in magnitude and sign and are insignificant in most cases. The large spread is particularly evident for the AR counts in over the

---

<sup>5</sup>or nonstationarities

British Isles and southern Norway (regions 6 and 7), in which case the modelled CI ranges from significantly negative to significantly positive. Due to this large spread, the observed  $rs$  for the recent past never differ significantly from the modelled CI<sup>6</sup>, which gives confidence in the models' capability to correctly reproduce the observed teleconnections, or, since  $rs$  is mostly insignificant, the lack of relationship.

The CI obtained from fitting the t-distribution to the 13 modelled  $rs$  values *plus* the observed one or the recent past (hereafter: “full CI” and “full t-distribution”), is depicted by light grey bars. It describes variations in  $rs$  caused by the effects of internal atmospheric variability in the recent past and constitutes the *null distribution* (Wilks, 2006) of the attribution test described in Section 7.2.2. The corresponding *test statistic* is the *observed*  $rs$  for the period 1919-48, during which particularly strong ENSO teleconnections were found in Section 6.2.1). This value will hereafter be referred to as the “early-period”  $rs$ .

Remarkably, the strongly positive early period  $rs$  found in Morocco to western France, as well as the weaker, yet significant, negative link found in northern Norway *significantly differ* from the  $rs$  of the recent past. Consequently, changes in the external forcing likely play a role to explain these differences. Note that in this case the cumulative probability of the early period  $rs$  within full t-distribution is printed in red (see lower numbers at the bottom of each panel)

Apart from this, although the observed  $rs$  values for the recent past are insignificant in most cases, the CIs tend to be positive in southern Europe and negative in northern Europe, i.e. describe a correlation dipole.

The respective results for the OND season are shown in Figure 7.3. As was the case for JFM, the CIs for the recent past are broad and the perfect model assumption cannot be rejected in any single case. The early period  $rs$  do not significantly differ from the  $rs$  of the recent in most cases, indicating that the nonstationarities seen in observations are likely caused by internal atmospheric variability. Northern Norway is the only region where significant differences are found, pointing to the fact that external forcing must play a role to explain the nonstationarities there. From Morocco to western France, the  $rs$  values tend to be stronger for the ensemble-mean AR counts than for those obtained from individual members (compare squares with dots for a given model/colour), and this holds particularly true for the multi-model-mean AR counts (see magenta squares, also indicated with a black arrow in Figure 7.2f). Actually, relationships for the multi-model-mean AR counts are significant ( $\alpha = 0.05$ ) in more regions than this is case for observed relationships; namely in the three Iberian regions and western France. In the three northern regions (British Isles to northern Norway), in turn, relationships are not systematically stronger for the ensemble mean AR counts than for the counts from individual members and, in agreement with the observed value, are generally insignificant ( $\alpha = 0.05$ ).

Results for the ONDJFM season (see Figure 7.4) generally lie “in between” those obtained for OND and JFM. Significantly differing early period  $rs$  (as defined above)

<sup>6</sup>see first row of numbers at the bottom of the panels

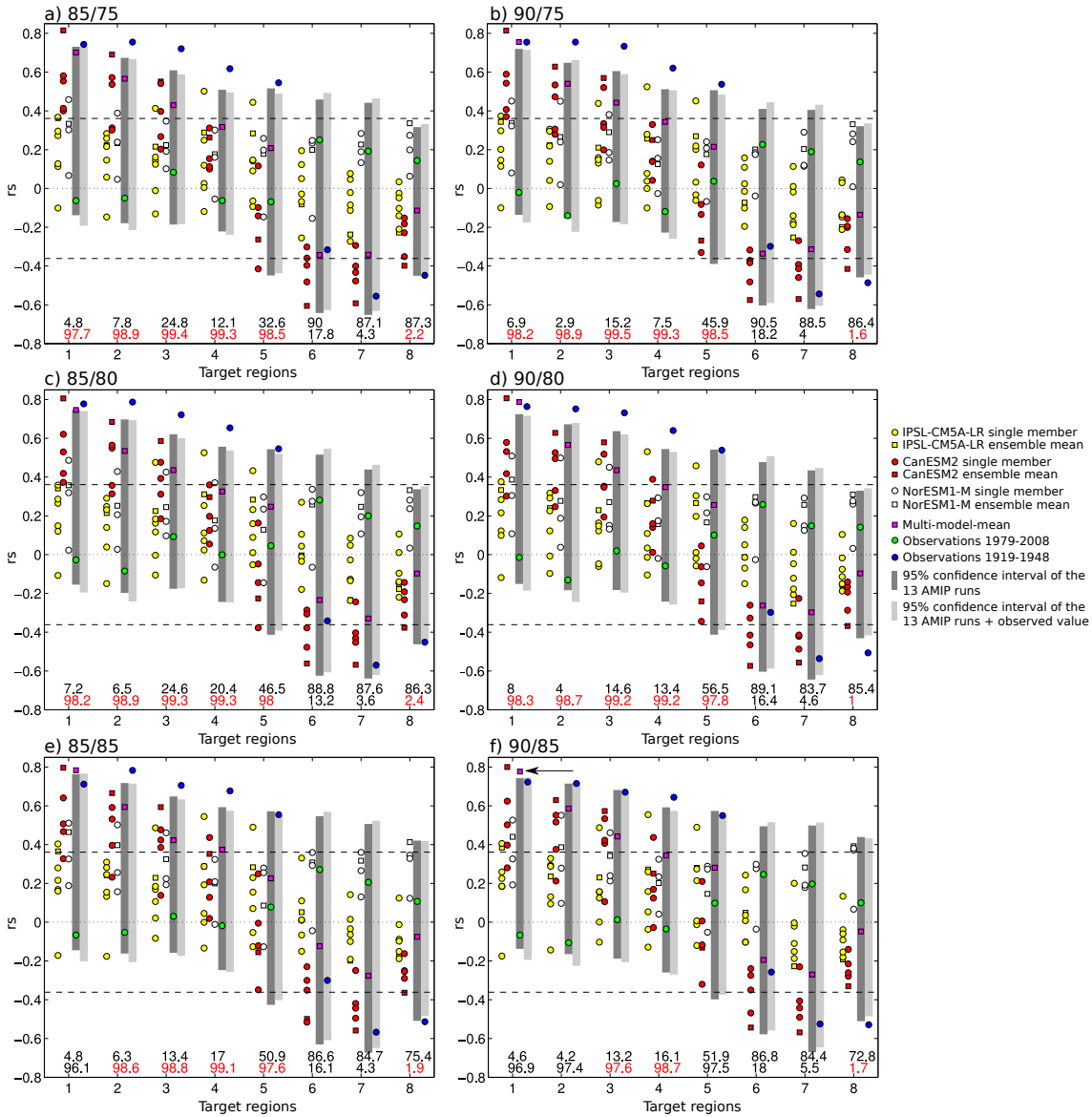


**Figure 7.2:** Robustness of the interannual Niño 3.4 - AR count relationships to internal atmospheric variability, expressed by variations in  $r_s$ . Dashed lines = critical values for  $\alpha = 0.05$ . Yellow = IPSL-CM5A-LR, red = CanESM2, white = NorESM1-M. Circles =  $r_s$  from the interannual AR counts of individual members. Squares =  $r_s$  from the counts *averaged* yearly over all members of a given model. Magenta squares and black arrow = multi-model-mean average over all 13 model experiments. All model responses are for 1979-2008. Green circles = observed  $r_s$  for the same period. Dark grey bars = 95% confidence intervals obtained from the 13 modelled  $r_s$  only. Light grey bars = dito, but for including the observed  $r_s$  of the same period. Dark blue circles = observed  $r_s$  for the 1919-1948 period. Upper numbers at the bottom of the panels = cumulative probabilities for the observed  $r_s$  of the 1979-2008 period within the *modelled* t-distribution for that period. Lower numbers = probabilities of the observed  $r_s$  of the 1919-1948 period within the *full* t-distribution for 1979-2008, see text for more details. Values < 2.5% or > 97.5% are printed in red. Results are for the *JFM* season and the AR counts in *Europe*. Source: own illustration

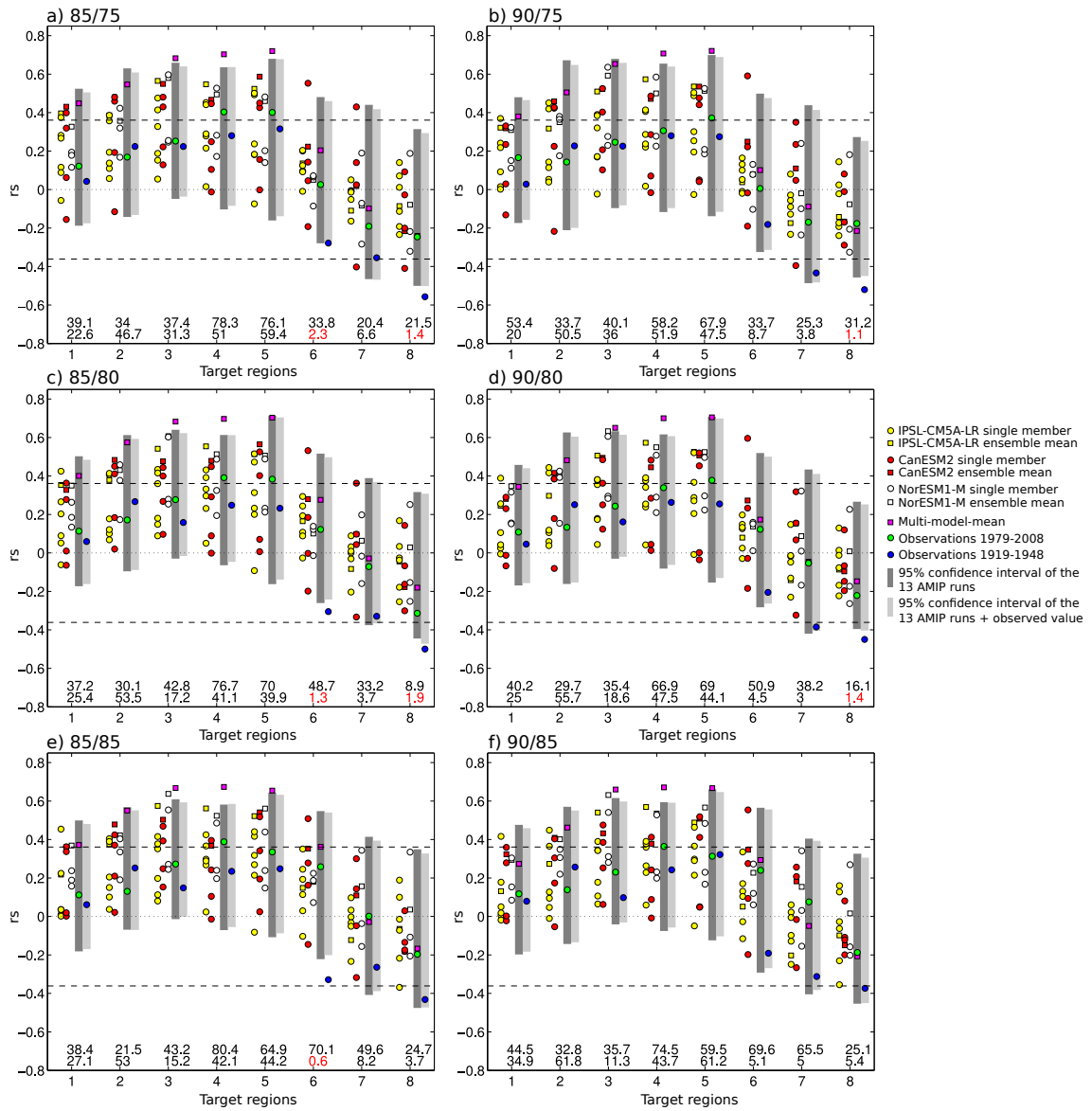


Figure 7.3: As Figure 7.2, but for the OND season. Source: own illustration

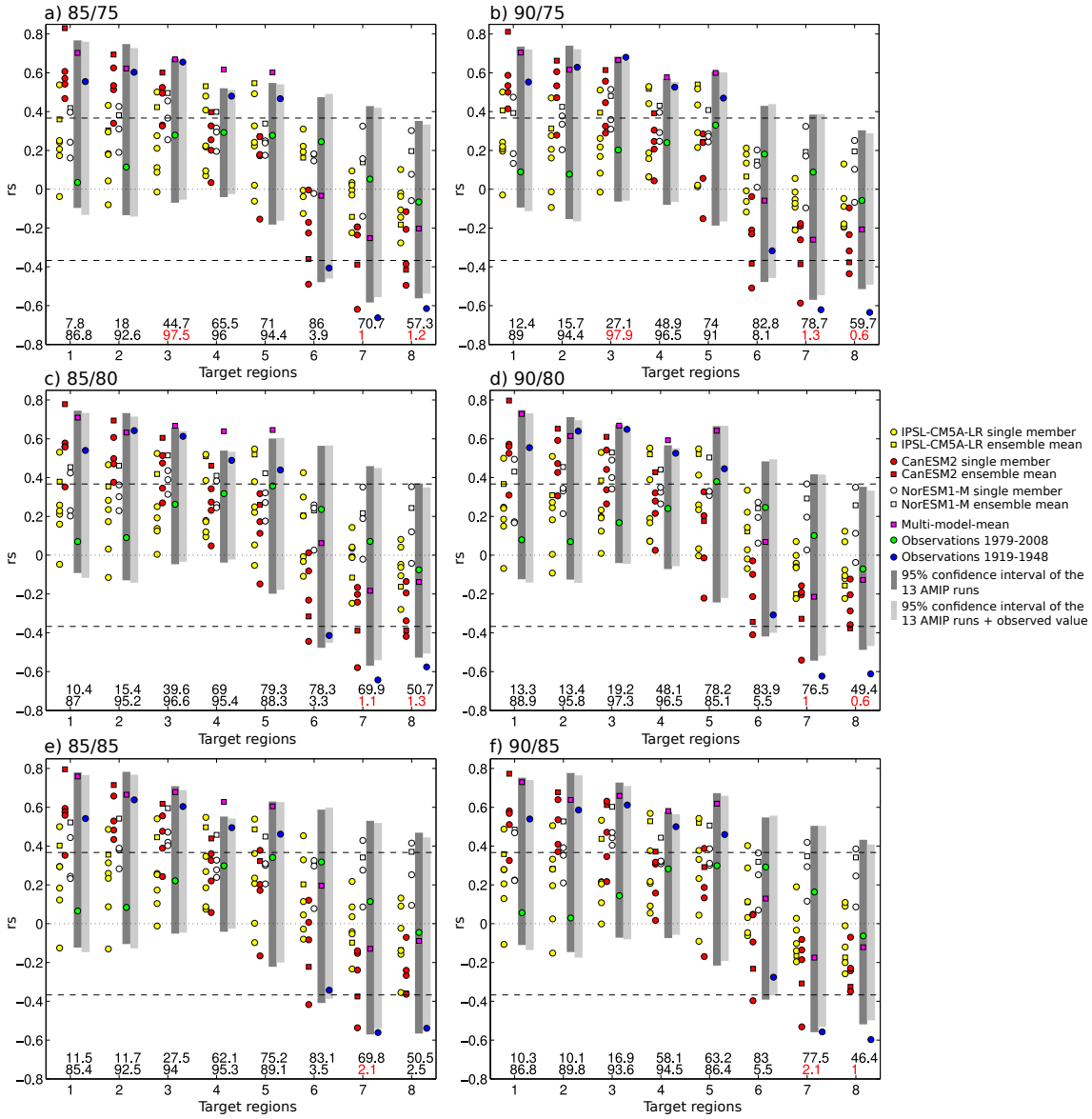


Figure 7.4: As Figure 7.3, but for the *ONDJFM* season. Source: own illustration

are found in northern and southern Norway, but not in the five southern regions.

The results for the west coast of North America are shown in Figures 7.5, 7.6 and 7.7. Apart from the results for the AR counts in the five individual target regions, ordered from the south to the north (see Figure 2.7), the counts in southern California were added to those in northern California-Oregon-Washington (target region 1+2) and the counts in British Columbia were added to those in the southern Gulf of Alaska (target region 3+4). All in all, 7 target regions are considered for this continent (see the x-axes). The two larger target regions are added to assess whether a broadening of the spatial scale alters the results<sup>7</sup>. To take into account that the Great Pacific Climate Shift in 1976/77 (e.g. Mantua et al., 1997) might have modulated the strength of the teleconnections to these regions, the “early” season has been redefined to cover the 1946-1976 time period. The definition of the “recent past” remains unchanged, i.e. refers to the post-shift period 1979-2008.

In comparison with the results for Europe, the modelled CIs are generally narrower in western North America, meaning that the model performance and attribution tests have more statistical power.

During the JFM season (see Figure 7.6) the observed  $rs$  in the recent past (green dots) are significant in NorthCal-OR-WA and the British Columbia. In spite of the aforementioned increase in statistical power, the “perfect model assumption” cannot be rejected ( $\alpha = 0.05$ ) in virtually any case (40 out of 42). The tendency for stronger teleconnections in the multi-model-mean (magenta squares) is clearly evident in British Columbia only. At the spatial scale of single regions (1-5), the pre-shift  $rs$  does not significantly differ from the post-shift value in any case. However, significant results are obtained 1) if the scale of the analysis is widened, i.e. if the counts in British Columbia *and* the southern Gulf of Alaska are joined together (see target region 3+4), or 2) if the test-level is relaxed to 10%, in which case significant results are obtained in each of the two aforementioned individual regions—at least for some percentile threshold combinations. In these few cases, changes in external forcing as e.g. exerted by the Pacific Decadal Oscillation (Gershunov and Barnett, 1998) are needed to explain the  $rs$  values prior to the shift. Generally, however, they are not.

In many aspects, the results for the OND season are similar to those obtained in JFM (compare Figures 7.5 and 7.6). Differences are found in observed  $rs$  for the recent past (green dots), becoming insignificant in NorthCal-OR-WA and significant in the southern Gulf of Alaska (for most percentile threshold combinations). Likewise, the pre-shift  $rs$  does not significantly differ from the post-shift  $rs$  in any case, i.e. even if the target regions are joined or the test-level is relaxed.

During the ONDJFM season (see Figure 7.7), the model performance test is not passed in five out of forty-two cases (i.e. 12%), which can be partly explained by the comparatively modelled CIs for this season and the associated increase in statistical power. For the case of target region 3+4, and assuming a test level of 10%, the pre-shift  $rs$  significantly differs from the post shift value for all but one

<sup>7</sup>This was suggested by an anonymous referee of a corresponding study that is currently under revision.

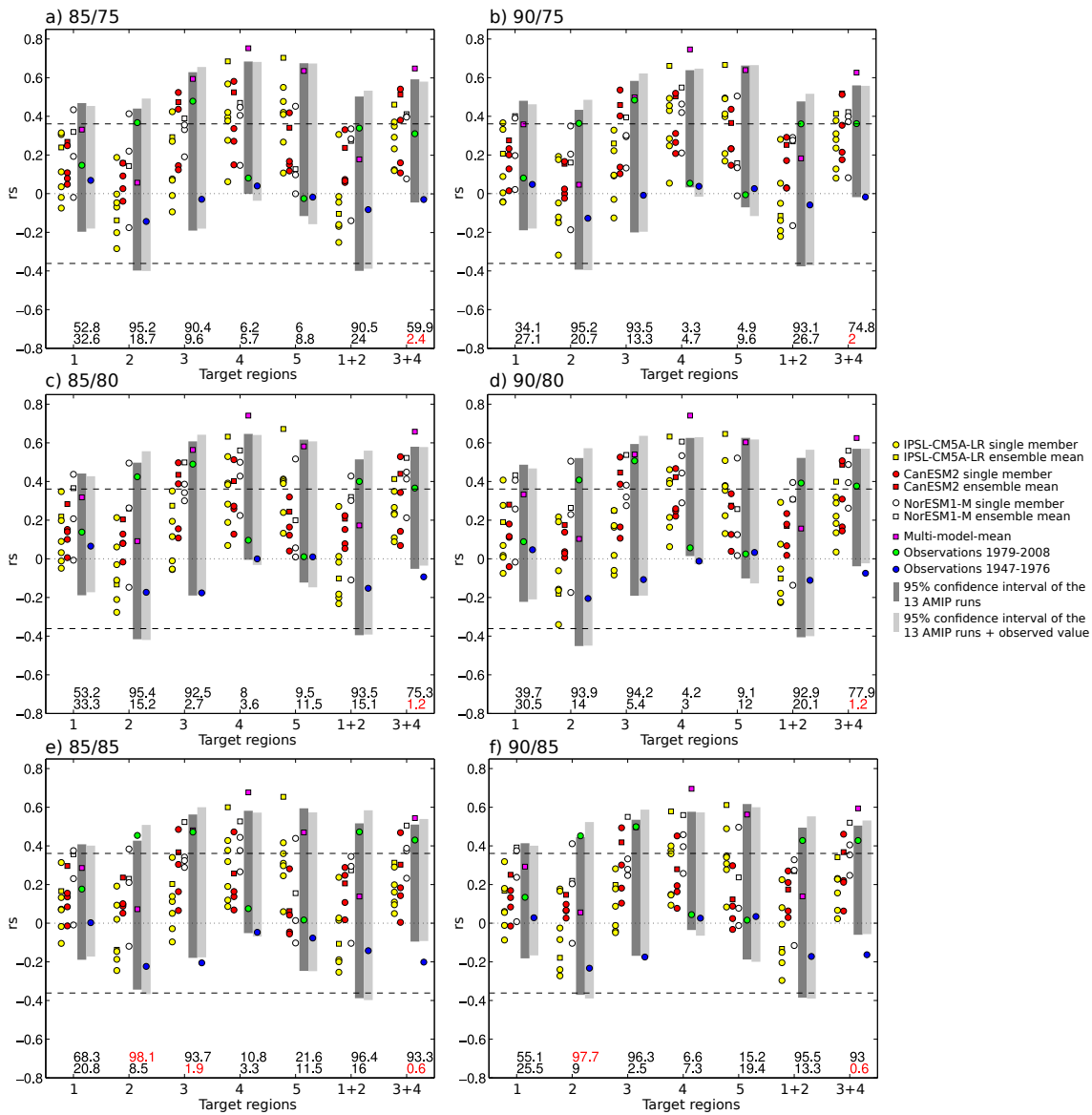


**Figure 7.5:** Robustness of the interannual Niño 3.4 - AR count relationships to internal atmospheric variability, expressed by variations in  $r_s$ . Dashed lines = critical values for  $\alpha = 0.05$ . Yellow = IPSL-CM5A-LR, red = CanESM2, white = NorESM1-M. Circles =  $r_s$  from the interannual AR counts of individual members. Squares =  $r_s$  from the counts *averaged* yearly over all members of a given model. Magenta squares and black arrow = multi-model-mean average over all 13 model experiments. All model responses are for 1979-2008. Green circles = observed  $r_s$  for the same period. Dark grey bars = 95% confidence intervals obtained from the 13 modelled  $r_s$  only. Light grey bars = ditto, but for including the observed  $r_s$  of the same period. Dark blue circles = observed  $r_s$  for the 1947-1976 period. Upper numbers at the bottom of the panels = cumulative probabilities for the observed  $r_s$  of the 1979-2008 period within the *modelled* t-distribution for that period. Lower numbers = probabilities of the observed  $r_s$  of the 1919-1948 period within the *full* t-distribution for 1979-2008, see text for more details. Values < 2.5% or > 97.5% are printed in red. Results are for the *JFM* season and the AR counts in *western North America*. Source: own illustration

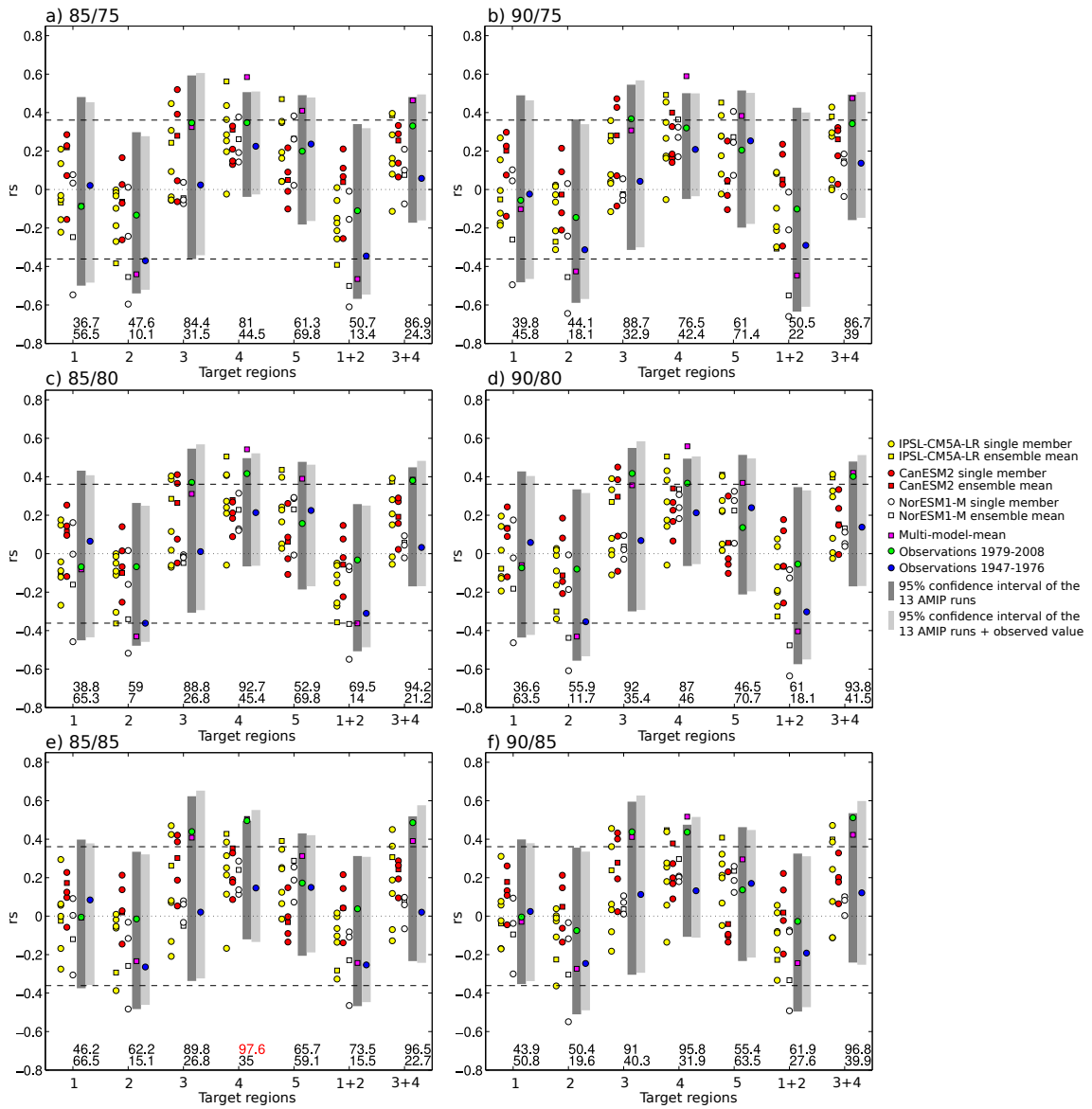


Figure 7.6: As Figure 7.5, but for *OND* season. Source: own illustration

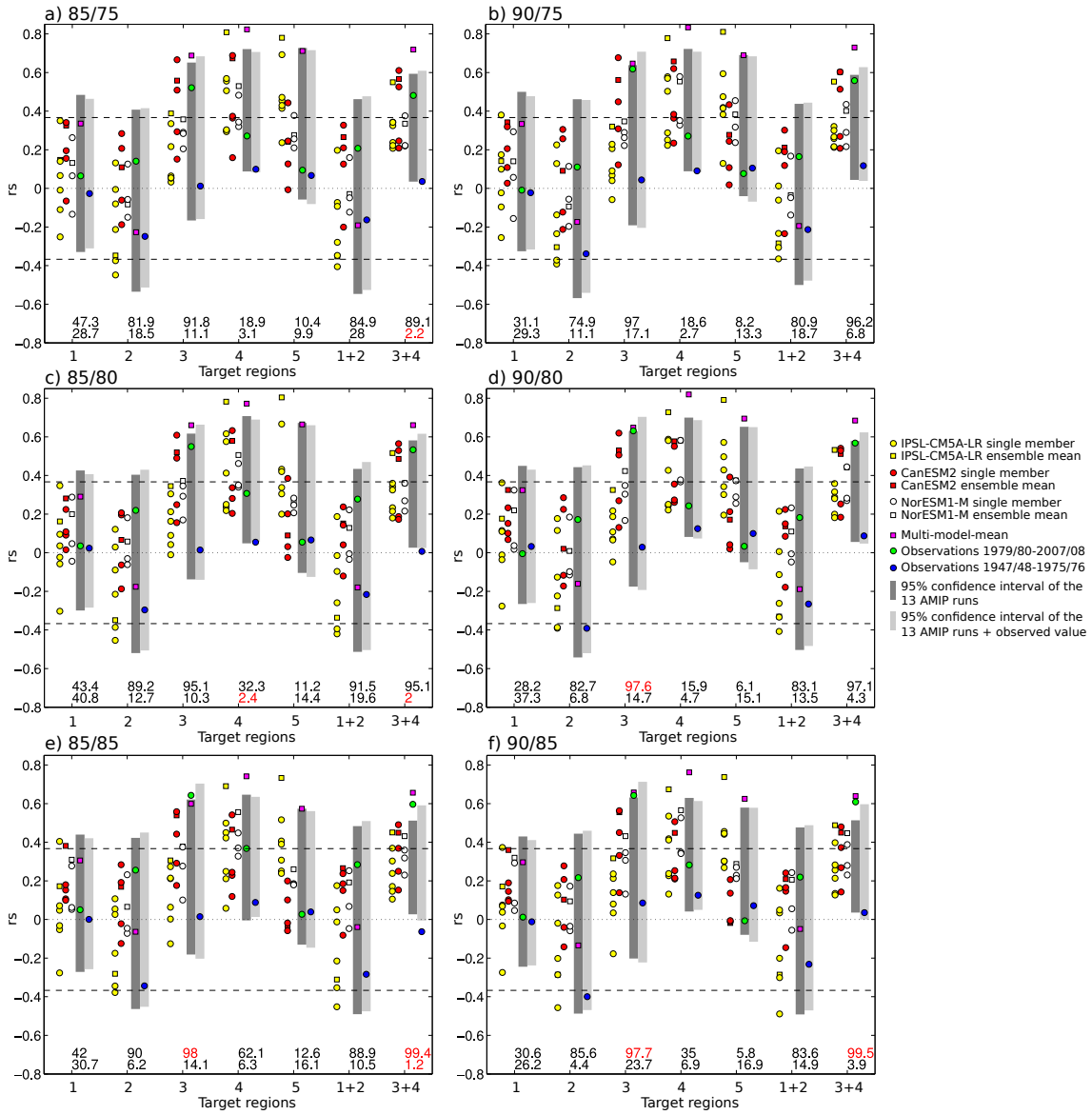


Figure 7.7: As Figure 7.5, but for *ONDJFM* season. Source: own illustration

percentile-threshold combination. In all other cases results are insignificant.

### 7.3.2 Results from the Community Atmosphere Model

This section asks whether ENSO teleconnections to the regional AR-counts considered here also develop in the model world if the prescribed external forcing is limited to SST variations in the tropical Pacific only. To this aim, a large number of idealized numerical modelling experiments was conducted with the Community Atmosphere Model version 3.1 at a relatively high spatio-temporal resolution (see Section 7.1.2). Due to the massive computation and storage capacities needed for such an effort, only the OND season and the AR counts in Europe are considered.

Figure 7.8 shows the modelled AR count response to SST forcing in the tropical Pacific as defined in Equation 7.1 in terms of the  $rs$ . As in Section 7.3.1, results for the AR-counts from individual members of the ensemble are indicated by *circles* and those for the AR-counts averaged over all members by *squares* (both are coloured red since there is only one model in this case). In this case, the modelled t-distribution is fit to the ten  $rs$  values obtained from the ten members and the modelled CI is (see Equations 7.2 and 7.3) is depicted with grey bars. The correlation between the observed PWP index and the observed AR-counts is indicated by a green dots. Since the modelled  $rs$  values stem from 32 model years, i.e. one year for each prescribed SST forcing scenario (see Equation 7.1), the observed  $rs$  is likewise calculated upon 32 years of observations, namely for the 1979-2010 period. Because the pre-1979 period is not considered in this section, the AR-counts from ERA-Interim are used as observations<sup>8</sup>. Note that the idealized SST forcing time series used to run CAM3.1 is not identical to the observed PWP index, meaning that the  $rs$  drawn from observations is not directly comparable to the  $rs$  drawn from the model results. To have a visual reference, the observed  $rs$  is nevertheless displayed, and so is its cumulative probability within the modelled t-distribution (the row of number at the bottom of each row).

Due to the close agreement between the distinct reanalysis datasets (see Chapter 5), and also between the Niño 3.4 and PWP indices (see Section 6.2.2), the teleconnections between the PWP index and the AR counts from ERA-Interim displayed here are very similar to those obtained in Section 6.2.2 (compare green dots in Figure 7.8 with Figure 6.9). In fact, the AR counts in the three southernmost regions (Morocco to western Iberia) are slightly more strongly linked to the PWP index than to the Niño 3.4 index, leading to significant relationships for more percentile-threshold combinations.

In what concerns the modelled relationships, results are similar to the those obtained from the AMIP experiments above (see Section 7.3.1). The ENSO-AR link in the five southern European regions is significantly positive ( $\alpha = 0.05$ ) for the ensemble-mean AR counts but much weaker and mostly insignificant for the

<sup>8</sup>Among the four considered reanalysis datasets, ERA-Interim is assumed to be the most realistic for the post-1979 period

counts from individual members. Also, with  $rs$  values occasionally exceeding +0.8, the ensemble-mean relationships are stronger than the observed ones. This might either reflect that the observed and simulated  $rs$  are not strictly comparable or, alternatively, that other forcing agents than tropical Pacific SSTs weaken the observed link which would be otherwise stronger. Remarkably, a significant inverse link is seen for the ensemble-mean AR counts in northern Europe that is missing in both observations and AMIP experiments. This disagreement might point to the fact that the ENSO-AR link seen in observations and AMIP experiments might have turned out significant if forcing agents unrelated to ENSO would have been “turned off”, which of course is impossible in the real world. Finally, for the “filtered” ENSO-AR links assessed in this section, variations caused by internal atmospheric are largest over the British Isles (see grey bars in Figure 7.8).

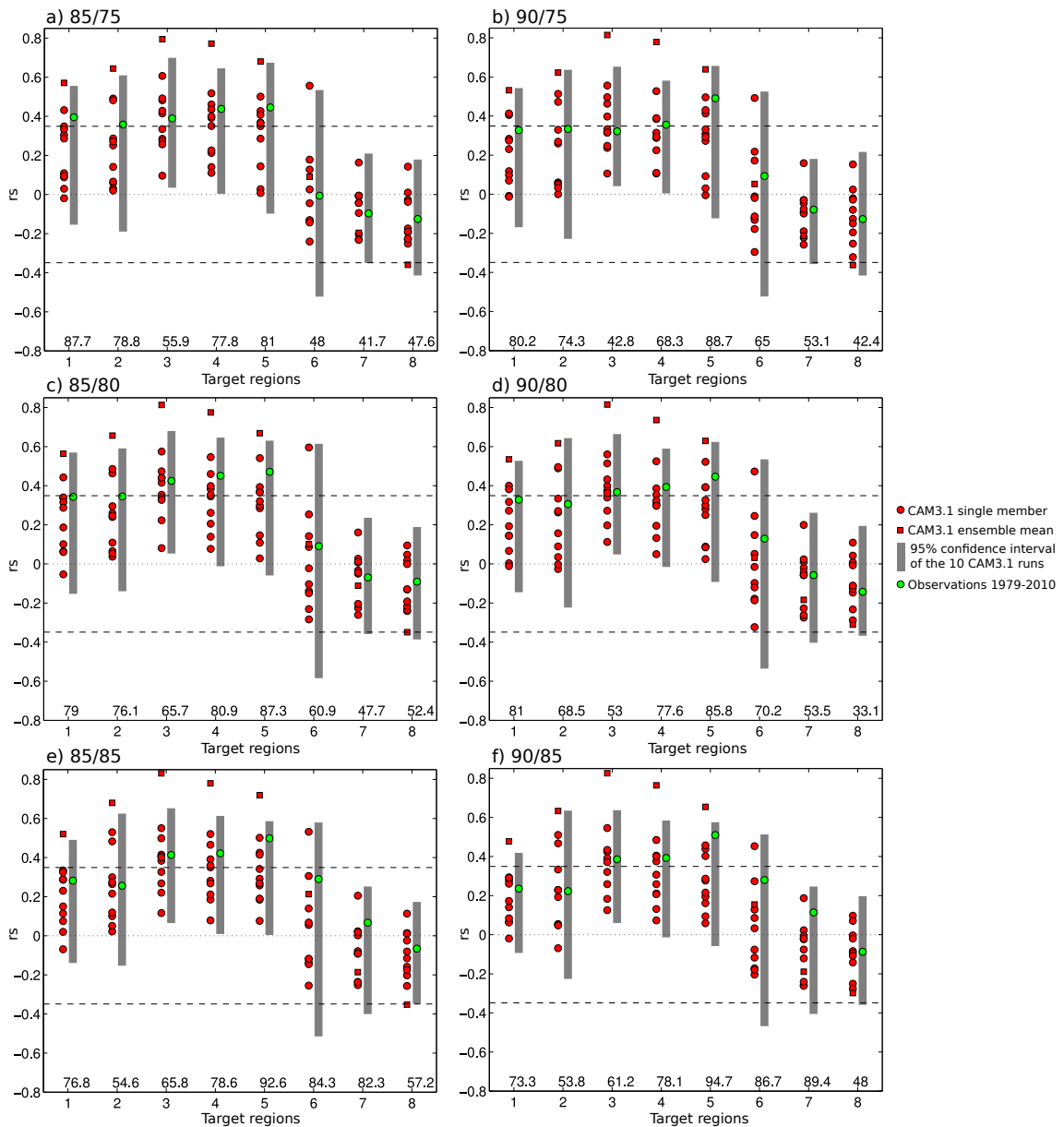


**Figure 7.8:** Robustness of the interannual Pacific Warm Pool - AR count relationships to internal atmospheric variability, expressed by variations in  $r_s$ . Dashed lines = critical values for  $\alpha = 0.05$ . All model results are depicted in red and are for the home-made CAM3.1 experiments forced with SST variations in the tropical Pacific only. Circles =  $r_s$  from the interannual AR counts of individual members. Squares =  $r_s$  from the counts averaged yearly over all members of CAM3.1. Model responses are for 32 model years (see Section 7.1.2 for details). Light green circles = observed  $r_s$  for the period 1979-2009. Dark grey bars = 95% confidence intervals obtained from the 10 modelled  $r_s$ . Numbers at the bottom of the panels = cumulative probabilities for the observed  $r_s$  of the 1979-2008 period within the “model-only” t-distribution for that period. Values < 2.5% or > 97.5% are printed in red. Results are for the European AR counts in OND. See text for more details. Source: own illustration



---

## CHAPTER 8

---

### Extension to Other Predictand Variables and Teleconnections

In the aforementioned chapter, it was asked whether ENSO teleconnections to regional atmospheric river counts are robust to perturbation due to internal atmospheric variability. Beyond this question, it is of course interesting to apply the methodological framework presented in Section 7.2 to other predictand variables such as temperature and precipitation, and also to other teleconnections than those triggered by ENSO. This extension is undertaken in this last working step of the thesis. To this aim, the robustness test proposed in Section 7.2.1 is not applied to seasonal AR counts, but to seasonally aggregated precipitation, temperature, mean sea level pressure and the geopotential at 500 hPa instead. Unlike IVT, these “classical” variables are readily available from ECMWF’s newly developed ERA-20CM dataset, which is a ten member ensemble of AGCM experiments forced with prescribed, time-varying external forcing agents. Therefore, these experiments are often referred to as “AMIP-like” (Hersbach et al., 2015). In comparison to AMIP, the ERA-20CM experiments are preferable for several reasons and are thus applied in this chapter instead. One key advantage of the ERA-20CM experiments is their temporal coverage spanning 111 years (1900-2010), instead of the 30 years covered by most AMIP runs (1979-2008). Having such a long period at hand, it is e.g. possible to assess teleconnections triggered by *multidecadal* SST oscillations.

In Section 8.1, the ERA-20CM dataset and the methods applied in this chapter will be described. In Section 8.2.1 the robustness of the teleconnections triggered by ENSO will be tested for the classical predictand variables mentioned above, taking into account the entire 111-year period. Section 8.2.2 will challenge the usefulness to assess teleconnections with very short time periods in the presence of internal atmospheric variability (e.g. Mariotti et al., 2002). Section 8.2.3 is of preliminary

nature and will assess the robustness of the teleconnections exerted by the AMO and PDO. Parts of the results presented in this Chapter were published in Brands (2017).

## 8.1 The ERA-20CM Dataset and Applied Methods

All the variables used in the present chapter are calculated upon monthly mean data from the European Centre for Medium-Range Weather Forecasts AGCM ensemble developed within the ERA-20CM project, run at a horizontal resolution of  $1.125^\circ \times 1.125^\circ$  (Hersbach et al., 2015), which is much finer than the resolution of most AMIP experiments. Each of the ten model runs forming this ensemble is forced by one realization of the SST and sea-ice dataset HadISST2 (Titchner and Rayner, 2014; Kennedy et al., 2015), which, in the case of SSTs, is itself an ensemble covering the range of observational uncertainty along the twentieth century.

This external forcing setup is slightly distinct from the deterministic forcing applied in the AMIP experiments from CMIP5, in which case all AGCMs were run with the the same prescribed SSTs assumed to be “true” (Gates, 1992). Thus, the robustness estimates obtained from ERA-20CM in this chapter not only include the effect of internal atmospheric variability, but also variability arising from observational uncertainties in the prescribed SSTs. To estimate how relevant these differences are for ENSO teleconnections, the Niño 3.4 index was calculated separately for the ten distinct SST forcing datasets used by ERA-20CM, and then pairs were mutually correlated using a correlation matrix. This was done for the four main seasons of the year and, to take into account larger observational uncertainties as one moves backwards in time, for the periods 1900-2010 and 1900-1950. Since the obtained correlation coefficients for these two periods are always larger than +0.97 and +0.92 respectively, differences in SST forcing are negligible for the Niño 3.4 region even during the first half of the twentieth century.

However, even in case the observational uncertainties were larger, as could be the case for other SST indices like the PDO and AMO (see Section 8.2.3), this would not invalidate the argumentation line followed here because observational uncertainties should also be taken into account when critically interpreting a teleconnection drawn from *observations*<sup>1</sup>. Indeed, the inclusion of observational uncertainty is convenient since it further augments the degree or realism (and thus the power) of the applied robustness test (see also Section 7.2.1). For the sake of simplicity and consistency to the rest of the thesis, the term “internal atmospheric variability” in this chapter also includes variations in the teleconnection’s strength caused by observational uncertainty.

Apart from the differences in the prescribed SSTs, the time-varying external forcing agents prescribed to ERA-20CM comprise sea-ice cover, greenhouse gases, ozone, aerosols and solar activity, all assumed to be deterministic (Hersbach et al.,

---

<sup>1</sup>which are subject to both internal atmospheric variability and observational uncertainty

2015). This list is more complete than that of the AMIP experiments, which again augments the power of the robustness test.

To measure the strength of a given teleconnection, the seasonal-mean time series of the predictor index (e.g. the seasonal mean Niño 3.4 index) is correlated with the concurrent predictand time series on the grid-box scale (e.g. seasonal precipitation totals) using the Pearson correlation coefficient ( $r$ ), which is more frequently used for correlating continuous variables than the rank correlation coefficient<sup>2</sup>. For a given predictand, grid-box and season of the year, this is done separately for each of the ten members of the ERA-20CM ensemble (Hersbach et al., 2015), thereby obtaining a sample of ten  $r$ -values representing pseudo-empirical variations in the strength of the teleconnection that are caused by internal atmospheric variability. This sample is then used to obtain a 95% CI for these variations as described in Section 7.2.1<sup>3</sup>. Since the early twentieth century is considered during which many regions of the world were essentially unobserved, reanalysis data are not used in this Chapter. This means that “modelled CIs”, as defined in Section 7.3.1, are applied here in any case.

For consistency with Brands (2017), all time series except the AMO and PDO indices<sup>4</sup> are linearly detrended prior to calculating  $r$ . The respective results for the raw time series (not shown) are in close agreement. Unlike above for the analyses of AR counts in the *extratropics*, where serial correlation of the year-to-year times series can be generally assumed to be negligible (Brands et al., 2014), analyses in this section include the *tropics* where the serial correlation indeed might play a role. Therefore, in this Chapter, the critical values for a significant  $r$  are obtained from a two-tailed t-test *corrected* for the effect of serial correlation (see Equation 6.1). Note that if the serial correlation is zero, the corrected t-test returns the same results as the standard version of the test.

## 8.2 Results Obtained from ERA-20CM

### 8.2.1 ENSO Teleconnections during the 1900-2010 Period

The 1900-2010 results for the *geopotential height* at 500 hPa (Z500) are shown in Figure 8.1. The lower end of the 95% confidence interval for variations in  $r$  due to internal atmospheric variability is displayed in the panels on the left and the upper end is shown in the panels on the right. The four rows refer to the four standard seasons of the year. To keep the figures simple, only the regions where teleconnections were found to be “robust”, as defined in Sections 7.2.1, are displayed. Accordingly, when referring to “negative” or “positive” correlations in the forthcoming, these are *robust* unless otherwise stated<sup>5</sup>.

<sup>2</sup>which was used in the former sections to correlate *count* variables

<sup>3</sup>in this case,  $z \pm 2.262$  in Equations 7.2 and 7.3

<sup>4</sup>which are detrended by definition

<sup>5</sup>Note that the non-robust results are available from the supplementary material of Brands (2017)

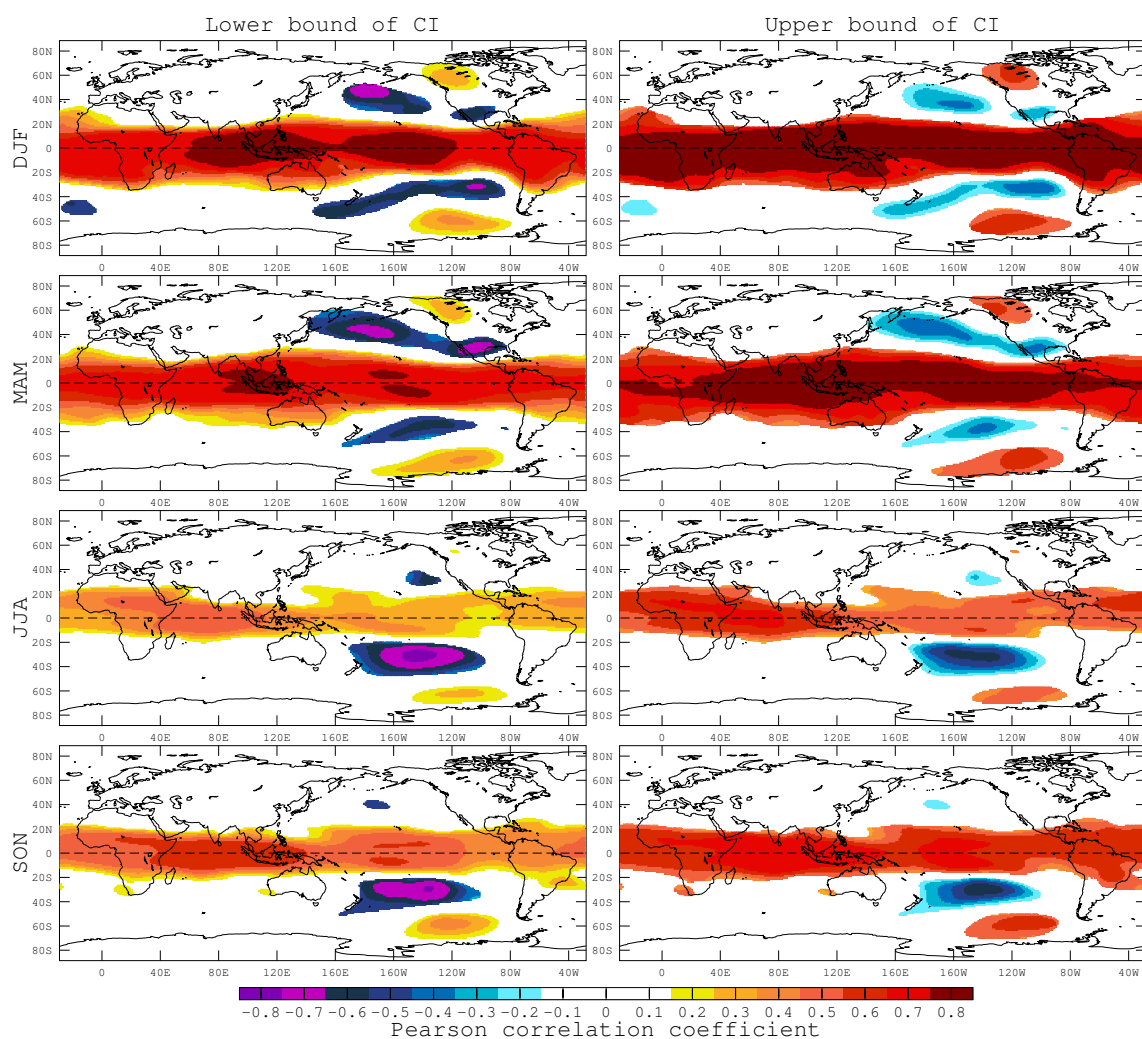


**Figure 8.1:** 95 % confidence interval (CI) for variations in the correlation coefficient between the seasonal mean Niño 3.4 index and the geopotential height at 500 hPa caused by internal atmospheric variability. The lower and upper bounds of the CI are shown in the left and right column respectively. Only those grid boxes where the response to ENSO is robust are shown, otherwise grid boxes are blanked out. The considered time period is 1900-2010. Source: own illustration

For  $Z500$ , positive correlations are found in the entire tropics, indicating above-normal geopotential height fields due to the tropospheric warming induced by El Niño events and opposite conditions during La Niña (for the sake of conciseness, only the El Niño dynamics will be described hereafter). In the extratropics, robust teleconnections are found in an area reminiscent of the Pacific-North American pattern (PNA) in the Northern Hemisphere (Wallace and Gutzler, 1981) and the Pacific-South American pattern (PSA) in the Southern Hemisphere (Mo and Paegle, 2001). Notably, the dipole of robust teleconnections located in the extratropical south Pacific is stable throughout all seasons whereas the PNA-like pattern in the Northern Hemisphere exhibits a pronounced seasonal cycle, i.e. is robust during DJF and MAM but not so during SON. During DJF (i.e. the austral Summer), robust teleconnections are found in the South Atlantic, thereby completing the PSA-like tripole pattern. In the remaining regions of the extratropics, teleconnections are not robust irrespective of the season of the year.

Correlations for *mean sea level pressure* (*MSLP*, see Figure 8.2) are similar to those found for  $Z500$  but the robust areas are generally more confined to the Pacific Ocean basin. The most remarkable differences in the MSLP results are 1) the lack of a robust response in northwestern Canada (i.e. one pole of the PNA) during DJF and MAM, and 2) the appearance of a robust response region in central Asia during JJA.

Correlations for *precipitation* (see Figure 8.3) are positive along the equatorial Pacific ranging from South America in the East to the eastern tip of the Maritime continent in the West. This is flanked by a “boomerang” (Trenberth et al., 1998) of negative correlations at both sides of the equator which converges over the central part of the Maritime Continent and, during JJA and SON, extends well into the Indian Ocean basin.

In central America and northern South America (Colombia, Venezuela, Guyana, Suriname and French Guinea) negative relationships are found for each season except MAM, during which such a relationship is found in northeastern Brazil. In North America, precipitation results reflect those obtained for  $Z500$  mentioned above. During DJF, positive correlations are found over Mexico and the U.S. sunbelt (excluding California), which is contrasted by negative values in the northwestern United States and southwestern Canada. During MAM, negative correlations disappear in this continent and the belt of positive values shifts to the North, covering California, Arizona and parts of Utah and Nevada. During JJA and SON, results are not robust in virtually the entire continent.

During the JJA and SON seasons, the robust teleconnection dipole found for  $Z500$  over the South Pacific is also visible in the results for precipitation. Remarkably, positive correlations are obtained for MAM precipitation in parts of West Antarctica, which is due to above-normal advection of oceanic air masses from the North during El Niño events that can be deduced from the respective results for mean sea level pressure (see Figure 8.2).

The negative relationship found for  $Z500$  over the South Atlantic during the

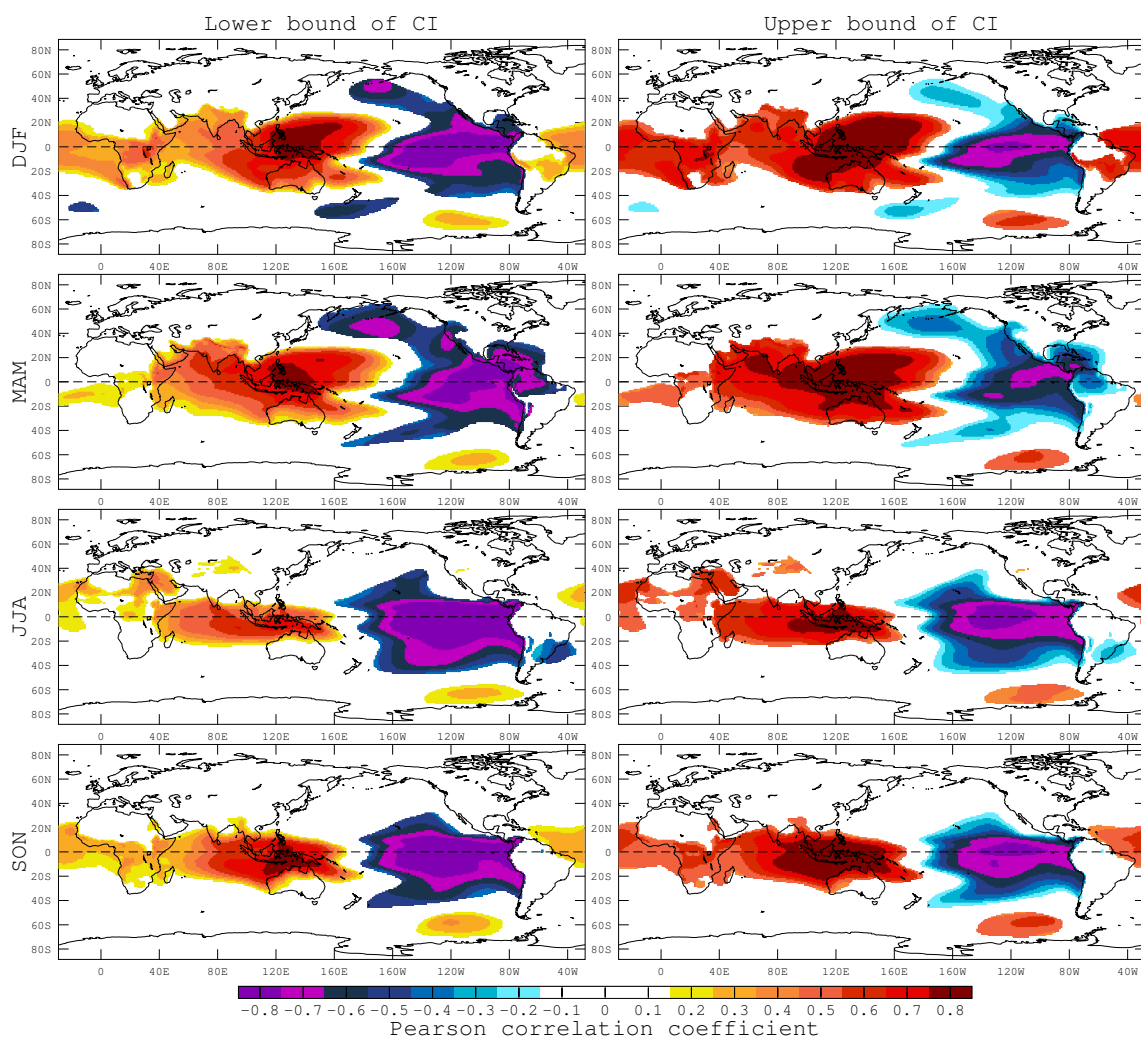


Figure 8.2: As Figure 8.1, but for mean sea level pressure. Source: own illustration

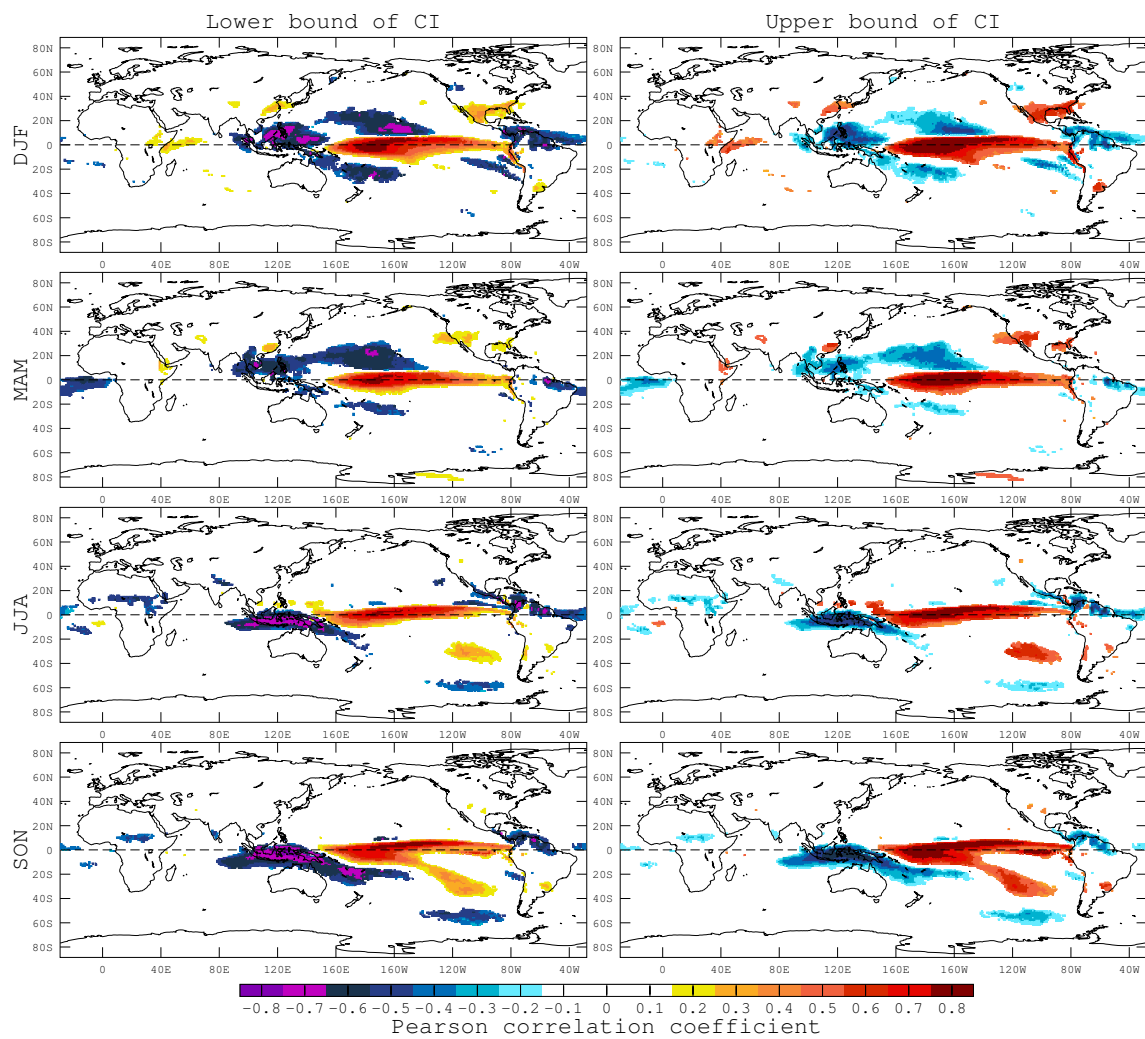


Figure 8.3: As Figure 8.1, but for precipitation. Source: own illustration

austral Summer (DJF) is associated with a positive relation for precipitation over parts of Argentina and Uruguay. In spite of its relatively coarse resolution, ERA-20CM is able to reproduce the opposite sign of the precipitation teleconnections on either side of the Andes (Garreaud et al., 2009).

Teleconnections over the equatorial Atlantic and sub-Saharan Africa clearly follow the seasonal march of the Intertropical Convergence Zone and are negative along this line, indicating that reduced convective rainfall activity during El Niño events is a robust ENSO teleconnection. Importantly, during the core of the West African monsoon (JJA), negative  $r$ -values are observed over a large fraction of sub-Saharan Africa including the Sahel. However, teleconnections to the South of the equator are not robust in Africa. Around the Horn of Africa, positive  $r$ -values are found during the DJF and MAM seasons. During the former season, these extend well into the northwestern Indian Ocean.

Over the Indian subcontinent, a core of negative  $r$ -values moves southward as the monsoon season passes, i.e. appears over the Himalayas during the JJA season and over southern India during the SON season.

Further to the East, positive  $r$ -values are obtained over eastern China, the Yellow-Sea and South Korea during the dry season (DJF). During MAM, when seasonal precipitation amounts are generally more copious implying that modifications by ENSO can have a greater effect on society (Diaz et al., 2001), positive values are found in southern China.

For *two-metre air temperature* (T2m, see Figure 8.4), results are similar to those obtained for precipitation, but the area of robust teleconnections is larger. Thus, the response to ENSO is robust in the tropics and in the PNA and PSA regions, but generally not so in the remaining regions of the extratropics. During DJF and MAM, a robust correlation dipole is found in Alaska/northern Canada on the one hand and Mexico/the U.S. Gulf coast on the other. Unlike for precipitation, temperature teleconnections are not robust over Argentina and Uruguay but robust over New Zealand during any season.

### 8.2.2 ENSO Teleconnections during Specific Time Periods

In previous studies, the observed ENSO teleconnections to North America were found to be particularly strong after the Great Pacific Climate Shift in 1976/77 (Mantua et al., 1997) and this enhancement was attributed to external forcing from (multi)decadal SST oscillations in the North (Gershunov and Barnett, 1998) and/or Tropical Pacific (Diaz et al., 2001). Comparing the periods 1948-76 and 1977-99, during which the PDO was in its negative and positive phase respectively, Diaz et al. (2001) found a correlation dipole in the Z500 field over North America during the late period which is absent in the early period (see their Plate 5). Applying the robustness test proposed here to the same temporal configuration (the February-March-April season is considered) reveals that, during the late period, the southern centre of the dipole (i.e. the negative correlations in the southern U.S./Mexico and to the

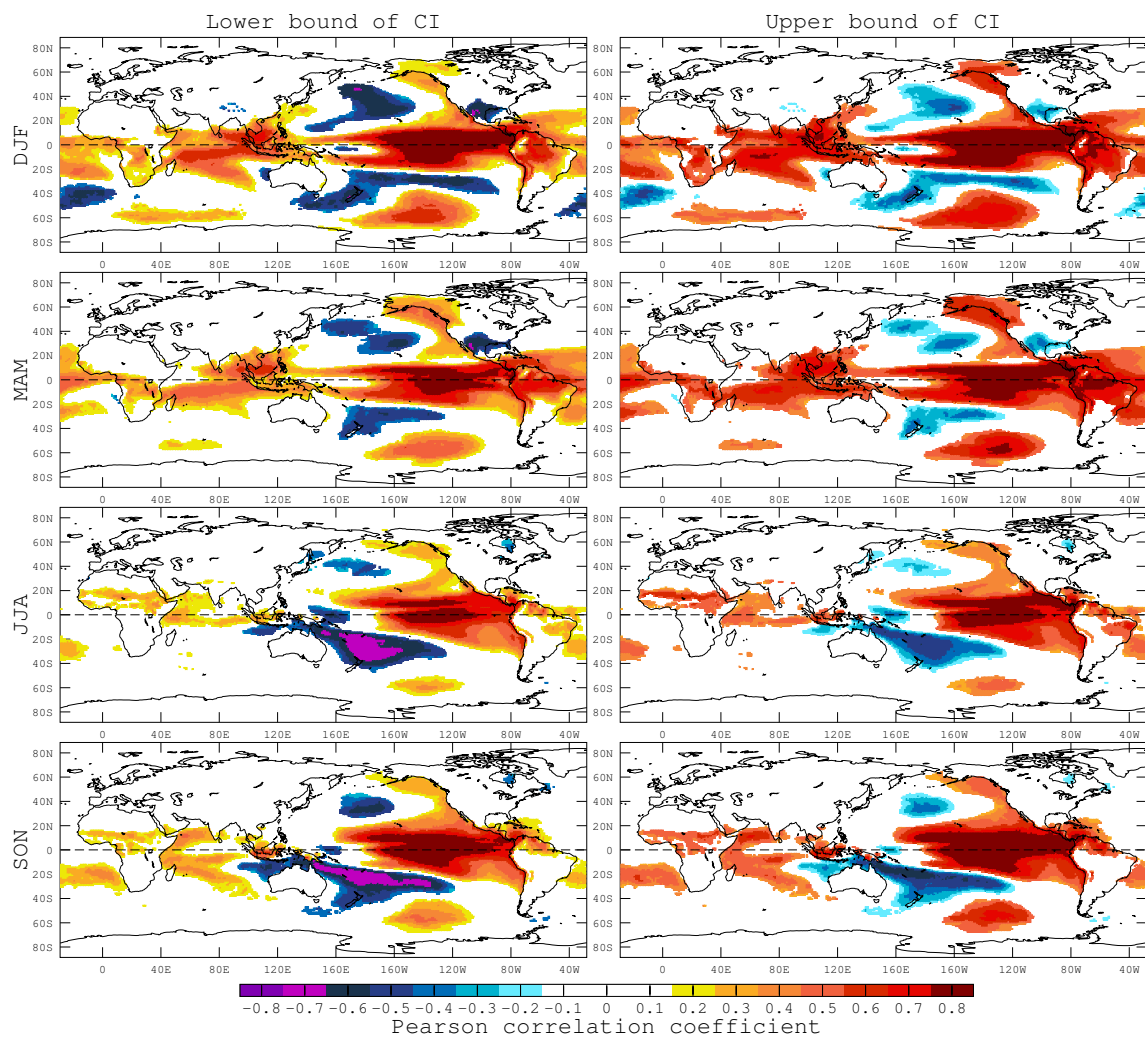
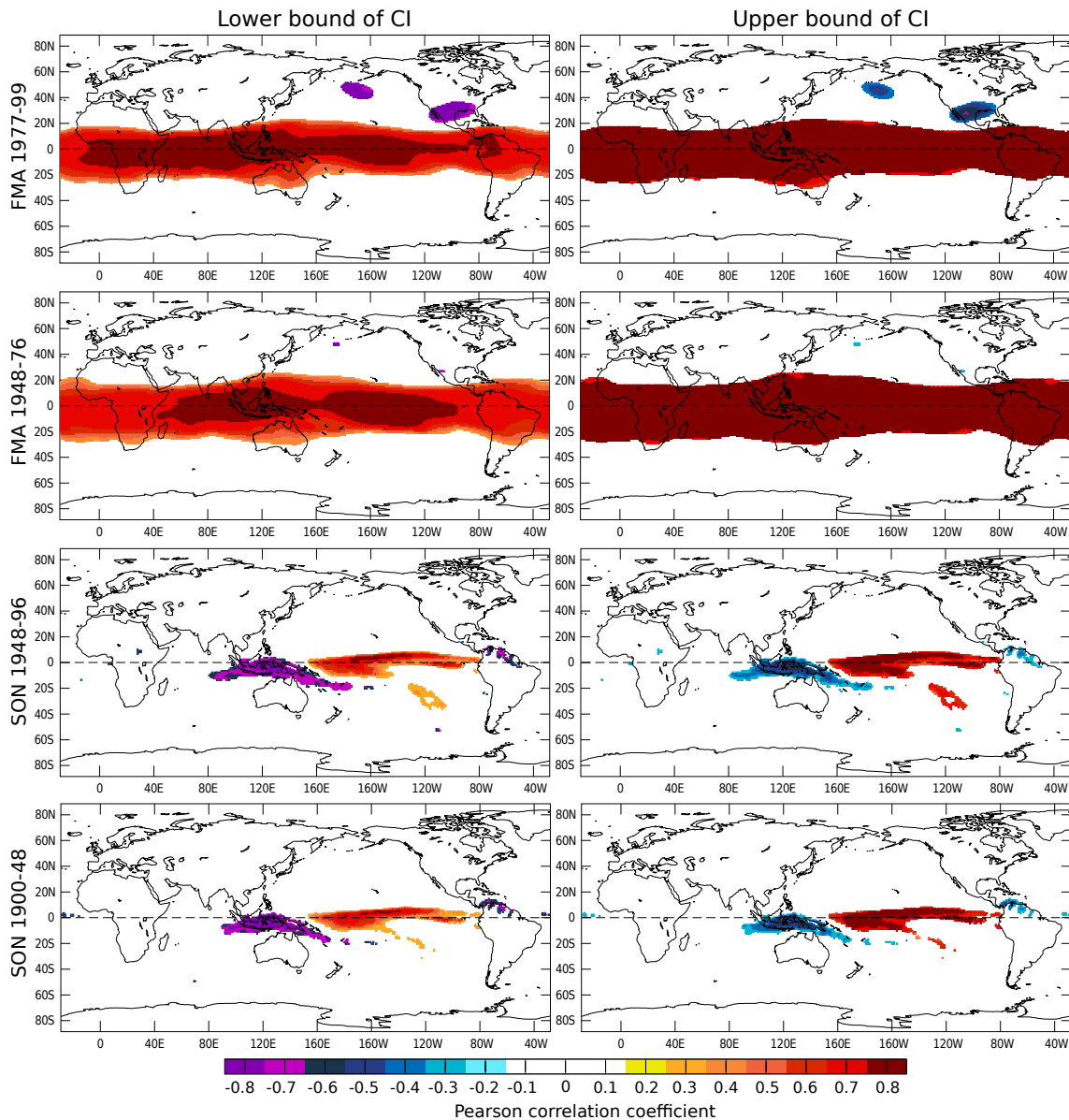


Figure 8.4: As Figure 8.1, but for two metre air temperature. Source: own illustration



**Figure 8.5:** As Figure 8.1, but for the shorter time periods and seasons indicated on the left of each row. These time periods coincide with the positive (1977-99, first row) and negative (1948-76, second row) phase of the PDO and with periods during which the observed ENSO teleconnections to southern Europe were found to be significant (1948-96, third row) or insignificant (1900-48, fourth row) in previous studies (see text for more details). The upper four panels are for Z500 and the lower four panels for precipitation. Source: own illustration

South of Aleutian Islands) is robust to internal atmospheric variability whereas the northern centre over Canada is not (see first row in Figure 8.5). During the early period, no robust teleconnection to the extratropics is found at all (see second row). This is remarkable since the late period is shorter than the early one, meaning that the magnitude of  $r$  must be larger to yield significance.

Similarly, Mariotti et al. (2002) found that ENSO teleconnections to September-October-November (SON) precipitation in southern Europe were significant during the second half of the twentieth century (1948-1996) but spurious during the first half (see their Figure 1). The analyses conducted here reveal that this teleconnection is neither robust during the first nor during the second half of the century (see third and fourth row in Figure 8.5), or, to put it in another way, no appreciable differences are found between them.

Figure 8.6 is a replicate of Figure 8.5, but using 90% confidence intervals for calculating 1) the significance of  $r$  and 2) the confidence interval describing variations in  $r$  due to internal variability<sup>6</sup>. This relaxation leads to similar results, except to the South of the Aleutian Islands, where teleconnections for  $Z500$  during FMA 1948-77 pass the robustness criteria in a much larger area.

Furthermore, Figure 6 in Mariotti et al. (2002) —described in the Introduction to this thesis (see Section 2.7)— was replicated with the methods proposed here (see Section 7.2.1). To this aim, confidence intervals for variations in the correlation coefficient between the Niño 3.4 index and areal average precipitation in the western Mediterranean (30°N - 45°N, 10°W - 20°E) were computed for a sliding 20-year period running forward from 1900-19 to 1991-2010 by one year in each step. This was done for the MAM and SON seasons. As can be seen from Figure 8.7a and b, a robust ENSO response as defined here is not yielded in any of the 92 subperiods. Rather, individual  $r$ -values (blue dots) have such a large spread that the confidence limits (black lines) frequently range from significantly negative to significantly positive (dashed red lines = critical values). As for the observed teleconnections in Mariotti et al. (2002), results from individual model runs (light green lines) can indeed break through the critical values in specific time periods. For comparison, computations were repeated for SON areal average precipitation in Indonesia (10°S - 5°N, 90°E - 140°E, see Figure 8.7c). Except during 1932-51 to 1954-73, the corresponding confidence intervals are entirely below the critical value for a significantly inverse relationship, indicating that this tropical precipitation regime is generally well constrained to ENSO. Plotting the standard deviation of the concurrent seasonal mean Niño 3.4 index in the same panel (grey boxes) reveals that the aforementioned non-robust response period coincides with weak ENSO activity. Plotting this activity (x-axis) against the width (panel c1) and centre (c2) of the confidence interval further shows that increased ENSO activity is clearly associated with reduced uncertainty and stronger teleconnections in this region. Figures 8.5 and 8.7 underline that internal atmospheric variability becomes more important when shorter time periods are considered.

<sup>6</sup>in this case,  $z = \pm 1.833$  in Equations 7.2 and 7.3

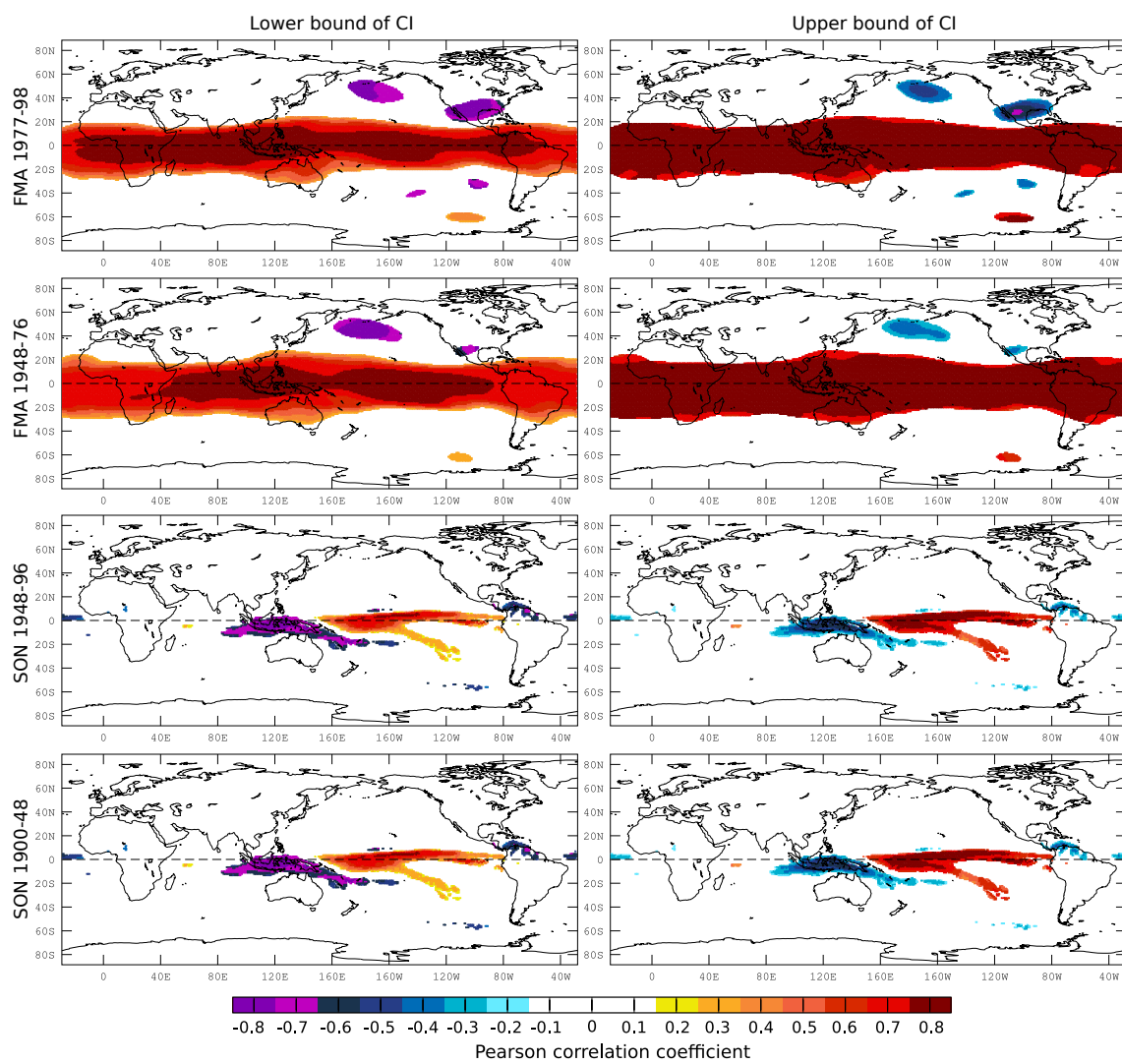
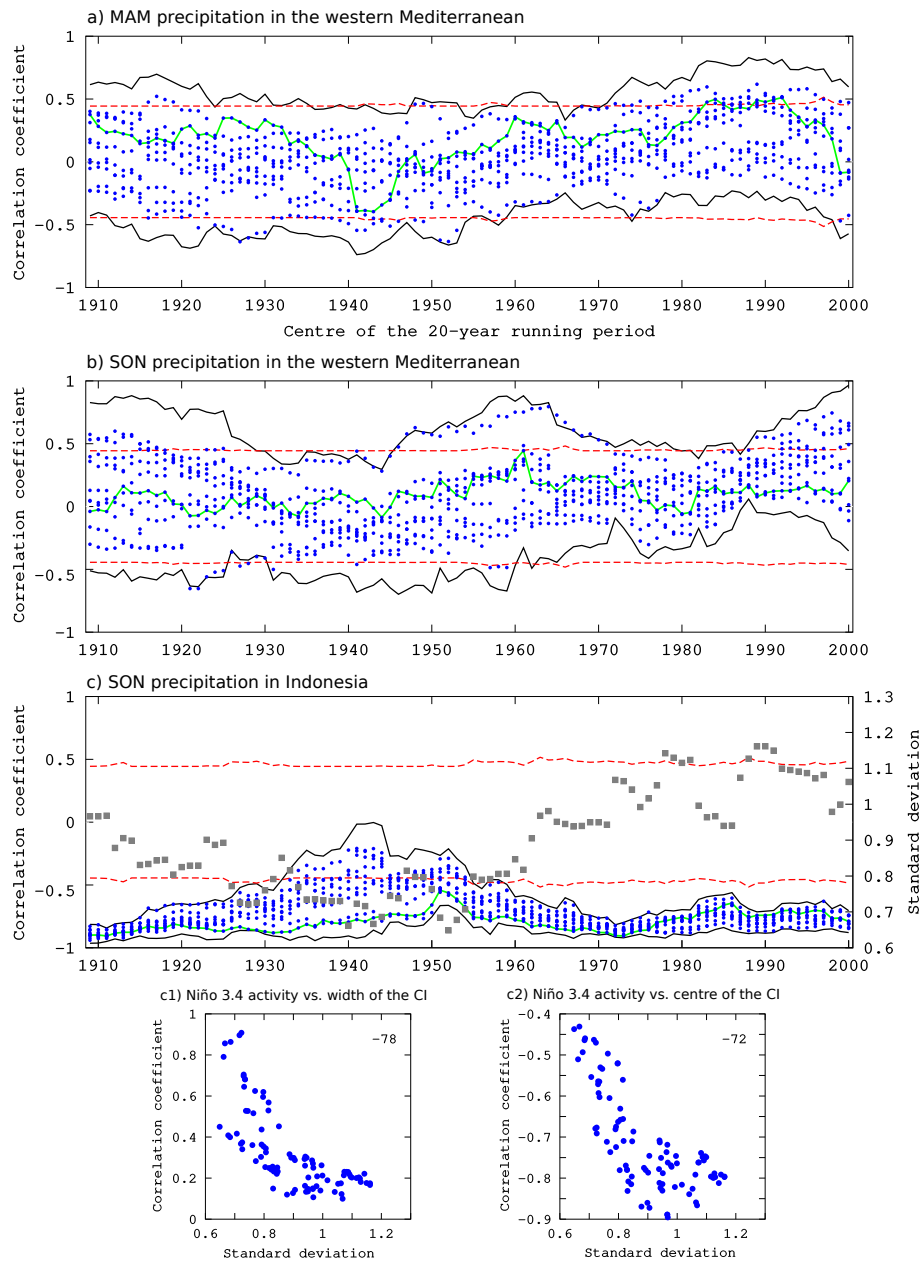


Figure 8.6: As Figure 8.5, but for 90% confidence intervals. Source: own illustration



**Figure 8.7:** *Running robustness* analysis for the Pearson correlation coefficient between the Niño 3.4 index and areal average precipitation for the indicated regions and seasons, using a sliding 20-year window. Blue dots = results from the individual ERA-20CM members. Black lines = limits of the confidence interval for variations due to internal atmospheric variability. Dashed lines = critical values for a significant correlation. 95% significance levels are assumed. Light green lines = results for a single model run. Grey boxes = ENSO activity represented by the standard deviation of the Niño 3.4 index time series. For Indonesia, ENSO activity (on the x-axis) is plotted against the width (c1) and centre (c2) of the confidence interval; the respective rank correlation coefficients are shown in the upper right corners. Source: own illustration

### 8.2.3 Teleconnections Triggered by the AMO and PDO

Taking advantage of the 111-year record available for the ERA-20CM model ensemble, in this last results section, it is asked whether the teleconnections exerted by the PDO and AMO are robust to internal atmospheric variability. To this aim, the robustness test described in Section 7.2.1 is applied for the Pearson correlation coefficient between the seasonal mean values of the *PDO*, or alternatively the *AMO*, and the concurrent values for MSLP, precipitation and T2m around the entire globe.

As is the case for the Niño 3.4 index, the *PDO* and *AMO* indices are calculated separately for each of the ten SST realization of the HadISST2 dataset used to run the ten members of the ERA-20CM model ensemble. The *AMO* is defined as the areal average SST of the North Atlantic Ocean<sup>7</sup>. Prior to calculating the areal average time series, the monthly global<sup>8</sup> mean SST is removed from the concurrent monthly values on the grid-box scale, as was suggested by (Trenberth and Shea, 2006). The *PDO* was calculated similar to Zhang et al. (1997). First, the monthly global mean is subtracted as for the *AMO*. Then, principal component analysis is applied to the seasonal mean values of the North Pacific SSTs<sup>9</sup> and the principal component time series of the leading EOF is retained. To assure that the leading EOF indeed corresponds to the typical horseshoe pattern of the *PDO*, the DJF pattern of the SST realization used to force the first member of ERA-20CM is checked by eye. All other 39 patterns (four seasons of the year  $\times$  ten model members minus the one observed by eye) are then correlated with this reference pattern. The resulting pattern correlation coefficients are  $> +0.71$  in any case, i.e. even for the summer EOFs, meaning that the EOF patterns obtained from HadISST2 can be reasonable assumed to reflect the *PDO*.

The *PDO* and *AMO* indices calculated upon a specific HadISST2 realization are then correlated with the simulated predictand from the respective atmospheric realization and this procedure is repeated for each of the ten members of the ensemble. The thereby obtained ten Pearson correlation coefficients are then used to fit the t-distribution describing variations in the teleconnection's strength that are caused by internal atmospheric variability (see Section 7.2.1).

For the link between the *AMO* and the global MSLP patterns (see Figure 8.8), negative relationships are found in the tropical Atlantic and positive ones in the tropical Pacific. During the MAM season, the strength of this dipole is clearly weaker than during the remaining seasons. Similar to the ENSO links discussed above (see Section 8.2.1) the negative correlations found in the Atlantic basin follow the location of the ITCZ, i.e. are displaced to the respective summer hemisphere. Hence, during the JJA season, negative correlations even reach the western Iberian Peninsula and the Rocky Mountains (both located in the extratropics) and also cover almost the entire Sahara desert from the Atlantic Ocean in the west to the Red Sea in the east.

<sup>7</sup>i.e. from 0°N to 60°N and from 70°W to 0°W

<sup>8</sup>i.e. from 60°S to 60°N

<sup>9</sup>i.e. from 20°N to 60°N and from 140°E to 120°W

During the the SON season, negative links are found in the tropical rainforests of the Congo and Amazon basins to both sides of the Atlantic, as well as over the Maritime Continent, where they also manifest during the DJF season.

Albeit being generally much sparser, the robust response areas for *precipitation* (see Figure 8.9) make sense from a physical point of view when seen in conjunction with the aforementioned results for MSLP. During the positive phase of the AMO, the reduction in MSLP induced by above-normal SSTs in the North Atlantic favours convective precipitation there. The anomalously low MSLP values in the Sahara during this phase strengthen west African Monsoon which, in turn, leads to above normal JJA rainfall in the entire Sahel region. During the same season, positive links are found in central America and the Guayanas and a distinct negative correlation pattern is found in the very west of the Amazon basin, at the foot of the Andes. Dynamically, this area might reflect the descending branch of a local Hadley cell which is reinforced during the positive phase of the AMO.

Particularly during the JJA and SON seasons, the T2m in almost the entire North Atlantic Ocean basin are positively linked to the AMO, reflecting the close relationship between sea surface and air temperatures. *In the Atlantic region* these links abruptly end along the coastlines and only a few inland links can be found that would imply changes in the circulation triggered by the AMO. These relatively remote links are mostly bound to the JJA season and comprise 1) a correlation dipole for the Guayanas vs. the Amazon basin reflecting the SLP pattern described above and 2) positive links to the temperatures of the Great Lakes, the Atlas mountains, Egypt and the Gulf of Persia. Note that the positive links to the British Isles (particularly in Ireland) can be simply explained by proximity to the Atlantic Ocean. However, there do exist remote teleconnections to regions *outside the Atlantic Ocean basin*. In agreement with the results found for MSLP and precipitation, a negative relationship to the AMO is found for the T2m in the equatorial Pacific during all seasons except MAM. Remarkably, negative links are found over a large fraction of the Southern Hemisphere ocean areas during the austral summer and autumn (DJF and MAM). Due the lack of data during the early twentieth century, the latter teleconnections are not documented in previous studies based on observations (e.g. Trenberth and Shea, 2006), nor can they be fully explained by covariability with ENSO since the respective patterns are similar, but far from being identical, particularly during the MAM season (compare Figure 8.10 to Figure 8.4). However, since these teleconnections only appear in the T2m fields (and not in the circulation fields), they might simply arise from the fact that the SSTs used to force the ERA-20CM experiments are correlated in a similar way. This question should be assessed in future studies.

As shown by Figures 8.11 and 8.12 for the examples of MSLP and T2m, the robustness of the teleconnections with the PDO is similar to the respective results for ENSO, but the robust areas are smaller and coincide with those found for ENSO in almost any case (compare with Figures 8.2 and 8.4). This suggests that ENSO instead of the PDO might be causal to most of the teleconnections seemingly exerted by the PDO, which could be further assessed by removing the inter-annual variability

related to e.g. the Niño 3.4 index from the PDO index. This issue is left open for future studies.

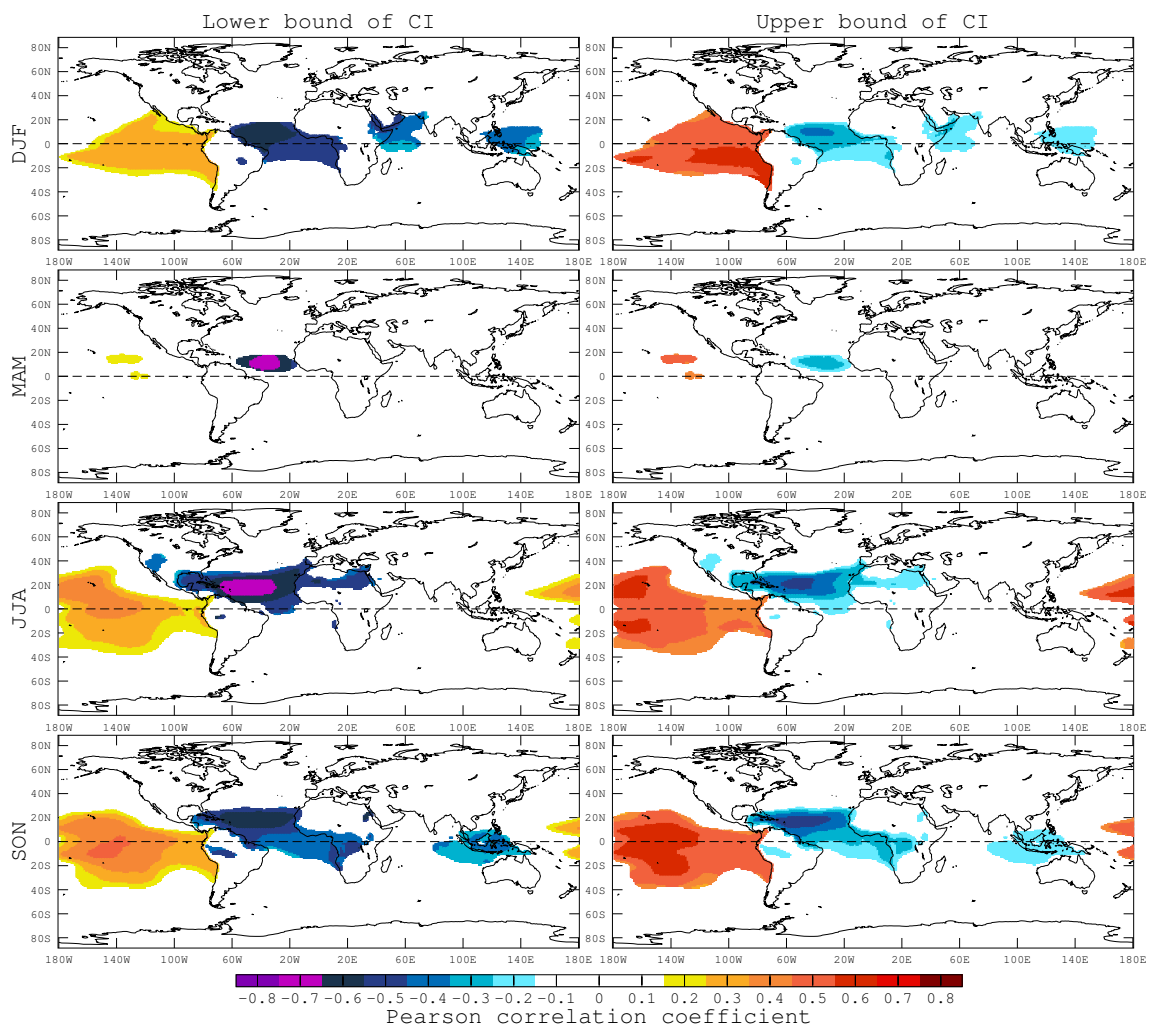
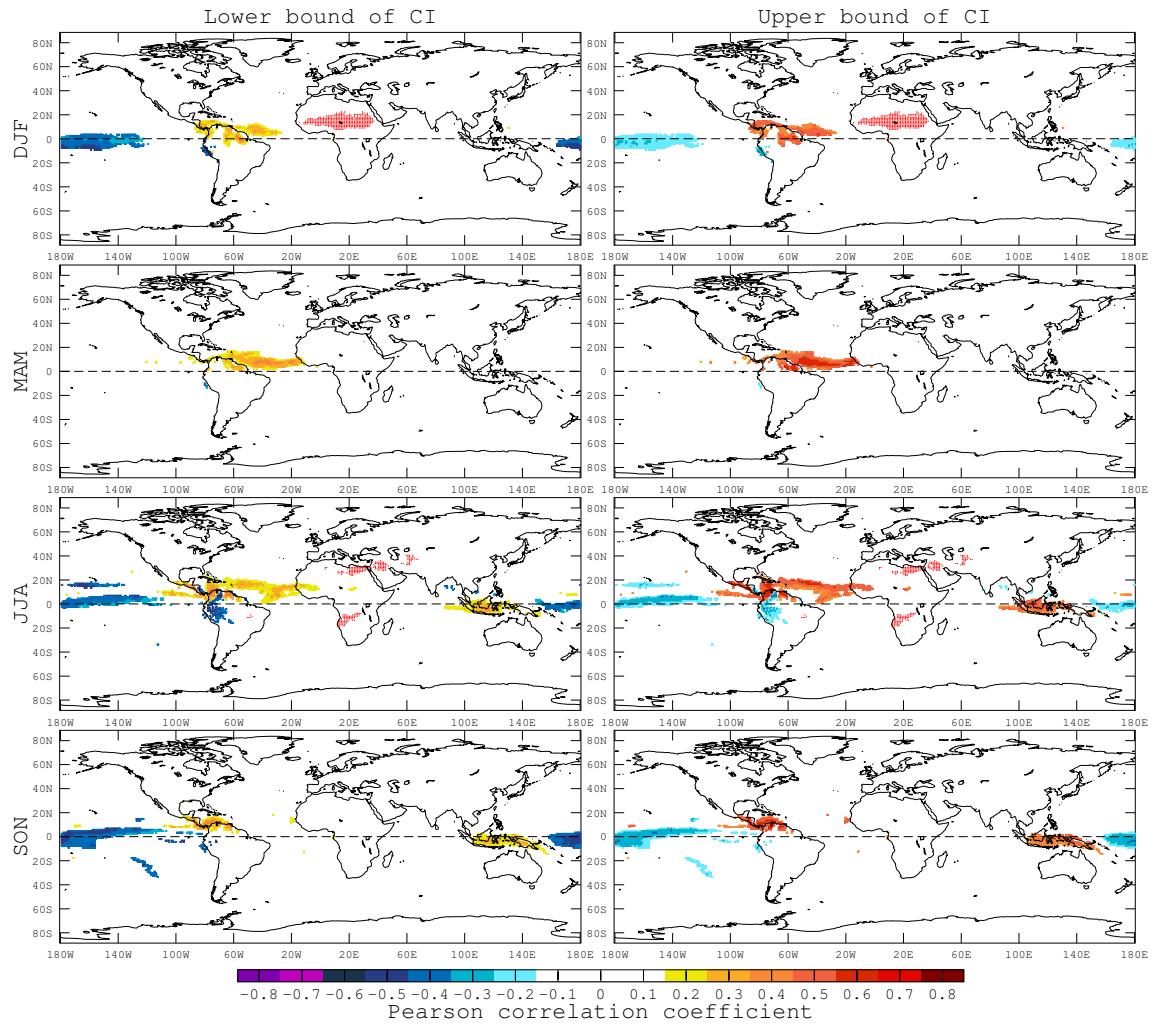
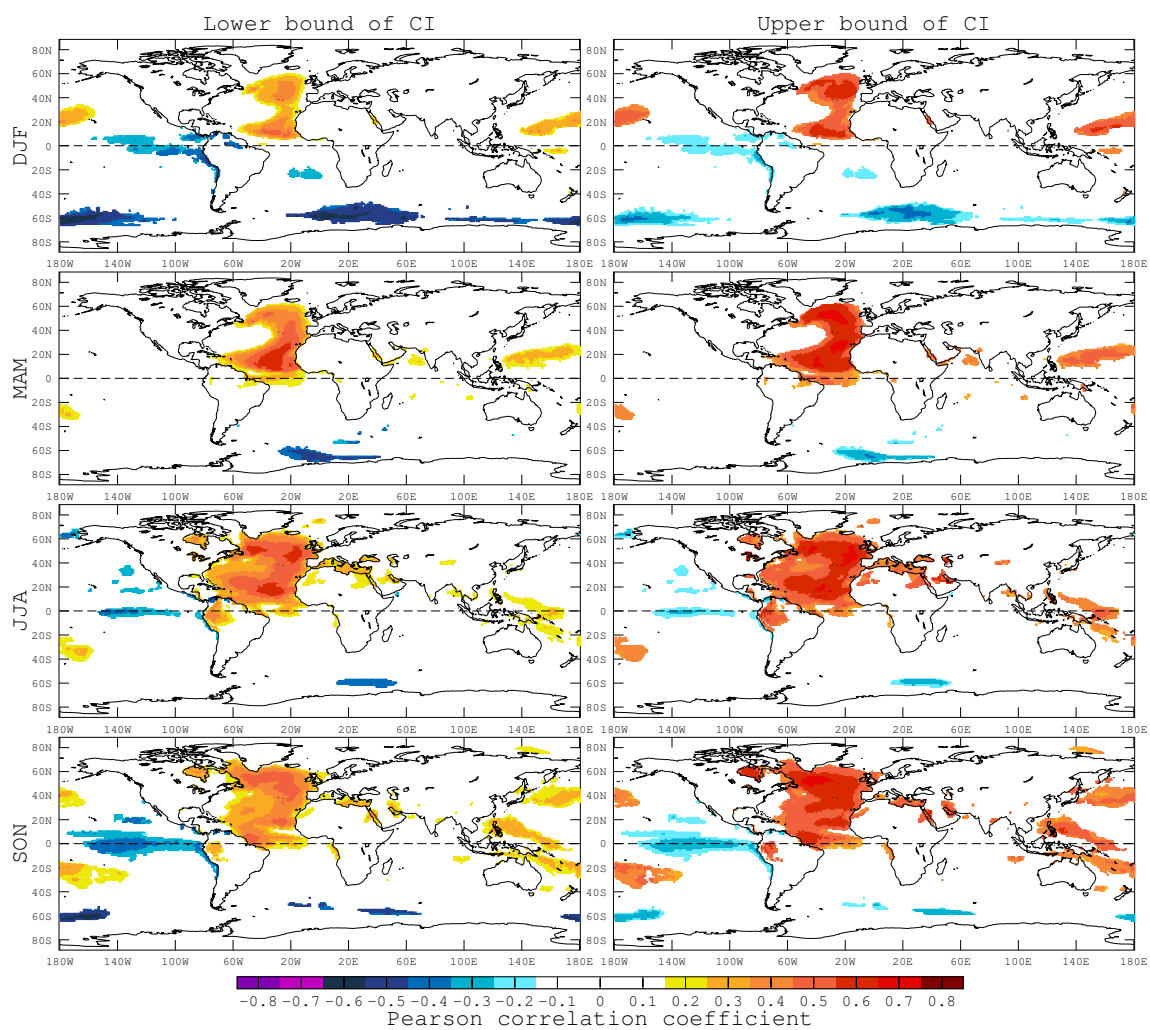


Figure 8.8: As Figure 8.1, but for the AMO and mean sea level pressure. Source: own illustration



**Figure 8.9:** As Figure 8.1, but for the AMO and precipitation. Areas shaded in red refer to missing values due to zero precipitation. Source: own illustration



**Figure 8.10:** As Figure 8.1, but for the AMO and two metre air temperature. Source: own illustration

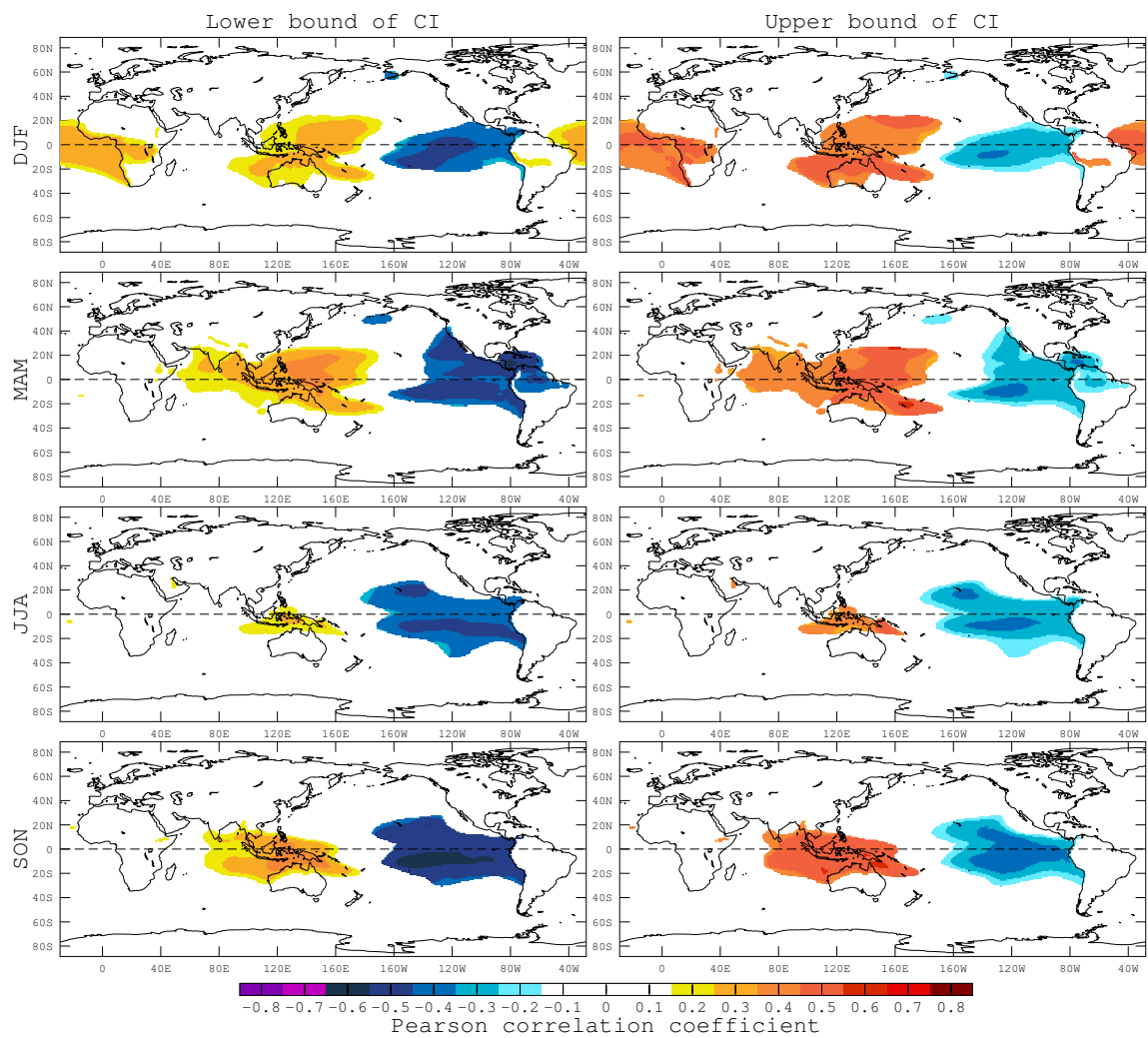
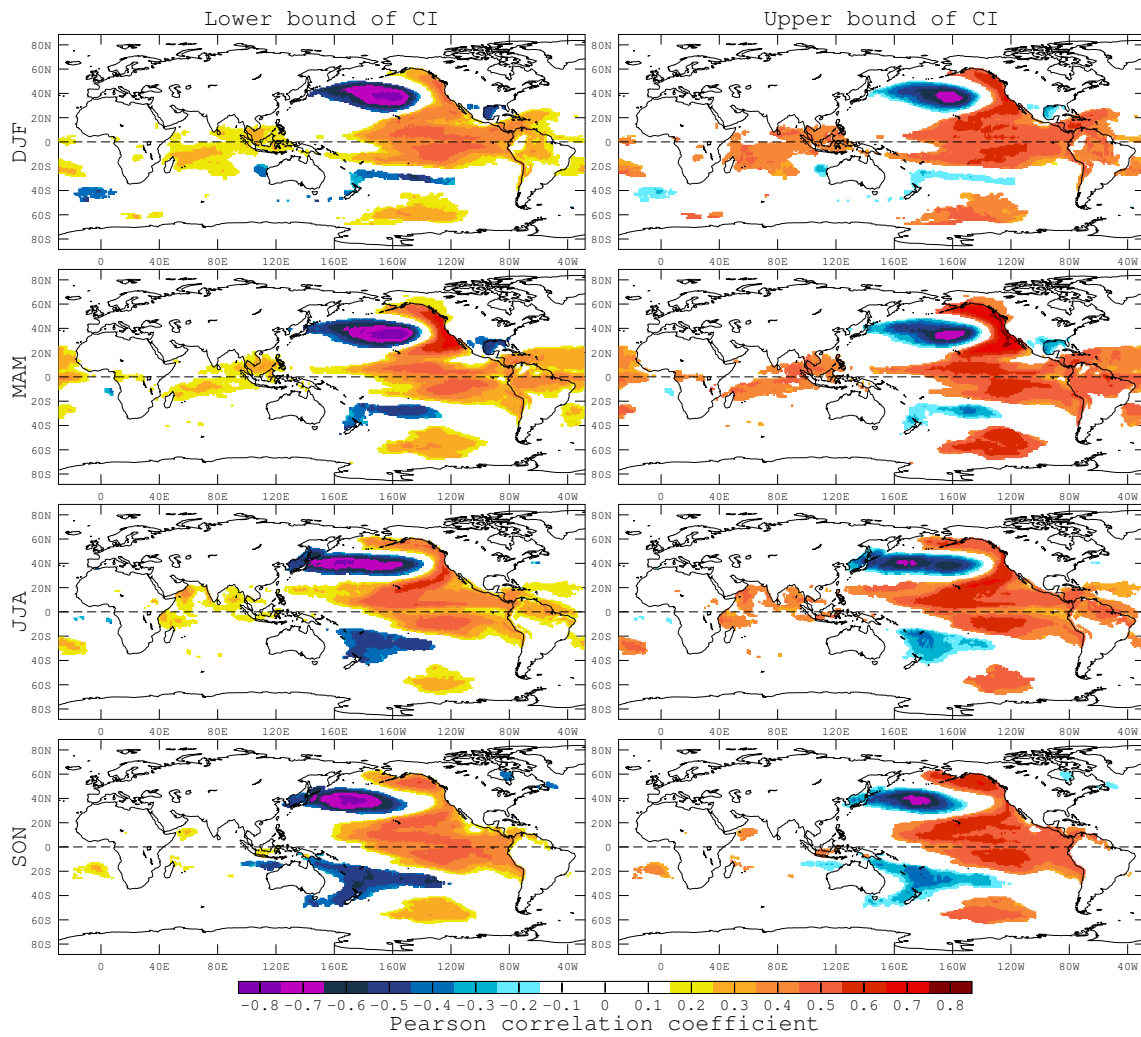


Figure 8.11: As Figure 8.1, but for the PDO and mean sea level pressure. Source: own illustration



**Figure 8.12:** As Figure 8.1, but for the PDO and two metre air temperature. Source: own illustration

---

## CHAPTER 9

---

### Summary, Discussion and Conclusions

This thesis' final chapter provides the synthesis of the results and a comparison to the findings from previous studies. This is done separately for the results drawn from observations (Section 9.1) and idealized numerical model experiments (Section 9.2). Assuming that these experiments are “surrogates” for the real world (von Storch et al., 2004), Section 9.2 could have also been entitled “Take Care when Interpreting Teleconnections Drawn from Observations” and underlines the error one might commit when assessing a probabilistic system, such as remote ENSO-teleconnections, with deterministic methods. This is commonly done in this field of the atmospheric sciences, also by the author himself (e.g. Brands et al., 2012c). Ideas for future studies are provided in Section 9.3.

#### *9.1 Lessons Learned from Observations*

##### *9.1.1 Atmospheric Teleconnections to Regional AR Counts*

In Chapter 4 of the present thesis, a novel algorithm for the detection and tracking of atmospheric rivers was developed that operates on the *intensity* and *direction* of the vertically integrated water vapour transport taken from reanalysis data. This algorithm was applied to four distinct reanalysis datasets to detect the presence and characteristics of atmospheric rivers (ARs) in 13 target regions along the west coasts of Europe (including North Africa) and North America on six-hourly timescale.

On the basis of these time series, more than 150 thousand maps documenting each individual AR-event in the above regions were generated, covering the time period 1900-2014. With these maps the most extensive publicly available historical AR archive available to date was built at <http://www.meteo.unican.es/>

[atmospheric-rivers](#), including six-hourly AR occurrence/absence times series in netCDF format. While these maps and the corresponding data can be easily cross-compared with hydrological variables on the local scale (e.g. extreme precipitation, flooding and landslides) by the scientific community (e.g. [Lavers et al., 2011](#)), the present thesis followed another approach.

Namely, the focus was put on seasonally accumulated AR occurrence counts and it was asked whether any empirical-statistical relationships can be found with the atmospheric and oceanic climate indices relevant for the climate in Europe and North America. This approach is useful 1) because seasonal AR counts are known to be closely related to the concurrent precipitation sums (e.g. [Neiman et al., 2008](#); [Lavers and Villarini, 2015](#)) and 2) because particularly SST variations in the *tropics* are predictable several month ahead (e.g. [Barnston et al., 2012](#)). Consequently, any remote relationship between regional AR counts and tropical SSTs could be potentially exploited for the purpose of long-term water supply forecasts ([Gamiz-Fortis et al., 2008](#)), *provided that this teleconnection is robust to the effects of internal climate variability* (see conclusion in Section 9.2). Unlike in AR-precipitation studies, ARs are here considered the *predictands*, and not *the predictors*.

Since reanalysis data are known to be uncertain, particularly during the early twentieth century ([Compo et al., 2011](#); [Poli et al., 2016](#)) and with regard to variables related to atmospheric moisture (e.g. [Brands et al., 2012b,a, 2013](#)), it was necessary to assess the reliability of the seasonal AR counts derived from this kind of data prior to looking at the teleconnections. To this aim, in Chapter 5, the AR counts from the NOAA-CIRES Twentieth Century and ECMWF ERA-20C reanalysis datasets were mutually compared using a “running” window looping through the period 1900-2010 by one year in each step. In addition, the linear decadal trends were computed *once* for the 1950-2010 period. This was done separately for the October-to-December (OND) and January-to-March (JFM) seasons. The following main results were obtained:

1. Differences in the mean of the two reanalyses (i.e. the biases) are especially pronounced in, but not limited to, the early twentieth century. With up to  $> 100\%$ , the biases during this early period are more severe in western North America than in Europe (see Section 5.1 for details).
2. With rank correlation coefficients ( $rs$ )  $\geq +0.6$ , along the west coast of Europe, the two reanalyses produce a similar inter-annual variability even at the start of the twentieth century. This is in sharp contrast to the near to zero  $rs$  found along the west coast of North America during the same period. In this region,  $rs$  steadily increases until approximately 1945-75 and thereafter remains constant at a level  $\geq +0.8$  (see Section 5.2 for details).
3. Both reanalyses indicate a positive linear trend for the OND counts in Europe. They also agree on a meridional dipole in the sign of the trend during the JFM season, with positive values in northern and negative values in southern

Europe. In western North America, trends are consistently positive from British Columbia to the northern Gulf of Alaska. However, albeit the two reanalyses generally agree on the sign of the trends, they do not agree on whether the trends are significant or not, neither in Europe nor in western North America (see Section 5.3 for details).

These findings should be taken into account when evaluating the bias of e.g. the CMIP5 Earth System Models (Taylor et al., 2012) against either of the two long-term reanalyses, particularly during the early twentieth century. They are also expected to hinder the association of specific AR events from either of the two reanalyses with hydrological extreme events documented by other sources (e.g. Champion et al., 2015).

The search for the *precursors* of seasonal AR activity was conducted in Chapter 6, which is subdivided into the analysis of atmospheric and oceanic precursors (see Section 6.1 and 6.2). In what concerns the precursors in the atmosphere, the first working step consisted of tracing back the AR counts' link to the NAO or Aleutian Low (for the case of Europe and North America respectively) using the same 31-year running correlation analysis previously applied for reanalysis comparison. Note that, if not otherwise stated, the following results are *unambiguous* i.e. hold valid irrespective of the applied reanalysis and percentile thresholds used to define an AR. For comparison with other studies (e.g. Lavers et al., 2012; Ramos et al., 2015) the October-to-March (ONDJFM) season is considered in addition. The following main results were obtained (see Section 6.1.1 for details):

4. The AR-NAO links found in Europe depict a correlation dipole with positive values in the north and negative ones in the south that is reminiscent of the dipole found for precipitation in many previous studies (e.g. Hurrell, 1995).
5. During the course of the twentieth century, the correlation dipole in OND gradually moves northwards until approx. 1925-1955. From approx. 1955-1985 until 1980-2010, it then moves back to the south.
6. Due to large reanalysis uncertainties at the start of the century, the teleconnection patterns for western North America differ largely between the two long-term reanalyses until approximately 1940-1970. From 1940-1970 onwards, these uncertainties are generally small and results are likely to reflect real processes.
7. The degree of stationarity of the relationship to the Aleutian Low largely depends on the considered season. In British Columbia and the southern Gulf of Alaska a significantly negative link is found during the JFM season from 1955-85 onwards. During the OND season, this link gradually vanishes in the same period. In the northern Gulf of Alaska, the OND link is constantly at the the limit of significance during the whole second half of the century. The

respective JFM link steadily weakens, actually becoming insignificant from 1970-2000 onwards.

In Section 6.1.2, the search for atmospheric drivers of seasonal AR-occurrence counts was extended to circulation patterns others than the NAO and Aleutian Low. This was done for the period 1950-2010, during which reanalysis differences were found to be generally small in Chapter 5. The following main results were obtained:

8. In comparison to other circulation indices, the NAO is the most important atmospheric driver of AR activity in western Europe if the results are seen as a whole.
9. During the OND season, significantly positive links to the East Atlantic pattern were found along the Atlantic coast of Iberia and France. During this season, these are stronger in magnitude than the negative links to the NAO, which is consistent with the results from Ramos et al. (2015).
10. During both OND and JFM, significantly negative links to the Scandinavian index were found over the British Isles, which is consistent with the results from Lavers et al. (2012).
11. It was additionally shown that these negative links hold over Norway and that they are generally stronger during JFM than during OND.
12. If persistent instead of instantaneous ARs are considered, the NAO links were here found to drop to insignificance over the British Isles and western Iberia. This may partly explain why the respective links found in Lavers et al. (2012) and Ramos et al. (2015), obtained from considering persistent events only, are weak or even insignificant.
13. During the JFM season, significantly positive links to the PNA were found in British Columbia and in the entire Gulf of Alaska, which is in agreement with the results from Guan and Waliser (2015). During the OND season, these links are generally weaker, and insignificant in British Columbia.
14. During the JFM season, significantly negative links to the West Pacific pattern were found along the U.S. west coast.

### 9.1.2 Oceanic Teleconnections to Regional AR counts

In Section 6.2, the methods applied for assessing teleconnections triggered by the atmosphere (see Section 6.2), were exactly replicated for the teleconnections triggered by *sea surface temperatures* (SSTs). To this aim, in Section 6.2.1, the 31-year running correlation analysis was conducted for the link *between the Niño 3.4 index and the regional AR counts in both Europe and western North America*. The following main results were obtained:

15. In *none* of the 13 considered target regions, this link is significant during the entire study period. Rather, it is characterized by strong nonstationarities and significant results are only obtained during certain subperiods and seasons, specified as follows.
16. From approximately 1955-1975, the link is significantly positive along the the Bay of Biscay (i.e. in northern Iberia and western France) during the OND season. Prior to that period, namely in between approx. 1945-75 and 1950-80, the link is displaced to the south, being significant in Morocco, southern and western Iberia (in the latter region until 1974-2004).
17. In Europe, the link is strongest during the early twentieth century and the JFM season. For this period, significantly positive  $rs$  partly in excess of +0.8 are found from Morocco to western France, i.e. in five target regions as defined here. In these periods, the link experiences a harsh drop in magnitude in the time periods centred on the late 1930s.
18. In Scandinavia, the JFM link is significantly negative during the period 1915-45 to 1925-55.
19. Over the British Isles, the link is *insignificant* during the entire study period.
20. In western North America, the link is significantly positive from North California to British Columbia, but only after the Great Pacific Climate shift in 1976/77 (Mantua et al., 1997) and during the JFM season. These results are in agreement with Guan and Waliser (2015).
21. In the southern Gulf of Alaska, the OND link is significantly positive in between 1931-61 and 1943-73, i.e. prior to the Great Pacific Climate shift.
22. Albeit variations in the strength of the link are correlated with the time-mean AMO and/or PDO indices in some regions, this correlation is not significant if serial correlation is taken into account. This means that the statistical evidence for a modulation through the AMO or PDO is *weak*.

The seasonal AR counts's link to oceanic predictor variables others than the SST variations in the Niño 3.4 region were assessed in Section 6.2.2 for the fixed period 1950-2010. The following main findings were made:

23. Results for the Pacific Warm Pool index are in very close agreement to those obtained from the Niño 3.4 index indicating that the two indices can be used interchangeably to assess ENSO teleconnections in the context of the present study.
24. During the OND season, significantly positive links to the Tropical North Atlantic (TNA) pattern were found in Morocco and southern Iberia. During the JFM season, these links are significant only in Morocco.

25. During the OND season, relationships to the Western Hemisphere Warm Pool are similar to those found for the TNA. During the JFM season, these relationships are insignificant.
26. For the relationships with the AMO, a correlation dipole with positive  $rs$  in the north and negative  $rs$  in the south was detected during the OND season. However, only the negative relationships found in Morocco are significant.
27. Except for a few individual percentile thresholds, a significantly positive relationship with the PDO was found in northern Iberia and western France during the ONDJFM season.
28. The AR counts in western North America are more closely linked to the PDO than to any of the two ENSO indices. During the OND season, a significantly positive link is found in the northern Gulf of Alaska. During the JFM season, this link is displaced to the south, yielding significance in the southern Gulf of Alaska and British Columbia. The ONDJFM results lie in between, i.e. are significant in the southern and northern Gulf of Alaska.
29. The links to the IPO are similar to those obtained for the PDO, but systematically weaker.
30. Relationships with the NPGO are generally insignificant, except in northern California-Oregon-Washington, where this link is significantly negative during the JFM season for roughly half of the applied percentile threshold combinations, irrespective of the considered reanalysis.

All in all, the observational results for Europe indicate that the AR counts in OND around the Bay of Biscay are linked to ENSO during the late twentieth century and the recent past and that a more general ENSO link involving the entire European west coast including North Africa was active during the first half the century. This link has a dipole character reminiscent of the aforementioned link to the NAO, but with the signs reversed, i.e. El Niño events are associated with above-normal AR activity in southern Europe and below-normal activity in northern Europe. It is the AR count manifestation of the “canonical El Niño winter signal” (Broennimann, 2007), which was first described in Walker (1923, 1924) and Walker and Bliss (1932). Significant ENSO-AR links were found in more European than western North American regions. This is perhaps surprising, given the shorter geographical distance to the source region of the teleconnection, but can be explained by the poor reanalysis agreement in western North America at the start of the century and also by the impact of internal atmospheric variability on SST-induced teleconnections, summarized in the next Section. Concerning SST variables others than those describing ENSO, the TNA and WHWP are relevant in southern Europe. From British Columbia to the Gulf of Alaska, the PDO links are stronger than the ENSO links.

## 9.2 *Lessons learned from Idealized Numerical Model Experiments*

Apart from the observational approach summarized above, in Chapter 7, a second approach based on the results from idealized numerical modelling experiments was applied to shed some light on the question how observational results should be interpreted in the light of internal atmospheric variability. In this view, a teleconnection drawn from observation is the outcome of one *single* realization of the atmosphere responding to the observed external forcing. However, due to the probabilistic nature of the climate system (Lorenz, 1963), this response would have been different if the atmosphere would have been allowed to “re-run” once again with this forcing. A detailed description of this theoretical concept and its implications for the study of teleconnections was provided in Sections 2.4, 2.5 and 2.7.

In the present thesis, the atmosphere was allowed to re-run many times with the observed external forcing, thereby taking into account its probabilistic nature. This was done with the help of idealized of numerical model experiments run with Atmosphere General Circulation Models (AGCMs), used as surrogates for the real atmosphere (von Storch et al., 2004). For the sake of conciseness, only teleconnections triggered by ENSO were considered in the model world. Three distinct families of AGCM experiments were used for this purpose and each family is associated with specific statistical tests that would have been impossible to conduct<sup>1</sup> on the basis of the (deterministic) observational record only. The experiments and associated test, described in detail in Section 7.2, 7.1.1 and 7.1.2, comprised:

- A The AMIP experiments conducted within the framework of CMIP5 (Gates, 1992; Taylor et al., 2012), covering the period 1979-2008. A total of 13 experiments from 3 different AGCMs was applied. These experiments were run with the observed SST and sea-ice cover variations around the entire globe and are used to ask 1) if the observed ENSO-AR teleconnections are robust to perturbation due internal atmospheric variability and 2) if the nonstationarities in the teleconnections’ strength, seen in the observational record of the twentieth century, can be attributed to this kind of variability.
- B Home-made experiments with the Community Atmosphere Model 3.1 (CAM3.1 Collins et al., 2006). A total of 10 experiments was run over 32-model years. Each model year corresponds to a distinct forcing exerted by the SSTs in the Pacific Warmpool region Hoerling et al. (2001). In each year, the SST anomaly pattern gradually increases from realistic cold conditions to realistic warm conditions, reflecting la Niña events, neutral events and El Niño events. The ten distinct model runs were run at the High Performance Computing Cluster of the Santander Meteorology Group and differ from each other only by the initial conditions they were started from. As opposed to the AMIP

---

<sup>1</sup>the way it was done here

experiments, The SST forcing used for these experiments was *regionally confined* the tropical Pacific only. This experiment family was used to ask whether ENSO teleconnections to the OND AR counts in Europe hold if a *regional* forcing strategy is employed instead of the *global* one used to run the AMIP experiments. Confirmation would strengthen the hypothesis that SST variations in the tropical Pacific are indeed causal for the development of the teleconnection.

- C The ECMWF ERA-20CM ten-member AGCM ensemble covering the extended period 1900-2010 (Hersbach et al., 2015). The forcing of these experiments is similar to that of the AMIP experiments but more realistic since it comprises the effects of additional external forcing agents. This experiment family was used to extend the methodological concepts presented here to 1) other predictand variables, more commonly used than seasonal AR-counts, like e.g. seasonal mean temperature and aggregated precipitation and 2) other teleconnections than ENSO, namely the PDO and AMO. Thereby, the well-known ENSO teleconnections maps (e.g. Ropelewski and Halpert, 1987) and some nonstationarities seen in previous studies based on observations (e.g. Mariotti et al., 2002) were critically re-assessed, taking into account the effect of internal atmospheric variability.

With this experimental setup, the following main results were obtained:

31. ENSO-teleconnections to the regional AR-counts considered here are by no means robust to perturbation caused by internal atmospheric variability. This points to the fact that the few significant results seen in observations, e.g. for the OND AR counts in southern Europe, just arose because the unique realisation of internal atmospheric variability was favourable during the considered time period (1979-2008). This implies that the timing of future favourable conditions is essentially unpredictable (see Section 7.3.1).
32. For both the AMIP and CAM3.1 experiments, the ensemble-mean AR count response to ENSO is often similar to the observed response whereas the response seen in individual model experiments is not (see Section 7.3.1 and 7.3.2). An explanation for this could not be found in framework of the present thesis.
33. Similar to what is seen in observations, the ensemble-mean AR count response in OND obtained from CAM3.1 is significantly positive from Morocco to western France (see Section 7.3.2). This points to the fact that these counts are indeed *causally* related to SST variations in the tropical Pacific and corroborates similar results found for precipitation in previous studies (Shaman and Tziperman, 2011; Shaman, 2014b,a).
34. The particularly strong positive association between ENSO and the southern European AR counts, observed during the early twentieth century in JFM, can very likely *not* be attributed solely to variations due to internal atmospheric

variability in the recent past ( $\alpha = 0.05$  in most cases). Therefore, changes in the external forcing likely contributed to the development of the enhanced relationships in the early twentieth century (see Section 7.3.1).

35. The relationships between ENSO and the western North American AR counts observed prior to the Great Pacific Climate shift (Mantua et al., 1997) can be explained by post-shift variations due to internal climate variability ( $\alpha = 0.05$  in any case). This points to the fact that external forcing, as e.g. exerted by the PDO, is likely not needed to explain the nonstationarities found in observations (e.g. Gershunov and Barnett, 1998). See Section 7.3.1 for details.
36. An extension of the methodological concepts to a the ERA-20CM dataset reveals that ENSO teleconnections in the tropics are robust, whereas in the extratropics they are generally not, except in the areas affected by the Pacific-North American and Pacific-South American patterns (see Section 8.2.1).
37. Results do generally not improve in the extratropics when the robustness test is applied to specific sub-periods of the twentieth-century, during which significant correlations were found in previous studies based on observations (see Section 8.2.2).
38. ENSO teleconnections to North America during the FMA season, documented in observations by Diaz et al. (2001), constitute an exception from this general finding. Namely in the southern U.S. and Mexico, as well as to the south of the Aleutian Islands, the confidence interval for variations in the teleconnection due to internal atmospheric variability is larger after the Pacific Climate Shift than before, meaning that the robustness test proposed here is passed only during the former period (see Section 8.2.2).
39. The most striking result of the present thesis is that the nonstationarity of the ENSO teleconnection to western Mediterranean precipitation seen in observations (Mariotti et al., 2002) does not hold when internal atmospheric variability into account. Irrespective of the considered season<sup>2</sup>, this particular teleconnection is not found to be robust in any single 20-year period of the twentieth century (see Section 8.2.2).
40. Since the confidence interval describing variations in the strength of the aforementioned teleconnection is roughly constant along the entire twentieth century, no indication for a low-frequency modulation through any external forcing agent, e.g. suggested in Lopez-Parages and Rodriguez-Fonseca (2012), was found here.

---

<sup>2</sup>MAM and SON are considered here as in Mariotti et al. (2002)

41. In the extratropics, teleconnections exerted by the PDO and AMO are generally robust only in the direct vicinity of the source regions, namely in and around the the North Pacific and North Atlantic ocean basins, and more so for 2-metre air temperatures than for precipitation and variables describing atmospheric circulation. This points to the fact that only the response in the heat uptake (or cooling) of the air masses overlaying the anomalous SSTs is robust, whereas the circulation response is not. Exceptions were found to the south of the Aleutian Islands and in the subtropical central Pacific where the atmospheric circulation robustly responds to variations in the PDO. As well as the general circulation response in the tropics, these may, however, simply arise from co-variability with ENSO. Future work is needed to further assess these issues (see Section 8.2.3).

### 9.3 Future Work

The main constraint on the conclusions of the present thesis is that AGCMs are assumed to realistically reproduce the atmosphere's response to external forcing. Albeit the AGCMs applied here pass the model performance test proposed in Section 7.2 on most occasions, this is partly due to the fact that the modelled confidence intervals describing variations in the teleconnections' strength caused by internal climate variability is large, meaning that the statistical power of the test is low. There are two possible explanations for these large confidence intervals. The convenient explanation is that the real confidence intervals are indeed large. The less convenient one is that the AGCMs applied here overestimate the width of these intervals. Thus, perhaps the most important future working step is to simply repeat the analyses applied here to a the AMIP experiments from the Sixth Phase of the Coupled Model Intercomparison Project (CMIP6, [Eyring et al., 2016](#)). These will be run at a higher spatial and temporal resolution and, consequently, are expected to be more realistic than the AMIP experiments from CMIP5.

The methods proposed here might also be seen as a general framework to assess the robustness of *any* kind to teleconnection to the effects of internal atmospheric variability, provided that the external forcing agent presumably triggering the teleconnection is prescribed rather than internally simulated by the model. In the current generation of AMIP experiments, apart from the SSTs, this is also the case for sea-ice cover. However, the robustness test proposed here could be even applied to external forcing variables described by prognostic model variables if their climatology reasonably agrees with observations (e.g., [Furtado et al., 2015](#)). In this way, the presumable association between Eurasian snow cover in fall and the boreal winter climate on the northern Hemisphere ([Cohen and Entekhabi, 1999](#); [Brands et al., 2012c](#); [Brands, 2013](#); [Brands et al., 2014](#); [Brands, 2014](#)) could be re-assessed with the methods proposed here. In the light of the results found for ENSO here, it is hypothesized that these "snow-induced" links are equally not robust to the effects of internal atmospheric variability.

Also, instead of conducting the robustness test proposed here with the correlation coefficient it could also be conducted with the parameters of a statistical model or directly with the cross-validation results obtained from this model (e.g. [Eden et al., 2015](#)).

Finally, the robustness of externally forced teleconnections (as e.g. triggered by ENSO) to atmospheric river counts could be assessed on *global* scale. To this aim the AR detection algorithm developed in [Guan and Waliser \(2015\)](#) could be applied to a set of AMIP experiments, correlation worldmaps would be obtained for each experiment and the robustness test proposed here would then be conducted to this set of maps.



---

## Bibliography

- Bao, J., S. Michelson, P. Neiman, F. Ralph, and J. Wilczak, 2006: Interpretation of enhanced integrated water vapor bands associated with extratropical cyclones: their formation and connection to tropical moisture. *Mon. Weather Rev.*, **134** (4), 1063–1080, doi:{10.1175/MWR3123.1}.
- Barnston, A., and R. Livezey, 1987: Classification, seasonality and persistence of low-frequency atmospheric circulation patterns. *Mon. Weather Rev.*, **115** (6), 1083–1126, doi:{10.1175/1520-0493(1987)115<1083:CSAPOL>2.0.CO;2}.
- Barnston, A. G., M. K. Tippett, M. L. L’Heureux, S. Li, and D. G. DeWitt, 2012: Skill of real-time seasonal ENSO model predictions during 2002–11. Is our capability increasing? *Bull. Amer. Meteorol. Soc.*, **93** (5), 631–651, doi:{10.1175/BAMS-D-11-00111.1}.
- Barry, R., and A. Carleton, 2001: *Synoptic and dynamic climatology*. Routledge, London, UK.
- Bedia, J., S. Herrera, J. M. Gutierrez, G. Zavala, I. R. Urbieto, and J. M. Moreno, 2012: Sensitivity of fire weather index to different reanalysis products in the Iberian Peninsula. *Nat. Hazards Earth Syst. Sci.*, **12** (3), 699–708, doi:{10.5194/nhess-12-699-2012}.
- Bengtsson, L., and J. Shukla, 1988: Integration of space and in situ observations to study global climate change. *Bull. Amer. Meteorol. Soc.*, **69** (10), 1130–&, doi:{10.1175/1520-0477(1988)069<1130:IOSAIS>2.0.CO;2}.
- Bentsen, M., and Coauthors, 2013: The Norwegian Earth System Model, NorESM1-M - Part 1: description and basic evaluation of the physical climate. *Geosci. Model Dev.*, **6** (3), 687–720, doi:{10.5194/gmd-6-687-2013}.

- Bjerknes, J., 1969: Atmospheric teleconnections from the equatorial Pacific. *Mon. Weather Rev.*, **97** (3), 163–182, doi:{10.1175/1520-0493(1969)097<0163:ATFTEP>2.3.CO;2}.
- Bonan, G., K. Oleson, M. Vertenstein, S. Levis, X. Zeng, Y. Dai, R. Dickinson, and Z. Yang, 2002: The land surface climatology of the community land model coupled to the NCAR community climate model. *J. Clim.*, **15** (22), 3123–3149, doi:{10.1175/1520-0442(2002)015<3123:TLSCOT>2.0.CO;2}.
- Brands, S., 2013: Skillful seasonal predictions of boreal winter accumulated heating degree-days and relevance for the weather derivative market. *J. Appl. Meteorol. Climatol.*, **52** (6), 1297–1302, doi:{10.1175/JAMC-D-12-0303.1}.
- Brands, S., 2014: Predicting average wintertime wind and wave conditions in the North Atlantic sector from Eurasian snow cover in October. *Environ. Res. Lett.*, **9** (4), doi:{10.1088/1748-9326/9/4/045006}.
- Brands, S., 2017: Which ENSO teleconnections are robust to internal atmospheric variability? *Geophys. Res. Lett.*, **44** (3), 1483–1493, doi:{10.1002/2016GL071529}.
- Brands, S., J. M. Gutierrez, A. S. Cofino, and S. Herrera, 2012a: Comments on “Global and regional comparison of daily 2-m and 1000-hPa maximum and minimum temperatures in three global reanalyses”. *J. Clim.*, **25** (22), 8004–8006, doi:{10.1175/JCLI-D-12-00122.1}.
- Brands, S., J. M. Gutierrez, S. Herrera, and A. S. Cofino, 2012b: On the use of reanalysis data for downscaling. *J. Clim.*, **25** (7), 2517–2526, doi:{10.1175/JCLI-D-11-00251.1}.
- Brands, S., J. M. Gutiérrez, and D. San-Martín, 2017: Twentieth-century atmospheric river activity along the west coasts of Europe and North America: algorithm formulation, reanalysis uncertainty and links to atmospheric circulation patterns. *Clim. Dyn.*, **48** (9), 2771–2795, doi:{10.1007/s00382-016-3095-6}.
- Brands, S., S. Herrera, J. Fernandez, and J. M. Gutierrez, 2013: How well do CMIP5 Earth System Models simulate present climate conditions in Europe and Africa? *Clim. Dyn.*, **41** (3-4), 803–817, doi:{10.1007/s00382-013-1742-8}.
- Brands, S., S. Herrera, and J. M. Gutierrez, 2014: Is Eurasian snow cover in October a reliable statistical predictor for the wintertime climate on the Iberian Peninsula? *Int. J. Climatol.*, **34** (5), 1615–1627, doi:{10.1002/joc.3788}.
- Brands, S., S. Herrera, D. San-Martin, and J. M. Gutierrez, 2011: Validation of the ENSEMBLES global climate models over southwestern Europe using probability density functions, from a downscaling perspective. *Clim. Res.*, **48** (2-3), 145–161, doi:{10.3354/cr00995}.

- Brands, S., R. Manzanas, J. M. Gutierrez, and J. Cohen, 2012c: Seasonal predictability of wintertime precipitation in Europe using the snow advance index. *J. Clim.*, **25** (12), 4023–4028, doi:{10.1175/JCLI-D-12-00083.1}.
- Branstator, G., 1985: Analysis of general-circulation model sea-surface temperature anomaly simulations using a linear model. Part 1: forced solutions. *J. Atmos. Sci.*, **42** (21), 2225–2241, doi:{10.1175/1520-0469(1985)042<2225:AOGCMS>2.0.CO;2}.
- Bretherton, C., M. Widmann, V. Dymnikov, J. Wallace, and I. Blade, 1999: The effective number of spatial degrees of freedom of a time-varying field. *J. Clim.*, **12** (7), 1990–2009, doi:{10.1175/1520-0442(1999)012<1990:TENOSD>2.0.CO;2}.
- Broennimann, S., 2007: Impact of El Niño Southern Oscillation on European climate. *Rev. Geophys.*, **45** (2), doi:{10.1029/2006RG000199}.
- Broennimann, S., and Coauthors, 2009: Variability of large-scale atmospheric circulation indices for the Northern Hemisphere during the past 100 years. *Meteorol. Z.*, **18** (4, SI), 379–396, doi:{10.1127/0941-2948/2009/0389}.
- Browning, K. A., 1974: Mesoscale structure of rain systems in the British Isles. *J. Meteor. Soc. Japan*, **52** (3), 314–327.
- Butler, A. H., L. M. Polvani, and C. Deser, 2014: Separating the stratospheric and tropospheric pathways of El Niño-Southern Oscillation teleconnections. *Environ. Res. Lett.*, **9** (2), doi:{10.1088/1748-9326/9/2/024014}.
- Casanueva, A., C. Rodriguez-Puebla, M. D. Frias, and N. Gonzalez-Reviriego, 2014: Variability of extreme precipitation over Europe and its relationships with teleconnection patterns. *Hydrol. Earth Syst. Sci.*, **18** (2), 709–725, doi:{10.5194/hess-18-709-2014}.
- Champion, A. J., R. P. Allan, and D. A. Lavers, 2015: Atmospheric rivers do not explain UK summer extreme rainfall. *J. Geophys. Res.-Atmos.*, **120** (14), 6731–6741, doi:{10.1002/2014JD022863}.
- Charlton-Perez, A. J., and Coauthors, 2013: On the lack of stratospheric dynamical variability in low-top versions of the CMIP5 models. *J. Geophys. Res.-Atmos.*, **118** (6), 2494–2505, doi:{10.1002/jgrd.50125}.
- Chiang, J., Y. Kushnir, and A. Giannini, 2002: Deconstructing Atlantic Intertropical Convergence Zone variability: Influence of the local cross-equatorial sea surface temperature gradient and remote forcing from the eastern equatorial Pacific. *J. Geophys. Res.-Atmos.*, **107** (D1-D2), doi:{10.1029/2000JD000307}.
- Chiang, J., and A. Sobel, 2002: Tropical tropospheric temperature variations caused by ENSO and their influence on the remote tropical climate. *J. Clim.*, **15** (18), 2616–2631, doi:{10.1175/1520-0442(2002)015<2616:TTTVCB>2.0.CO;2}.

- Cohen, J., and D. Entekhabi, 1999: Eurasian snow cover variability and Northern Hemisphere climate predictability. *Geophys. Res. Lett.*, **26** (3), 345–348, doi:{10.1029/1998GL900321}.
- Collins, W. D., and Coauthors, 2006: The formulation and atmospheric simulation of the Community Atmosphere Model version 3 (CAM3). *J. Clim.*, **19** (11), 2144–2161, doi:{10.1175/JCLI3760.1}.
- Compo, G. P., and Coauthors, 2011: The Twentieth Century Reanalysis Project. *Q. J. R. Meteorol. Soc.*, **137** (654, A), 1–28, doi:{10.1002/qj.776}.
- Cram, T. A., and Coauthors, 2015: The International Surface Pressure Databank version 2. *Geosci. Data J.*, **2** (1), 31–46, doi:{10.1002/gdj3.25}.
- Dacre, H. F., P. A. Clark, O. Martinez-Alvarado, M. A. Stringer, and D. A. Lavers, 2015: How do atmospheric rivers form? *Bull. Amer. Meteorol. Soc.*, **96** (8), 1243–1255, doi:{10.1175/BAMS-D-14-00031.1}.
- Dee, D. P., and Coauthors, 2011: The ERA-Interim reanalysis: configuration and performance of the data assimilation system. *Q. J. R. Meteorol. Soc.*, **137** (656, Part a), 553–597, doi:{10.1002/qj.828}.
- Deser, C., A. Phillips, and J. Hurrell, 2004: Pacific interdecadal climate variability: linkages between the tropics and the North Pacific during boreal winter since 1900. *J. Clim.*, **17** (16), 3109–3124, doi:{10.1175/1520-0442(2004)017<3109:PICVLB>2.0.CO;2}.
- Dettinger, M. D., F. M. Ralph, T. Das, P. J. Neiman, and D. R. Cayan, 2011: Atmospheric rivers, floods and the water resources of California. *Water*, **3** (2), 445–478, doi:{10.3390/w3020445}.
- Di Lorenzo, E., and Coauthors, 2008: North Pacific Gyre Oscillation links ocean climate and ecosystem change. *Geophys. Res. Lett.*, **35** (8), doi:{10.1029/2007GL032838}.
- Diaz, H., M. Hoerling, and J. Eischeid, 2001: ENSO variability, teleconnections and climate change. *Int. J. Climatol.*, **21** (15), 1845–1862, doi:{10.1002/joc.631}.
- Dufresne, J.-L., and Coauthors, 2013: Climate change projections using the IPSL-CM5 Earth System Model: from CMIP3 to CMIP5. *Clim. Dyn.*, **40** (9-10, SI), 2123–2165, doi:{10.1007/s00382-012-1636-1}.
- Eden, J. M., G. J. van Oldenborgh, E. Hawkins, and E. B. Suckling, 2015: A global empirical system for probabilistic seasonal climate prediction. *Geosci. Model Dev.*, **8** (12), 3947–3973, doi:{10.5194/gmd-8-3947-2015}.

- Eiras-Barca, J., S. Brands, and G. Miguez-Macho, 2016: Seasonal variations in North Atlantic atmospheric river activity and associations with anomalous precipitation over the Iberian Atlantic Margin. *J. Geophys. Res.-Atmos.*, **121** (2), 931–948, doi:{10.1002/2015JD023379}.
- Enfield, D., A. Mestas-Nunez, D. Mayer, and L. Cid-Serrano, 1999: How ubiquitous is the dipole relationship in tropical Atlantic sea surface temperatures? *J. Geophys. Res.-Oceans*, **104** (C4), 7841–7848, doi:{10.1029/1998JC900109}.
- Enfield, D., A. Mestas-Nunez, and P. Trimble, 2001: The Atlantic Multidecadal Oscillation and its relation to rainfall and river flows in the continental US. *Geophys. Res. Lett.*, **28** (10), 2077–2080, doi:{10.1029/2000GL012745}.
- Eyring, V., S. Bony, G. A. Meehl, C. A. Senior, B. Stevens, R. J. Stouffer, and K. E. Taylor, 2016: Overview of the Coupled Model Intercomparison Project Phase 6 (CMIP6) experimental design and organization. *Geosci. Model Dev.*, **9** (5), 1937–1958, doi:{10.5194/gmd-9-1937-2016}.
- Fasullo, J. T., and K. E. Trenberth, 2008: The annual cycle of the energy budget. Part II: meridional structures and poleward transports. *J. Clim.*, **21** (10), 2313–2325, doi:{10.1175/2007JCLI1936.1}.
- Franzke, C., S. B. Feldstein, and S. Lee, 2011: Synoptic analysis of the Pacific-North American teleconnection pattern. *Q. J. R. Meteorol. Soc.*, **137** (655, B), 329–346, doi:{10.1002/qj.768}.
- Frias, M. D., S. Herrera, A. S. Cofino, and J. M. Gutierrez, 2010: Assessing the skill of precipitation and temperature seasonal forecasts in Spain: windows of opportunity related to ENSO events. *J. Clim.*, **23** (2), 209–220, doi:{10.1175/2009JCLI2824.1}.
- Furtado, J. C., J. L. Cohen, A. H. Butler, E. E. Riddle, and A. Kumar, 2015: Eurasian snow cover variability and links to winter climate in the CMIP5 models. *Clim. Dyn.*, **45** (9-10), 2591–2605, doi:{10.1007/s00382-015-2494-4}.
- Gamiz-Fortis, S., D. Pozo-Vazquez, R. M. Trigo, and Y. Castro-Diez, 2008: Quantifying the predictability of winter river flow in Iberia. Part II: seasonal predictability. *J. Clim.*, **21** (11), 2503–2518, doi:{10.1175/2007JCLI1775.1}.
- Garaboa-Paz, D., J. Eiras-Barca, F. Huhn, and V. Perez-Munuzuri, 2015: Lagrangian coherent structures along atmospheric rivers. *Chaos*, **25** (6), doi:{10.1063/1.4919768}.
- Garreaud, R. D., M. Vuille, R. Compagnucci, and J. Marengo, 2009: Present-day South American climate. *Paleogeogr. Paleoclimatol. Paleoecol.*, **281** (3-4, SI), 180–195, doi:{10.1016/j.palaeo.2007.10.032}.

- Gates, W., 1992: AMIP - The Atmospheric Model Intercomparison Project. *Bull. Amer. Meteorol. Soc.*, **73** (12), 1962–1970, doi:{10.1175/1520-0477(1992)073(1962:ATAMIP)2.0.CO;2}.
- Gershunov, A., and T. Barnett, 1998: Interdecadal modulation of ENSO teleconnections. *Bull. Amer. Meteorol. Soc.*, **79** (12), 2715–2725, doi:{10.1175/1520-0477(1998)079(2715:IMOET)2.0.CO;2}.
- Gimeno, L., R. Nieto, M. Vázquez, and D. Lavers, 2014: Atmospheric rivers: a mini-review. *Front. Earth Sci.*, **5** (2), doi:doi:10.3389/feart.2014.00002.
- Gimeno, L., and Coauthors, 2012: Oceanic and terrestrial sources of continental precipitation. *Rev. Geophys.*, **50**, doi:{10.1029/2012RG000389}.
- Gimeno, L., and Coauthors, 2016: Major mechanisms of atmospheric moisture transport and their role in extreme precipitation events. *Annu. Rev. Environ. Resour.*, **41**, 117–141, doi:10.1146/annurev-environ-110615-085558.
- Giorgi, F., and R. Francisco, 2000: Uncertainties in regional climate change prediction: a regional analysis of ensemble simulations with the HadCM2 coupled AOGCM. *Clim. Dyn.*, **16** (2-3), 169–182, doi:{10.1007/PL00013733}.
- Gorodetskaya, I. V., M. Tsukernik, K. Claes, M. F. Ralph, W. D. Neff, and N. P. M. Van Lipzig, 2014: The role of atmospheric rivers in anomalous snow accumulation in East Antarctica. *Geophys. Res. Lett.*, **41** (17), 6199–6206, doi:{10.1002/2014GL060881}.
- Grotch, S., and M. MacCracken, 1991: The use of general circulation models to predict regional climatic change. *J. Clim.*, **4** (3), 286–303, doi:{10.1175/1520-0442(1991)004(0286:TUOGCM)2.0.CO;2}.
- Guan, B., N. P. Molotch, D. E. Waliser, E. J. Fetzer, and P. J. Neiman, 2013: The 2010/2011 snow season in California’s Sierra Nevada: Role of atmospheric rivers and modes of large-scale variability. *Water Resour. Res.*, **49** (10), 6731–6743, doi:{10.1002/wrcr.20537}.
- Guan, B., and D. E. Waliser, 2015: Detection of atmospheric rivers: evaluation and application of an algorithm for global studies. *J. Geophys. Res.-Atmos*, **120** (24), 12 514–12 535, doi:{10.1002/2015JD024257}.
- Guan, B., D. E. Waliser, N. P. Molotch, E. J. Fetzer, and P. J. Neiman, 2012: Does the Madden-Julian Oscillation influence wintertime atmospheric rivers and snowpack in the Sierra Nevada? *Mon. Weather Rev.*, **140** (2), 325–342, doi:{10.1175/MWR-D-11-00087.1}.

- Guemas, V., L. Auger, and F. J. Doblas-Reyes, 2014: Hypothesis testing for autocorrelated short climate time series. *J. Appl. Meteorol. Climatol.*, **53** (3), 637–651, doi:{10.1175/JAMC-D-13-064.1}.
- Gutiérrez, J., R. Cano, A. Cofiño, and C. M. Sordo, 2004: *Redes probabilísticas y neuronales en las ciencias de la atmósfera*. Ministerio de Medio Ambiente, Madrid, Spain, 249 pp.
- Halpert, M., and C. Ropelewski, 1992: Surface-temperature patterns associated with the Southern Oscillation. *J. Clim.*, **5** (6), 577–593, doi:{10.1175/1520-0442(1992)005<0577:STPAWT>2.0.CO;2}.
- Hannachi, A., I. T. Jolliffe, and D. B. Stephenson, 2007: Empirical orthogonal functions and related techniques in atmospheric science: a review. *Int. J. Climatol.*, **27** (9), 1119–1152, doi:{10.1002/joc.1499}.
- Hardiman, S. C., N. Butchart, P. H. Haynes, and S. H. E. Hare, 2007: A note on forced versus internal variability of the stratosphere. *Geophys. Res. Lett.*, **34** (12), doi:{10.1029/2007GL029726}.
- Henley, B. J., J. Gergis, D. J. Karoly, S. Power, J. Kennedy, and C. K. Folland, 2015: A tripole index for the Interdecadal Pacific Oscillation. *Clim. Dyn.*, **45** (11-12), 3077–3090, doi:{10.1007/s00382-015-2525-1}.
- Hersbach, H., C. Peubey, A. Simmons, P. Berrisford, P. Poli, and D. Dee, 2015: ERA-20CM: a twentieth-century atmospheric model ensemble. *Q. J. R. Meteorol. Soc.*, **141** (691, B), 2350–2375, doi:{10.1002/qj.2528}.
- Higgins, R., J. Schemm, W. Shi, and A. Leetmaa, 2000: Extreme precipitation events in the western United States related to tropical forcing. *J. Clim.*, **13** (4), 793–820, doi:{10.1175/1520-0442(2000)013<0793:EPEITW>2.0.CO;2}.
- Hoerling, M., A. Kumar, and T. Xu, 2001: Robustness of the nonlinear climate response to ENSO's extreme phases. *J. Clim.*, **14** (6), 1277–1293, doi:{10.1175/1520-0442(2001)014<1277:ROTNCR>2.0.CO;2}.
- Horel, J., and J. Wallace, 1981: Planetary-scale atmospheric phenomena associated with the Southern Oscillation. *Mon. Weather Rev.*, **109** (4), 813–829, doi:{10.1175/1520-0493(1981)109<0813:PSAPAW>2.0.CO;2}.
- Hourdin, F., and Coauthors, 2013: Impact of the LMDZ atmospheric grid configuration on the climate and sensitivity of the IPSL-CM5A coupled model. *Clim. Dyn.*, **40** (9-10, SI), 2167–2192, doi:{10.1007/s00382-012-1411-3}.
- Hurrell, J., 1995: Decadal trends in the North-Atlantic Oscillation - Regional temperatures and precipitation. *Science*, **269** (5224), 676–679, doi:{10.1126/science.269.5224.676}.

- Hurrell, J., Y. Kushnir, G. Ottersen, and M. Visbeck, 2003: *The North Atlantic Oscillation: climate significance and environmental impact*, Geophysical Monograph Series, Vol. 134. AGU, Washington, D. C., 279 pp.
- Iglesias, I., M. N. Lorenzo, and J. J. Taboada, 2014: Seasonal predictability of the East Atlantic pattern from sea surface temperatures. *PLoS One*, **9** (1), doi: {10.1371/journal.pone.0086439}.
- Ineson, S., and A. A. Scaife, 2009: The role of the stratosphere in the European climate response to El Niño. *Nat. Geosci.*, **2** (1), 32–36, doi: {10.1038/NGEO381}.
- Jiang, T., and Y. Deng, 2011: Downstream modulation of North Pacific atmospheric river activity by East Asian cold surges. *Geophys. Res. Lett.*, **38**, doi: {10.1029/2011GL049462}.
- Kalnay, E., and Coauthors, 1996: The NCEP/NCAR 40-year reanalysis project. *Bull. Amer. Meteorol. Soc.*, **77** (3), 437–471.
- Kennedy, J., and Coauthors, 2015: The Met Office Hadley Centre Sea Ice and Sea-Surface Temperature data set, version 2: 2. Sea-surface temperature analysis. *in preparation*.
- Kerr, R., 2000: A North Atlantic climate pacemaker for the centuries. *Science*, **288** (5473), 1984–1986, doi: {10.1126/science.288.5473.1984}.
- Kim, H.-M., and M. A. Alexander, 2015: ENSO’s modulation of water vapor transport over the Pacific-North American region. *J. Clim.*, **28** (9), 3846–3856, doi: {10.1175/JCLI-D-14-00725.1}.
- Kim, J., D. E. Waliser, P. J. Neiman, B. Guan, J.-M. Ryoo, and G. A. Wick, 2013: Effects of atmospheric river landfalls on the cold season precipitation in California. *Clim. Dyn.*, **40** (1-2), 465–474, doi: {10.1007/s00382-012-1322-3}.
- Kirkevåg, A., and Coauthors, 2013: Aerosol-climate interactions in the Norwegian Earth System Model-NorESM1-M. *Geosci. Model Dev.*, **6** (1), 207–244, doi: {10.5194/gmd-6-207-2013}.
- Knippertz, P., and H. Wernli, 2010: A Lagrangian climatology of tropical moisture exports to the Northern Hemispheric extratropics. *J. Clim.*, **23** (4), 987–1003, doi: {10.1175/2009JCLI3333.1}.
- Knippertz, P., H. Wernli, and G. Glaeser, 2013: A global climatology of tropical moisture exports. *J. Clim.*, **26** (10), 3031–3045, doi: {10.1175/JCLI-D-12-00401.1}.
- Kok, C., and J. Opsteegh, 1985: Possible causes of anomalies in seasonal mean circulation patterns during the 1982-83 El Niño event. *J. Atmos. Sci.*, **42** (7), 677–694, doi: {10.1175/1520-0469(1985)042<0677:PCOAIS>2.0.CO;2}.

- Kumar, A., and M. Hoerling, 1995: Prospects and limitations of seasonal atmospheric GCM predictions. *Bull. Amer. Meteorol. Soc.*, **76** (3), 335–345, doi:{10.1175/1520-0477(1995)076<0335:PALOSA>2.0.CO;2}.
- Kumar, K., B. Rajagopalan, and M. Cane, 1999: On the weakening relationship between the Indian monsoon and ENSO. *Science*, **284** (5423), 2156–2159, doi:{10.1126/science.284.5423.2156}.
- Lavers, D. A., R. P. Allan, G. Villarini, B. Lloyd-Hughes, D. J. Brayshaw, and A. J. Wade, 2013: Future changes in atmospheric rivers and their implications for winter flooding in Britain. *Environ. Res. Lett.*, **8** (3), doi:{10.1088/1748-9326/8/3/034010}.
- Lavers, D. A., R. P. Allan, E. F. Wood, G. Villarini, D. J. Brayshaw, and A. J. Wade, 2011: Winter floods in Britain are connected to atmospheric rivers. *Geophys. Res. Lett.*, **38**, doi:{10.1029/2011GL049783}.
- Lavers, D. A., and G. Villarini, 2013: The nexus between atmospheric rivers and extreme precipitation across Europe. *Geophys. Res. Lett.*, **40** (12), 3259–3264, doi:{10.1002/grl.50636}.
- Lavers, D. A., and G. Villarini, 2015: The contribution of atmospheric rivers to precipitation in Europe and the United States. *J. Hydrol.*, **522**, 382–390, doi:{10.1016/j.jhydrol.2014.12.010}.
- Lavers, D. A., G. Villarini, R. P. Allan, E. F. Wood, and A. J. Wade, 2012: The detection of atmospheric rivers in atmospheric reanalyses and their links to British winter floods and the large-scale climatic circulation. *J. Geophys. Res.-Atmos.*, **117**, doi:{10.1029/2012JD018027}.
- Leathers, D., B. Yarnal, and M. Palecki, 1991: The Pacific-North American Teleconnection pattern and United States Climate. Part 1: regional temperature and precipitation associations. *J. Clim.*, **4** (5), 517–528, doi:{10.1175/1520-0442(1991)004<0517:TPATPA>2.0.CO;2}.
- Leung, L. R., and Y. Qian, 2009: Atmospheric rivers induced heavy precipitation and flooding in the western US simulated by the WRF regional climate model. *Geophys. Res. Lett.*, **36**, doi:{10.1029/2008GL036445}.
- Liu, X., X. Ren, and X.-Q. Yang, 2016: Decadal changes in multiscale water vapor transport and atmospheric river associated with the Pacific Decadal Oscillation and the North Pacific Gyre Oscillation. *J. Hydrometeorol.*, **17** (1), 273–285, doi:{10.1175/JHM-D-14-0195.1}.
- Lopez-Parages, J., and B. Rodriguez-Fonseca, 2012: Multidecadal modulation of El Niño influence on the Euro-Mediterranean rainfall. *Geophys. Res. Lett.*, **39**, doi:{10.1029/2011GL050049}.

- Lorenz, E., 1963: Deterministic nonperiodic flow. *J. Atmos. Sci.*, **20** (2), 130–141, doi:{10.1175/1520-0469(1963)020(0130:DNF)2.0.CO;2}.
- Lorenzo, M. N., J. J. Taboada, and L. Gimeno, 2008: Links between circulation weather types and teleconnection patterns and their influence on precipitation patterns in Galicia (NW Spain). *Int. J. Climatol.*, **28** (11), 1493–1505, doi:{10.1002/joc.1646}.
- Madden, R., and P. Julian, 1971: Detection of a 40-50 day oscillation in the zonal wind in the tropical Pacific. *J. Atmos. Sci.*, **28** (5), 702–&, doi:{10.1175/1520-0469(1971)028(0702:DOADOI)2.0.CO;2}.
- Mann, H. B., 1945: Nonparametric tests against trend. *Econometrica*, **13** (3), 245–259, doi:{10.2307/1907187}.
- Mantua, N., S. Hare, Y. Zhang, J. Wallace, and R. Francis, 1997: A Pacific interdecadal climate oscillation with impacts on salmon production. *Bull. Amer. Meteorol. Soc.*, **78** (6), 1069–1079, doi:{10.1175/1520-0477(1997)078(1069:APICOW)2.0.CO;2}.
- Manzanas, R., S. Brands, D. San-Martin, A. Lucero, C. Limbo, and J. M. Gutierrez, 2015: Statistical downscaling in the tropics can be sensitive to reanalysis choice: a case study for precipitation in the Philippines. *J. Clim.*, **28** (10), 4171–4184, doi:{10.1175/JCLI-D-14-00331.1}.
- Maraun, D., and Coauthors, 2010: Precipitation downscaling under climate change: recent developments to bridge the gap between dynamical models and the end user. *Rev. Geophys.*, **48**, doi:{10.1029/2009RG000314}.
- Mariotti, A., N. Zeng, and K. Lau, 2002: Euro-Mediterranean rainfall and ENSO - a seasonally varying relationship. *Geophys. Res. Lett.*, **29** (12), doi:{10.1029/2001GL014248}.
- McPhaden, M. J., S. E. Zebiak, and M. H. Glantz, 2006: ENSO as an integrating concept in Earth science. *Science*, **314** (5806), 1740–1745, doi:{10.1126/science.1132588}.
- Mo, K., and J. Paegle, 2001: The Pacific-South American modes and their downstream effects. *Int. J. Climatol.*, **21** (10), 1211–1229, doi:{10.1002/joc.685}.
- Murphy, A., and R. Winkler, 1987: A general framework for forecast verification. *Mon. Weather Rev.*, **115** (7), 1330–1338, doi:{10.1175/1520-0493(1987)115(1330:AGFFFV)2.0.CO;2}.
- Neale, R. B., J. Richter, S. Park, P. H. Lauritzen, S. J. Vavrus, P. J. Rasch, and M. Zhang, 2013: The mean climate of the Community Atmosphere Model (CAM4)

- in forced SST and fully coupled experiments. *J. Clim.*, **26** (14), 5150–5168, doi:{10.1175/JCLI-D-12-00236.1}.
- Neiman, P., P. Persson, F. Ralph, D. Jorgensen, A. White, and D. Kingsmill, 2004: Modification of fronts and precipitation by coastal blocking during an intense landfalling winter storm in southern California: observations during CALJET. *Mon. Weather Rev.*, **132** (1), 242–273, doi:{10.1175/1520-0493(2004)132<0242:MOFAPB>2.0.CO;2}.
- Neiman, P., F. Ralph, A. White, D. Kingsmill, and P. Persson, 2002: The statistical relationship between upslope flow and rainfall in California’s coastal mountains: observations during CALJET. *Mon. Weather Rev.*, **130** (6), 1468–1492, doi:{10.1175/1520-0493(2002)130<1468:TSRBUF>2.0.CO;2}.
- Neiman, P. J., F. M. Ralph, G. A. Wick, J. D. Lundquist, and M. D. Dettinger, 2008: Meteorological characteristics and overland precipitation impacts of atmospheric rivers affecting the west coast of North America based on eight years of SSM/I satellite observations. *J. Hydrometeorol.*, **9** (1), 22–47, doi:{10.1175/2007JHM855.1}.
- New, M., M. Hulme, and P. Jones, 2000: Representing twentieth-century space-time climate variability. Part II: development of 1901–96 monthly grids of terrestrial surface climate. *J. Clim.*, **13** (13), 2217–2238, doi:{10.1175/1520-0442(2000)013<2217:RTCSTC>2.0.CO;2}.
- Newell, R., N. Newell, Y. Zhu, and C. Scott, 1992: Tropospheric Rivers? - A pilot study. *Geophys. Res. Lett.*, **19** (24), 2401–2404, doi:{10.1029/92GL02916}.
- Newman, M., G. N. Kiladis, K. M. Weickmann, F. M. Ralph, and P. D. Sardeshmukh, 2012: Relative contributions of synoptic and low-frequency eddies to time-mean atmospheric moisture transport, including the role of atmospheric rivers. *J. Clim.*, **25** (21), 7341–7361, doi:{10.1175/JCLI-D-11-00665.1}.
- Niiler, P., N. Maximenko, and J. McWilliams, 2003: Dynamically balanced absolute sea level of the global ocean derived from near-surface velocity observations. *Geophys. Res. Lett.*, **30** (22), doi:{10.1029/2003GL018628}.
- Nobre, P., and J. Shukla, 1996: Variations of sea surface temperature, wind stress, and rainfall over the tropical Atlantic and South America. *J. Clim.*, **9** (10), 2464–2479, doi:{10.1175/1520-0442(1996)009<2464:VOSSTW>2.0.CO;2}.
- Palmer, T., 1999: A nonlinear dynamical perspective on climate prediction. *J. Clim.*, **12** (2), 575–591, doi:{10.1175/1520-0442(1999)012<0575:ANDPOC>2.0.CO;2}.
- Palmer, T., F. Doblas-Reyes, R. Hagedorn, and A. Weisheimer, 2005: Probabilistic prediction of climate using multi-model ensembles: from basics to applications.

- Philos. Trans. R. Soc. B-Biol. Sci.*, **360** (1463), 1991–1998, doi:{10.1098/rstb.2005.1750}.
- Payne, A. E., and G. Magnusdottir, 2014: Dynamics of landfalling atmospheric rivers over the North Pacific in 30 years of MERRA reanalysis. *J. Clim.*, **27** (18), 7133–7150, doi:{10.1175/JCLI-D-14-00034.1}.
- Payne, A. E., and G. Magnusdottir, 2015: An evaluation of atmospheric rivers over the North Pacific in CMIP5 and their response to warming under RCP 8.5. *J. Geophys. Res.-Atmos.*, **120** (21), 11 173–11 190, doi:{10.1002/2015JD023586}.
- Pereira, S., A. M. Ramos, J. L. Zezere, R. M. Trigo, and J. M. Vaquero, 2016: Spatial impact and triggering conditions of the exceptional hydro-geomorphological event of December 1909 in Iberia. *Nat. Hazards Earth Syst. Sci.*, **16** (2), 371–390, doi:{10.5194/nhess-16-371-2016}.
- Poli, P., and Coauthors, 2016: ERA-20C: An atmospheric reanalysis of the twentieth century. *J. Clim.*, **29** (11), 4083–4097, doi:{10.1175/JCLI-D-15-0556.1}.
- Qian, B., J. Corte-Real, and H. Xu, 2000: Is the North Atlantic Oscillation the most important atmospheric pattern for precipitation in Europe? *J. Geophys. Res.-Atmos.*, **105** (D9), 11 901–11 910, doi:{10.1029/2000JD900102}.
- Quayle, R., 1989: The Wolbach dataset for global climate monitoring - philanthropy and climatology. *Bull. Amer. Meteorol. Soc.*, **70** (12), 1570.
- Ralph, F., P. Neiman, and G. Wick, 2004: Satellite and CALJET aircraft observations of atmospheric rivers over the eastern North Pacific ocean during the winter of 1997/98. *Mon. Weather Rev.*, **132** (7), 1721–1745, doi:{10.1175/1520-0493(2004)132<1721:SACAOO>2.0.CO;2}.
- Ralph, F. M., T. Coleman, P. J. Neiman, R. J. Zamora, and M. D. Dettinger, 2013: Observed impacts of duration and seasonality of atmospheric-river landfalls on soil moisture and runoff in coastal northern California. *J. Hydrometeorol.*, **14** (2), 443–459, doi:{10.1175/JHM-D-12-076.1}.
- Ramos, A. M., R. Tome, R. M. Trigo, M. L. R. Liberato, and J. G. Pinto, 2016: Projected changes in atmospheric rivers affecting Europe in CMIP5 models. *Geophys. Res. Lett.*, **43** (17), 9315–9323, doi:{10.1002/2016GL070634}.
- Ramos, A. M., R. M. Trigo, M. L. R. Liberato, and R. Tome, 2015: Daily precipitation extreme events in the Iberian Peninsula and its association with atmospheric rivers. *J. Hydrometeorol.*, **16** (2), 579–597, doi:{10.1175/JHM-D-14-0103.1}.
- Rayner, N., E. Horton, D. Parker, C. Folland, and R. Hackett, 1996: Version 2.2 of the Global sea-Ice and Sea Surface Temperature data set, 1903–1994. *Climate Research Technical Note 74*, Bracknell, UK, Hadley Centre, 21 pp.

- Rayner, N., D. Parker, E. Horton, C. Folland, L. Alexander, D. Rowell, E. Kent, and A. Kaplan, 2003: Global analyses of sea surface temperature, sea ice, and night marine air temperature since the late nineteenth century. *J. Geophys. Res.-Atmos.*, **108** (D14), doi:{10.1029/2002JD002670}.
- Reynolds, R., N. Rayner, T. Smith, D. Stokes, and W. Wang, 2002: An improved in situ and satellite SST analysis for climate. *J. Clim.*, **15** (13), 1609–1625, doi:{10.1175/1520-0442(2002)015<1609:AIISAS>2.0.CO;2}.
- Rivera, E. R., and F. Dominguez, 2016: Projected changes in atmospheric river events in Arizona as simulated by global and regional climate models. *Clim. Dyn.*, **47** (5-6), 1673–1691, doi:{10.1007/s00382-015-2927-0}.
- Rodo, X., E. Baert, and F. Comin, 1997: Variations in seasonal rainfall in southern Europe during the present century: relationships with the North Atlantic Oscillation and the El Niño Southern Oscillation. *Clim. Dyn.*, **13** (4), 275–284, doi:{10.1007/s003820050165}.
- Rodriguez-Fonseca, B., and Coauthors, 2016: A review of ENSO influence on the North Atlantic. A non-stationary signal. *Atmosphere*, **7** (7), doi:{10.3390/atmos7070087}.
- Rodriguez-Puebla, C., A. Encinas, and J. Saenz, 2001: Winter precipitation over the Iberian peninsula and its relationship to circulation indices. *Hydrol. Earth Syst. Sci.*, **5** (2, SI), 233–244.
- Ropelewski, C., and M. Halpert, 1987: Global and regional scale precipitation patterns associated with the El Niño/Southern Oscillation. *Mon. Weather Rev.*, **115** (8), 1606–1626, doi:{10.1175/1520-0493(1987)115<1606:GARSPP>2.0.CO;2}.
- Ropelewski, C., and M. Halpert, 1996: Quantifying Southern Oscillation - precipitation relationships. *J. Clim.*, **9** (5), 1043–1059, doi:{10.1175/1520-0442(1996)009<1043:QSOPR>2.0.CO;2}.
- Schulzweida, U., 2017: *CDO User's Guide*. Max Planck Institute for Meteorology, Hamburg, Germany.
- Shaman, J., 2014a: The seasonal effects of ENSO on atmospheric conditions associated with European precipitation: model simulations of seasonal teleconnections. *J. Clim.*, **27** (3), 1010–1028, doi:{10.1175/JCLI-D-12-00734.1}.
- Shaman, J., 2014b: The seasonal effects of ENSO on European precipitation: observational analysis. *J. Clim.*, **27** (17), 6423–6438, doi:{10.1175/JCLI-D-14-00008.1}.
- Shaman, J., and E. Tziperman, 2011: An atmospheric teleconnection linking ENSO and southwestern European precipitation. *J. Clim.*, **24** (1), 124–139, doi:{10.1175/2010JCLI3590.1}.

- Shields, C. A., and J. T. Kiehl, 2016: Atmospheric river landfall-latitude changes in future climate simulations. *Geophys. Res. Lett.*, **43** (16), 8775–8782, doi:{10.1002/2016GL070470}.
- Sodemann, H., and A. Stohl, 2013: Moisture origin and meridional transport in atmospheric rivers and their association with multiple cyclones. *Mon. Weather Rev.*, **141** (8), 2850–2868, doi:{10.1175/MWR-D-12-00256.1}.
- Stainforth, D. A., M. R. Allen, E. R. Tredger, and L. A. Smith, 2007: Confidence, uncertainty and decision-support relevance in climate predictions. *Philos. Trans. R. Soc. A-Math. Phys. Eng. Sci.*, **365** (1857), 2145–2161, doi:{10.1098/rsta.2007.2074}.
- Stensrud, D., 2007: *Parametrization schemes*. Cambridge University Press, New York, USA.
- Sterl, A., 2004: On the (in)homogeneity of reanalysis products. *J. Clim.*, **17** (19), 3866–3873, doi:{10.1175/1520-0442(2004)017<3866:OTIORP>2.0.CO;2}.
- Sterl, A., G. J. van Oldenborgh, W. Hazeleger, and G. Burgers, 2007: On the robustness of ENSO teleconnections. *Clim. Dyn.*, **29** (5), 469–485, doi:{10.1007/s00382-007-0251-z}.
- Stickler, A., and Coauthors, 2014: ERA-CLIM historical surface and upper-air data for future reanalyses. *Bull. Amer. Meteorol. Soc.*, **95** (9), 1419–1430, doi:{10.1175/BAMS-D-13-00147.1}.
- Stocker, T. F., and Coauthors, 2013: *Climate Change 2013: The Physical Science Basis*. Cambridge University Press, Cambridge, UK, 1535 pp.
- Straus, D., and J. Shukla, 2002: Does ENSO force the PNA? *J. Clim.*, **15** (17), 2340–2358, doi:{10.1175/1520-0442(2002)015<2340:DEFTP>2.0.CO;2}.
- Sturaro, G., 2003: A closer look at the climatological discontinuities present in the NCEP/NCAR reanalysis temperature due to the introduction of satellite data. *Clim. Dyn.*, **21** (3-4), 309–316, doi:{10.1007/s00382-003-0334-4}.
- Taylor, K. E., R. J. Stouffer, and G. A. Meehl, 2012: An overview of CMIP5 and the experiment design. *Bull. Amer. Meteorol. Soc.*, **93** (4), 485–498, doi:{10.1175/BAMS-D-11-00094.1}.
- Tebaldi, C., and R. Knutti, 2007: The use of the multi-model ensemble in probabilistic climate projections. *Philos. Trans. R. Soc. A-Math. Phys. Eng. Sci.*, **365** (1857), 2053–2075, doi:{10.1098/rsta.2007.2076}.
- Thorne, P. W., and R. S. Vose, 2010: Reanalyses suitable for characterizing long-term trends. Are they really achievable? *Bull. Amer. Meteorol. Soc.*, **91** (3), 353+, doi:{10.1175/2009BAMS2858.1}.

- Titchner, H. A., and N. A. Rayner, 2014: The Met Office Hadley Centre Sea Ice and Sea Surface Temperature data set, version 2: 1. Sea ice concentrations. *J. Geophys. Res.-Atmos.*, **119** (6), 2864–2889, doi:10.1002/2013JD020316.
- Toniazzo, T., and A. A. Scaife, 2006: The influence of ENSO on winter North Atlantic climate. *Geophys. Res. Lett.*, **33** (24), doi:{10.1029/2006GL027881}.
- Trenberth, K., 1997: The definition of El Niño. *Bull. Amer. Meteorol. Soc.*, **78** (12), 2771–2777, doi:{10.1175/1520-0477(1997)078<2771:TDOENO>2.0.CO;2}.
- Trenberth, K., G. Branstator, D. Karoly, A. Kumar, N. Lau, and C. Ropelewski, 1998: Progress during TOGA in understanding and modeling global teleconnections associated with tropical sea surface temperatures. *J. Geophys. Res.-Atmos.*, **103** (C7), 14 291–14 324, doi:{10.1029/97JC01444}.
- Trenberth, K., and J. Hurrell, 1994: Decadal atmosphere-ocean variations in the Pacific. *Clim. Dyn.*, **9** (6), 303–319, doi:{10.1007/BF00204745}.
- Trenberth, K., and D. Paolino, 1980: The Northern Hemisphere sea-level pressure data set: trends, errors and discontinuities. *Mon. Weather Rev.*, **108** (7), 855–872, doi:{10.1175/1520-0493(1980)108<0855:TNHSLP>2.0.CO;2}.
- Trenberth, K. E., and D. J. Shea, 2006: Atlantic hurricanes and natural variability in 2005. *Geophys. Res. Lett.*, **33** (12), doi:{10.1029/2006GL026894}.
- Trigo, R., D. Pozo-Vazquez, T. Osborn, Y. Castro-Diez, S. Gamiz-Fortis, and M. Esteban-Parra, 2004: North Atlantic oscillation influence on precipitation, river flow and water resources in the Iberian peninsula. *Int. J. Climatol.*, **24** (8), 925–944, doi:{10.1002/joc.1048}.
- Uppala, S., and Coauthors, 2005: The ERA-40 re-analysis. *Q. J. R. Meteorol. Soc.*, **131** (612, B), 2961–3012, doi:{10.1256/qj.04.176}.
- van Den Dool, H. M., 1994: Searching for analogues, how long must we wait? *Tellus A*, **46**, 314–324.
- von Salzen, K., and Coauthors, 2013: The Canadian Fourth Generation Atmospheric Global Climate Model (CanAM4). Part I: representation of physical processes. *Atmos.-Ocean*, **51** (1), 104–125, doi:{10.1080/07055900.2012.755610}.
- von Storch, H., E. Zorita, J. Jones, Y. Dimitriev, F. Gonzalez-Rouco, and S. Tett, 2004: Reconstructing past climate from noisy data. *Science*, **306** (5696), 679–682, doi:{10.1126/science.1096109}.
- Walker, G. T., 1923: Correlation in seasonal variations of weather: a preliminary study of world weather. *Mem. Indian Meteorol. Dep.*, **24** (VIII), 75–131.

- Walker, G. T., 1924: Correlation in seasonal variation of weather: a further study of world weather. *Mem. Indian Meteorol. Dep.*, **24 (XI)**, 225–232.
- Walker, G. T., and E. W. Bliss, 1932: World weather v. *Mem. R. Meteorol. Soc.*, **4 (36)**, 53–84.
- Wallace, J., and D. Gutzler, 1981: Teleconnections in the geopotential height field during the Northern Hemisphere winter. *Mon. Weather Rev.*, **109 (4)**, 784–812, doi:{10.1175/1520-0493(1981)109<0784:TITGHF>2.0.CO;2}.
- Wallace, J., E. Rasmusson, T. Mitchell, V. Kousky, E. Sarachik, and H. von Storch, 1998: The structure and evolution of ENSO-related climate variability in the tropical Pacific: lessons from TOGA. *J. Geophys. Res.-Oceans*, **103 (C7)**, 14 241–14 259, doi:{10.1029/97JC02905}.
- Wang, C., and D. Enfield, 2001: The tropical Western Hemisphere warm pool. *Geophys. Res. Lett.*, **28 (8)**, 1635–1638, doi:{10.1029/2000GL011763}.
- Wang, C., and D. Enfield, 2003: A further study of the tropical Western Hemisphere warm pool. *J. Clim.*, **16 (10)**, 1476–1493, doi:{10.1175/1520-0442-16.10.1476}.
- Wang, J., H. Cole, D. Carlson, E. Miller, K. Beierle, A. Paukkunen, and T. Laine, 2002: Corrections of humidity measurement errors from the Vaisala RS80 radiosonde - application to TOGA COARE data. *J. Atmos. Ocean. Technol.*, **19 (7)**, 981–1002, doi:{10.1175/1520-0426(2002)019<0981:COHMEF>2.0.CO;2}.
- Warner, M. D., C. F. Mass, and E. P. Salathe, Jr., 2015: Changes in winter atmospheric rivers along the North American west coast in CMIP5 climate models. *J. Hydrometeorol.*, **16 (1)**, 118–128, doi:{10.1175/JHM-D-14-0080.1}.
- Wilks, D. S., 2006: *Statistical methods in the atmospheric sciences*. 2nd ed., Elsevier Academic Press, Amsterdam, the Netherlands.
- Winckler, J., 1960: Balloon study of high-altitude radiations during the International Geophysical Year. *J. Geophys. Res.*, **65 (5)**, 1331–1359, doi:{10.1029/JZ065i005p01331}.
- Yulaeva, E., and J. Wallace, 1994: Signature of ENSO in global temperature and precipitation fields derived from the Microwave Sounding Unit. *J. Clim.*, **7 (11)**, 1719–1736, doi:{10.1175/1520-0442(1994)007<1719:TSEOEIG>2.0.CO;2}.
- Zhang, Y., J. Wallace, and D. Battisti, 1997: ENSO-like interdecadal variability: 1900–93. *J. Clim.*, **10 (5)**, 1004–1020, doi:{10.1175/1520-0442(1997)010<1004:ELIV>2.0.CO;2}.
- Zhu, Y., and R. Newell, 1994: Atmospheric rivers and bombs. *Geophys. Res. Lett.*, **21 (18)**, 1999–2002, doi:{10.1029/94GL01710}.

- 
- Zhu, Y., and R. Newell, 1998: A proposed algorithm for moisture fluxes from atmospheric rivers. *Mon. Weather Rev.*, **126** (3), 725–735, doi:{10.1175/1520-0493(1998)126<0725:APAFMF>2.0.CO;2}.